RECONSTRUCTION OF PROTONS IN THE TOTEM ROMAN POT DETECTORS AT THE LHC

A thesis submitted to The University of Manchester for the degree of
Doctor of Philosophy
in the Faculty of Engineering and Physical Sciences.

2008

HUBERT NIEWIADOMSKI

SCHOOL OF PHYSICS AND ASTRONOMY

Contents

The dissertation contains 42720 words.

List of Tables

List of Figures

Abstract

The University of Manchester
Hubert Niewiadomski
Doctor of Philosophy

RECONSTRUCTION OF PROTONS IN THE TOTEM
ROMAN POT DETECTORS AT THE LHC

5 June 2008

The TOTEM experiment at the LHC will measure the total proton-proton cross-section with precision of 1 %, elastic proton scattering over a wide range in momentum transfer $-t \cong p^2\theta^2$ up to 10 GeV^2 and diffractive dissociation, including single, double and central diffraction topologies. The total cross-section will be measured with the luminosity independent method that requires simultaneous measurements of the total inelastic rate and the elastic proton scattering down to squared four-momentum transfers of a few 10^{-3} GeV^2, corresponding to leading protons scattered in angles of microradians from the interaction point. This will be achieved using the T1 and T2 telescopes together with the Roman Pot devices. The Roman Pots will be equipped with silicon microstrip detectors of an innovative structure at the detector edge reducing the conventional dead width of 0.5 – 1 mm to 50 – 60 μm, compatible with the requirements of the experiment. This dissertation reports on the tracking performance of the Roman Pots in view of the physics programme of TOTEM. Performance tests of the silicon detectors are referred. The multidimensional polynomial model of the LHC optical functions is introduced and the influence of the LHC optics on the proton acceptance and reconstruction resolution is analysed. Finally the thesis presents the simulation and reconstruction software of the Roman Pot detectors in the LHC environment and its application to the studies of the selected TOTEM running scenarios.

Declaration

No portion of the work referred to in the thesis has been submitted in support of an application for another degree or qualification of this or any other university or other institute of learning.

Copyright statement

Acknowledgements

Many people have contributed directly or indirectly to the work presented in this thesis. Let me mention a few.

I would like to thank my CERN supervisors: Prof. Dr. Karsten Eggert, the Spokesman of TOTEM, and Valentina Avati, for all your knowledge, care, enormous help, thesis reading and the time you spent giving me explanations and plenty of good advices.

I am indebted to Dr. Cinzia Da Via and Prof. Dr. Stephen Watts — my supervisors from Manchester University, for their advices, supervision, for enormous help, discussions and also for the thesis reading.

I am gratefull to all the people with whom I have been developing the TOTEM software. I would like to express my gratitude especially to Leszek Grzanka, Dr. Fabrizio Ferro and Jan Kaspar, and also to Dr. Kenneth Oesterberg, Dr. Giuseppe Latino, Mirko Beretti and Erik Bruecken. Thank you for your help and collaboration.

Also, I would like to stress out how pleasant it was to work in these years in the CERN group of the TOTEM experiment directed by enthusiastic Prof. Dr. Ernst Radermacher and Prof. Dr. Karsten Eggert. Let me thank to all the people from whom I have learnt a lot about physics, semiconductors, electronics, detectors, LHC optics, simulations, software and various other aspects of the TOTEM experiment: Dr. Gennaro Ruggiero, Dr. Mario Deile, Dr. Walter Snoeys, Gueorgui Antchev, Dr. Simone Giani, Dr. Emilio Radicioni, Prof. Dr. Risto Orava, Dr. Paul Aspell and F. Lucas Rodriguez.

Let me also thank all my friends for your patience and for all the great times we had together during these years. Let me also thank Prof. Gilles Cachemaille, Ave Sikk, Prof. Danielle Borst and the Director Philippe Dinkel from Geneva Conservatory of Music for their patience and understanding.

I would like to express my deep gratitude to my family, my parents Jadwiga and Zdzisław, my brother Karol and my grandparents Janina and Antoni. I do not think that without your support this work would have been possible. I would also like to thank my uncle Krzysztof for "A Brief History of Time" by Hawking.

Finally, I would like to greatly acknowledge CERN, the TOTEM Collaboration, the University of Manchester and the University of Brunel for funding this thesis.

Geneva, June 2008

Hubert Niewiadomski

The Author

Hubert Niewiadomski was born on 3 March 1979 in Siedlce, Poland. In years 1994–1998 he was granted the scholarschip of Polish Children's Fund. In 1998 he won the National Physics Competition for Secondary School Students. In years 1998–2003 he was a student of the Faculty of Electronics and Information Technology of Warsaw University of Technology. During that time he was involved in the research carried out by Prof. Tadeusz Łuba and Dr. Piotr Sapiecha in the Division of Telecommunications Fundamentals in the field of logic synthesis, pattern recognition, machine learning and artificial neural networks. He was granted several awards by the University and by the Ministry of Education. In 2003 he graduated with highest distinction with the Master Thesis titled "Serial Decomposition of Feedforward Neural Networks".

Since 2003 Hubert Niewiadomski has been working in the CERN group of the TOTEM experiment. In years 2003–2007 he participated in the fixed target and coasting beam tests of the "edgeless" silicon detectors, for which he prepared the analysis and (partially) the monitoring software. After the beam tests, basing on the acquired data, he was studying the performance of the CTS/planar and 3D/planar microstrip detectors. In addition, he carried out the analysis of the first TOTEM GEM detector tests.

Hubert Niewiadomski also actively participated in the development of the TOTEM software. He prepared the majority of the simulation and the reconstruction software of the Roman Pot detectors. This includes the full Geant4 geometry model of the Roman Pots, the simulation of signal response of silicon detectors and the readout chips, the LHC proton transport modeling and, finally, proton kinematics reconstruction based on the Roman Pot tracks detected in the Roman Pots. With the application of this software he performed numerous analyses of proton acceptance and kinematics reconstruction resolution for various TOTEM running scenarios.

Hubert Niewiadomski is also a student of the Vocal Department of Geneva Conservatory of Music and is the organist of the Polish Catholic Mission is Switzerland.

Dominus possedit me in initio viarum suarum, antequam quidquam faceret a principio. Ab aeterno ordinata sum, et ex antiquis, antequam terra fieret. Nondum erant abyssi et ego iam concepta eram: necdum fontes aquarum eruperant: necdum montes gravi mole constiterant: ante colles ego parturiebar: adhuc terram non fecerat, et flumina, et cardines orbis terrae. Quando praeparabat caelos, aderam: quando certa lege et gyro vallabat abyssos: quando aethera firmabat sursum, et librabat fontes aquarum: quando circumdabat mari terminum suum, et legem ponebat aquis, ne transirent fines suos; quando appendebat fundamenta terrae. Cum eo eram cuncta componens: et delectabar per singulos dies, ludens coram eo omni tempore, ludens in orbe terrarum, et deliciae meae esse cum filiis hominum. Nunc ergo filii, audite me: Beati qui custodiunt vias meas. Audite disciplinam, et estote sapientes, et nolite abicere eam. Beatus homo qui audit me, et qui vigilat ad fores meas quotidie, et observat ad postes ostii mei. Qui me invenerit, inveniet vitam, et hauriet salutem a Domino.

Liber Proverbiorum 8. 23-35

To my Parents and my Brother

Chapter 1

Introduction

The TOTEM [1, 2] experiment will measure the total proton-proton cross-section with a luminosity-independent method and study elastic and diffractive scattering at the LHC [8, 9]. To achieve optimum forward coverage for charged particles emitted by the pp collisions in the interaction point IP5, two tracking telescopes, T1 and T2, will be installed on each side in the pseudorapidity region $3.1 \leq |\eta| \leq 6.5$, and Roman Pot (RP) stations will be placed in the proximity of the LHC beams at distances of $\pm 147\,\mathrm{m}$ and $\pm 220\,\mathrm{m}$ from IP5. The TOTEM experiment is described in Chapter 3, while the LHC accelerator is described in Chapter 2.

Detailed understanding of the Roman Pot tracking performance is crucial for the physics programme of TOTEM and is the subject of this thesis.

The Roman Pots are special movable beam-pipe insertions designed to detect leading protons at a few millimetres from the beam centre. The proton detectors in the Roman Pots (Section 4.3) are silicon devices designed by TOTEM with the specific objective of reducing the insensitive area at the edge facing the beam to only a few tens of microns. High efficiency up to the physical detector border is an essential feature in view of maximising the experiment's acceptance for protons scattered elastically or diffractively at the interaction point at polar angles down to a few microradians. The beam tests of this devices and their edge behaviour studies, done by the candidate, are reported in Chapter 5.

The physics acceptance and measurement capabilities of the RP devices strongly depend upon the LHC optics which is determined by the machine lattice configuration, which is discussed in detail in Chapter 6. As a result, the simulation and reconstruction software has to be based on the software model of the LHC proton transport. Since TOTEM is interested in measurements of protons in wide range of four momentum transfer squared ($0.001 < -t < 10\,\mathrm{GeV}^2$) and large interval

of fractional momentum loss ($0 < -\xi < 0.25$), the emerging nonlinearities of the machine optical functions have to be treated precisely. In order to avoid the time consuming proton tracking though the accelerator lattice, a software package able to find automatically the multidimensional polynomial approximation of the proton LHC transport, for all the TOTEM running conditions, has been developed by the candidate and is reported in Section 6.4.

The software capable of simulating the Roman Pot detectors in the LHC environment has been developed by the candidate and is described in Chapter 7. The geometry and the materials of the Roman Pots, as well as parts of the LHC beam-line, were defined in a Geant4 [3, 4] compliant way. The signal generation of silicon detectors and the response of the electronics has been modelled. The simulation software was used to study the performance of the Roman Pot in terms of proton interactions with its materials, which is reported in Section 7.5 and mainly to provide data for the physics reconstruction procedures.

The reconstruction software developed by the candidate is reported in Chapter 8. It can be provided with data originating from the simulation, from the test beam and from the real experiment. It is capable of finding the proton tracks in the RP devices and, with the use of the optics parameterisation, it reconstructs the proton kinematics. In addition, the RP reconstruction software can be used in the future for common TOTEM-CMS running [5]. It is coded in a commom software framework and can incorporate CMS data, such as primary vertex postion reconstructed with CMS central detector.

Finally, the simulation and the reconstruction packages were used together in order to perform the acceptance and the resolution studies of reconstruction with Roman Pots. The selected results are presented in Chapter 9. In Section 9.1, the acceptance and the resolution studies for the $\beta^* = 90\,\mathrm{m}$ optics are reported. Section 9.2 discusses the potential physics performance of a new studied location of the TOTEM near-beam detectors in the IR3 region. In this case the simulations were carried out with the $\beta^* = 0.5\,\mathrm{m}$ optics. The proton acceptance and reconstruction resolution, based on the performed analyses for all the key running scenarios, is summarised in Section 9.3.

Chapter 2

The Large Hadron Collider

The motivation to construct the Large Hadron Collider [8] (LHC) at the European Center for Particle Physics (CERN) comes from the fundamental questions in Particle Physics. The complete understanding of the Standard Model [10] and the search of the phenomena beyond it requires a high energy and a high luminosity collider.

2.1 Objectives of the Large Hadron Collider

Our current understanding of the Universe is incomplete. The Standard Model of particles and forces summarises our present knowledge of particle physics. The Standard Model has been tested by various experiments and it has proven particularly successful in anticipating the existence of previously undiscovered particles. However, it leaves many unsolved questions, which the LHC will help to answer [6, 7].

- It is observed that some particles are very heavy while others have no mass at all. The photon and the gluons are massless, while the $W^{\pm}$ and the Z^0 each weighs as much as 80 to 90 proton masses. The most massive fundamental particle found so far is the top quark. It weighs about the same as a nucleus of gold. The electron, on the other hand, is approximately 350,000 times lighter than the top quark, and the mass of the electron-neutrino is $< 3\,\mathrm{eV}$. Why is there such a range of masses? The Standard Model explains the origin of mass with the so-called Higgs mechanism which assumes that the whole of space is filled with a 'Higgs field'. Particles acquire their masses by interacting with this field. Particles that interact intensely with the Higgs field are heavy, while those that have feeble interactions are light. The Higgs

field has at least one new particle associated with it, the Higgs boson, which has not been observed yet. If such a particle exists, experiments at the LHC will be able to detect it.

- The Standard Model does not offer a unified description of all the fundamental forces, as it remains difficult to construct a theory of gravity similar to those for the other forces. Supersymmetry — a theory that hypothesises the existence of more massive partners of the standard particles we know — could facilitate the unification of fundamental forces. If supersymmetry is right, then the lightest supersymmetric particles should be found at the LHC.

- Cosmological and astrophysical observations have shown that all the visible matter accounts for only 4 % of the Universe. The search is open for particles or phenomena responsible for dark matter (23 %) and dark energy (73 %). A very popular idea is that dark matter is made of neutral — yet undiscovered — supersymmetric particles.

- The LHC will also help us to investigate the mystery of antimatter. Matter and antimatter must have been produced in the same amounts at the time of the Big Bang but from what we have observed so far, our Universe is made only of matter. Why? The LHC could help to provide an answer.

- Another question that will be addressed by the LHC is whether quarks and leptons are elementary particles as they seem to be today or if they are made up of sub-constituents. The LHC will also allow precise measurements and tests of the Standard Model (i.e. b and top-quark physics) due to the large available statistics.

- In addition to the studies of proton-proton collisions, heavy-ion collisions at the LHC will provide a window onto the state of matter that would have existed in the early Universe, called quark-gluon plasma. When heavy ions collide at high energies they form for an instant a fireball of hot, dense matter that can be studied by the experiments.

Six experiments will perform the high energy particle physics research in the LHC: A Large Ion Collider Experiment (ALICE), ATLAS, the Compact Muon Solenoid (CMS), the Large Hadron Collider beauty (LHCb) experiment, the Large Hadron Collider forward (LHCf) experiment and the TOTal Elastic and diffractive

cross section Measurement (TOTEM) experiment. ALICE, ATLAS, CMS and LHCb are installed in four huge underground caverns built around the four collision points of the LHC beams. TOTEM will be installed close to the CMS interaction point and LHCf will be installed near ATLAS. The locations of the experiments are visible in Figure 2.1.

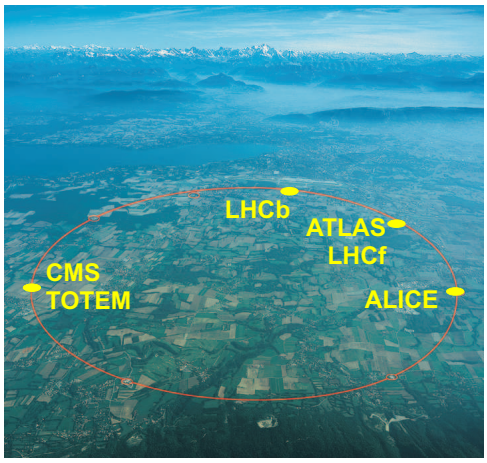

Figure 2.1: Aerial view of the LHC and its experiments.

- ALICE is a detector specialised in analysing lead-ion collisions. It will study the properties of quark-gluon plasma, a state of matter where quarks and gluons, under conditions of very high temperatures and densities, are no longer confined inside hadrons.

- ATLAS and CMS are general purpose detectors designed to cover the widest possible range of physics at the LHC, from the search for the Higgs boson to supersymmetry (SUSY) and extra dimensions.

- LHCb specialises in the study of the slight asymmetry between matter and antimatter present in interactions of B-particles (particles containing the b quark).

- LHCf is a small experiment that will measure particles produced very close to the direction of the beams in the proton-proton collisions at the LHC. The motivation is to test models used to estimate the primary energy of the ultra high-energy cosmic rays.

- The TOTEM experiment and its detectors will be discussed in details in the following sections of this dissertation.

2.2 The LHC

The full understanding of the physics reach of the TOTEM experiment requires a good understanding of the machine and of the beam parameters.

The LHC is a circular accelerator with 26.7 km circumference located in the existing tunnel of the LEP (Large Electron Positron collider) at $50 \div 100$ m under ground level [76, 8]. The LHC will reuse the existing accelerators as injectors. Prior to being injected into the main accelerator, the particles will be prepared through a series of machines that successively increase the particle energy levels. The first system will be the linear accelerator (Linac2) generating 50 MeV protons which will feed the Proton Synchrotron Booster (PSB). Protons will be then injected at 1.4 GeV into the Proton Synchrotron (PS). Finally, the Super Proton Synchrotron (SPS) will be used to increase the energy of protons from 26 GeV up to 450 GeV. Such protons will be injected to the LHC.

Two counter-rotating proton beams will circulate in separate beam pipes installed in the common magnets. The protons will be accelerated up to an energy of 7 TeV. After having reached this energy these two beams, moving in opposite directions, will cross at four interaction points (IP) along the beam line. These are represented by stars in Figure 2.2.

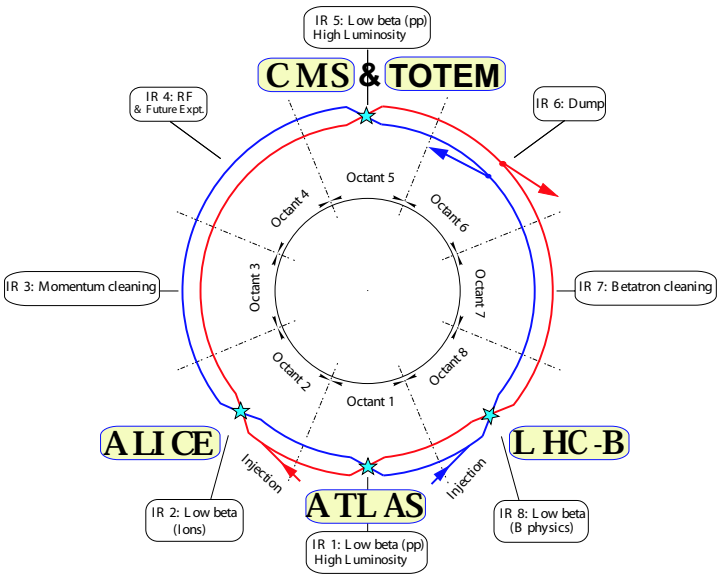

Figure 2.2: Schematic layout of the LHC. The four interaction points in which the beams circulating in opposite directions cross are indicated by stars.

The acceleration of protons up to such energies puts stringent technological

constraints on the machine. The strength of the accelerator dipole magnets depends on the bending radius of the beam trajectory[1]. The bending radius is determined by the LEP tunnel and a 8.33 T dipole magnetic field is needed in order to keep the proton beams on their trajectory. Such a strong magnetic field can only be achieved at an acceptable cost using superconducting technology [11]. The LHC magnet coils are made of niobium-titanium cables which are cooled down to 1.9 K with superfluid helium. A summary of the most important nominal machine parameters is given in Table 2.1. A detailed information on LHC design and operating conditions can be found in [9].

Beam Energy	TeV	7
Injection energy	TeV	0.45
Dipole field	T	8.33
Number of dipole magnets		1232
Number of main quadrupoles		392
Number of corrector magnets		about 8000
Protons per bunch, N_p		1.1×10^{11}
Number of bunches, n_b		2808
Circulating beam current	A	0.584
Norm. transverse emittance	μm rad	3.75
β^* (IP5)	m	0.55
Beam size (IP5)	μm	16.7
Beam divergence (IP5)	μrad	30.3
Luminosity (IP5)	$\mathrm{cm}^{-2}\mathrm{s}^{-1}$	10^{34}
Stored beam energy	MJ	362
Total stored energy	GJ	$\sim$1

Table 2.1: The LHC main nominal parameters [9]. The beam size, the beam divergence and the luminosity are given for the IP5 interaction point.

The energy stored in the superconducting magnets is very high and can potentially cause severe damages, when the superconducting state suddenly disappears. The resistive transition from the superconducting to the normal-conducting state is called *quench*. A quench occurs when part of the superconducting coil ceases to be superconducting. This can happen when the energy deposited by the entering particles heats up locally the magnet material so that it leaves the superconducting state maintained at a temperature of $\sim$ 1.9 K. When this happens, that particular spot is subject to rapid ohmic heating, which raises the temperature of the surrounding regions. This pushes these into the normal state as well, which leads

[1]The needed dipole bending magnetic field B is given by $B = \frac{3.335pc}{\varrho}\frac{\mathrm{Tm}}{\mathrm{GeV}}$, where p is the momentum of the proton, c is the speed of light and ϱ is the bending radius.

to more heating. The entire magnet rapidly becomes normal. The magnet can be damaged by localised heating, large mechanical forces or excessive voltages. A reliable active quench protection circuit is needed to bring safely the current down to zero when a quench occurs.

The vacuum inside the beam pipe will be as low as 10^{-11} Pa to keep the number of collisions of the beam particles with residual gas molecules present in the beam pipe as low as possible.

When two bunches cross in the centre of a physics detector only a tiny fraction of the particles collide to produce the events. The event rate R in a collider is proportional to the interaction cross section σ and the factor of proportionality is called *luminosity*:

$$R = \mathcal{L}\sigma. \tag{2.1}$$

In order to observe the phenomena of very low cross-section (like the Higgs boson) with sufficiently high statistics, it is important to reach the highest possible luminosity.

The luminosity $\mathcal{L}$ is defined by the machine parameters as

$$\mathcal{L} = f n_b \frac{N_p^1 N_p^2}{4\pi\sigma_x^*\sigma_y^*}, \tag{2.2}$$

where f is the revolution frequency (11246 Hz, determined by the circumference of the LEP tunnel) and σ_x^*, σ_y^* are the horizontal and vertical beam sizes at the interaction point, respectively. The two beams are composed of n_b bunches of N_p^1 and N_p^2 protons respectively. For the target LHC runs, $N_p^1 \cong N_p^2 \cong 0.1 \cdot 10^{11}$ – $1.1 \cdot 10^{11}$, $n_b = 43$ – 2835 and $\sigma_x^* = \sigma_y^* = 16.7\,\mu$m. The beam sizes and thus the luminosity depend on the configuration of the magnets which act on the beams like optical elements. This is described in more details in Section 6.2.

The parameters given in Table 2.1 correspond to the target luminosity of the LHC. The centre of mass energy of colliding proton pair will be $\sqrt{s} = 14$ TeV. By adjusting the beam parameters, the luminosity can be varied within the range $\mathcal{L} = 10^{28} - 10^{34}\,\mathrm{cm^2 s^{-1}}$.

Estimation of the luminosity directly from the beam parameters, using Equation 2.2, does not lead to precise results and more accurate methods need to be applied. The TOTEM experiment will measure the LHC luminosity via the Optical Theorem (see Section 3.1.1). For some running scenarios a precision of 1 % should be achieved.

Chapter 3

The TOTEM experiment

The TOTEM experiment [1, 12, 13] will measure the total proton-proton cross-section with the luminosity-independent method based on the Optical Theorem, which requires a detailed study of the elastic scattering cross-section down to a squared four-momentum transfer[1] of $|t| \sim 10^{-3}\,\mathrm{GeV}^2$ and the measurement of the total inelastic rate. Furthermore, TOTEM's physics programme aims at a deeper understanding of the proton structure by studying elastic scattering with large momentum transfers, and via the diffractive processes — partly in cooperation with CMS [5], located at the same interaction point, IP5. Hence TOTEM focuses on physics complementary to the programmes of the general-purpose experiments at the LHC, and therefore had to design the detectors that will be capable of meeting the challenge of triggering and recording events in the very forward region.

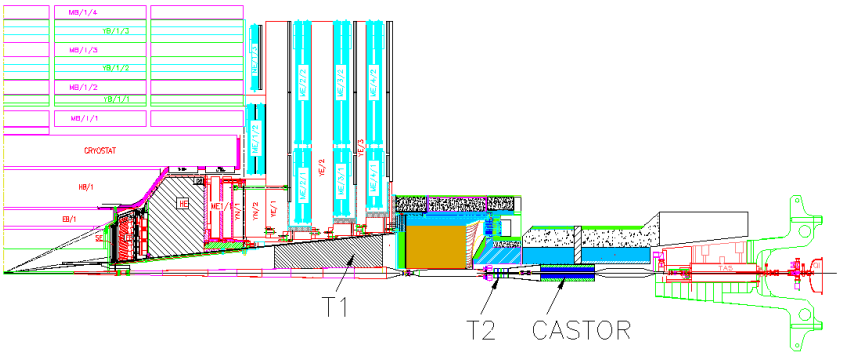

Figure 3.1: The CMS detector with the TOTEM forward trackers T1 and T2. Note also the planned forward calorimeter CASTOR (under CMS's responsibility).

[1]The four momentum transfer squared t is defined by $t \equiv (p' - p)^2$, where p and p' are the four momenta of the incoming and outgoing particles or systems of particles respectively.

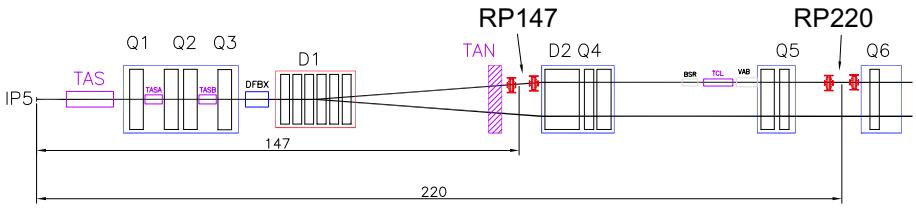

Figure 3.2: The LHC beam line and the Roman pots at 147 m (RP147) and 220 m (RP220).

To perform these measurements, TOTEM requires a good acceptance for particles produced at very small angles with respect to the beam. TOTEM's coverage in the pseudorapidity[2] range of $3.1 \leq |\eta| \leq 6.5$ on both sides of the interaction point is accomplished by two telescopes for inelastically produced particles (Figure 3.1). This is complemented by detectors in special movable beam-pipe insertions — so-called Roman Pots — placed at 147 and 220 m from the interaction point, designed to track leading protons at a few mm from the beam centre (Figure 3.2).

The telescope closest to the interaction point (T1, centred at $z = 9$ m) consists of Cathode Strip Chambers CSC (Section 3.2.1), while the second one (T2, centred at 13.5 m) exploits newly developed Gas Electron Multipliers GEM detectors (Section 3.2.2). The proton detectors in the Roman Pots (Section 3.3 and Chapter 4) are silicon devices designed to suit the TOTEM requirements, with the specific objective of reducing the insensitive area at the edge towards the beam to only a few tens of microns. This efficiency up to the physical detector border is an essential feature in view of maximising the experiment's acceptance for protons scattered elastically or diffractively at polar angles down to a few microradians. In addition to these detector developments, special beam optics have been conceived to optimise proton detection in terms of acceptance and resolution (Section 6.3).

The read-out of all TOTEM subsystems is based on the custom-developed digital VFAT chip [14]. The TOTEM Data Acquisition System (DAQ) is designed to be compatible with the CMS DAQ to make common data taking possible.

[2]The pseudorapidity η is defined by $\eta \equiv -\ln(\tan(\Theta/2))$, where Θ is the forward angle.

3.1 The physics programme

The TOTEM apparatus with its unique coverage at high rapidities[3] (Figure 3.3, left) is the ideal tool for studying forward phenomena, including elastic and diffractive scattering. Furthermore, since energy flow and particle multiplicity of generic inelastic events peak in the forward region (Figure 3.3, right), TOTEM accepts about 99.5 % of all non-diffractive minimum bias events.

The key application of the TOTEM acceptance at high rapidities is the luminosity-independent measurement of the total cross-section based on the Optical Theorem.

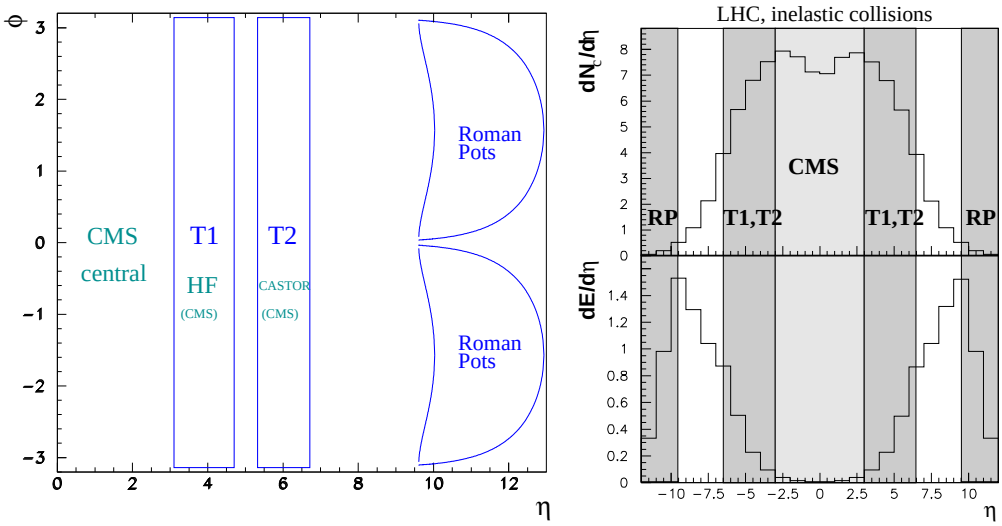

Figure 3.3: Left: Detector coverage in the pseudorapidity-azimuth plane. Right: pseudorapidity distribution of charged particle multiplicity and energy flow for generic inelastic collisions at 14 TeV.

3.1.1 Total *pp* cross-section

A precise measurement of the total pp cross-section σ_{tot} and of the elastic scattering over a large range in the squared four-momentum transfer t (Section 3.1.2) is of primary importance for distinguishing between different models of soft proton interactions.

[3]The rapidity y is defined as $y = \frac{1}{2}\ln\left(\frac{E+p_z}{E-p_z}\right)$, where E is the total energy and p_z is the momentum component parallel to the beam. For particle momentum $p \gg m$, the rapidity and pseudorapidity are approximately equal: $y \approx -\ln(\tan(\Theta/2)) \equiv \eta$. m is the rest mass of the particle and Θ is the forward angle.

It was shown in the past that the proton-proton total cross-section $\sigma_{tot}(s)$[4] increases with increasing centre of mass energy $\sqrt{s}$. First evidence was given by measurements done at the CERN intersecting storage rings (ISR) for $\sqrt{s}$ between 30 GeV and 62 GeV [16]. Since then, measurements have been performed at $\sqrt{s} =$ 1.8 TeV (CDF [17] and E811 [18]) and up to $\sim$ 30 TeV with cosmic rays [19]. Figure 3.4 summarises the existing measurements of σ_{tot} from low energies up to collider and cosmic-ray energies. The solid error band shows the statistical errors to the best fit with $\sigma_{tot} \propto \ln^{\gamma}(s)$ and $\gamma = 2.0$. Unfortunately the large uncertainties of the cosmic-ray data and the 2.6 standard-deviations discrepancy between the two final results from TEVATRON [20] make an extrapolation to higher energies uncertain, leaving a wide range for the expected value of the total cross-section at the LHC energy of $\sqrt{s} = 14$ TeV, typically from 90 to 130 mb. Taking into account all available data, the COMPETE collaboration [21] has made an overall fit of the energy dependence of the total cross-section and the ratio ρ of the real to imaginary parts of the elastic scattering amplitude, and predict for the LHC:

$$\sigma_{tot} = 111.5 \pm 1.2^{+4.1}_{-2.1}\,\text{mb}\,, \quad \rho = 0.1361 \pm 0.0015^{+0.0058}_{-0.0025}\,. \tag{3.1}$$

The precision of the extrapolation is dominated by the ambiguity in the TEVATRON data (second error).

Many models have been developed to describe the proton-proton total cross-section (see [1] and the references therein). A theoretical attempt is provided by the *geometrical model* in which high-energy scattering is seen as the shadow of the absorption [22, 23, 24]. The interacting hadrons are viewed as extended objects made of some hadronic matter which is assumed to have the same shape as the electric charge distribution.

The *impact picture* [25] model predicts that σ_{tot} should increase as $\ln^2 s$ with increasing centre of mass energy $\sqrt{s}$. A schematic representation of the expanding proton in this impact picture is shown in Figure 3.5, where the proton core, almost completely absorbing (i.e. black), has a radius growing as $\ln s$, whereas the peripheral region, only partially absorbing (i.e. gray), has a width independent of s.

TOTEM will measure the total pp cross-section σ_{tot} and the luminosity $\mathcal{L}$ in-

[4]The centre of mass energy $\sqrt{s}$ is defined as: $s = (p_1 + p_2)^2 = (p_1' + p_2')^2$, where p_1, p_2 and p_1', p_2' are the 4-momenta of the incoming and outgoing elastically scattered protons. The four-momentum p is defined as $p = (E, \vec{p})$, where E is the energy and $\vec{p}$ is the 3-momentum of the particle. The Lorentz invariant product is defined as $p_1 p_2 \equiv E_1 E_2 - \vec{p}_1 \cdot \vec{p}_2$.

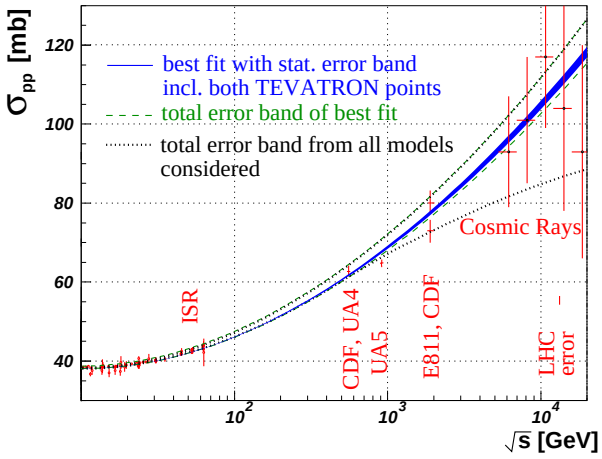

Figure 3.4: COMPETE fits [21] to all available pp and $p\bar{p}$ scattering data with statistical (blue solid) and total (green dashed) error bands, the latter taking into account the Tevatron ambiguity. The outermost curves (dotted) give the total error band from all parameterisations considered.

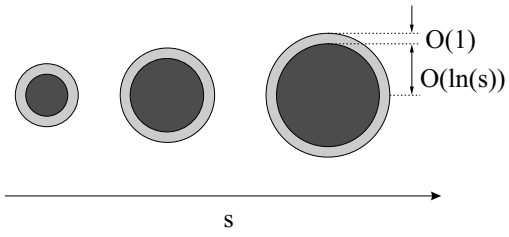

Figure 3.5: Schematic representation of the expanding proton according to the impact picture [26].

dependently by taking advantage of the Optical Theorem [27]:

$$\mathcal{L}\,\sigma_{tot}^2 = \frac{16\pi}{1+\rho^2}\cdot\left.\frac{\mathrm{d}N_{el}}{\mathrm{d}t}\right|_{t=0}. \tag{3.2}$$

With the additional relation

$$\mathcal{L}\,\sigma_{tot} = N_{el} + N_{inel} \tag{3.3}$$

one obtains a system of 2 equations which can be resolved for σ_{tot} or $\mathcal{L}$ independently of each other:

$$\sigma_{tot} = \frac{16\pi}{1+\rho^2}\cdot\frac{\mathrm{d}N_{el}/\mathrm{d}t|_{t=0}}{N_{el}+N_{inel}}, \tag{3.4}$$

$$\mathcal{L} = \frac{1+\rho^2}{16\pi}\cdot\frac{(N_{el}+N_{inel})^2}{\mathrm{d}N_{el}/\mathrm{d}t|_{t=0}} \tag{3.5}$$

Hence the quantities to be measured are the following:

- $\mathrm{d}N_{el}/\mathrm{d}t|_{t=0}$: The nuclear part of the elastic cross-section extrapolated to $t = 0$ (see Section 3.1.2). The expected uncertainty of the extrapolation depends on the acceptance for elastically scattered protons at a determined beam optics.

- The total elastic rate N_{el} measured by the Roman Pot system and completed by the extrapolation of the nuclear part $\mathrm{d}N_{el}/\mathrm{d}t$ to $t = 0$.

- The inelastic rate N_{inel} consisting of diffractive ($\sim$18 mb at LHC) and minimum bias ($\sim$65 mb at LHC) events. It will be measured by T1 and T2.

For the rate measurements it is important that all TOTEM detector systems have level-1 trigger capability. The parameter $\rho = \frac{\mathcal{R}[f_{el}(0)]}{\mathcal{I}[f_{el}(0)]}$, where $f_{el}(0)$ is the forward nuclear elastic amplitude, has to be taken from external theoretical predictions, e.g. [21]. Since $\rho \sim 0.14$ enters only in a $1 + \rho^2$ term, its impact is small.

At an early stage with non-optimal beams, TOTEM will measure the total cross-section and the luminosity with a precision of about 5 %. After having understood the initial measurements and with improved beams at $\beta^* = 1535\,\mathrm{m}$, a precision around 1 % should be achievable.

3.1.2 Elastic *pp* scattering

Much of the interest in large-impact-parameter collisions centres on elastic scattering and soft inelastic diffraction. High-energy elastic nucleon scattering represents the collision process in which the most precise data over a large energy range have been gathered [28].

The differential cross-section of elastic pp interactions at the LHC, as predicted by different models [29], is given in Figure 3.6. Large differences between the models are expected, and hence a high-precision measurement up to $|t| \cong 10\,\mathrm{GeV}^2$ will help to better understand the structure of the proton.

Increasing $|t|$ means looking deeper into the proton at smaller distances[5]. Several t-regions with different behaviour can be distinguished:

[5] Assuming the probing beam itself consists of pointlike particles, the resolution is limited by the de Broglie wavelength of these particles, which is $\lambda = \frac{h}{p}$, where p is the beam momentum and h is Planck's constant. Thus the beams of high momentum have short wavelengths and can have high resolution. By analogy to the optical microscope, the resolution becomes: $\Delta r \simeq \frac{\lambda}{\sin\Theta} = \frac{h}{p\sin\Theta} \simeq \frac{h}{\sqrt{|t|}}$, where Δr is the spatial resolution, Θ is the scattering angle and t is the four momentum transfer squared [30].

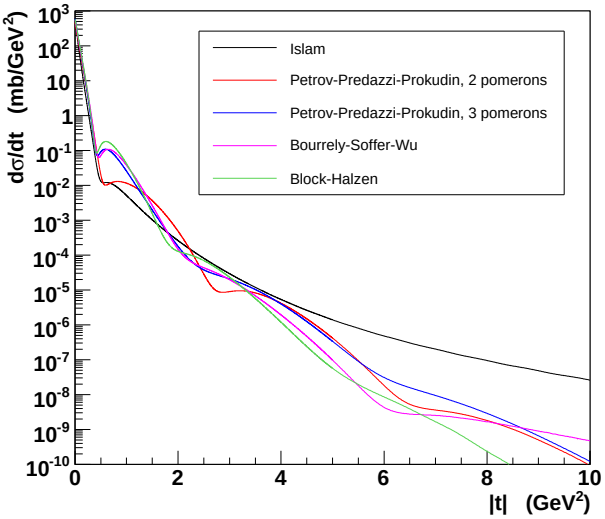

Figure 3.6: Differential cross-section of elastic scattering at 14 TeV as predicted by various models.

- $|t| < 6.5 \times 10^{-4}\,\mathrm{GeV}^2$ (at $\sqrt{s}$=14 TeV): The Coulomb region where elastic scattering is dominated by photon exchange: $d\sigma/\mathrm{d}t \sim 1/t^2$.

- $10^{-3}\,\mathrm{GeV}^2 < |t| < 0.5\,\mathrm{GeV}^2$: The nuclear region described in a simplified way by "single-Pomeron exchange"[6] with an approximately exponential cross-section $d\sigma/\mathrm{d}t \sim \mathrm{e}^{-B\,|t|}$ (Figure 3.7, left). This quasi-exponential domain is important for the extrapolation of the nuclear part $\mathrm{d}N_{el}/\mathrm{d}t$ of the differential counting-rate to $t = 0$, needed for the measurement of σ_{tot}. The t-dependence of the exponential slope $B(t) = \frac{d}{\mathrm{d}t} \ln \frac{d\sigma}{\mathrm{d}t}$ reveals slight model-dependent deviations from the exponential shape (Figure 3.7, right). This theoretical uncertainty contributes to the systematic error of the total cross-section measurement [2].

- Between the above two regions, the nuclear and Coulomb scattering interfere, complicating the extrapolation of the nuclear cross-section to $t = 0$.

- $0.5\,\mathrm{GeV}^2 < |t| < 1\,\mathrm{GeV}^2$: A region exhibiting the diffractive structure of the proton (diffractive peak).

- $|t| > 1\,\mathrm{GeV}^2$: The domain of central elastic collisions at high $|t|$, described by perturbative QCD, e.g. in terms of triple-gluon exchange with a predicted cross-section proportional to $|t|^{-8}$. The model dependence of the predictions

[6] Nuclear elastic and diffractive scattering are characterised by the exchange of hadronic colour singlets, for which the Pomeron is one model.

being very pronounced in this region, measurements will be able to test the validity of the different models.

The elastic scattering differential cross-section extends over 11 orders of magnitude and has therefore to be measured with several different optics scenarios. With different beam optics and running conditions (Section 6.3), TOTEM will cover the $|t|$-range from $2 \times 10^{-3}\,\mathrm{GeV}^2$ to about $10\,\mathrm{GeV}^2$.

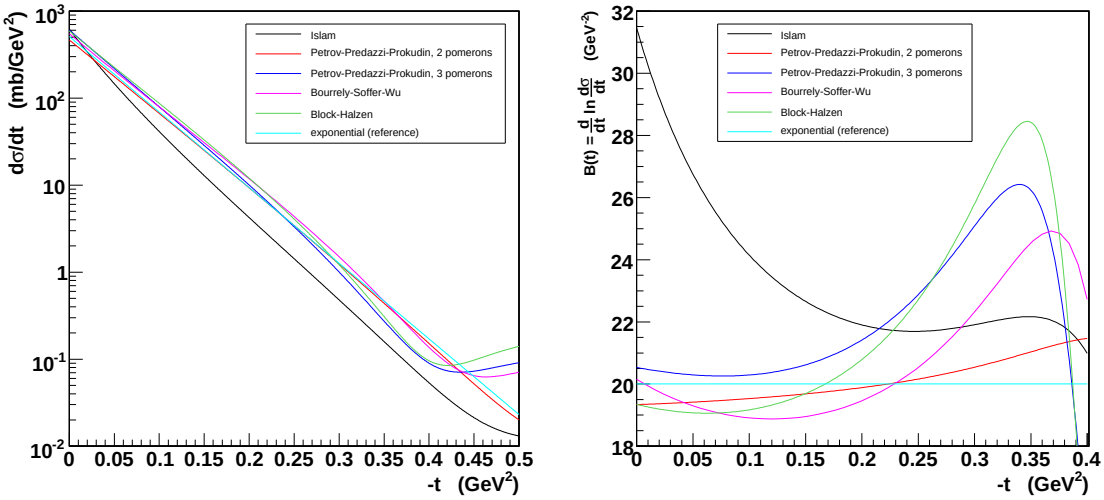

Figure 3.7: Left: Differential cross-section of elastic scattering at 14 TeV as predicted by various models, focussing on the quasi-exponential domain at low $|t|$. Right: Exponential slope of the differential cross-section. The deviations from a constant slope show how the cross-sections differ from a pure exponential shape.

3.1.3 Diffraction

The term *diffraction* in high-energy physics (or hadronic diffraction) is used in strict analogy with the familiar optical phenomenon that occurs when a beam of light meets an obstacle whose dimensions are comparable to its wavelength. To the extent that the propagation and the interaction of extended objects such as the hadrons are nothing but the absorption of their wave function caused by the many inelastic channels open at high energy, the use of the optical terminology seems appropriate. Diffractive scattering — comprising Single Diffraction, Double Diffraction, Central Diffraction (Double Pomeron Exchange), and higher order (Multi Pomeron) processes — represents about 15 % of the total cross-section at 14 TeV. Many details of these processes with close ties to proton structure and low-energy QCD are still not understood. The majority of diffractive events (Figure 3.8) exhibits intact (leading) protons in the final state, characterised by

their four-momentum transfer squared t and their fractional momentum loss $\xi \equiv \Delta p/p$. These protons can be detected in Roman Pot detectors far away from the interaction point. The other main signature of diffractive events — large gaps in the scattering products' rapidity distribution due to exchange of colour singlets (Pomerons) between the interacting protons — will be optimally exploitable when the detectors of CMS and TOTEM will be combined for common data taking with an unprecedented rapidity coverage, as discussed in [5]. However, already in stand-alone running TOTEM will be able to measure ξ-, t- and mass distributions in soft Double Pomeron and Single Diffraction events.

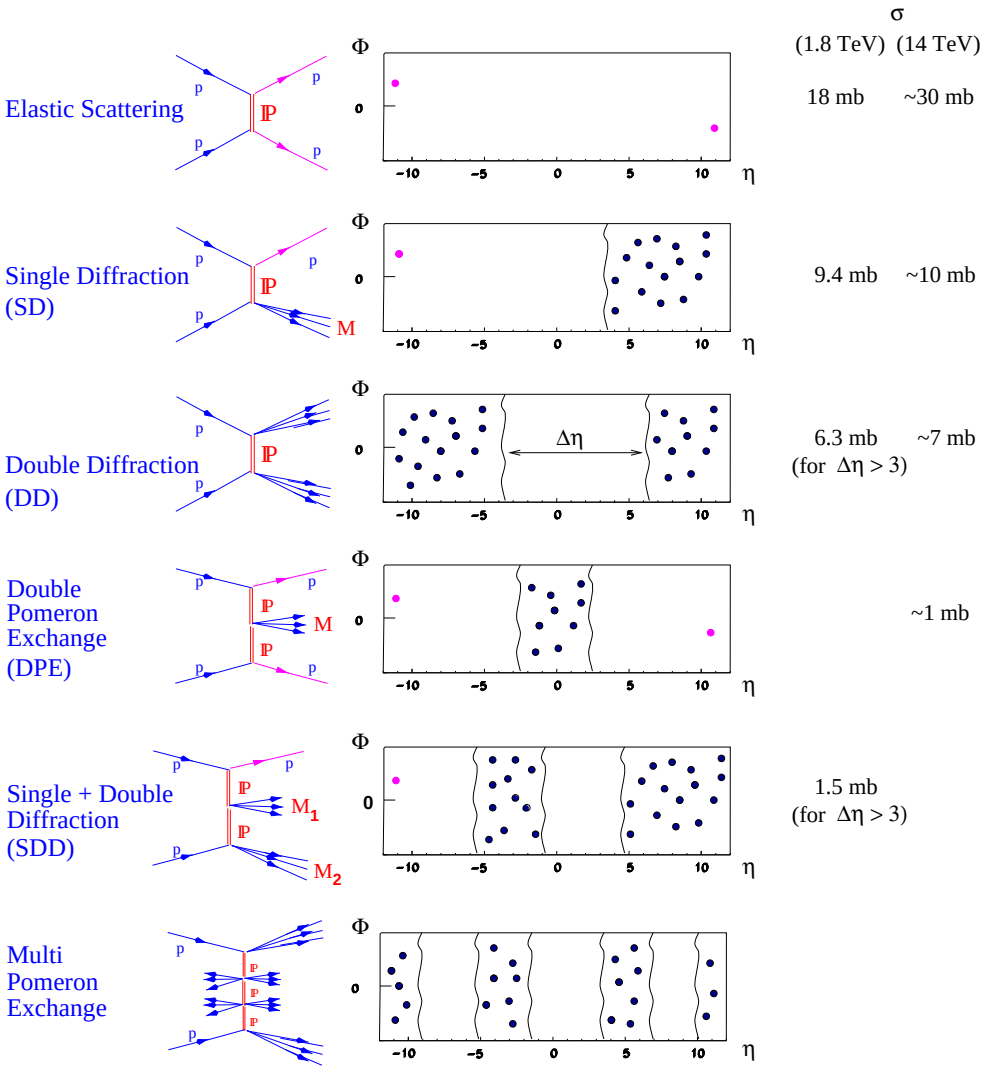

Figure 3.8: Diffractive process classes and their cross-sections measured at Tevatron and estimated for the LHC.

3.2 The inelastic detectors

The detectors dedicated to the measurement of the inelastic rate have to be in an angular range such as to detect particles from almost all events. The TOTEM forward telescopes cover a rapidity range of about 4 units and will be installed in the forward regions of CMS (Fig. 3.1) on both sides (arms) of the IP:

- T1 ($3.1 \leq |\eta| \leq 4.7$) is made of 5 planes per arm, each consisting of 6 trapezoidal Cathode Strip Chambers (CSC), and will be installed in the CMS End Caps between the vacuum chamber and the iron of the magnet, at a distance of 7.5 to 10.5 m from the IP.

- T2 ($5.3 \leq |\eta| \leq 6.5$) is made of 20 half circular sectors of GEM (Gas Electron Multiplier) detectors per arm and will be installed between the vacuum chamber and the inner shielding of the HF[7] calorimeter at an average distance of 13.5 m from the IP.

The main requirements of these detectors are:

- to provide a fully inclusive trigger for minimum bias and diffractive events, with an expected loss of a few per cent of the inelastic rate;

- to enable the reconstruction of the primary vertex of an event, in order to disentangle beam-beam events from the background via a partial event reconstruction (mainly the tracks coming from the primary vertex);

- a detector arrangement which is left-right symmetric with respect to the IP, in order to have a better control of the systematic uncertainties.

In addition to the measurement of the total inelastic rate, T1 and T2 will be key detectors for the study of inelastic processes either by TOTEM or by the joint CMS/TOTEM experiments [5]. At low luminosities ($\mathcal{L} < 10^{31}\,\mathrm{cm}^{-2}\mathrm{s}^{-1}$):

- The integrated inclusive Single Diffractive (SD) and Double Pomeron Exchange (DPE) cross-sections can be measured, as well as their t and M dependence (where M is the mass of the diffractive system). SD and DPE events have a clean signature in TOTEM and can be triggered requiring at least one track in T1/T2 in coincidence with the proton(s) detected in the Roman Pots.

[7] HF is a CMS forward hadron calorimeter.

- T1 and T2 contribute to the detection and measurement of the rapidity gaps in diffractive events, which may provide a complementary measurement of the fractional momentum loss of the surviving proton(s), as well as shed new light on the problem of the rapidity gap survival probability.

- The telescopes' coverage and granularity allow the measurement of the charged multiplicity in the forward region, providing important information for the cosmic ray physics community (mainly to tune their event generators).

At higher luminosity, in the range $10^{31} < \mathcal{L} < 10^{33}\,\mathrm{cm}^{-2}\mathrm{s}^{-1}$, T2 can be used in the joint CMS/TOTEM experiment for hard diffraction and forward physics studies. The possibility of exploiting T2 track information in the study of rare processes such as single-diffractive proton dissociation into three very forward jets is still under investigation.

3.2.1 T1 telescope

The T1 telescope, installed in two cone-shaped regions in the endcaps of CMS, at $\pm 7.5\,\mathrm{m}$ from the IP5, detects charged particles in the pseudo-rapidity range $3.1 \leq |\eta| \leq 4.7$. Each telescope consists of five *cathode strip chambers* [31, 32] (CSC), equally spaced in z and forms approximately a 2.7 m-long cone of the radius between 0.5 and 0.6 m (Figure 3.9).

A detector plane is composed of six CSC wire chambers covering roughly a region of 60° in ϕ. The overlap is provided between adjacent detectors to cover with continuous efficiency the approximately circular region of each telescope plane.

The cathode strip chamber is a multiwire proportional chamber whose two cathode planes are segmented into parallel strips. Under application of a suitable voltage, a particle crossing the detector generates an avalanche in the proximity of an anode wire, which induces on the cathode strips a charge signal. Recording the charge and finding the centroid of this charge distribution allows a precise determination of the position where the avalanche has developed.

The arrangement of strips and wires is presented in Figure 3.10. The cathode electrodes are parallel strips obtained as gold-plated tracks oriented at ±60° with respect to the direction of the wires. The anode of the detector is composed of gold-plated tungsten wires. The orientations of the cathode strips and of the anode wires allow for three measurements in the plane of the position of the avalanche. This provides three measured coordinates for each particle track, which significantly help to reduce the number of fake hits from random combinations ("ghosts").

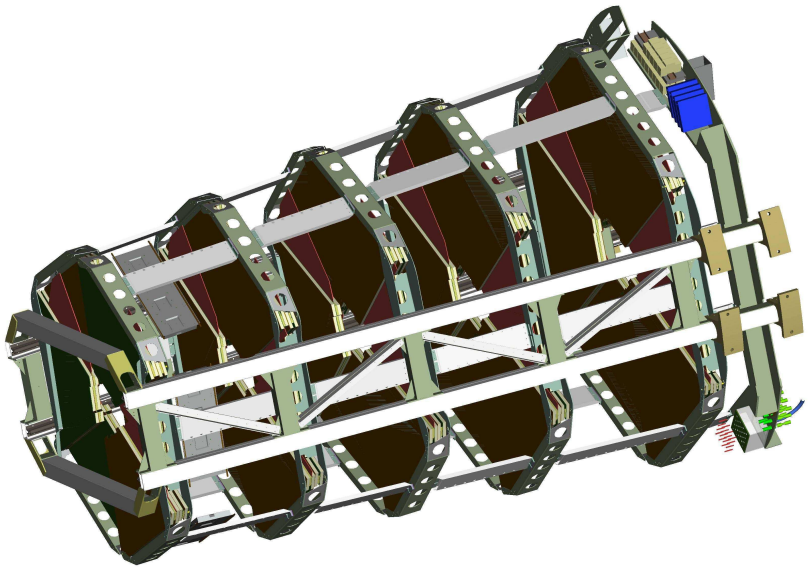

Figure 3.9: T1 assembly (one arm) with the support structure. Some of the spacers between the detector planes and one support bar for the cathode read-out electronics are visible. On the right-hand side, the service support frame and the fixation plates securing the whole assembly to the internal surface of the CMS flux return yoke can be seen.

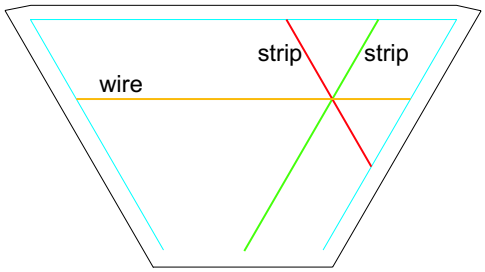

Figure 3.10: The arrangement of strips and wires in a detector plane.

The precision of the reconstructed space point is of the order of 0.5 mm. This allows the reconstruction of the primary collision vertex in the transverse plane within a few mm, good enough to discriminate between beam-beam and beam-gas events.

The main purpose of T1 is to contribute to the measurement of the inelastic pp cross section and thus of the total cross section (Section 3.1.1). Therefore the main requirement is an efficiency as close as possible to 100% in the luminosity regime ($\mathcal{L} \sim 10^{28}$ – $10^{29}\text{cm}^{-2}\text{s}^{-1}$) where the measurement will be performed. At $\mathcal{L} = 10^{28}\text{cm}^{-2}\text{s}^{-1}$, the inelastic interaction rate will be about 1 kHz. The average

number of charged particles per event in T1 is expected to be ~ 40.

Gas detectors of this kind are slow, but the response time for a CSC with a 10.0 mm gas gap is still compatible with the expected hit rates for TOTEM. Moreover, they have small material densities which is important because they are positioned in front of forward calorimeters.

The ageing properties of the TOTEM CSCs have been also tested. The detectors have not shown any loss of performance after irradiation with the accumulated dose equivalent to about 5 years of running at the luminosity of $10^{30}\text{cm}^{-2}\text{s}^{-1}$.

3.2.2 T2 telescope

The T2 telescopes, located at ± 13.5 m on both sides of IP5 (Figure 3.1), detect charged particles in the pseudorapidity range of $5.3 \leq |\eta| \leq 6.5$.

Generic requirements for the T2 (like for T1) include a fully inclusive trigger for diffractive events, hit pattern reconstruction for vertex finding to be used in discriminating against possible beam-gas background and for left-right symmetric alignment of telescopes for better control of the systematic effects.

The T2 telescope has been designed for good coverage of forward physics processes with varying beam conditions both at low luminosities (total cross-section and soft diffractive scattering) and at moderate luminosities (semi-hard diffractive scattering, low-x physics). Moreover, the T2 telescope is expected to operate up to luminosities of the order of $10^{33}\,\text{cm}^{-2}\text{s}^{-1}$ [1] where hard diffraction, heavy particle searches and physics beyond the standard model could be probed.

The gaseous electron multipliers (GEM) were selected for detectors of the T2 telescope thanks to their high rate capability, good spatial resolution, robust mechanical structure and excellent ageing characteristics.

In each T2 arm, 20 semi-circular GEM planes — with overlapping regions — are interleaved on both sides of the beam vacuum chamber to form ten detector planes of full azimuthal coverage (Figure 3.11). The GEMs are installed as pairs with a back-to-back configuration. This arrangement of active detector planes allows both track coordinates and local trigger — based on hit multiplicities and track routes pointing to the interaction region — to be obtained.

The shape of the GEM detector used in T2 telescope is semi-circular with an active area covering an azimuthal angle of 192° and extending from 43 mm up to 144 mm in radius from the beam axis (Figure 3.12).

Three GEM foils are used as a cascade in one detector (Figure 3.13) to reduce the discharge probability below 10^{-12} [33].

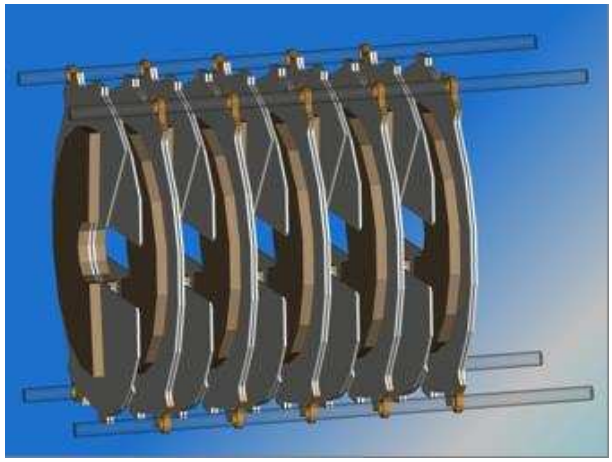

Figure 3.11: A CAD drawing depicting the arrangement of the 20 consecutive half-planes of Gaseous Electron Multiplier (GEM) detectors in one of the two T2 telescopes. In each detector layer, two GEM half-planes are slid together for maximal azimuthal angle coverage. With the ten double detector layers both high efficiency for detecting the primary tracks from the interaction point and efficient rejection of interactions with the LHC vacuum chamber is achieved.

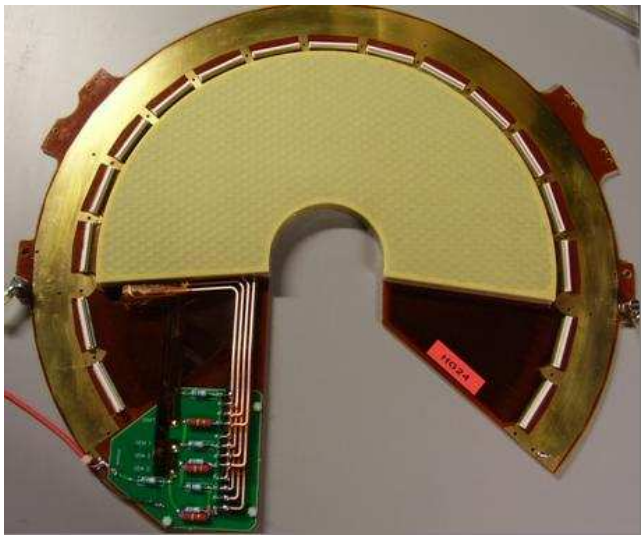

Figure 3.12: The TOTEM T2 GEM detector without front-end electronics and cooling pipes.

At the design value of the operating voltage, the gas amplification over all the three foils will be roughly 8000. The thickness of the drift space is 3 mm, whereas the transfer 1 and 2 and the induction gaps are all 2 mm (see Figure 3.13). The corresponding electric fields over the gaps are approximately 2.4 kV/cm and 3.6 kV/cm, respectively.

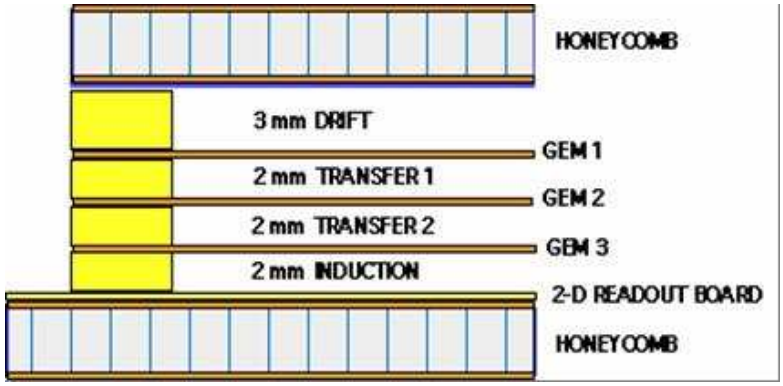

Figure 3.13: A side view of the T2 GEM detector structure: Three Gaseous Electron Multiplier (GEM) amplification stages are realised by three perforated and Cu-clad polyimide foils supported by honeycomb plates. A 3 mm drift space is followed by two 2 mm deep charge transfer regions (TRANSFER1 and TRANSFER2) and a 2 mm charge induction space. The large signal charges are collected, in two dimensions, by a read-out board underneath of the induction layer. The lightweight construction and support materials are chosen for low-Z material budget and mechanical robustness.

The readout board contains 2×256 concentric strips for the radial coordinates and a matrix of 1560 pads for azimuthal coordinates and for the T2 local trigger (Figure 3.14).

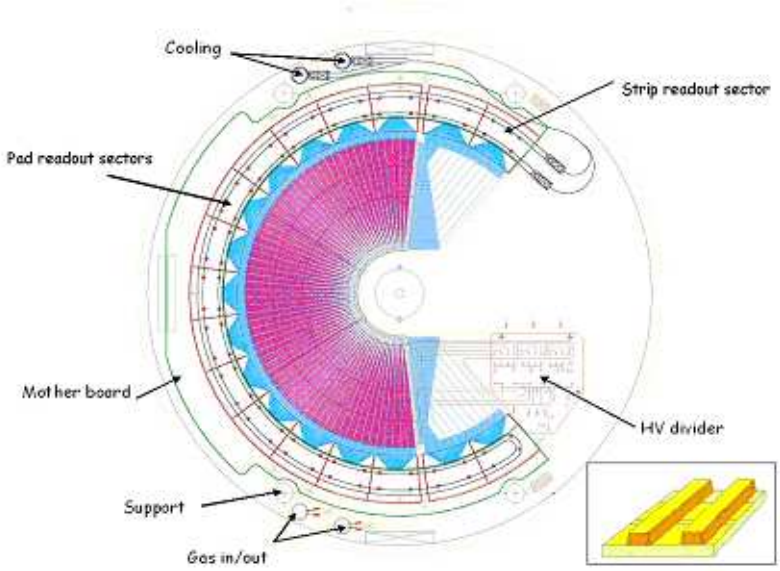

Figure 3.14: The design drawing of the TOTEM T2 GEM detector. The strip-pad structure of the readout is shown in the insert.

The strips lie on top of the pads. The width and spacing of the strips are 80 μm and 400 μm respectively. To reduce the occupancy, the strips are divided into two parts, each covering 96° in azimuthal angle.

The pads are divided into 65 radial sectors each containing 24 pads with sizes ranging from $2 \times 2\,\mathrm{mm}^2$ close to the vacuum chamber wall to $7 \times 7\,mm^2$ at the outer edge of the semi-circular planes.

3.3 Roman Pots in the LHC

The TOTEM's RP system is symmetric with respect to the interaction point IP5, allowing the detection of both surviving protons in elastic and central diffractive events. On each side, two stations of Roman Pots will be mounted on the beam pipes. The RP positions, with respect to the interaction point, were defined in an interplay with the development of the special optics used by TOTEM, with constraints given by the space available between the LHC machine components. The centre of the first station (RP147) is placed at 149.6 m from IP5, and the second (RP220) at 217.3 m. Between the two stations, the dipole magnet D2 provides a dispersion[8] difference which helps in momentum reconstruction. For local track reconstruction and angular trigger selections, each RP station is composed of two units. These units are separated by a distance which is limited by the presence of other beam elements. The stations RP147 and RP220 span distances of 2 m and 6 m respectively. Each RP unit consists of 3 pots, 2 approaching the beam vertically and 1 horizontally. In summary, a total of 8 identical Roman Pot units or 24 individual pots are installed for the TOTEM experiment at the LHC.

Figure 3.15 shows the design of a RP station (RP147). Each of the 2 units (Figure 3.16, left) is made of two vacuum chambers (Figure 3.16, right), one with two vertical pots and one with a single horizontal pot. The vacuum chamber of the vertical RP is also equipped with a Beam Position Monitor (BPM). BPM is a device capable of measuring the beam transverse position. The measurement is performed with four buttons. The beam position is obtained from the analysis of their electromagnetic pick-up signals.

The single horizontal pot in each unit serves 2 purposes. Firstly, given the difficulty of the alignment of the RPs with respect to each other, overlaps between the horizontal pots and the vertical one are foreseen in order to correlate their positions via common particle tracks (see Figure 3.17). Secondly, the horizontal

[8]Dispersion is discussed in Section 6.2.3.

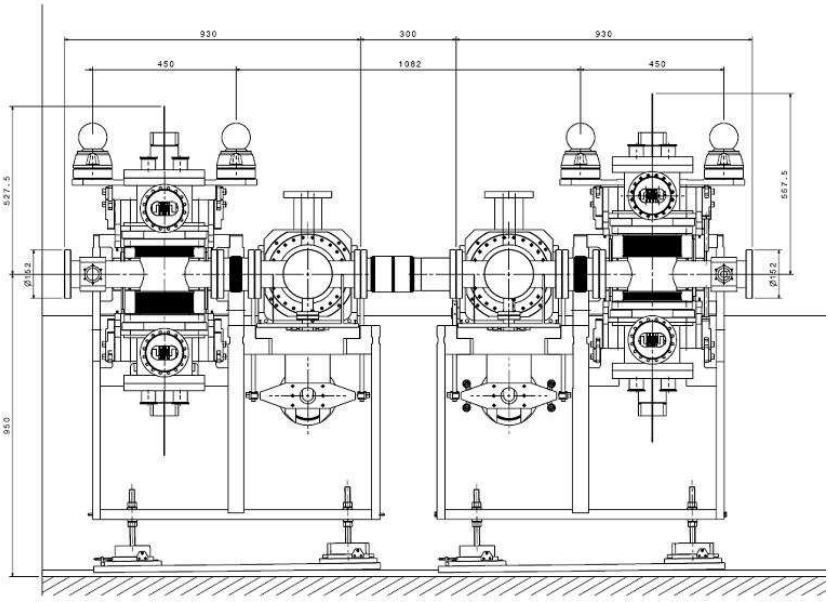

Figure 3.15: Design drawing of a RP station, i.e. an assembly of two RP units.

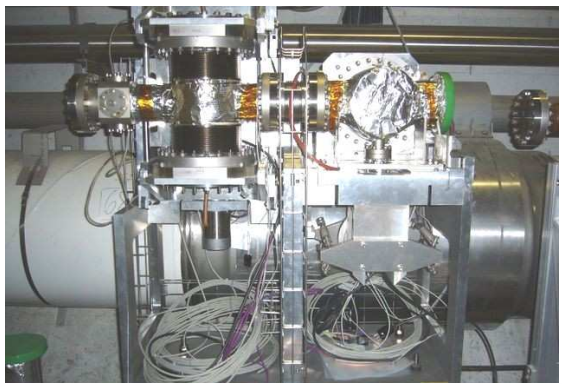

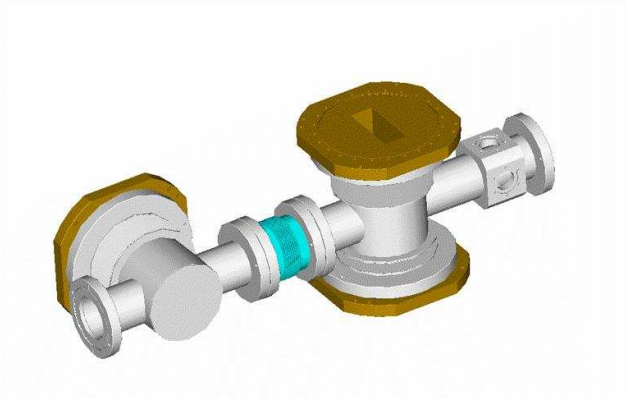

Figure 3.16: Left: Installation of the first RP unit in the LHC. Right: The vacuum chambers of a RP unit accommodating the horizontal and the vertical pots and the Beam Position Monitor.

pot, which is placed on the radially outer side of the LHC ring, completes the acceptance for diffractively scattered protons deviated in that direction by their momentum loss.

The Roman Pot devices and their silicon detectors are discussed in detail in Chapter 4.

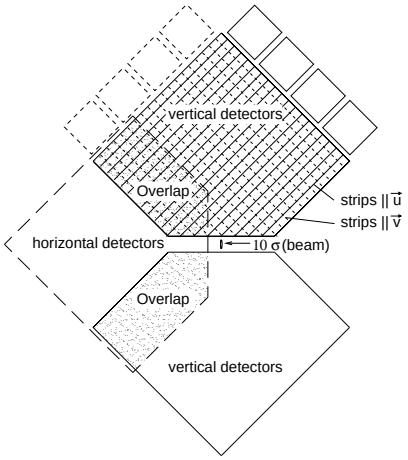

Figure 3.17: The overlap between the horizontal and vertical detectors.

Chapter 4

The Roman Pot detectors

The detection of very forward protons in movable beam insertions — called Roman Pots (RP) — is an experimental technique used for the first time at the ISR [16] in years 1970–1972.

It has been successfully employed in other machines like the SPS, TEVATRON, RHIC and DESY. Detectors are placed inside a secondary vacuum vessel, called pot, and moved into the primary vacuum of the machine through vacuum bellows. In this way, the detectors are physically separated, by a thin window, from the primary vacuum, which is thus preserved against an uncontrolled out-gassing of the detector's materials.

4.1 The Roman Pot detector's mechanics

Each pot is equipped with a stack of 10 planes of a newly developed silicon microstrip detectors with active volumes already at $\sim$50 μm from their physical edge (Section 4.3). Half of them will have their strips oriented at an angle of $+45^\circ$ with respect to the edge facing the beam, and the other half at an angle of -45° — see Figure 3.17. This configuration has the advantage that the hit profiles in the two projections are equivalent. The disadvantage of having only two readout projections is the difficulty of high multiplicity events reconstruction.

The measurement of each track projection in five planes is advantageous for the reduction of uncorrelated background events via majority coincidences, requiring e.g. collinear hits in a majority of the planes.

The challenging constraints of the LHC, such as the thin high-intensity beam, the Ultra High Vacuum and the high radiation fluxes have required the development of new Roman Pots.

In order to maximise the detector acceptance, one of its edges needs to be positioned as close as possible to the beam. For this reason the bottom window of the RP, which separates the Pot secondary vacuum form the machine primary vacuum, is reduced to a thickness of only 150 μm. To reach this goal new technologies were developed. This is one of the main differences of the RPs designed for earlier machines. Another crucial challenge is the radiation hardness of the silicon sensors and of the RP electronics.

The pot (Figure 4.1) provides a volume with secondary vacuum where the detectors and the services are enclosed. It is a stainless steel 50 mm $\times$ 124 mm $\times$ 105 mm rectangular box, with 2 mm wall thickness outside the thin window, visible in the picture with a diamond shape.

Figure 4.1: The pot with the thin window. The lateral sides of the window are 0.5 mm thick, while the bottom is 0.15 mm thick to reduce the insensitive space between the beam and the detectors inside the pot. The Ferrite collar (black in the figure) is needed to reduce the beam coupling impedance.

Each pot is independently moved by radiation hard micro-stepping motors. The nominal mechanical pot-positioning resolution of the driving mechanism is 5 μm, but the final precision depends on the assembly of the motors and the roller screws. The stepper motors are equipped with angular resolvers which give the absolute position of each pot with respect to the nominal beam axis. Additional displacement inductive sensors (LVDT) provide the absolute position of each pot.

4.2 Planar silicon detectors

The RP detectors of the TOTEM experiment will track the high-energy protons coming from the interaction point. Semiconductor sensors offer attractive properties for charged particle tracking purposes [34]. An incident particle generates a certain amount of free charge carriers in a small volume allowing dense detector packaging to be made and short charge collection time ($\mathcal{O}(10\,\mathrm{ns})$). In particular with microstrip detectors it is possible to achieve a spatial resolution better than $20\,\mu$m, depending on sensing elements pitch, which in TOTEM equals $66\,\mu$m.

4.2.1 Ionising radiation interaction with silicon

When a charged particle crosses a semiconductor, it continuously loses energy. Predominant is the inelastic interaction with the electrons of lattice atoms. As a result, electrons are excited from the valence into the conduction band. The basic principle of semiconductor devices consists in detecting the hereby created free electrons' and holes' currents by applying an electric field to the opposite polarity electrodes. In high energy physics, the semiconductor radiation detectors are used primarily for particle tracking.

The stopping power is defined as $S \equiv -\mathrm{d}E/\mathrm{d}x$. This represents the amount $\mathrm{d}E$ of energy deposited in the semiconductor by the charged particle for a crossed distance $\mathrm{d}x$. In a semi-classical theoretical model in which the energy transfer from the incident particle to electrons is treated as a function of the impact parameter, this stopping power is given by the Bethe-Bloch formula [58, 59, 60]

$$-\frac{\mathrm{d}E}{\mathrm{d}x} = kz^2\frac{Z}{A}\frac{1}{\beta^2}\left[\frac{1}{2}\ln\frac{2m_e c^2\beta^2\gamma^2 T_{max}}{I^2} - \beta^2 - \frac{\delta}{2}\right], \tag{4.1}$$

with parameters given in Table 4.1.

The parameter δ takes the density effect into account. This effect becomes relevant for a relativistic ($\beta\gamma \geq 2$) particle. In this case, it is not appropriate to consider the effect of the incident particle on one electron in one atom at the a time and then sum up incoherently the energy transfers to all the electrons. The interaction range of the particle extends over a large amount of lattice constants. As a consequence, the strength of the interaction with an atom far away from the particle is reduced by all surrounding atoms which produce perturbing fields at the chosen atom position. T_{max} is the maximum kinetic energy which can be imparted

Parameter	Description
$k = 4\pi N_A r_e^2 m_e c^2$	$= 0.31\,\mathrm{MeV{\cdot}g^{-1}cm^{-2}}$
z	atomic number of the incident particle
Z	atomic number of the lattice atoms
A	atomic mass of the medium
T_{max}	maximum kinetic energy transferred to a free electron in an interaction
I[eV]$=(10 \pm 1) \cdot Z$	mean ionisation potential per atomic electron
δ	density effect correction to ionisation energy loss

Table 4.1: Parameters related to Equation 4.1.

to a free electron in a single collision and is given by [60]

$$T_{max} = \frac{2m_e c^2 \beta^2 \gamma^2}{1 + 2\gamma m_e/M + (m_e/M)^2}, \tag{4.2}$$

where m_e is the mass of the electron and M is the mass of the incident particle.

Delta-electrons are generated as part of the electronic excitation process. For high energy particles the maximum transferable energy T_{max} is nearly as high as their total energy. However, the probability for such a transfer is low. The energy which is lost in transfers below certain T_{cut} value corresponds approximately to the energy deposited in the thin detector [61]. It is customary to use a modified stopping power formula, which excludes transfers above the energy T_{cut}, and call this the "restricted energy loss" [64]. Obviously, the energy loss of the particle itself is not physically restricted, but only its manifestation in the detector. The stopping power S in silicon as a function of the incident particle energy is shown in Figure 4.2. For $\beta\gamma$-values larger than $\sim$3, the stopping power is constant and independent of the thickness for thin detectors. Particles crossing the medium and releasing such minimum energy are called minimum ionising particles (MIP).

For 7 TeV protons impinging on silicon, the mean energy loss is 99 keV for a thickness of 300 μm, representing $1.4{\cdot}10^{-6}$ % of original energy. Thus all detectors described in this thesis are considered thin. The stopping power represents the mean energy loss ΔE_{mean} of particles for a given energy. The stochastic nature of the energy loss process causes fluctuations in the actual energy loss of individual particles integrated over the same thickness. For thick absorbers in which the energy loss exceeds one half of the original energy, the probability distribution function of the energy loss is Gaussian. For thin absorbers the probability den-

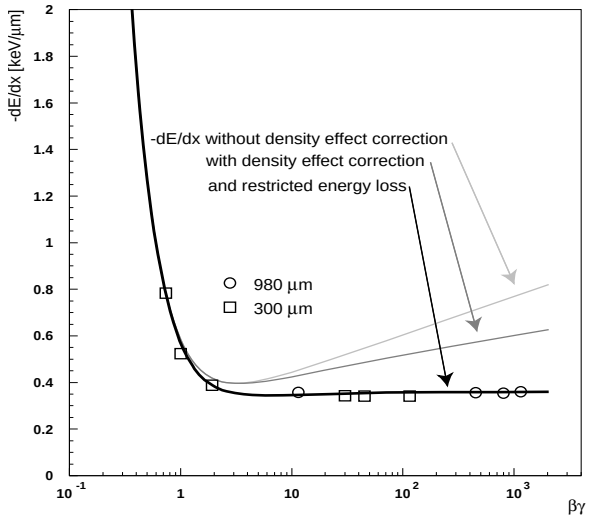

Figure 4.2: Mean energy deposition in silicon as a function of reduced incident particle momentum ($p/(mc) = \beta\gamma$). The density effect and the restriction of the maximal energy loss T_{max} to T_{cut}=500 keV become important at high energies. The circular (rectangular) data were gathered with a 980 μm (300 μm) thick detector [61].

sity function $f(\Delta E_{mean}$,x) follows a Landau distribution[1] [63]. This distribution is plotted in Figure 4.3 for two different thicknesses of a silicon detector. The energy loss is often expressed in terms of the mean energy w needed to create an electron-hole pair in silicon ($w = 3.62$ eV at 300 K). The most probable energy loss for a thickness of 300 μm corresponds to 24,000 electron-hole pairs, whereas the mean energy loss (300 μm·0.35 keV/μm from Figure 4.2) corresponding to 27,500 electrons is slightly larger due to the asymmetric shape of the Landau probability distribution.

4.2.2 Microstrip detectors

Microstrip detector geometry is based on an array of regularly arranged parallel p-n junctions. The junctions consist of a highly doped shallow p^+ region ($\mathcal{O}(1\,\mu\text{m})$) on a very low-doped n substrate and a backside of a highly doped shallow n^+ layer. While the strong doping of the p^+ region gives a space charge region extending through all the n-type substrate, the n^+ region allows a good ohmic contact. Typically the width of the strips is of the order of a few tens of microns and the distance between two strips less than 100 μm. The *pitch* is defined as the distance

[1]Landau distribution can be computed on the basis of the following formula: $p(x) = \frac{1}{\pi}\int_0^\infty e^{-t\ln t - xt}\sin(\pi t)\,\mathrm{d}t$.

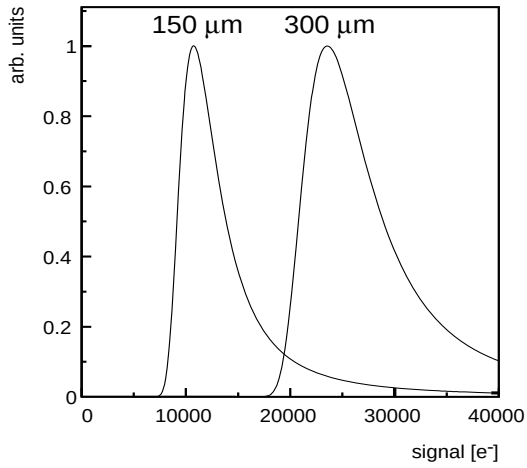

Figure 4.3: Landau distribution computed numerically for a 300 μm and a 150 μm thick detector. The most probable values are 24,000 and 11,000 electrons respectively [65].

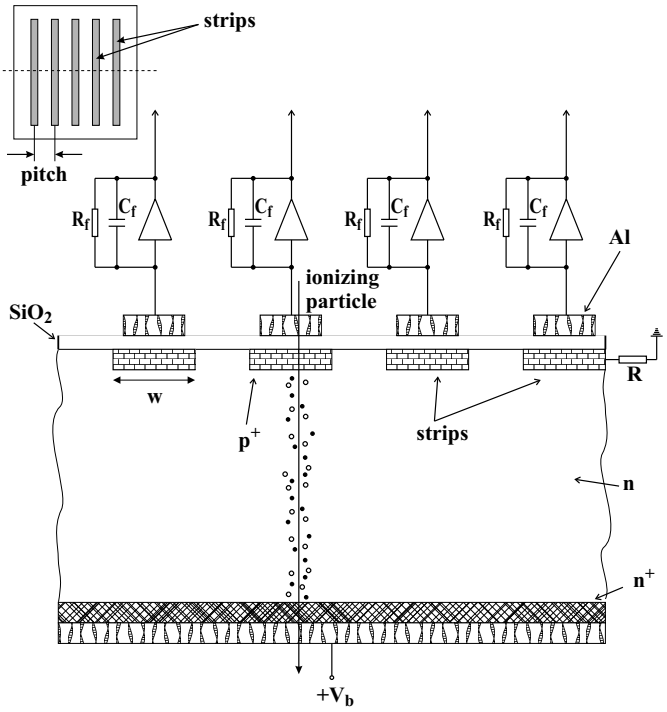

Figure 4.4: Top view and cross-section (along the dashed line) of a strip detector. The strips are AC coupled to the readout electronics by a thin insulating silicon dioxide layer between the strip and the aluminium layer.

between the centre of two adjacent strips. Each of these strips can be connected to a separate read-out channel. This geometry has been developed to measure the position of single particles traversing the detector.

Signal generation The basic working principle is the following: a particle crossing the detector sensitive volume generates free electron-hole pairs. These charge carriers are collected by the corresponding strip (see Figure 4.4) and this signal is fed to a read-out channel associated to the strip[2]. In order to collect charge generated in the whole n-type region an electric field must be non zero everywhere in the detector bulk. This is achieved by operating the detector in a depleted mode, i.e. by applying a reverse bias voltage $V_b > V_{fd}$, where V_{fd} is the depletion biasing voltage[3]. The mean charge created in a 300 μm thick silicon detector is 24,000 electrons, corresponding to a charge of 3.8 fC.

Charge sharing The electric field of a biased microstip detector, far enough from the surface containing the readout strips, is approximately normal to the detector surface and the motion of the generated charge carriers on average follows the field lines. Thus the charge created along a tilted track is shared between several consecutive strips, which form a cluster.

However, the movement of the generated charge carriers has also a random, thermal component. This results in the diffusion of charge. Thus even if the track is perpendicular to the sensor surface, as it is in the case of the RP devices, the charge sharing still can be observed and its intensity depends upon detector's pitch, thickness, the type of the silicon used and the biasing voltage. Generally, higher biasing voltage reduces the charge collection time and thus decreases the effect of the diffusion, which leads to the reduction of the charge sharing.

Readout electronics The basic function of a preamplifier is to amplify weak signals from a detector and to drive them through the cable that connects the preamplifier with the rest of the equipment. At the same time, it must add the least amount of noise possible. Since the input signal at the preamplifier is generally weak, preamplifiers are normally mounted as close as possible to the detector so as to minimise cable length. If the input capacitance varies during operation, which is the case of silicon detectors whose intrinsic capacitance varies with temperature, the charge-sensitive preamplifier is the best choice. Schematics of the basic design

[2]In reality the process of signal generation is more complex. The free charge carriers generated in silicon detectors by the traversing particle drift due to the electric field, inducing mirror charge on the electrodes. The evolution of signal (pulse) can be measured by adequate electronics. The theoretical computation of this signal is not trivial in case of microstrip detectors where the charge generated is collected by a system of multi-electrodes. The signal generation can be computed with the application of Ramo's theorem (see [65, 54, 34]).

[3]The region is said to be depleted when it contains no free charge carriers.

for this type of amplifier are shown in Figure 4.4. The basic idea is to integrate the charge carried by the incoming pulse on the capacitor C_f. The output voltage V_{out} is proportional to [61]

$$V_{out} \cong -\frac{Q_{in}}{C_f}, \tag{4.3}$$

where Q_{in} is the input charge, i.e. the charge signal produced in the detector. The output signal is thus insensitive to variations in the input capacitance C_{in}. Before a new signal can be processed (this corresponds to charging again the input capacitance with a new input charge Q_{in}), the integrated charge of the previous event on the feedback capacitor must be removed. The simplest method for this reset is a discharge through a feedback resistor R_f (also shown in Figure 4.4) in parallel to the feedback capacitance C_f. Thus the feedback capacitor is discharged exponentially in time with a time constant $\tau_{reset} = C_f R_f$.

Noise The signal-to-noise ratio is a key design specification of detectors since with an electronic noise level reaching the signal level no reliable operation is possible any more. Sources of noise are the detector capacitance, the leakage current and the noise generated in the readout electronics.

The term *noise* refers to spontaneous fluctuations in the current passing through, or the voltage developed across, semiconductor bulk materials or devices. Noise is generally classified into *thermal noise, flicker noise* and *shot noise*. Thermal noise occurs in any conductor or semiconductor and is caused by the random motion of the current carriers. It is independent of frequency. Flicker noise is important at low frequencies and its origin is not unique. Shot noise constitutes the major noise source in a reverse biased semiconductor detector. It is independent of frequency at low and intermediate frequencies. At higher frequencies the shot noise spectrum becomes frequency-dependent. This noise is a consequence of the discrete nature of electric charge and represents the statistical fluctuations δN in the number of charge carriers making up a charge $Q = eN$.

In general, each detector channel is characterised by the *equivalent noise charge* (ENC). The ENC describes noise pulse in terms of the charge pulse at the detector needed to create the same output.

For a more detailed discussion, the reader is referred to [66] and the references therein.

Coupling The microstrip detectors which are placed in the Roman Pots are AC coupled. A capacitor is introduced between the p^+ strip and the metallisation

that is in direct contact with the readout electronics. The capacitor is created by an insulating layer of silicon dioxide underneath the strip metallisation (see Figure 4.4).

Biasing The biasing of the strips is done by the *punch-through* mechanism which is discussed in detail in [34]. Figure 4.5 illustrates its principles. Before a bias

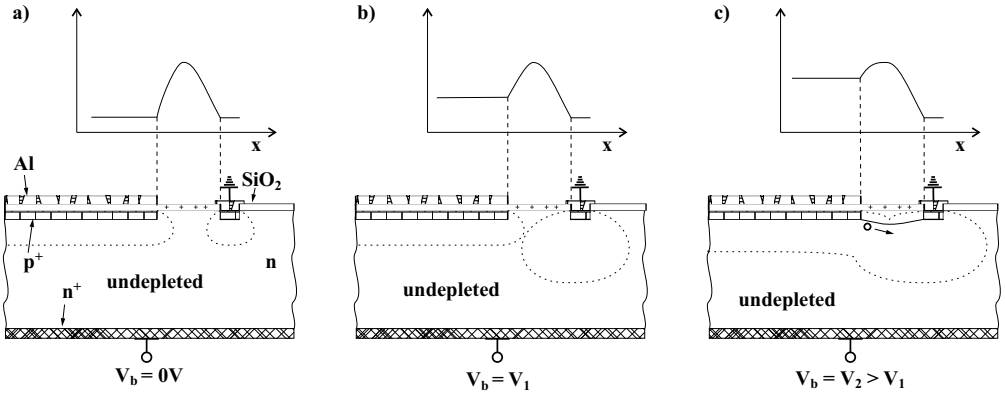

Figure 4.5: The Punch-Through mechanism. (a) Before application of a bias voltage ($V_b = 0\,\mathrm{V}$). (b) At the onset of punch-through $V_b = V_1$, where the space-charge region around the biased p^+ implant has grown so as to just touch the other region. (c) At larger bias voltage $V_b = V_2$, when the potential difference between both p^+ implants is constant.

voltage is applied, $V_b = 0\,\mathrm{V}$, (a), only a small region around both p^+ implants is depleted of charge carriers. The depletion regions of the strips and of the biasing ring are separated from each other and no current is flowing. At the onset of punch-through, $V_b = V_1$, (b), the space-charge region around the biased p^+ implant grows so as to just touch the other region. At larger bias voltage, $V_b = V_2$, (c), the space-charge region grows deeper into the bulk. The potential difference between both p^+ implants is constant and this difference is also called the *punch-through voltage*.

4.3 Edgeless silicon detectors

Silicon detectors fabricated with standard planar technology require terminating structures to reduce electric field maxima at the detector periphery to prevent the edge saw cut from affecting their performance, and to avoid breakdown. They are generally a sequence of floating guardrings surrounding the sensitive part of the device and adding an external dead volume, which can be, depending on the application, as big as the substrate thickness, or even larger. This multi-ring

structure, called *Voltage Terminating Structure*, controls the potential distribution between the detector's sensitive area and the cut edge to have a vanishing potential drop at the chip cut. The insensitive margin increases with the number of rings, and for high voltage applications, as it is the case for silicon detectors used in harsh radiation environments, it can be more than 1 mm wide. For the TOTEM experiment such long border length would be impossible.

4.3.1 Detectors with Current Terminating Structure

The requirements outlined above triggered the development of a new terminating structure that allows detectors fabricated with standard planar technology to reach full sensitivity within less than 100 μm from the cut edge and to operate with high bias at room temperature [44].

The silicon strip sensors of the TOTEM experiment are single-side AC p^+-n microstrip detectors with 512 strips and a pitch of 66 μm processed on very high resistivity n-type silicon wafers ($> 10\,k\Omega\,cm$), 300 μm thick. All of them have the new so-called *Current Terminating Structure* (CTS) on one edge, i.e. the edge facing the beam. The CTS and its biassing scheme are shown in Figure 4.6.

In case of the CTS devices, the potential applied to bias the device is applied also across the cut edges. This is done via a guardring that reaches the cut edge and that surrounds the whole sample. This external guardring, also called *Current Terminating Ring* (CTR) collects the current generated at the highly damaged region close to the cut edge, avoiding its diffusion into the sensitive volume, and is decoupled from the biassing electrode inside the CTR. In this manner the sensitive volume can start closer to the cut edge. To prevent any further diffusion of this edge current into the sensitive volume another implanted ring, the clean-up ring (CR), is placed between the CTR and the sensitive volume.

For devices with this type of CTS, the leakage current in the sensitive volume (I_{BE}) which contributes to noise is not affected by the edge current ($I_{CTR} + I_{CR}$). The leakage current and the edge current have been shown to be completely decoupled. Moreover, for such devices, the charge collection efficiency has been shown to rise steeply from the edge of the sensitive volume reaching full efficiency within a few tens of micrometers [44] (see Chapter 5).

A picture of the planar edgeless silicon detector for the TOTEM Roman Pots and a detail of the CTS are shown in Figure 4.7.

In these sensors the negative potential of the strips is provided via punch-through [80, 34] with a biassing electrode (BE) placed inside the CR and the CTS,

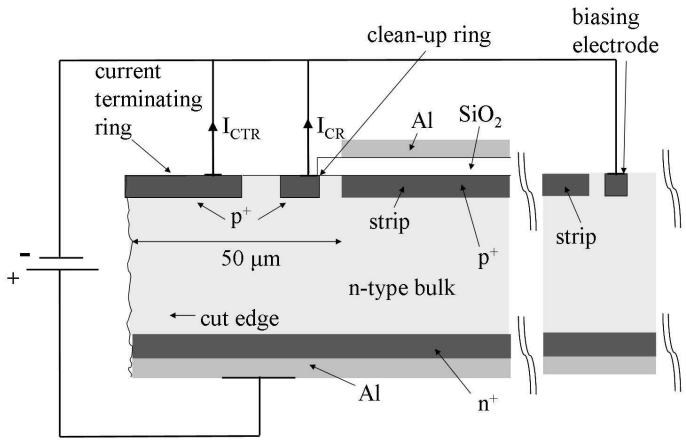

Figure 4.6: Cross-section of a silicon detector with CTS in the plane parallel to the strips and its biassing scheme.

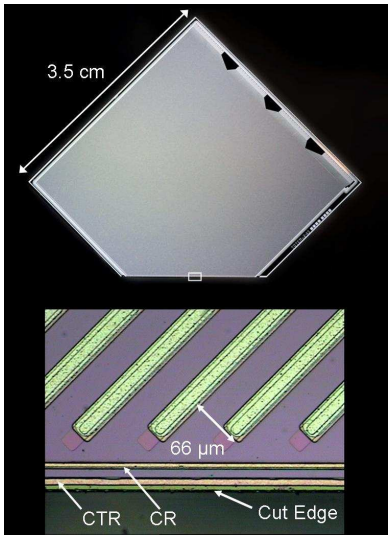

Figure 4.7: Picture of a Planar Edgeless Detector with CTS (top). The magnification of a portion of the chip cut region (bottom) shows the detail of the CTS.

and integrated into a standard voltage terminating structure on all the sides where the sensitivity to the edge is not required. The strips on the detector are at an angle of 45° with respect to the edge facing the beam, as can be seen at the bottom of Figure 4.7.

The radiation hardness the edgeless silicon detectors has been evaluated. Whilst an irradiation of up to 10^{13} p/cm^2 does not change the detector behaviour, stronger

irradiated detectors ($1.4 \times 10^{14}\,\mathrm{p/cm^2}$) need a much higher bias voltage of up to 450 V to be fully efficient. Presently, a radiation of $10^{14}\,\mathrm{p/cm^2}$ is considered as an upper limit for a functioning detector.

4.3.2 Planar-3D detectors

In addition to the planar silicon detectors with CTS, TOTEM is considering equipping the RPs partly with another novel type of sensor — so called *active edge* detector [81]. In these devices the central part is a conventional planar microstrip detector while the electrode at the edge is fabricated using standard 3D processing [82]. In this configuration, the free edges of a planar detector are deep etched and n^+ dopant is diffused in. Then the sensor is removed from wafer again by etching, avoiding in this way the typical surface defects produced by saw cuts. The edges of the sensor become an extension of the back-side n^+ electrode to the front side, as shown schematically in Figure 4.8 (left). This enclosing n^+ electrode

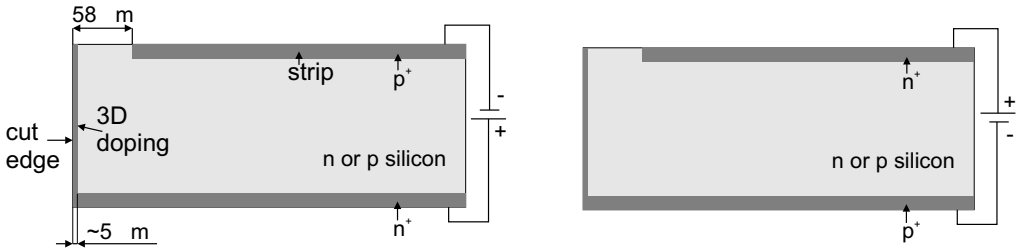

Figure 4.8: Sketch of a planar-3D detector. Left: The edge on the left hand side of the sketch, is an extension of the backside n^+ electrode and allows full control of the electric field lines at the edge. Right: Planar/3D detector with inverted doping scheme.

— the "active edge" — completely defines the electric field lines when a reverse bias voltage is applied. In this configuration the electric field lines do not need to be kept far from the edge to avoid high leakage current generated at the cut surface flowing into the active region but will be controlled by what is now an active electrode.

The advantages of this approach with respect to standard planar technology are the following:

- The surface leakage current, usually present after the device has been saw-cut, is suppressed.

- The dead area which would be otherwise needed for guard rings and to control the bulge of the electric field in planar detectors is reduced to no more than a few microns.

- There should be no insensitive volume in the central region.

The use of planar/3D detectors with inverted doping scheme (see Figure 4.8, right) is also considered. In its case, before irradiation, the depletion develops from the back-plane electrode towards the strips. After irradiation with protons, when the n-type bulk silicon becomes a p-type, the depletion again develops from the strip surface towards the back-plane. Such devices are observed to be more radiation tolerant.

The planar-3D design is best suited for a low to moderate radiation environment (up to 10^{14} n/cm^2 if operated at $-20°$C) since the central part is a traditional planar sensor, and the edge is not equipped to cope with very high electric fields (like multi-guard rings). This would be adequate for the low luminosity TOTEM runs. For higher luminosities, detectors in the radiation-hard full-3D design [82, 84] would be suitable, due to their lateral depletion over much smaller distances than the wafer thickness.

Prototypes of planar-3D detectors have been tested in the 2004 testbeam together with the CTS detectors. Both the efficiency rise at the edge and the spatial resolution of the planar-3D detectors were measured to be very similar to those of the CTS detectors.

Performance and the edge efficiency of final CTS and planar-3D sensors, integrated to a complete readout chain consisting of front-end electronics and a data acquisition system, were studied both in a fixed target and a coasting beam experiment. The results are presented in Chapter 5.

Chapter 5

"Edgeless" detector performance

The edge sensitivity of the small size prototype CTS detectors has been tested with a high energy (∼100 GeV) muon beam in the X5 area at CERN [51, 44, 1]. The observed steep effciency rise ($< 10\,\%$ at $x = 0\,\mu$m and $> 90\%$ at $x = 51 \pm 5\,\mu$m, where $x = 0\,\mu$m corresponds to the mechanical edge of the sensor) was compliant with the requirements of the Roman Pot detectors in terms of its edge sensitivity and also of general performance. Based on this experience, final size detectors were developed.

The final size "edgeless" detectors, integrated to a complete readout chain consisting of front-end electronics and a data acquisition system, were studied in fixed target experiments. Their performance was also investigated in a coasting beam experiment in the Super Proton Synchrotron (SPS)[1], under conditions close to those expected at the LHC.

In this chapter the results of the beam tests are reported. The candidate implemented the majority of the off-line analysis algorithms, actively participated in the experimental part, analysed the acquired data and achieved the presented results. The track reconstruction and the software alignment approach were partially based on [46, 47, 48, 49].

[1]The Super Proton Synchrotron (SPS) is a particle accelerator at CERN of an operating energy of 400 GeV. It was commissioned on 17 June 1976. Although it was originally designed to accelerate protons, the SPS has also been used to accelerate antiprotons, electrons and positrons (for use as the injector for CERN's LEP electron-positron collider) and heavy ions. The SPS is to be used as the final pre-injector for CERN's Large Hadron Collider.
Now the SPS is used to provide the proton beams for fixed-target experiments.

5.1 Detector tests with analogue readout

"Edgeless" silicon detectors of both Current Terminating Structure (CTS) [51] and 3D technology [81, 82] have been tested in autumn 2004 with a ∼100 GeV muon beam in the SPS X5 area at CERN. The edges were manufactured in both CTS and 3D technologies as described in Section 4.3. The sensors had a final size and a strip pitch of 66 μm. They were assembled into 4 packages each consisting of 8 detectors as shown in Figure 5.1. The majority (24 detectors) were read

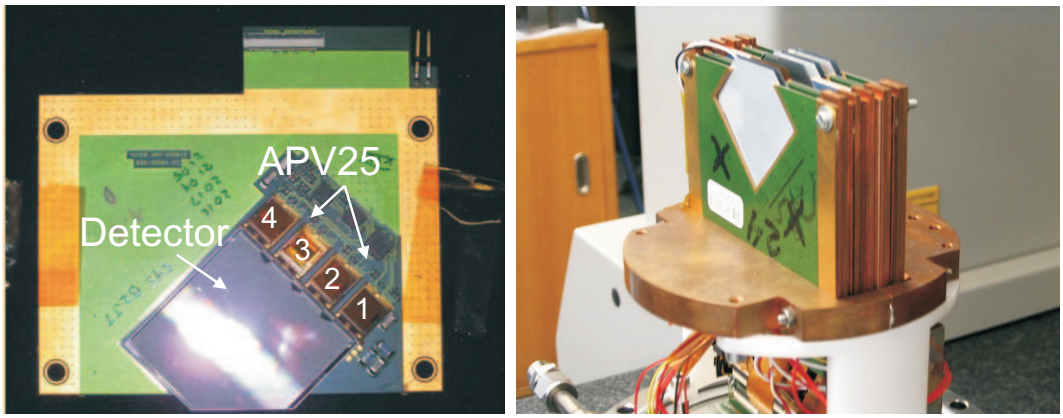

Figure 5.1: Left: Picture of a hybrid with a planar microstrip detector, 3.4 × 3.4 cm^2 large, mounted on it. The detector is connected electrically to the 4 APV25 readout chips via wire bonds. Right: A package of 8 hybrids.

out with CMS's analogue APV25 chips [52, 53] (see Appendix A.1) while a few were equipped with prototypes of TOTEM's own front-end chip, the VFAT [14] (see Appendix B.1), to test its trigger functionality. Each detector was glued to a hybrid-board and bonded to 4 (either APV25 or VFAT) chips, each capable of reading out 128 strips. The TOTEM hybrid is presented in Figure 5.1 (left). The packages formed a telescope placed inside a vacuum tube (see Figures 5.2 and 5.3). The tracking information was acquired through APV25 chips which were connected to the CMS-like front-end electronics described in Appendix A.2.

5.1.1 Jitter correction

The charge induced on each of a detector strips, is fed into the APV25 preamplifier and shaper. Their output is continuously sampled at 40 MHz and stored in a 192-cell-deep analogue pipeline. When the chip is triggered the appropriate cell columns are fed through the Pulse Shape Processor into the multiplexer. The

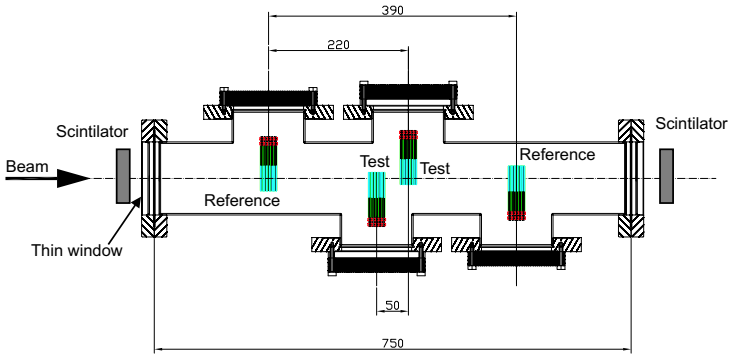

Figure 5.2: Arrangement of the test and reference detectors with respect to the beam axis (dashed line) inside a test vacuum tube.

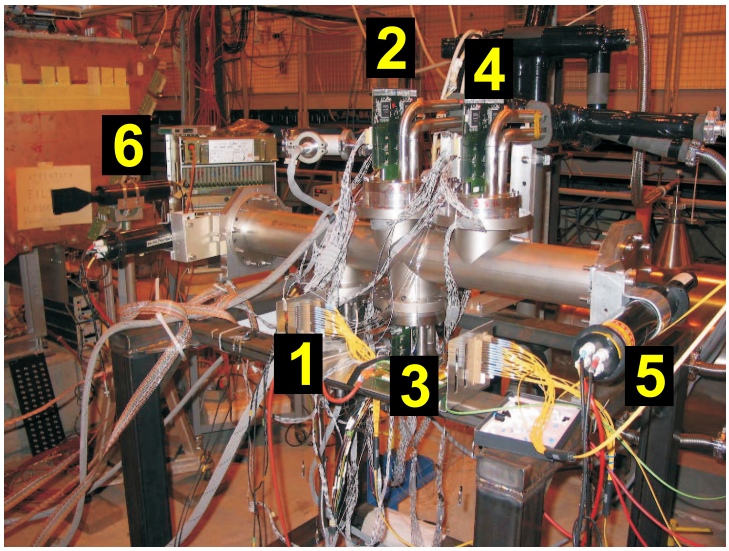

Figure 5.3: A photograph of the test telescope. 1 and 4 are the reference detectors, 2 and 3 are the test detectors, 5 and 6 are the trigger scintillators.

multiplexer serialises the 128 channels and streams them out preceded by the header at the frequency of 20MHz. A pair of APV25 chips is connected to the APV25 Analogue Signal Multiplexer (APVMUX) which interleaves the two APV25 output streams and drives the optical transmitter at 40 MHz. The analogue data stream (see Figure 5.4) is transported via analogue optical link to the Front End Driver (FED), which finally digitises the analogue signals and sends the resulting data buffers to the data acquisition software (see Figure A.4 in Appendix A.2). The sequence of light pulses in the optical link is non-consecutive with respect to the order of the detector strips (see Equation A.1). Hence the buffer contents need to be reordered before further strip related analysis can be performed.

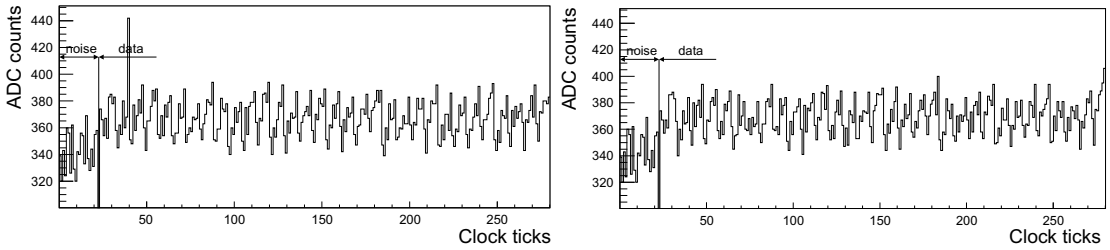

Figure 5.4: Two different events of the same detector during the same run sampled by the Front End Driver (FED). The peak in the left plot is a signal of a detected particle. First 24 clock ticks should correspond to the header which is not available in the data.

Due to a not fully understood problem of the Data Acquisition System (DAQ) electronics clock synchronisation, the sequence of the output data stream of several key detectors exhibited a jitter of a few clock cycles. This resulted in the shifts of the data in the FED buffers making the direct reordering not successful. Figure 5.5 shows the correlation of the reconstructed cluster position between two detectors of parallel strips with tracks orthogonal to their surface. For correct events the correlation plot shows the straight line (left). When at least one of the detectors jitters the complex structure is observed (right).

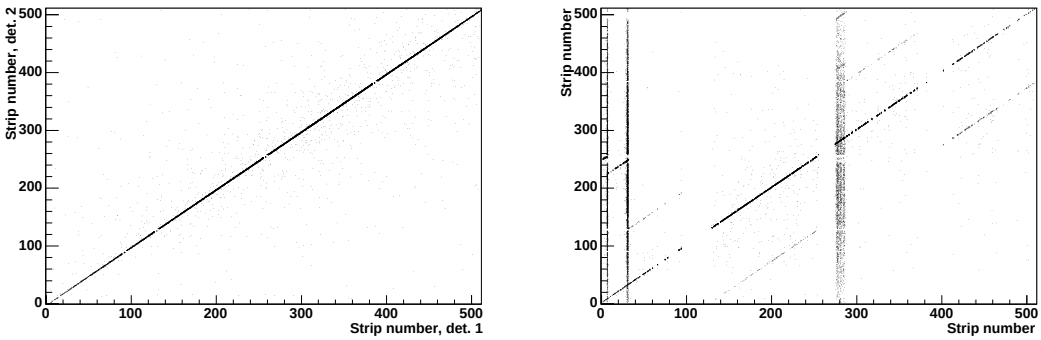

Figure 5.5: The correlation of the position of reconstructed impact points between two detectors of parallel strips with the particle beam orthogonal to detector planes. In case of correct events the correlation plot shows the straight line since about the same strips of the detectors are hit (left plot). When the readout of at least one of the detectors jitters, the hit position is wrongly reconstructed and the complex structure is observed (right).

Unfortunately, the APV25 headers were not available in the sampled data and jitter correction had to be based only on the buffer sequence properties. The pedestal value is constant for a given strip during the test run. Since the detector

hit multiplicities were low, the shape of the quasi-periodic structure of the analogue data stream (see Figure 5.4) of a given optical link, resulting from several stages of multiplexion, was invariable for all the events. The shifts of the buffers of the run were computed with respect to the reference event, for which the shift was manually discovered by means of raw data inspection. The subrange of each buffer was treated as a stochastic process[2]. The sequence shift τ between the reference x_i sequence and the corrected one y_i was computed by finding the maximum of the correlation function $\mathrm{Corr}(\tau)$ with respect to the shift τ value. The correlation function is defied as:

$$\mathrm{Corr}(\tau) = \frac{\sum_{i=a}^{b}(x_i - \overline{x})(y_{i-\tau} - \overline{y})}{N\sigma(x)\sigma(y)}, \tag{5.1}$$

where $N = b - a + 1$ is the number of buffer samples used for resynchronisation, a and b are the beginning and the end of the range, $\overline{x} = \sum_{i=a}^{b} x_i/N$ is the mean value of x_i, $\sigma(x) = \sqrt{\sum_{i=a}^{b}(x_i - \overline{x})^2/N}$ is the standard deviation of x_i, $\overline{y} = \sum_{i=a}^{b} y_{i-\tau}/N$ is the mean value of y_i and $\sigma(y) = \sqrt{\sum_{i=a}^{b}(y_{i-\tau} - \overline{y})^2/N}$ is the standard deviation of y_i.

The examples of the correlation functions $\mathrm{Corr}(\tau)$ and of the reconstructed shifts distribution are shown in Figure 5.6. The left and the middle plots show the correlation functions in the case of the correct and shifted event, respectively. The maximum of the function indicates the shift of the analysed data buffer.

The ineffectiveness of the applied algorithm was $\mathcal{O}(10^{-5})$. The application of the jitter correction algorithm increased from 2 to 5 the number of available reference detector pairs. This significantly improved the reliability and precision of the reconstructed tracks which is very important for the edge behaviour studies.

5.1.2 Detector performance

The performance of the final size detectors for different bias voltages was studied with the setup shown in Figure 5.2. The detector pedestals, noise and signals are given in ADC counts. These quantities are defined in Appendix A.3. Total amount of 1.4 million events was registered for different detector and DAQ configurations. All the results shown below were obtained with the representative CTS detector, which was operated at a reverse bias voltage of 100 V, at the temperature

[2] A stochastic process with state space X is a collection of X-valued random variables indexed by a set T ("time"). That is, a stochastic process F is a collection $\{F_t : t \in T\}$, where each F_t is an X-valued random variable.

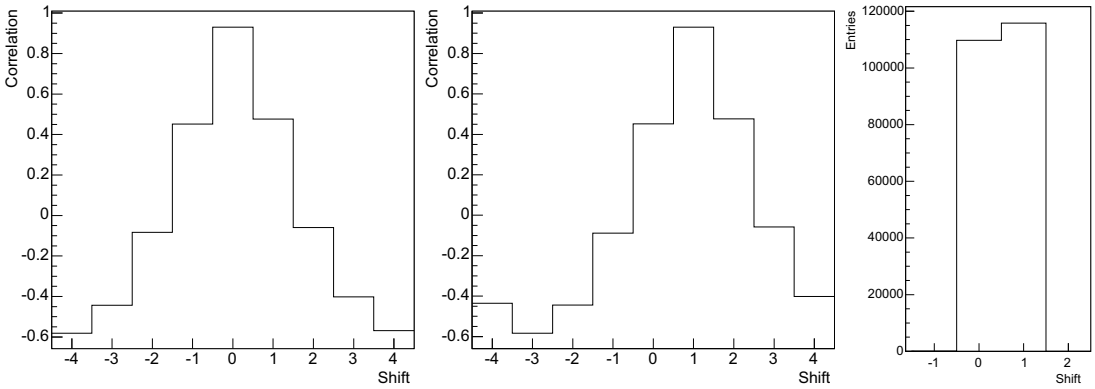

Figure 5.6: Left: The correlation function defined by Equation 5.1. The maximum of the function is at 0, which indicates that there is no shift between the analysed event and the reference one. Middle: The correlation function has the maximum at 1, which corresponds to the shift of 1 clock tick of the analysed event with respect to the reference one. The shape of the function shows that correction of shift values up to several clock ticks is possible. Right: Distribution of corrected shifts of one of the analogue optical links exhibiting the jitter.

of $\sim -10°$C.

The test consisted of the pedestal run (about 5000 events) and of the data taking run (about 29000 events). During both runs, the detector was operated at the same reverse bias voltage and was placed in the running muon beam. In the pedestal run, the system provided a random trigger thus not correlated with traversing particles. In the data taking run, the trigger was supplied by the two scintillators placed at both ends of the test vacuum tube. The pedestals of the detector are shown in Figure 5.7. Since, as mentioned before, the detector was bonded to four APV25 chips, 4 strip ranges of 128 strips corresponding to the chips are visible. The typical pedestal gradient proper to the APV25 chip (see Appendix A.1) is seen for all four APV25 chips. The 128-th channel of each chip has a significantly higher pedestal standard deviation (raw mode noise) than for any other channel. This is due to the fact that this channel was left floating because it could not be bonded to the detector due to a mismatch between the bonding pads on the detector and on the APV25 chips. It has been observed systematically that the unbonded outer channel exhibits higher noise than all other grounded channels. The common mode corrected noise is shown in Figure 5.8.

Also the channels next to the unbonded one have a slightly higher noise. The noise of the four unbonded channels is significantly higher. Both noisy channels in the first APV25 chip (90 and 91) are due to a mistake in the detector layout.

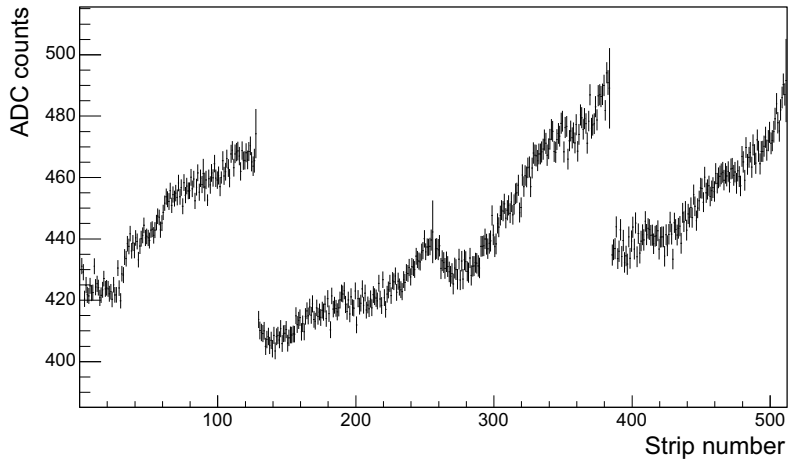

Figure 5.7: Pedestals of the tested CTS detector. The typical pedestal gradient proper to the APV25 chips is seen for all four APV25 devices bonded to the detector.

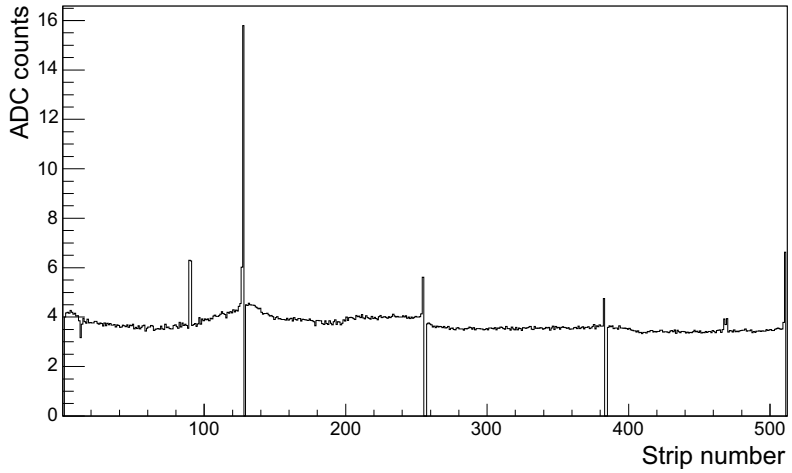

Figure 5.8: Common mode corrected noise of a CTS detector. The unbonded channels, corresponding to 128^{th}, 256^{th}, 384^{th} and 512^{th} detector strips, exhibit higher noise values.

The noise of the APV25 chip is proportional to the input capacitance. Due to the particular layout of the detector, the strips bonded to chip 1 (see Figure 5.1) do not all have the same length. The lengths range from 20.64 mm to 30.72 mm. Thus, the input capacitance of the longest strip is expected to be roughly 1.5 times larger than that of the shortest strip. This effect seems to be insignificant compared to the noise of the analogue DAQ system, however it is observed in the digital readout — see Figure 5.40 in Section 5.2.

Example common mode distributions of the four APV25 chips bonded to the detector are plotted in Figure 5.9. Since the standard deviation of the distributions

is often between 3 and 4 ADC units, the correction of the common mode noise highly reduces, even by up to 40 %, the observed strip noise. The comon mode noise distributions, for the longer runs, were usually of non-gaussian shape. This was caused by the analogue readout, which slightly changed its operating parameters with time.

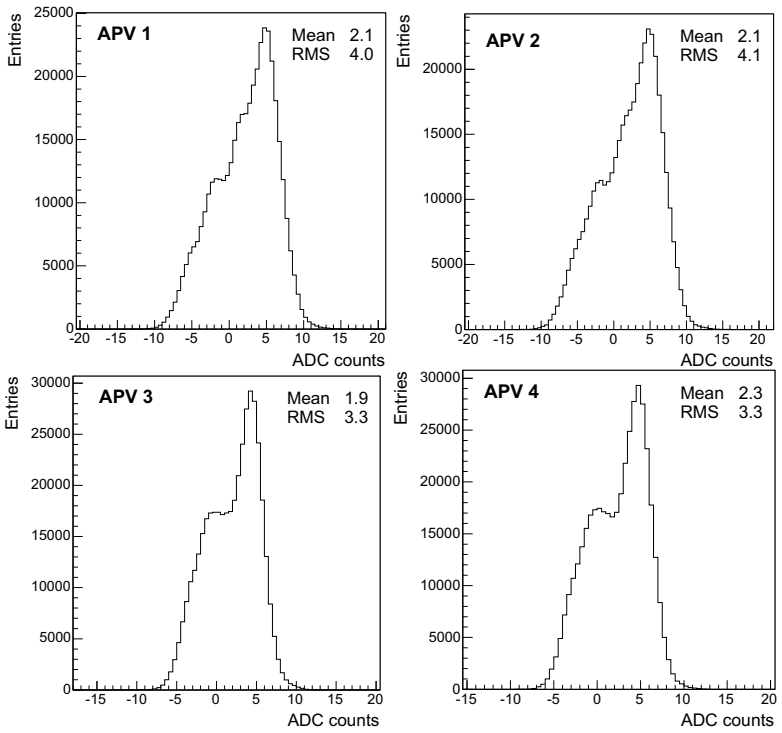

Figure 5.9: Common mode distributions of the four APV25 chips bonded to the CTS detector. The standard deviation of the distributions is between 3 and 4 ADC units.

The mean signal and its standard deviation for all channels is shown in Figure 5.10. The higher standard deviations for the first and last detector channels are caused by lower hit statistics. This is also evidenced by the beam profiles shown in Figure 5.12 (right).

The mean values of signal-to-noise ratios for each detector strip are plotted in Figure 5.11. Figure 5.12 (left) shows the signal-to-noise distribution. The most probable value of the signal-to-noise ratio of the 300 μm detector is 27. The corresponding beam profile is shown in Figure 5.12 (right).

The behaviour of the detectors was tested with various reverse bias voltages. The mean signal-to-noise ratio as a function of the applied reverse bias voltage in the range 5–150 V is plotted in Figure 5.13 for the same detector operated at the same temperature. The full depletion voltage is $\sim$34 V [54]. Since the sampling

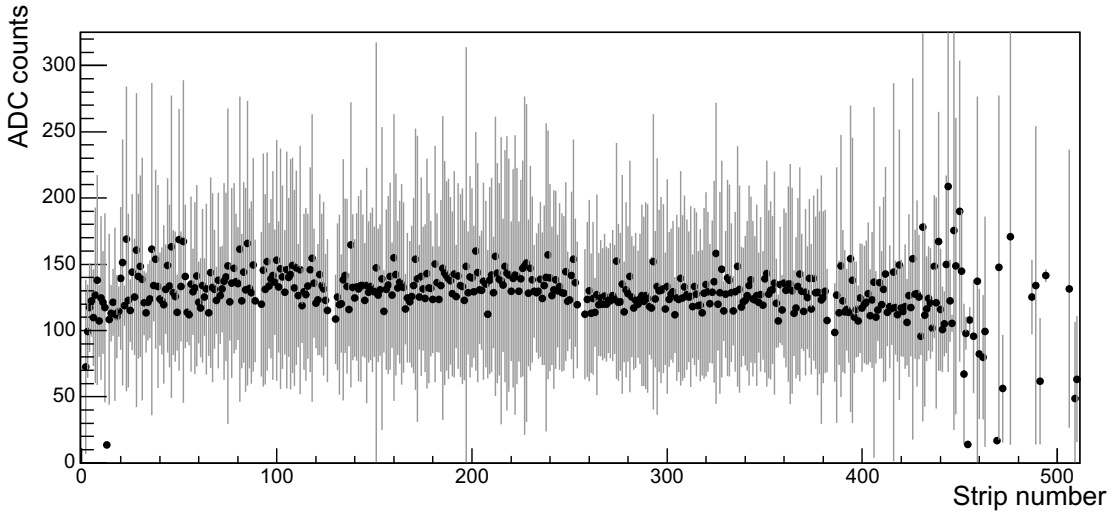

Figure 5.10: Mean signal profile and signal standard deviation profile of the detector channels. High standard deviations and missing points for groups of first and last detector strips are caused by low hit statistics.

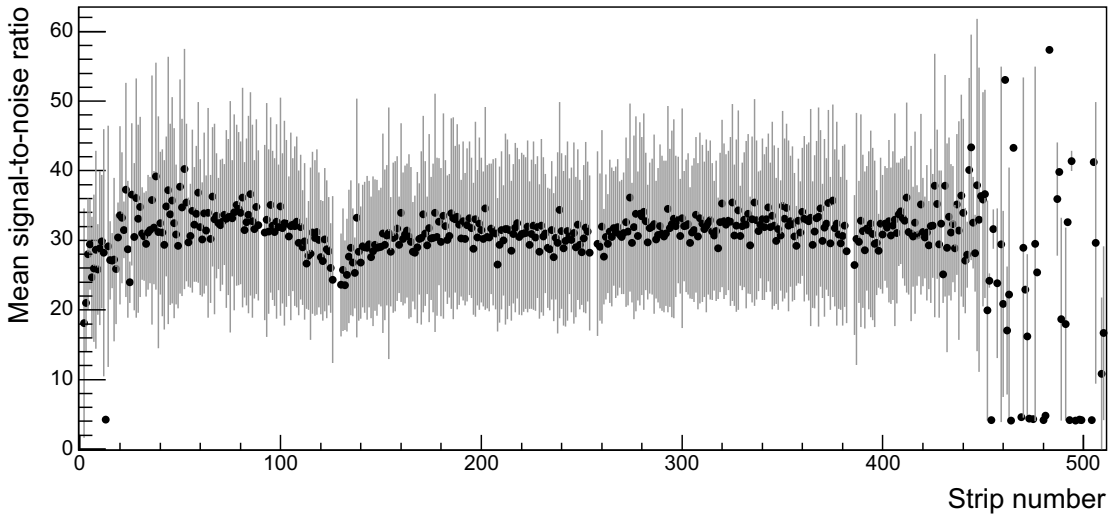

Figure 5.11: Mean values of signal-to-noise ratio and their standard deviations. High standard deviations and missing points for first and last detector strips are caused by low hit statistics.

time of the APV25 chip is short (75 ns in peak mode), the increase in the signal-to-noise ratio for voltages above this value is due to a faster collection of the electron-hole pairs generated in the detector bulk.

The calibration of an ADC unit with respect to the absolute amount of charge detected by the APV25 chips was not possible with the available electronics setup. However, the amount of the detector noise can be roughly estimated. Metrology measurements report a thickness of $279 \pm 3\,\mu$m for this detector. Hence, assuming

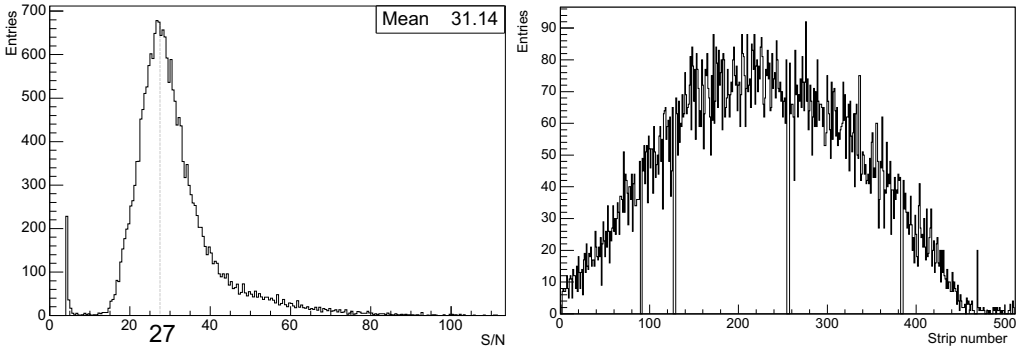

Figure 5.12: Left: The distribution of signal-to-noise ratio (S/N) for a CTS detector operated at reverse bias voltage of 100 V. The most probable S/N value is 27, the mean S/N value is 31. Right: Beam profile measured with a muon beam. The visible gaps correspond to unbonded and noisy strips, which were excluded from the impact point reconstruction.

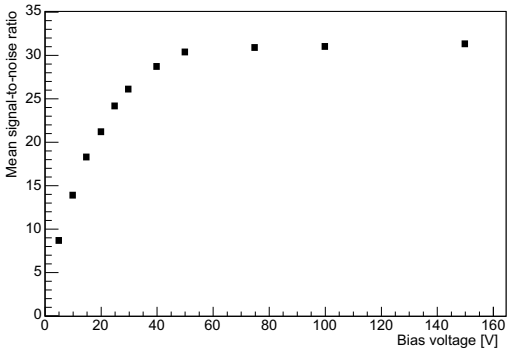

Figure 5.13: Mean signal-to-noise values of the CTS detector at a temperature of $-10°$C as a function of the reverse bias voltage.

a collected charge of $\sim 22,200$ electrons[3] for the detector operated in the overdepleted mode with most probable signal-to-noise ratio of 27, the mean noise of the assembly detector-front-end chip is ~ 800 electrons. According to Figure A.3, this corresponds to a total input capacitance seen by the preamplifier of each channel of ~ 15 pF in the peak mode.

Because of contact problems with the kapton connections between the individual detector hybrids and the motherboards, several tracking detectors could not be read out correctly. Finally, the tests were performed with the use of 15 detectors: 2 and 3 pairs in the reference packages, and 2 and 3 detectors in the test packages. Although 9 out of 24 detectors were missing, high redundancy of the system design allowed us to carry out the foreseen tests of the sensitive CTS and 3D edges.

[3]From Section 4.2.1 one has a most probable signal of 24,000 e^- and 11,000 e^- for thicknesses of 300 μm and 150 μm respectively and the value given above is the result of a linear interpolation.

5.1.3 Telescope alignment

The assembly of the detectors as shown in Figures 5.2 and 5.3 was used to study the behaviour of active edges of the detectors. The outermost detector packages (1,4) were used as a reference to define tracks while the inner ones (2,3) served as devices under test.

The theoretical resolution σ of a 66 μm pitched strip detector, when charge sharing is not present, is $\sigma = 66\,\mu\text{m}/\sqrt{12} = 19\,\mu\text{m}$. The reference packages contained 2 and 3 working pairs of detectors. Thus the optimal interpolation resolution in the centre of the telescope is:

$$\sigma(x_{\text{centre}}) = \sqrt{\left(\frac{\sigma}{2\sqrt{2}}\right)^2 + \left(\frac{\sigma}{2\sqrt{3}}\right)^2} = 8.7\,\mu m, \tag{5.2}$$

which is enough to study the behaviour of ~ 50 micron-wide active edges of test detectors. In order to profit from this theoretical accuracy, the positions of all the detectors must be determined to a precision which is a fraction of the detector resolution. This task is accomplished with metrology measurements and with a software alignment algorithm.

Metrology measurements

After completing the beam tests, the detector assembly was precisely measured to determine the positions of the silicon detectors. Since the silicon devices were installed inside a vacuum tube and their positions could not have been measured directly, a 3 step measurement strategy had to be applied following the composition of the elements.

1. The vacuum tube assembly (Figure 5.3) was measured from the outside in a global coordinate system and 46 space points were taken both on the tube and on the external parts of each of the detector packages. The points were measured with 3 μm precision.

2. The detector packages (see Figure 5.1, right) were removed from the assembly and each of them was measured (64 space points per package, 3 μm precision) in its local coordinate system in order to refer the position of each hybrid to the position of the already measured outside parts of the packages.

3. The detector packages were dismounted. 13 points per hybrid (see Figure 5.1, left) were taken to find the position of the silicon detector with respect to

the hybrid. The measurement precision was only 30–50 μm due to nonsharp hybrid copper frames.

Alltogether ∼500 space points were combined and positions of all silicon detectors were computed with with a precision of a few tens of microns. Unfortunately, once the box was opened it was found that some of the detectors got unglued which caused the displacements of about a few hundred microns.

Track reconstruction and software alignment

The alignment precision achieved with the metrology measurements was not sufficient to perform the edge studies. A precision of few microns was required to study $\sim$ 50 microns large near-edge regions. In addition, due to thermal and vacuum related displacements, the positions of the detectors varied with time; thus run related alignment refinements were needed.

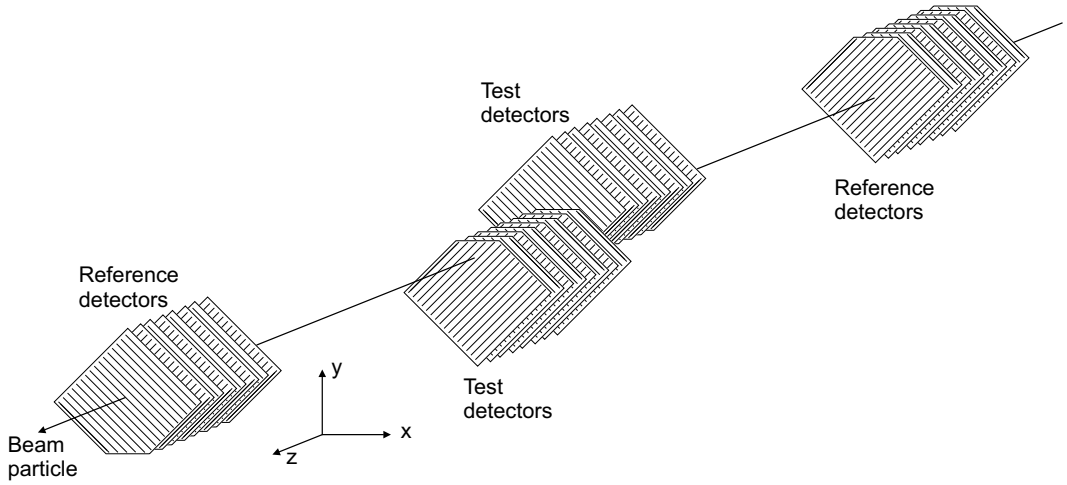

Figure 5.14: Spatial layout of the telescope and the definition of the global coordinate system. Detector wafers are parallel to the (x, y) plane. The beam is approximately parallel to z-axis. Each package consisted of 4 detector pairs of strips oriented orthogonally. The test packages (visible in the middle), are placed such that their edges are close to the (x, y) centre of the system. Due to readout problems, only 15 out of 24 detectors equipped with the APV25 chips were fully operative.

In the alignment procedure the straight high momentum muon tracks going through all the operable detectors were used. The multiple scattering influence is negligible[4] so that the particle trajectories were very smooth and formed a good

[4]For MIP tracks traversing 32 300 μm-thick silicon wafers, a RMS scattering angle $\sigma(\theta) \approx 0.9\,\mu$rad, which corresponds to a RMS transverse displacement $\sigma(x) \approx 0.3\,\mu$m, which is 2 orders of magnitude less than the resolution of the detectors ($\sim 20\,\mu$m).

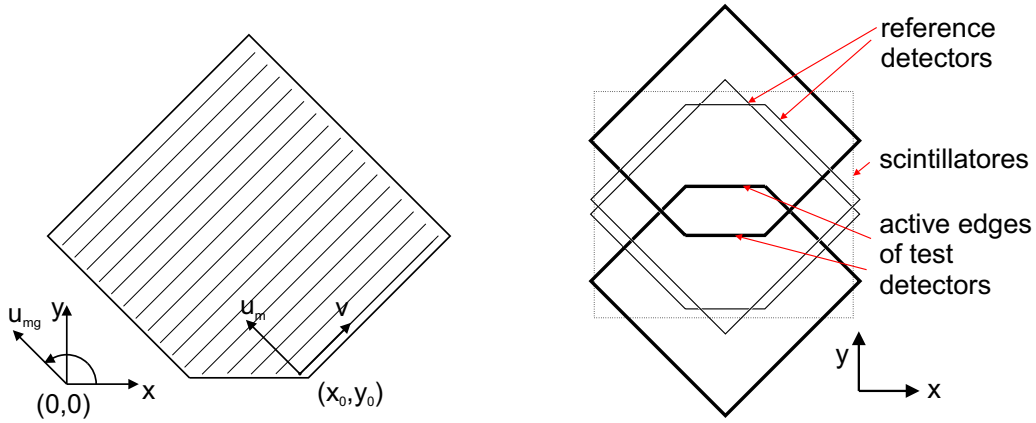

Figure 5.15: Left: Detector read-out coordinate system. The detector readout axis u_m is orthogonal to the strips and it originates from the end of the right-most detector strip. For the purpose of the reconstruction, the u_{mg}-axis is introduced (see Equation 5.7). It is parallel to the u_m-axis, but it originates from the the point $(x, y) = (0, 0)$. The v-axis is parallel to the strips and thus no readout in this direction is possible. The angle γ is the rotation of the detector read-out axis with respect to the x-coordinate of the global coordinate system. The detector planes are assumed to be perpendicular to the z-axis, not visible in the plot. Right: Projection of detector overlaps. The edges under test are seen in the centre of the reference detector overlap.

basis to align the detectors with respect to each other.

In the beginning, the misalignment of the detectors tried to be corrected with manual adjustments of shifts and rotations on the basis of the observed residual distributions. However, this procedure was not successful and finally an automated procedure was implemented.

Alignment algorithm The particle trajectories are fitted with straight lines. We denote the telescope coordinate system as x, y, z (see Figure 5.14), and the local detector system as u, v (Figure 5.15, left). The z axis is parallel to the beam, x axis is horizontal and y axis points upwards. The u-axis is along the measured coordinate and v-axis is parallel to the strips. Each detector hit is a 2D point (local u-coordinate and metrology measured sensor z-position).

The objective of the alignment procedure is to find Δu_i displacements of the detectors and the rotations $\Delta\gamma_i$ of the sensors from their nominal position. Software correction of detector displacements in v direction is not possible, because the detectors have no read-out in this direction. Since the particles are parallel to the z-axis (beam angular spread of $1.4\,\mu$rad), the metrology measurements of z-position of detector wafers are precise enough for the tracking. It is also assumed

that the detector planes are orthogonal to the z-axis of the global reference system, since small angular deviations from the orthogonality do not affect significantly the precision of track reconstruction.

Track reconstruction A straight line is parametrised in the telescope coordinate system as:

$$\begin{cases} x = a_1 + a_3 z \\ y = a_2 + a_4 z \end{cases} \tag{5.3}$$

Suppose that the u-axis makes an angle γ with the x-axis (rotation around z-axis) and that the u-origin lies on the z-axis. Then the u-coordinate of a point on a straight line reads:

$$u_g = \vec{g}\vec{a}, \tag{5.4}$$

where $\vec{g} = (\cos\gamma, \sin\gamma, z\cos\gamma, z\sin\gamma)$, $\vec{a}^{\mathrm{T}} = (a_1, a_2, a_3, a_4)$. The subscript g indicates that the u-coordinate originates from the z-axis of the global coordinate system. The vector $\vec{u}_g$ of N u-coordinates on the track is:

$$\vec{u}_g = \mathbf{G}\vec{a}, \tag{5.5}$$

where $\mathbf{G}$ is a $N \times 4$ matrix of the rows $\vec{g}_i$:

$$\vec{g}_i = (\cos\gamma_i, \sin\gamma_i, z_i\cos\gamma_i, z_i\sin\gamma_i). \tag{5.6}$$

Let u_m be the measurement in the local reference system of the detector, as defined in Figure 5.15, left. Each local u-measurement can be expressed in terms of global u_{mg} coordinate, since the global and local detector u-coordinates are parallel, just the local one originates from $\vec{O} = (x_0, y_0)$ point:

$$u_{mg} = u_m + \vec{u}\vec{O}^{\mathrm{T}}. \tag{5.7}$$

Now we denote the vector of measured coordinates associated to a track as $\vec{u}_{mg}$. Then the array of hit residuals ϵ_i is:

$$\vec{\epsilon} = \vec{u}_{mg} - \vec{u}_g. \tag{5.8}$$

The χ^2 function to be minimised to get the vector of track coefficients $\vec{a}$ reads:

$$\chi^2 = \vec{\epsilon}^{\mathrm{T}}\mathbf{V}^{-1}\vec{\epsilon}, \tag{5.9}$$

where $\mathbf{V}$ is the $N \times N$ covariance matrix of the measurements $\vec{u}_{mg}$. Since multiple scattering is negligible and detectors were randomly misaligned, we assume $\mathbf{V}$ is a diagonal matrix with elements $V_{ii} = \sigma_i^2$, where σ_i is the resolution of detector i. The vector of track parameters $\vec{a}$ is found by means of minimisation of χ^2. Equation 5.9 is a positively defined quadratic form and thus its minimum can be found analytically by calculating the stationary point. By expanding Equation 5.9 we obtain:

$$\chi^2 = (\mathbf{G}\vec{a} - \vec{u}_{mg})^{\mathrm{T}}\mathbf{V}^{-1}(\mathbf{G}\vec{a} - \vec{u}_{mg}). \tag{5.10}$$

Differentiating χ^2 with respect to $\vec{a}$ and putting it equal to $\vec{0}$ yields[5] :

$$\frac{\delta\chi^2}{\delta\vec{a}} = 2\mathbf{G}^{\mathrm{T}}\mathbf{V}^{-1}\mathbf{G}\vec{a} - 2\mathbf{G}^{\mathrm{T}}\mathbf{V}^{-1}\vec{u}_{mg} = \vec{0}. \tag{5.11}$$

By solving Equation 5.11 we get

$$\vec{a} = (\mathbf{G}^{\mathrm{T}}\mathbf{V}^{-1}\mathbf{G})^{-1}\mathbf{G}^{\mathrm{T}}\mathbf{V}^{-1}\vec{u}_{mg}. \tag{5.12}$$

The covariance matrices of track coefficients $\vec{a}$ and of the impact points $\vec{u}_g$ are obtained by error propagation from Equation 5.12 and Equation 5.5, respectively:

$$\mathbf{V}_{\vec{a}} = (\mathbf{G}^{\mathrm{T}}\mathbf{V}^{-1}\mathbf{G})^{-1} \tag{5.13}$$

$$\mathbf{V}_{\vec{u}_g} = \mathbf{G}\mathbf{V}_{\vec{a}}\mathbf{G}^{\mathrm{T}}. \tag{5.14}$$

Since $\mathbf{V}^{-1}$ is diagonal, the software implementation of Equations 5.12-5.14 is optimised to avoid multiplications by zero off-diagonal elements.

Computation of alignment corrections The metrology measurements were not precise enough to reach the desired track reconstruction accuracy and the remaining misalignments need to be corrected. The misalignments aimed to be corrected for are those in the local coordinate u_m and in the orientation parameter γ:

$$\begin{aligned} u_{m_i} &\longrightarrow u_{m_i} + \Delta u_i \\ \gamma_i &\longrightarrow \gamma_i + \Delta\gamma_i \end{aligned} \tag{5.15}$$

The alignment problem is to find the correction parameters $(\Delta u_i, \Delta\gamma_i)$, $i = 1, \ldots, N$, for N detectors. In principle there are four additional correction param-

[5]The derivative $\frac{\delta\chi^2}{\delta\vec{a}}$ denotes the vector of partial derivatives of χ^2 taken with respect to each of the components of the vector $\vec{a}$: $\frac{\delta\chi^2}{\delta\vec{a}} = \left(\frac{\delta\chi^2}{\delta a_1}, \frac{\delta\chi^2}{\delta a_2}, \ldots, \frac{\delta\chi^2}{\delta a_N}\right)^{\mathrm{T}}$.

eters per detector, which are, either redundant (shift along the strip direction) or negligible (two projections of the angle between the normal vector of the detector plane and the z-axis, shift in z-direction).

The alignment procedure is iterative and can be summarised as follows:

1. Only events of at most one cluster per detector are used.
2. The tracks with all $N = 17$ detectors are used.
3. A track fit (see Equation 5.12) for M tracks using so far the best alignment parameters is performed.
4. Bad tracks are rejected. The better known the detector displacements the more restrictive track cuts are applied.
5. A Grand χ^2 (see Equation 5.17) taken over M tracks is minimised to find the alignment corrections.
6. The procedure is repeated until the alignment corrections converge.

The Grand χ^2 taken over M tracks is defined as:

$$\chi^2_M = \sum_{j=1}^{M} \vec{\epsilon}_j^{\mathrm{T}} \mathbf{V}^{-1} \vec{\epsilon}_j, \tag{5.16}$$

where ϵ_j is a vector of residuals of track j. Since $\mathbf{V}$ is diagonal, we can write Equation 5.16 as:

$$\chi^2_M = \sum_{i=1}^{N} \sum_{j=1}^{M} \frac{\epsilon_{ij}^2}{\sigma_i^2}, \tag{5.17}$$

where the residuals ϵ_{ij} are defined as:

$$\epsilon_{ij} = u_{m_{ij}} + \Delta u_i - \cos(\gamma_i + \Delta\gamma_i)(a_{1j} + a_{3j} z_i - x_{0i}) - \sin(\gamma_i + \Delta\gamma_i)(a_{2j} + a_{4j} z_i - y_{0i}). \tag{5.18}$$

The point (x_{0i}, y_{0i}) is the metrology defined origin of the the coordinate system of i^{th} detector ($i = 1, \ldots, 17$). Coefficients Δu_i and $\Delta\gamma_i$ are alignment corrections. Index j runs over tracks. The alignment is made relative to the first and last working detector pairs. First of all the reference detectors were aligned and then the tested ones.

For each iteration over a batch of M tracks, equation 5.17 has to be minimised with respect to the vectors of corrections $\Delta\vec{u}$ and $\Delta\vec{\gamma}$. Because of the presence

of angular component $\Delta\vec{\gamma}$ the function is nonlinear and an iterative numerical minimisation has to be applied. We assume the function 5.17 to be quadratic-like and we just search for the stationary point. This defines a set of $2N$ equations:

$$\frac{\delta\chi^2_M}{\delta(\Delta u_i)} = 0, \quad \frac{\delta\chi^2_M}{\delta(\Delta\gamma_i)} = 0. \tag{5.19}$$

The equations 5.19 are solved iteratively with Newton's method. For each iteration the correction parameters are updated by means of

$$\begin{pmatrix} \Delta u_i \\ \Delta\gamma_i \end{pmatrix}_{\text{New}} = \begin{pmatrix} \Delta u_i \\ \Delta\gamma_i \end{pmatrix}_{\text{Old}} - \mathbf{H}(\chi^2_M)^{-1} \cdot \bigtriangledown\chi^2_M, \tag{5.20}$$

where $\mathbf{H}(\chi^2_M)$ denotes the $(2N \times 2N)$ matrix of second partial derivatives, defined with respect to the alignment correction coefficients. It turns out that $\mathbf{H}(\chi^2_M)$ consists of N (2×2) submatrices on the diagonal with the other elements equal 0. Hence, the software implementation of Equation 5.20 is decomposed into N (2×2) independent and detector related equations. The procedure was iterated until the updates of displacements reached submicron values.

Software alignment results In the very first phase of the analysis, large enough fit tolerances were necessary to recognise the tracks due to detector misalignments. The positions of the detectors are only metrology based.

Figures 5.16 and 5.17 show the residuals of the tracks reconstructed without any software alignment.

Figure 5.16 presents the residual distribution of a typical detector. A shift of 32 μm and a rotation of 0.9 mrad with respect to the measured positions is observed. Several detectors unfortunately got unglued from the hybrid, which caused large displacements visible in their residual distribution. In Figure 5.17 the residual distributions of an unglued detector are shown. The shift of 233 μm and the rotation of -18 mrad are visible.

After applying the alignment procedure the shifts and tilts of the detectors were corrected. The residuals after alignment corrections are shown in Figure 5.18 and in Figure 5.19. For these plots, the tracks were defined by the reference detectors. The position of test detector impact points was interpolated. The residuals are smeared by the error of the interpolation of the telescope tracks, of the order of 10 μm.

Figure 5.19 (a), (b) and (c) shows the resolutions of planar/CTS silicon de-

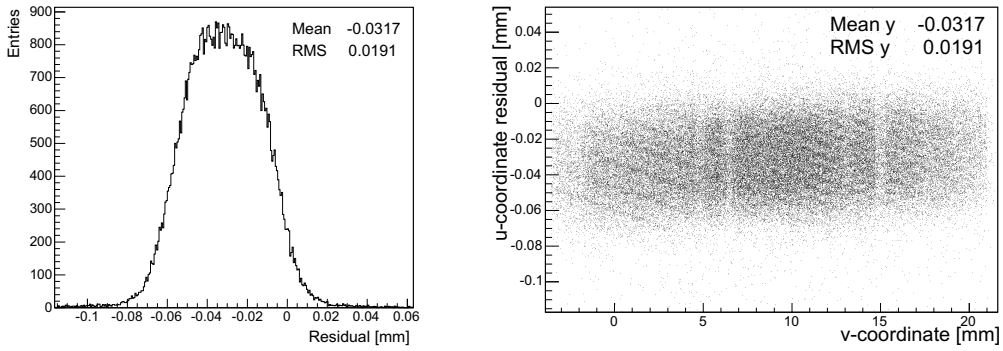

Figure 5.16: Left: Residual distribution of a typical detector shifted by 32 μm before applying the alignment algorithm. The mean of the histogram represents the detector shift with respect to the measured position. The RMS value of 19.1 μm, which is close to the nominal detector resolution, indicates that the orientation misalignment was low. Right: The residual distribution plotted as a function of the orthogonal coordinate. The tilt of the cloud (0.9 mrad) represents the orientation misalignment.

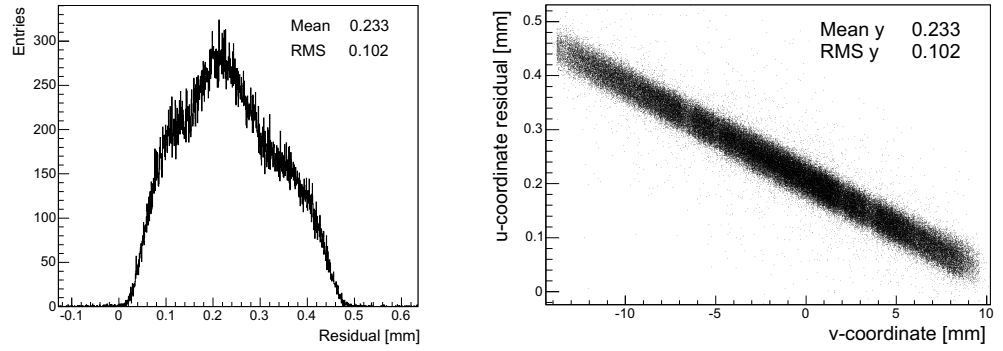

Figure 5.17: Left: Residual distribution of an unglued detector. The mean value indicates a high misalignment of 233 μm. The RMS value 102 μm of the histogram is considerably higher than the expected resolution of 19.1 μm. This results from large orientation misalignment. Right: The residual distribution plotted as a function of the orthogonal coordinate. The rotation misalignment of -18 mrad is visible in the tilt of the profile.

tectors and plot (d) represents a planar/3D detector. The RMS values values of the distributions are slightly better than the theoretical value of $66\,\mu m/\sqrt{12} = 19.05\,\mu m$. This is because of charge sharing ($\sim$ 20% of events of detectors a, b, c, and $\sim$ 36% of events of detector d). The shapes of the distributions are non-gaussian due to the fact that the majority of events exhibited no charge sharing. The planar/3D detector (d) was operated at a lower voltage than the others which resulted in higher fraction of events with charge division between two adjacent strips and a bit different shape of the distribution.

The accurate determination of the alignment precision is difficult to assess.

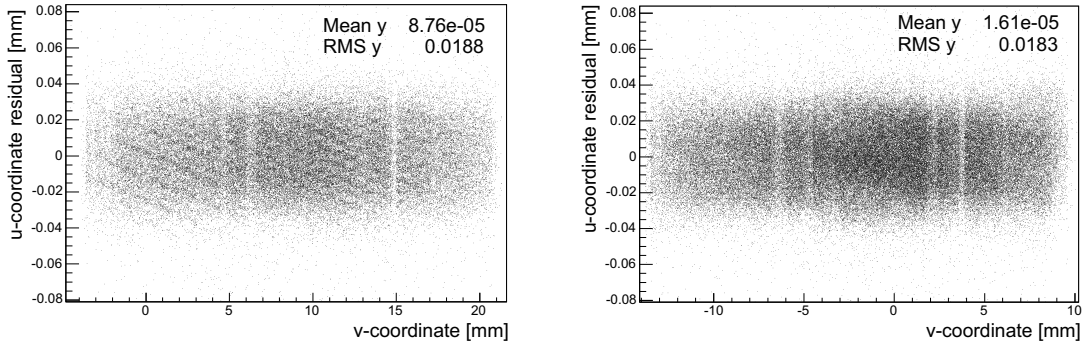

Figure 5.18: The residual distributions after applying the alignment algorithm. The left and right residual profiles correspond to those presented in Figures 5.16 and 5.17, respectively. The shifts and the tilts of the clouds were corrected. Both the typical detector (left) and the unglued one (right) exhibit the displacement of less than 0.1 μm, which corresponds to angular precision of $\sim 0.1\,\mu m/20\,mm = 5\,\mu$rad if 20 mm-long lever arm is assumed.

Since the shifts of all the residual distributions are less than 1 μm and since their RMS value is fully compatible with the expected detector resolution, the achieved alignment precision is estimated to be least at the level of a micron.

5.1.4 Edge performance studies

The test beam setup was used to determine the resolution and the behaviour of the efficiency[6] at the active edge of the test detectors. For these studies the detectors were operated at a temperature of around -10°C.

The CTS detectors in the test setup were biased at of 40 V, enough to overdeplete them. The 3D detector prototypes were biased at the lower voltage of 30 V due to higher leakage current and therefore were slightly undepleted.

The efficiencies of the test detectors with respect to their geometrical coordinates were computed as fractions of accepted tracks. A track was considered as accepted when the test detector registered a hit within $\pm 200\,\mu$m from the track. Figure 5.20 shows tracks accepted by two typical planar detectors, placed at the top and at the bottom test package. The impact point reconstruction precision in the centre of the telescope was better than 10 μm. Since the tracks were defined by altogether 10 detectors, the background rejection was very high and the background component of the efficiency profiles, computed in the following section, is not visible.

[6]Detector efficiency is the probability of detecting an event if it has taken place. In case of the planar silicon detectors it is the probability of detection of the passage of the particle through the detector plane.

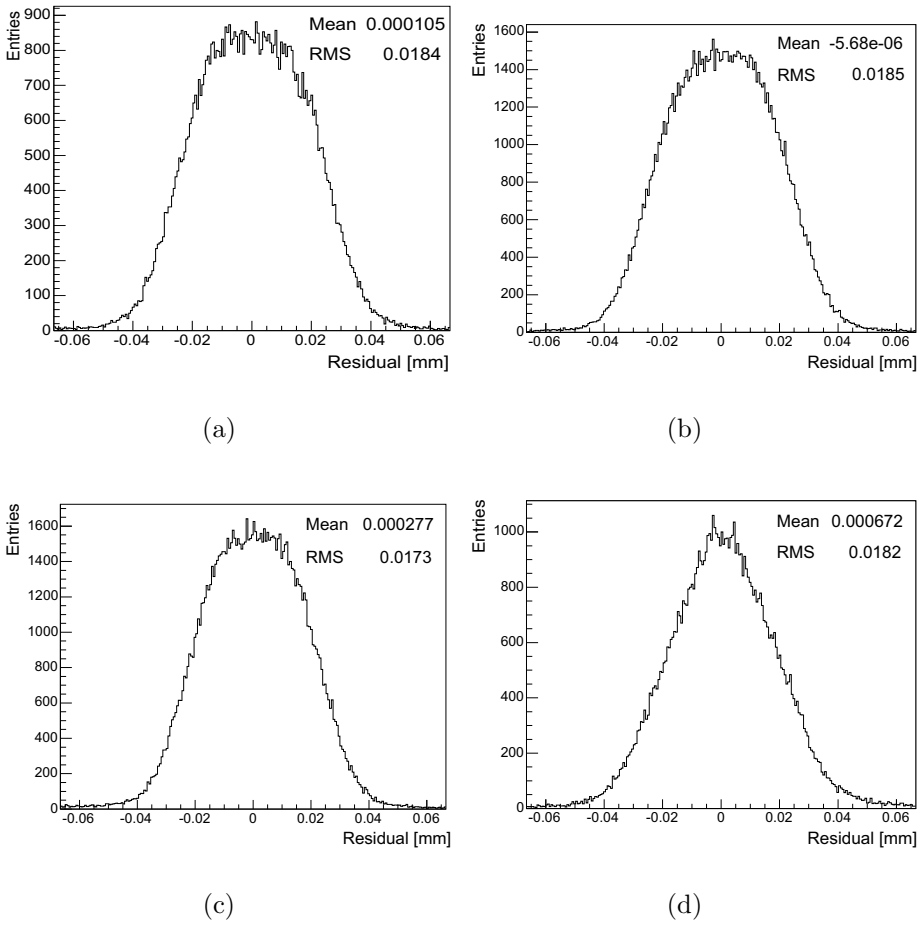

Figure 5.19: The test detector residual distributions. The tracks were defined by detectors other than the tested one and the position of impact points at tested detectors was interpolated. The residuals are smeared by 10 μm which is the error of the interpolation of the telescope tracks. Plots (a), (b) and (c) show the resolutions of planar/CTS silicon detectors and plot (d) represents a planar/3D detector.

The interpolation error of the telescope tracks was of the order of 10 μm.

CTS Edge

Cut edge position determination Four working CTS silicon detectors were available for the edge efficiency studies. The layout of their edges is shown in Figure 5.21. The cut of the sensor edge is by design 58 μm apart from the end of the strips. Left and right edges of the detector sensitive area are far from their corresponding wafer cuts and are equipped with a voltage terminating ring. Thus the influence of left and right cut edges on the electric field of the sensitive area in the nearby of lines A and B is highly reduced.

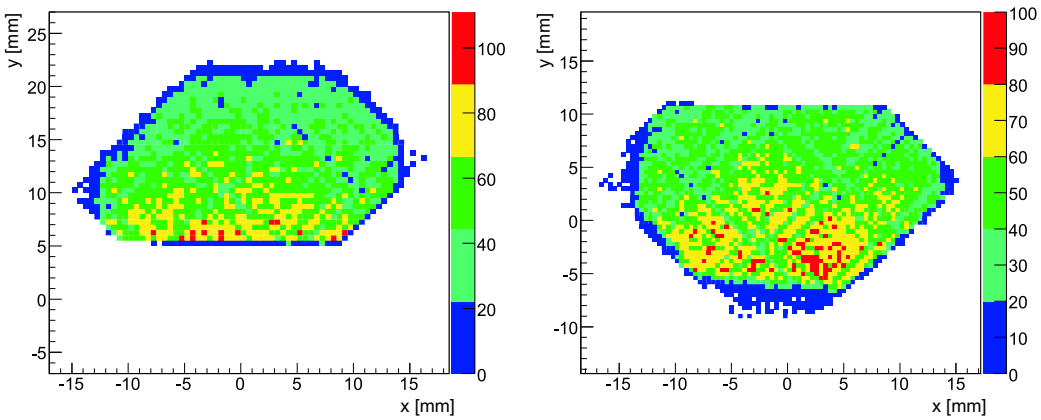

Figure 5.20: Tracks accepted by the 2 tested detectors placed at the top (left plot) and at the bottom (right plot) of the test package.

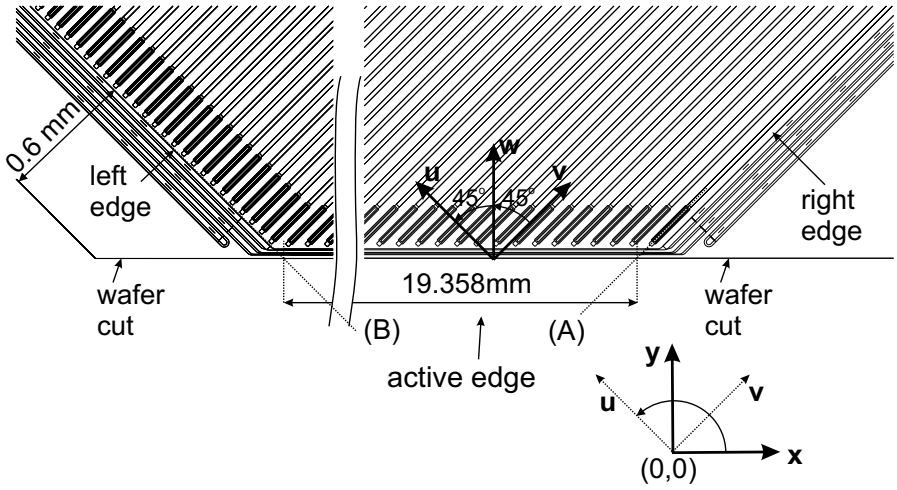

Figure 5.21: The edge of the CTS detector. In the picture, the coordinate system is presented. The unit vector $\vec{w}$ is orthogonal to the cut edge and it is taken as the direction of the edge efficiency profile. The u and v-axes are perpendicular (parallel) to the strips. Line A (parallel to the right edge) is defined by the right-most strip centre. Line B is parallel to the left edge and lies in the middle between the clean-up ring and the left strip ends. The distance between the two lines, measured along the cut edge, is 19.358 mm.

In order to relate the efficiency of the detector to its cut edge, the position of the edge has to be determined in the (x, y, z)-coordinate system. The combined reconstruction and alignment information was used to accomplish this task.

Again the unit vector $\vec{u}$ ($\vec{v}$) is orthogonal (parallel) to the strips. The unit vector $\vec{w}$ is orthogonal to the edge of the detector and lays in the detector plane. The coordinate system is shown in Figure 5.21. The alignment procedures described

in Section 5.1.3 determined precisely the rotation γ between x and u-axis, and the u-position of each detector.

By means of γ, the directions of vectors $\vec{u}$, $\vec{v}$ and $\vec{w}$ can be determined in the (x, y)-coordinate system. The software alignment defines the line A which goes through the centre of the first strip of the detector. However, to find out the position of the cut edge a v-coordinate alignment is needed in addition. Since the direction of v is very well known, and the electric field in the area of the strip ends (line B) can be assumed normal to the surface of the wafer, the position of the line B can be approximately determined by the efficiency behaviour of the left edge. The charge generated by the particles traversing line B is divided between the ends of the strips and the clean-up ring. The position of line B is then defined by the 50% efficiency position and its error — by the size of the acceptance drop area.

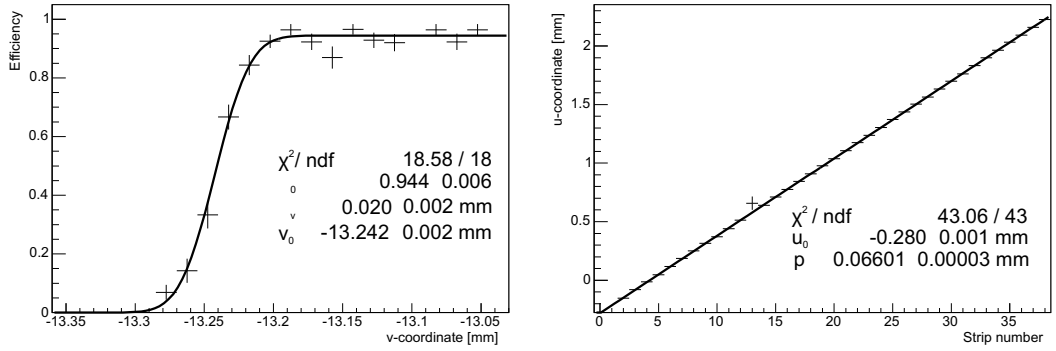

Figure 5.22: Left: Left edge efficiency as a function of the v-coordinate of the tested detector. The efficiency profile is used to determine the position of the left edge, as defined by line B in Figure 5.21. The plot is fitted with the function defined in Equation 5.21. The fitted parameters are shown in the plot. Right: The mean u-position of the impact point with respect to the strip number. The fitted line, defined by Equation 5.22, is used to determine the position of the right-most strip. The fitted parameter values are shown in the plot. The reconstructed p value is in perfect agreement of the design detector pitch of 66 μm.

Figure 5.22 (left) shows the typical efficiency behaviour of the left detector edge. The efficiency is fitted with the step function with Gaussian smearing:

$$\eta = \frac{\eta_0}{2}\left[1 + \mathrm{Erf}\left(\frac{v - v_0}{\sigma_v\sqrt{2}}\right)\right], \tag{5.21}$$

where η is the efficiency, η_0 is the plateau efficiency, Erf is the Gaussian error function, v_0 is the position of half-efficiency, σ_v characterises the size of the efficiency rise interval and is taken as the error of left edge estimation. For the analysed

left edge, the middle of the efficiency rise is at $v_0 = -13.242 \pm 0.0015\,\text{mm}$ and the assumed error of edge position estimation equals $\sigma_v = 20\,\mu\text{m}$.

The width of 10%-90% efficiency rise is $50 \pm 5\,\mu\text{m}$ and $v_0 = -13.242 \pm 0.0015\,\text{mm}$.

The profile of u-position of the impact point as a function of the strip number is presented in Figure 5.22 (right). The DAQ readout identifier of the right-most strip is 0. The u-position of the right-most strip can be calculated by means of the line fit:

$$u = p \cdot i + u_0, \tag{5.22}$$

where u is the mean value of the u-coordinate, p is the detector pitch, $i = 0, \ldots, 511$ is the strip number, u_0 is the position of the right-most strip. The values obtained for the discussed plot are: $p = 66.01 \pm 0.03\,\mu\text{m}$, $u_0 = -280.4 \pm 1\,\mu\text{m}$.

Once the positions of lines A and B are determined, the edge cut position, in direction w, can be calculated following the detector design by:

$$w_{\text{cut}} = \frac{u_0 + v_0}{\sqrt{2}} + \frac{19.358}{2}\,\text{mm}. \tag{5.23}$$

For the discussed detector the cut position is at $w_{\text{cut}} = 0.117 \pm 0.014\text{mm}$. The achieved cut position precision is rather low, but allows us to relate the detector efficiency to its physical design.

The cut edge positions of the other tested CTS detectors have been determined in the same way and the results are reported in Table 5.1.

CTS edge behaviour Finally, the edge efficiency was studied. Test detector impact points were projected on to w-coordinate (see Figure 5.21) orthogonal to the detector edge, and on this basis the edge efficiency profiles were computed. The obtained profiles (see Figure 5.23) were fitted with a step function with Gaussian smearing $\eta(w)$:

$$\eta = \frac{\eta_0}{2}\left[1 + \text{Erf}\left(\frac{w - w_0}{\sigma_w\sqrt{2}}\right)\right], \tag{5.24}$$

where η_0 is the plateau efficiency, Erf is the Gaussian error function, w_0 is the position of half-efficiency, σ_w represents the Gaussian smearing.

The fitted parameters were used to compute the 10 %-90 % efficiency rise interval $d_{10-90\,\%}$ and the distance between the cut edge and the 90 %-efficiency ($d_{\text{cut}-90\,\%}$). The results are summarised in Table 5.1. For 3 detectors the efficiency rises from 10 % to 90 % within less than $40\,\mu\text{m}$ and the distance from the cut edge and the 90 % efficiency is of the order of $50\,\mu\text{m}$. Only one of the de-

Det. id.	Cut edge position w_{cut} [μm]	Efficiency 50 % position w_0 [μm]	σ_w [μm]	10 %-90 % efficiency interval $d_{10-90\,\%}$ [μm]	Cut edge to 90 % eff. dist. $d_{\mathrm{cut}-90\,\%}$ [μm]	Efficiency plateau η_0 [%]	χ^2 / ndf
7	-19 ± 12	21 ± 1	17 ± 1	43 ± 3	62 ± 13	96.7 ± 0.5	40 / 57
11	117 ± 14	150 ± 2	14 ± 1	37 ± 3	52 ± 14	95.3 ± 0.6	57 / 61
12	-128 ± 14	-97 ± 1	11 ± 1	27 ± 3	45 ± 14	94.1 ± 1.0	38 / 57
13	81 ± 7	112 ± 1	11 ± 1	27 ± 3	45 ± 7	93.8 ± 0.8	53 / 51

Table 5.1: Results of the edge efficiency studies of 4 tested CTS detectors.

tectors (detector 7) has a bit larger insensitive edge volume ($d_{\mathrm{cut}-90\,\%} = 62\,\mu$m). The efficiency plateau for all the detectors is about 95 %. The efficiency loss is caused mainly by the unbounded and noisy strips of the studied detectors. The hit number was integrated all along the edge. Usually there were 12–16 missing strips over 512. This corresponds to an efficiency loss of $\sim 3\,\%$. The 2D efficiency profile in Figure 5.24 (left) shows the presence of missing strips. In addition, $\sim$1 % of the efficinency loss was caused by the non-optimal signal-to-noise ratio. The detectors were operated at 40 V. Although they were fully depleted, a small fraction of the charge was not collected within the integration time of the readout electronics. Figure 5.24 (right) shows the signal-to-noise distribution of one of the tested CTS detectors without applying any reconstruction cuts. Although the signal-to-noise ratio is not optimal (see Section 5.1.2), the signal peak is well separated from the noise, which indicates high detector efficiency. The most probable signal-to-noise ratio equals 18.

Since the bias voltage is applied by the punch through mechanism (see Section 4.2.1) the guard rings and the strips are at about the same potential. Thus charge generated in the vicinity of the cut edge is collected both by the guard rings (the current terminating ring and the clean-up ring) and by the detector strips. The further the impact point from the cut edge, the higher the fraction of charge collected by the strip. Since the noise of the detector (see Section 4.2.1), remains constant, the signal-to-noise ratio should deteriorate the closer the impact particle to the cut edge. Such a phenomenon is observed and shown in Figure 5.25 (left).

Since the detector strips are tilted at 45° with respect to the edge (see Figure 5.25, right), the collection of charge generated outside the geometrical strip area should cause a bias of the impact point reconstruction. Figure 5.26 (left) shows the 2D strip charge sharing profile. In reality, data of parallel strips have

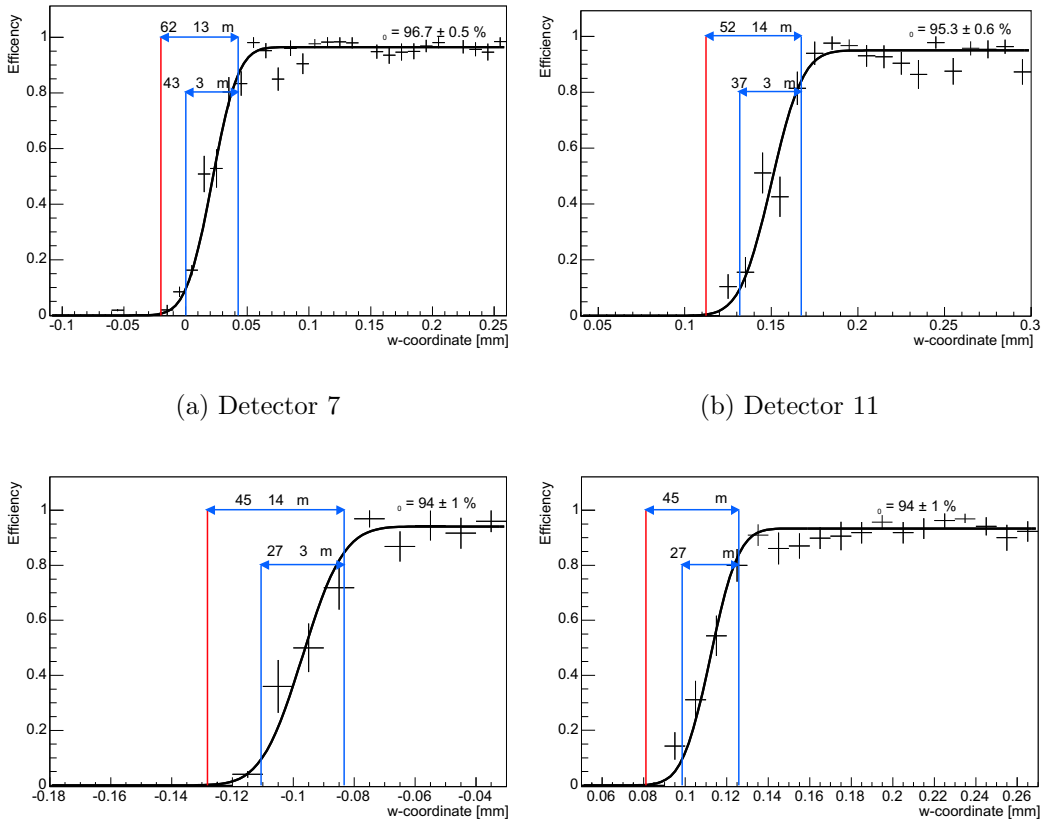

(a) Detector 7

(b) Detector 11

(c) Detector 12

(d) Detector 13

Figure 5.23: The efficiency profiles of the active edges of the CTS detectors. The left-most red vertical line gives the position of the wafer cut. The blue lines show the 10–90 % efficiency rise interval. The fit details are given in Table 5.1.

been superimposed to reduce statistical fluctuations. The fraction ϱ of the cluster charge Q_{Cluster} collected by the main strip of the cluster $\varrho = Q_{\text{Mainstrip}}/Q_{\text{Cluster}}$ as a function of the (x, y) impact point is plotted. The 2D detector hit point is reconstructed by the reference detectors. As was already discussed in Section 5.1.2, generally, the amount of charge sharing is low, which corresponds to ϱ values close to 1. A small presence of the charge sharing is only visible in the area between the strips. The width of the strip charge collection area is a bit enlarged because of the interpolation smearing of $\sim 10\,\mu$m.

The charge sharing profile, in addition, shows the directions of the charge collection. In the regions far from the edge, the charge is collected, as expected, in directions perpendicular to the strips. However, in the edge area, the direction of strip charge collection is observed to be orthogonal to the edge, which indicates, that the charge is collected from the areas not covered by the strips. This is

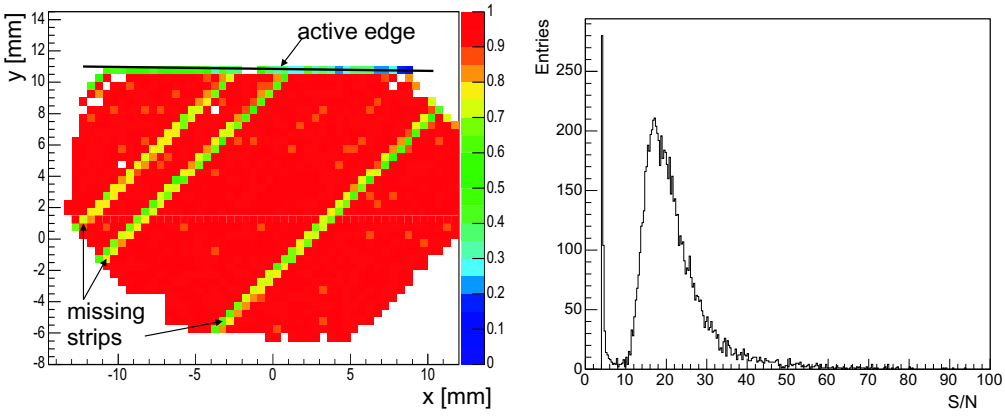

Figure 5.24: Left: 2D efficiency map of a CTS detector. The unbounded and noisy strips (rejected from the reconstruction) reduce the detector efficiency. Since 6 out of 208 strips at the edge are missing the projected edge efficiency is reduced by $\sim 3\,\%$. Right: Signal-to-noise distribution of the tested CTS detector operated at 40 V without any reconstruction cuts.

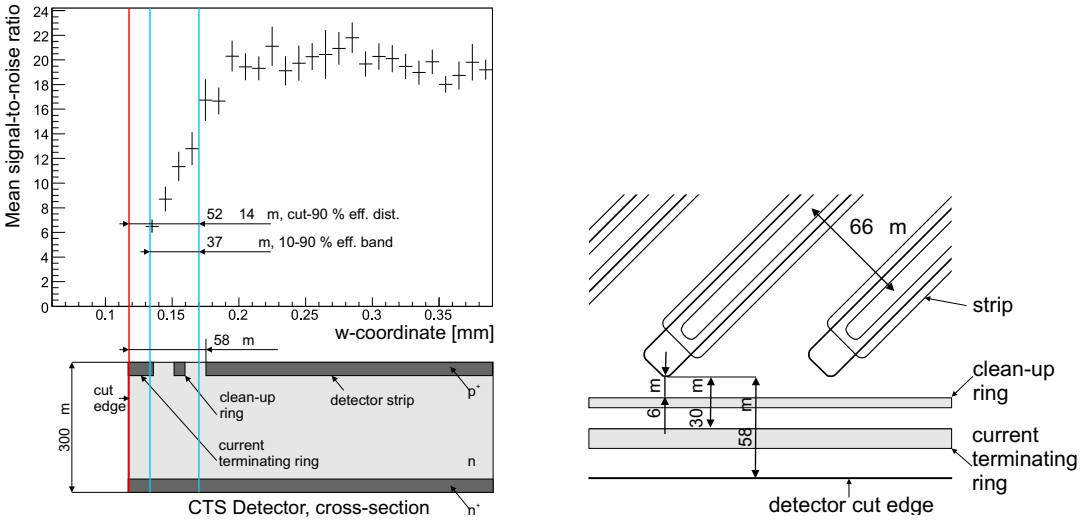

Figure 5.25: Left: CTS Detector signal-to-noise profile in the edge area and the corresponding detector cross-section (bottom). The observed signal-to-noise ratio decreases for the near-edge particles. The corresponding efficiency profile is shown in Figure 5.23 (b). The geometrical overlap indicates that the charge collected by the strips originates also from the volume below the current terminating ring and the clean-up ring. Right: CTS Detector edge layout.

consistent with the fact that the tested detector starts to be partially efficient in the volume close to the cut edge. Since the strips start only at 58 μm from the edge (see Figure 5.25, right), the charge is transported (by diffusion and by the electric field) towards the strips, thus in the direction approximately perpendicular to the

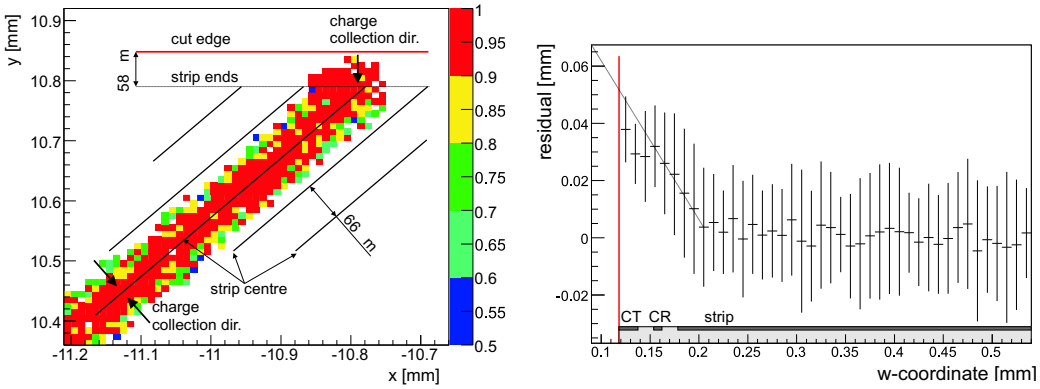

Figure 5.26: Left: Charge sharing 2D profile of one strip. The plotted values are the fraction of the cluster charge, collected by the main cluster strip, as a function of the impact point. The plot also demonstrates the direction of charge collection. Right: Bias of the residual as a function of the distance from the edge. The error bars show the resolution.

edge.

The alteration of the charge collection direction affects the residual distributions of the reconstructed hits. The residuals are computed as the difference between the impact point interpolated by the reference detectors and that reconstructed by the test detector. In Figure 5.26 (right) is presented the bias of the residuals as a function of the distance from the edge. The points show the residuals mean values while the bars indicate the RMS of the residual distribution. While the detector resolution is nearly constant throughout the sensor, the reconstructed hits become more biased closer to the cut edge. The bias value close to the cut is hard to estimate precisely due to the low statistics resulting from the low acceptance. However, if the observed linear trend is assumed, the extrapolated residual bias value is $\sim 50\,\mu$m. The residual is computed in local u, v-coordinate system, corresponding to a displacement of $50/\sqrt{2} = 35\,\mu$m perpendicular to the edge displacement. This is in agreement with the detector's edge layout (Figure 5.25, right).

The results of the beam tests are in good agreement with the CTS edge simulations, which are reported in [54].

Planar/3D Active Edge

The tests of a 3D active edge technology (see Section 4.3.2) were also performed during the same testbeam. The available prototype detector was $\sim 220\,\mu$m thick

and was operated at reverse bias voltage of 30 V. Due to an excess leakage current injected by a noisy strip, the sensor was therefore operated slightly underdepleted. This resulted in a mean signal-to-noise ratio of 16. The signal-to-noise distribution without any cuts is shown in Figure 5.27 (left). Since the most probable value of signal-to-noise is only 10, the signal peak is not well separated from the noise peak. Thus, if the signal-to-noise cut is set high enough to reject the noise — the detector is inefficient. On the other hand, if the cut is set low to optimise the detector efficiency, some fraction of the noise is accepted and non existing hits are reconstructed. In the following analysis, a signal-to-noise cut of 4 was applied and only well defined reference tracks were used to determine the events.

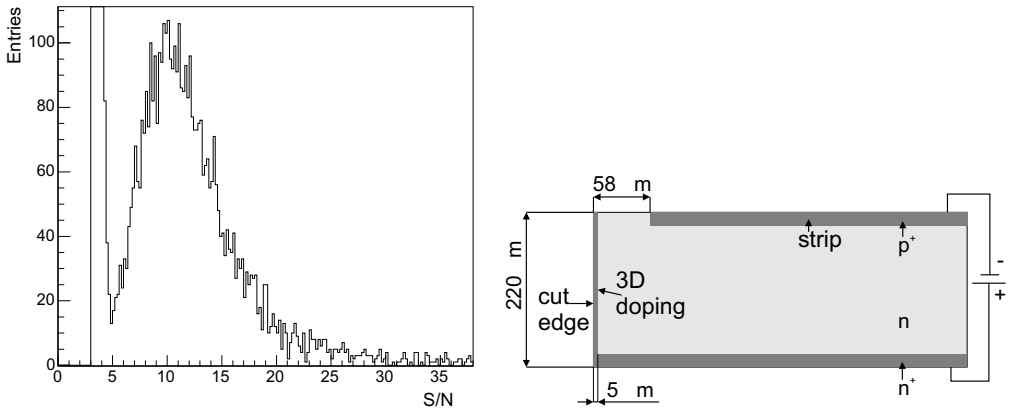

Figure 5.27: Left: Signal-to-noise profile of the tested 3D/planar detector operated at 30 V without any reconstruction cuts. Right: Cross-section of the tested 3D/planar detector. The distance between the strip end and the cut edge is 58 μm. The cut edge and the strips are reverse biased.

3D Active edge behaviour Figure 5.28 shows the 3D/planar detector layout together with the coordinate systems. The rotation γ and the position of the right-most detector strip in the u-coordinate system is defined by the alignment procedures previously described in Section 5.1.3. The coordinate w is defined in the direction orthogonal to the edge and the edge related profiles are defined in its direction. Since the v-alignment was not possible due to no readout in this direction, the w_{Cut}-position of the cut edge in the global reference system is again unknown.

The detector edges do not have any guard rings. Instead, the 5 μm wide near-cut volume is 3D doped transforming the entire sensitive volume's perimeter into an electrode, as can be seen in Figure 5.27 (right). The cut edge is heavily doped

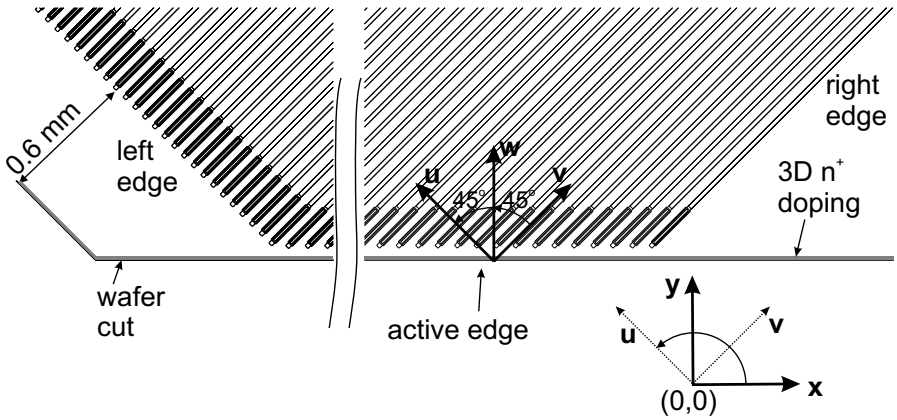

Figure 5.28: The active edge of a 3D/planar detector. In the picture, the coordinate system is presented. The unit vector $\vec{w}$ is orthogonal to the cut edge and it is taken as the direction of the edge efficiency profile. The u and v-axes are perpendicular (parallel) to the strips. The 3D doping is seen at the cut edge.

with n^+ trenches making the side edges an extension of the n^+ doped back side. The cut edge and the strips are reverse biased and the edge is an electrode allowing depletion to develop between the cut edge and the strips. Since the 58 μm-large "active edge" is much smaller than the thickness of the detector (220 μm), if the detector is depleted, the edge should be partially efficient.

In this way the edge is at the same potential as the back-plane electrode. The detector reverse bias voltage is applied directly between the strips and the edge. The region on the right from the 3D doped volume is then partially depleted. The electric field develops then between the 3D edge trenches and the strips and makes the near-edge volume efficient. The detailed analysis of the 3D active edge behaviour is given in [81].

On the basis of the above information, the cut position of the sensor is estimated to be $\sim 5\,\mu$m to the left from the left-most accepted track. The main error component of this estimate originates from the track interpolation uncertainty of $\sim 10\,\mu$m.

The efficiency profile of the tested active 3D edge is shown in Figure 5.29 (left). It was fitted with the step function with Gaussian smearing defined in Equation 5.24. The fit parameters are given in Table 5.2. The detector starts to be 90 % efficient at 35 μm from the cut edge. The fitted 10-90 % efficiency rise band is only 24 μm and its size was enlarged by the track interpolation uncertainty. The efficiency plateau η_0 equals 96.8 %. A few detector strips were either unbonded or noisy which caused the ~ 1 % loss of the w-projected efficiency. The dead strips

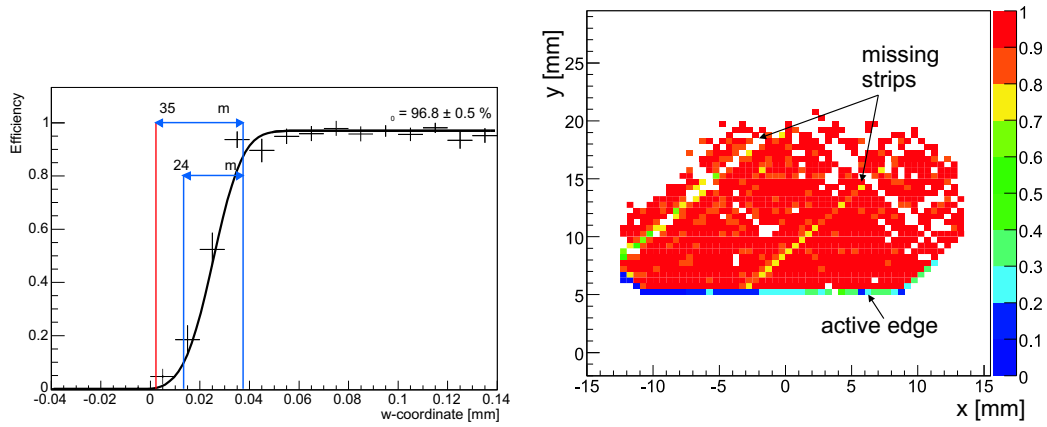

Figure 5.29: Left: The efficiency profile of the 3D active edge. The left-most red vertical line gives the cut position of the silicon detector. The blue lines show the 10-90 % efficiency rise interval. The details of the fit are given in Table 5.2. Right: 2D efficiency map of a 3D/planar detector. The unbounded and noisy strips, rejected from the reconstruction, reduce the efficiency of the detector. 2 out of 208 strips on the active edge are missing which reduces the projected edge efficiency by $\sim 1\,\%$.

Parameter	Fit result
Cut edge position w_{cut}	$2 \pm 10\,\mu$m
50 % efficiency position w_0	$25 \pm 1\,\mu$m
σ_w	$9.4 \pm 0.5\,\mu$m
10 %-90 % efficiency band $d_{10-90\,\%}$	$24 \pm 1\,\mu$m
Cut edge to 90 % eff. dist. $d_{\text{cut}-90\,\%}$	$35 \pm 10\,\mu$m
Efficiency plateau η_0	$96.8 \pm 0.5\,\%$
χ^2 / ndf	50 / 54

Table 5.2: Results of the efficiency fit of the 3D/planar detector.

are visible in the 2D efficiency map shown in Figure 5.29 (right). In addition, since the mean signal-to-noise was only 10 (see Figure 5.27, right), the signal-to-noise value of some of the clusters was below 4, and they were not accepted. This reduces the efficiency by another $\sim 2\,\%$.

The mean signal-to-noise profile near the active edge is shown in Figure 5.30 (left). It decreases from 16 in the regions far from the edge down to 9.5 for the volume adjacent to the cut edge. The corresponding efficiency profile is shown in Figure 5.29 (left). The geometrical overlap indicates that the charge collected by the strips originates also from the volume between the strip ends and the 3D doped area. The deterioration of signal-to-noise ratios in the edge vicinity is caused by the

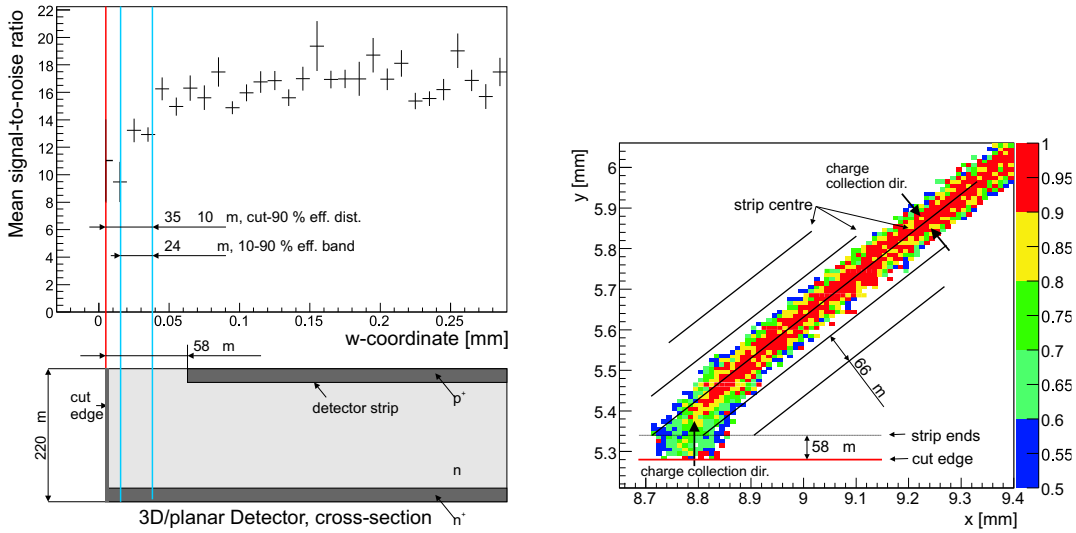

Figure 5.30: Left: 3D/planar detector signal-to-noise profile in the active edge area and the corresponding detector cross-section. Right: Charge sharing 2D map of one strip. The plotted values are the fraction of the cluster charge, collected by the main cluster strip, as a function of the impact point.

reduction of cluster signal, while the noise level was measured to remain constant. This indicates the presence of an undepeleted volume in the near-edge area, from where the generated charge cannot be collected. Certainly the 3D doped region is a part of this area.

Since all the charge generated in the near-edge depleted volume is collected by the strips and the edge size is of the order of the detector pitch, the volume between the strip-ends and the cut exhibits enhanced charge sharing. It is visible in Figures 5.30 (right) and 5.31 (left). The hits of parallel strips have been superimposed and the cumulative charge sharing and cluster size maps of one strip are presented. In the active edge area the majority of clusters contains two strips. In addition, the charge sharing can be observed in the areas approximately equally distant from the strip centres.

Sufficiently far from the edge, the charge is transported in the direction orthogonal to the strips. However, in the volume up to 200 μm from the cut, the direction of the charge collection is perpendicular to the edge.

Figure 5.30 (right) and Figure 5.31 (left) demonstrate also the direction of charge collection. Sufficiently far from the edge, the charge is transported in the direction orthogonal to the strips. However, the charge collection direction in the area of up to 200 μm from the sensor cut, has a strong component orthogonal to the edge. Since the 3D doping of the edge is at the same potential as the back-

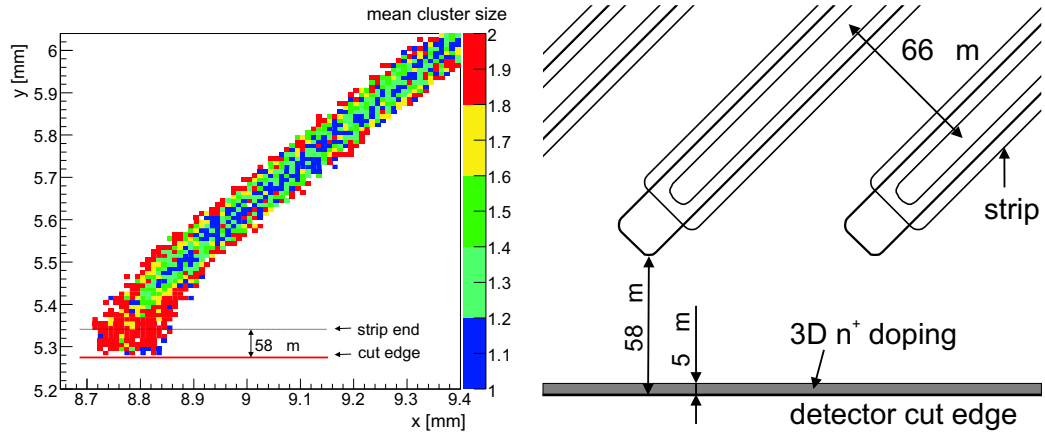

Figure 5.31: Left: Mean cluster size profile. In the areas where charge sharing is present, the clusters often contain 2 strips. For the impact points close to the edge, the average cluster size is 2. Double strip clusters are also visible in the areas between the strips. Right: 3D/planar detector active edge layout. The strips are tilted at 45° with respect to the edge.

plane electrode, the reverse bias voltage, between the strips and the back-electrode, is directly applied to the 58 μm large active edge. This high potential difference over a small distance creates a high electric field directed orthogonal to the edge and at an angle of 45° with respect to the strips (see Figure 5.31, right). The charge collection follows the electric field lines explaining the observed collection direction. This effect has a significant influence on the impact point reconstruction. The residual profile in the proximity of the edge is shown in Figure 5.32. The

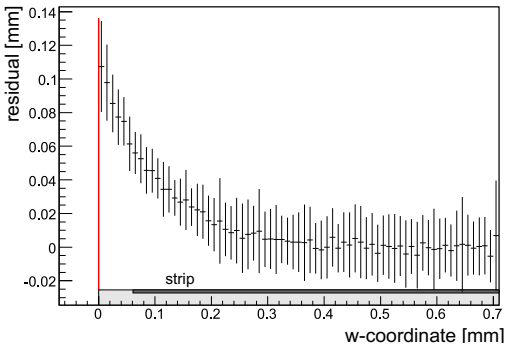

Figure 5.32: Bias of the residual as a function of the distance from the edge. The error bars show the resolution. While the resolution remains approximately constant, the impact point reconstruction bias increases up to 110 μm as the edge is approached. The corresponding 3D/planar detector cross-section is shown below the profile.

different direction of charge transport in the near-edge volume, compared to the centre of the detector creates a bias of the impact point reconstruction. While in the case of CTS sensors this bias was nearly negligible, the 3D/planar one shows a reconstruction bias value of up to 110 μm. In addition, the observed bias extends well outside the active edge region up to $\sim$200 μm far from the active edge. When the 3D/planar detectors will be inserted in the Roman Pots of the TOTEM experiment, where a resolution of 20 μm is assumed, such shifts have to be taken into consideration and corrected by the reconstruction software.

5.1.5 RP operation test in the SPS accelerator

The full system consisting of final size detectors bonded to front-end electronics, a Roman Pot and the data acquisition chain were tested in a coasting beam experiment [71] in the Super Proton Synchrotron (SPS) at CERN. A Roman Pot prototype was fabricated for this test and installed along the beam line of the SPS accelerator. The prototype had two vertical insertions, at the top and bottom of the beam-pipe, as can be seen in Figure 5.33. Each of the two insertions hosted four pairs of edgeless silicon detectors mounted back to back (see Figure5.1), of both 3D/planar and CTS type. The devices were operated at the temperature of $\sim -5^{\circ}$ C. In this early test, three pairs of sensors were used in each pot for tracking and were read out with the analogue APV25 chips. One pair was read out with the first prototype version of the digital VFAT chips. This delivered the fast-OR signal of all 512 strips which was used for triggering the data acquisition system in coincidence with the sum signal of the four pick-up electrodes of a beam position monitor located close to the detectors.

The motors moving the pots towards the beam, the detectors electronics and the cooling system stabilising the temperature of the detectors inside the pots were operated remotely.

In the retracted pot position, the thin windows were 40 mm away from the beam pipe axis. To watch the effect of the RPs movements on the beam quality, three beam loss monitors (BLMs) were installed near the unit: one at 56 cm upstream on the top of the beam pipe and two at 65 cm downstream, one on the top and one on the bottom of the pipe. The BLMs used were cylindrical ionisation chambers filled with air.

Results Three different bunch structures were tested in the SPS accelerator: 1 single bunch in the accelerator ring, 4 bunches equally spaced and 4 equally spaced

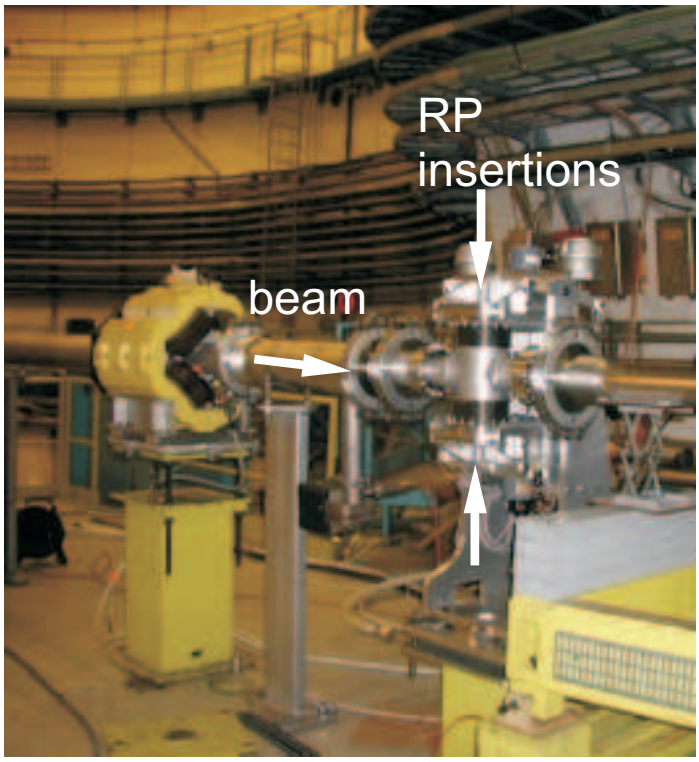

Figure 5.33: Picture of the Roman Pot prototype installed in the SPS tunnel for a coasting beam experiment. Two detector assemblies were inserted from the top and the bottom into the Roman Pot prototype (see arrows).

trains of 4 bunches of $8 \cdot 10^{10}$ 270 GeV protons with a revolution period of 23 μs.

Detector data were taken with the two pots positioned independently between 6 mm and 14 mm (beam $\approx$ 0.8 mm) from the beam pipe centre. Because of contact problems with the kapton connections between the individual detector/chip hybrids and the central electronics board of each pot, 4 out of the 16 detectors could not be read out. The high redundancy in the systems design however allowed us to carry out the experiment as planned.

Figure 5.34 shows the scraping of the beam periphery by the pot as measured with the BLMs. The down stream monitors show spikes whenever one of the pots approaches the pipe centre closer than 10 mm ($= 12.5\sigma$). As expected, the upstream BLM remains largely quiet, except when the bottom pot moves closer than $8\,\sigma$, which creates an increased halo travelling around the ring. The general trend of increasing beam losses is caused by a slow beam growth as its quality deteriorates.

The trigger rates measured in the top pot for different distances are shown in Figure 5.35. Given the SPS revolution period of 23 μs, the trigger probability varies

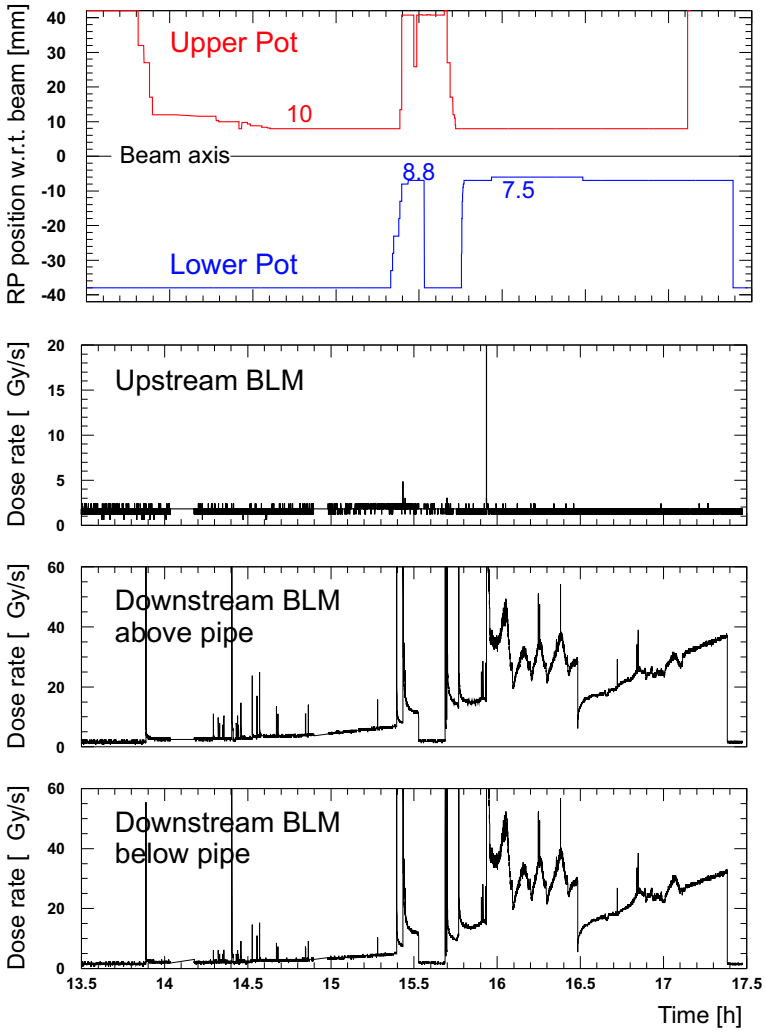

Figure 5.34: Synchronous measurements of the RP positions and the dose rates in the beam loss monitors over the duration of a data taking period.

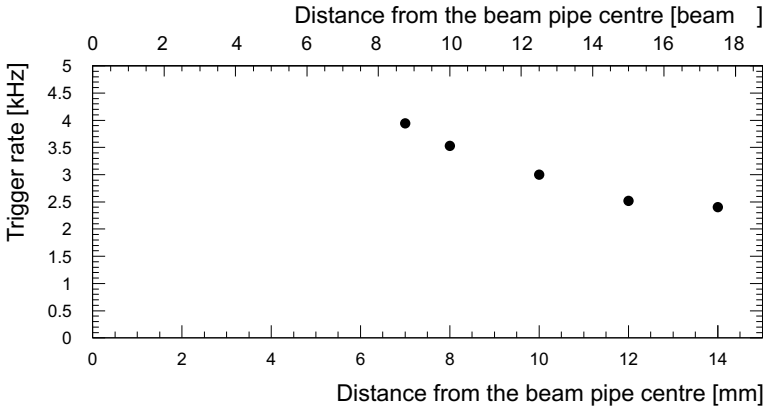

Figure 5.35: Trigger rate as a function of the window's distance from the beam pipe centre.

between one trigger per 11 bunches at $d = 7\,\text{mm}$ and one trigger per 18 bunches at $d = 14\,\text{mm}$. The latter distance corresponds to $17\,\sigma$. The observed variation of the rate with the distance is not big because all measurements were made more than $8\,\sigma$ from the beam centre where the halo is rather flat. The response of the tracking silicon detectors conforms to expectations. Figure 5.36 shows the halo

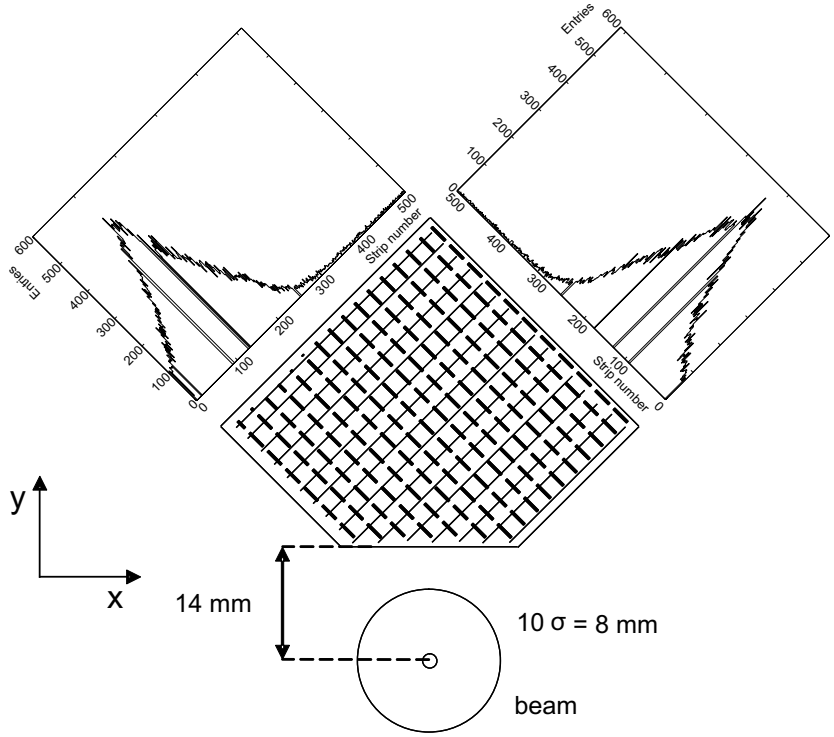

Figure 5.36: Profile of the beam halo as seen by two orthogonal detector planes at a distance of 14 mm from the beam centre. The data were taken with the bottom pot and the plot has been rotated by 180° around the beam axis for more convenience. Both detectors were operated at a reverse bias voltage of 40 V and a temperature of $\sim -5°$ C [73].

profiles measured by detector planes with orthogonal strips, which were operated at a reverse bias voltage of 40 V and a temperature of $\sim -5°$ C. For both detectors the strips with the highest amount of entries are, as expected, those closest to the beam centre.

Tracks were defined by 4 detectors. The signal-to-noise cut was set to 4 and the reconstructed tracks were required to be parallel to the beam.

The distribution of the tracks as a function of the y-axis (see Figure 5.36) in steps of $50\,\mu$m is shown in Figure 5.37. The efficiency of the detector assembly rises from 10 % to ~ 90 % within $50\,\mu$m as is evidenced by the inset.

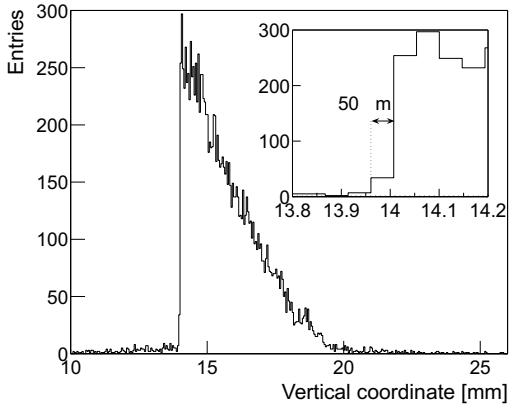

Figure 5.37: Track distribution as a function of the vertical space coordinate y. The data was recorded with four tracking detectors located in the top pot. The inset shows an enlargement of the y-values next to the edge of the detector's assembly.

5.2 Operation of CTS detectors with VFAT chips

During 2007, the silicon CTS detectors were tested in the H8 SPS beam with the final TOTEM electronics [2] (see Appendix B.2). Each detector was mounted on a hybrid card (see Figure 5.38) and was bonded to 4 VFAT chips.

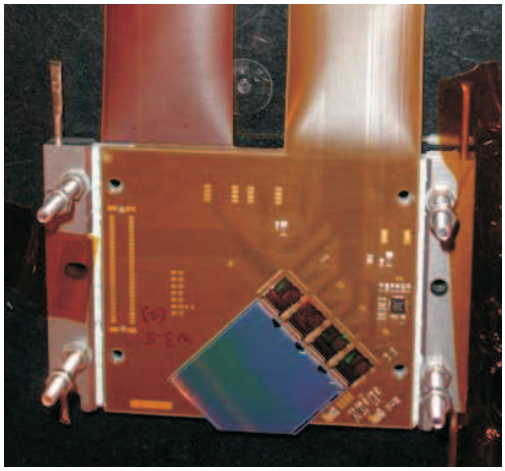

Figure 5.38: CTS detector glued to the final TOTEM hybrid board and bonded to 4 VFAT chips.

To set-up optimally the VFAT chips so that the efficiency of the silicon detectors is maximised and the noise is rejected, the value of the noise for each detector channel has to be evaluated. Since each channel of the VFAT chip has a built-in comparator, no analogue information on the signal generated by the particle traversing the detector is available. The only output infomation is whether the

collected charge was above the defined thereshold. However, the chip includes an internal calibration circuit, which is capable of injecting a test pulse of a known charge to an arbitrary input channel. By means of this functionality the noise profile can be determined.

The noise adds on to the injected charge. If a channel is pulsed with charge Q the comparator in reality checks whether $Q + N > T$, where N is the random variable corresponding to the noise distribution of a given channel and T is the defined threshold. Thus the noise distribution for a given threshold can be reconstructed by pulsing the detector with different known charge values and by counting the number of accepted events. During the noise scan procedure, each detector channel was pulsed 100 times with a given amount of charge. The charge value was increased in steps of 1 DAC[7] unit. In this way, for each detector channel, the profile of accepted events for a given threshold, as a function of the input charge, was computed. An example of such a profile (called also the "pulse S-curve") of one of the channels is shown in Figure 5.39 (left). The amount of injected charge, represented by the horizontal axis, is given in the internal chip DAC units. By means of the on-board DCU chip[8] the DAC units can be calibrated and expressed in terms of electron charge. One DAC unit equals approximately 500 e^-.

The pulse S-curve is an empirical cumulative distribution function of $Q + N$ random variable. Hence, the noise distribution can be reconstructed by performing the numerical differentiation on it. The empirical reconstructed distribution is given in Figure 5.39 (right). The mean value of 34.8 ± 0.2 DAC units corresponds to the threshold of $6 \cdot 10^3\, e^-$. The RMS value of 1.81 ± 0.13[9] DAC units gives the noise estimate of the channel of $900 \pm 65\, e^-$.

Figure 5.40 shows the detector noise profile, expressed in electrons. No outstandingly noisy channels were seen. The average strip noise is in the range of 900 – 1000 electrons respectively. First 208 channels are bonded on the detector active edge. The edge is tilted by 45° with respect to the strips (see Figure 5.38). Thus their length gradually increases with the strip number from 20.64 mm to 30.72 mm. So does the capacitance. Since the strip noise is proportional to its capacitance, an increase in the strip noise value as a function of the strip number is observed.

[7]Digital-to-analogue converter (DAC)

[8]The Detector Control Unit (DCU) chip [87] is an ASIC developed as the central building block of a monitoring system for the CMS Tracker. A single analogue-to-digital (A/D) converter is used inside the DCU to convert the input voltages using an analogue 8-to-1 multiplexer. The conversion results can then be read by the slow control system using the DCU I^2C interface [88].

[9]The RMS error $\sigma(\sigma_X)$ of the estimation of the standard deviation of the random variable X is given by $\sigma(\sigma_X) = \sigma_X/\sqrt{2N}$, where N is the number of samples.

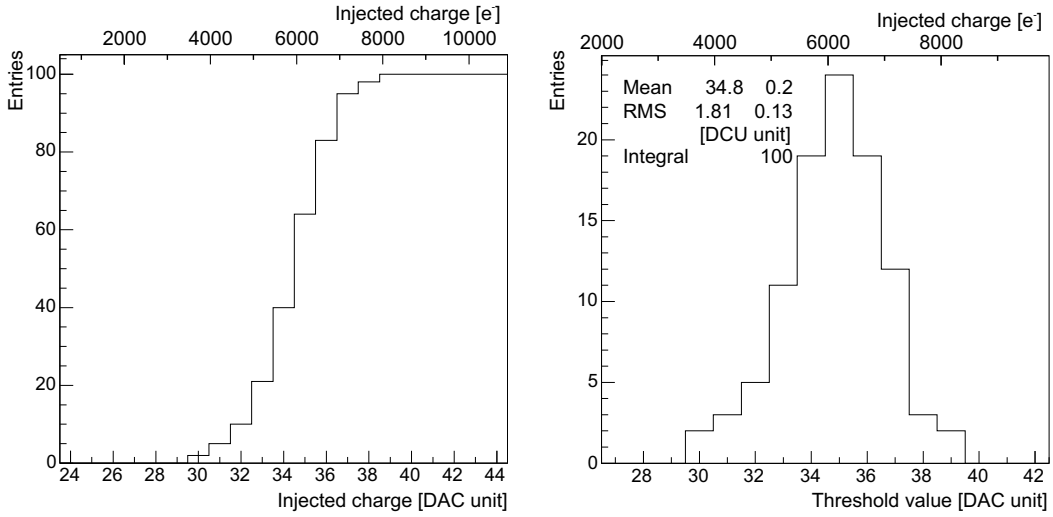

Figure 5.39: Left: Pulse S-curve of one of the detector channels. The channel was pulsed 100 times for each value of the injected charge. The number of events when the threshold value was exceeded is reported. Right: The noise distribution of one of the channels. The plot is computed by differentiation of the pulse S-curve. The mean value corresponds to the injected charge, while the RMS gives the noise estimate.

The noise difference of $\sim 100\,\mathrm{e}^-$ is estimated between the shortest and the longest strip.

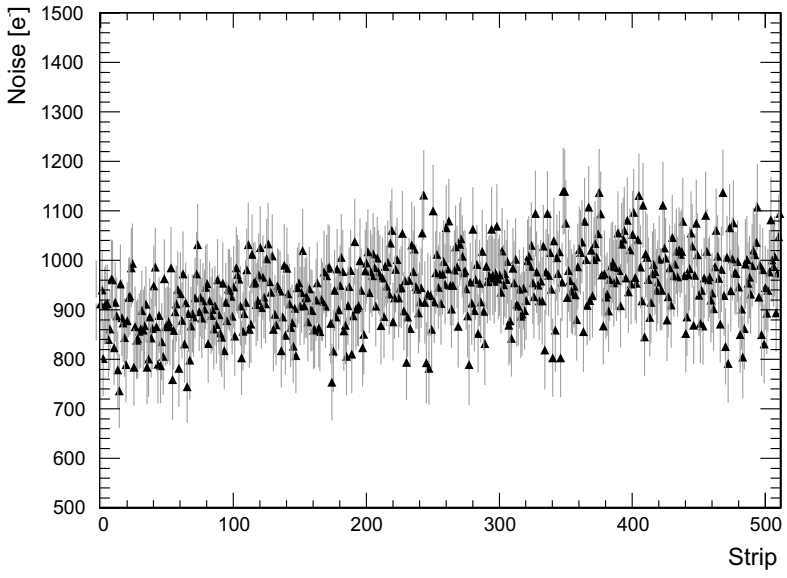

Figure 5.40: Noise at the different VFAT channels bonded to the edgeless detector biased with 150 V.

To perform further tests, the detectors were placed in the beam. In the H8

beam line, tracks were defined with a small size scintillator hodoscope, adjusted to fit the beam size and were approximately perpendicular to the detector plane. The hodoscope was divided into several sections and it was possible to trigger the detector with the tracks within $2 \times 2\,\mathrm{cm}^2$ large squares.

The impact points reconstructed by the pair of the tested CTS detectors (of strips orientated at 45°) is presented in Figure 5.41 (left). The majority of tracks are visible inside the black square in the centre of the plot, which corresponds to the particles traversing the active region of the hodoscope. The hits outside the active area are caused by the noise of the hodoscope. The cluster size distribution is plotted in Figure 5.41 (right). 90% of clusters contains only 1 strip. This is a typical scenario for the forward protons in the TOTEM experiment since they are parallel to the LHC beams and hence perpendicular to the detector planes within better than 1 mrad.

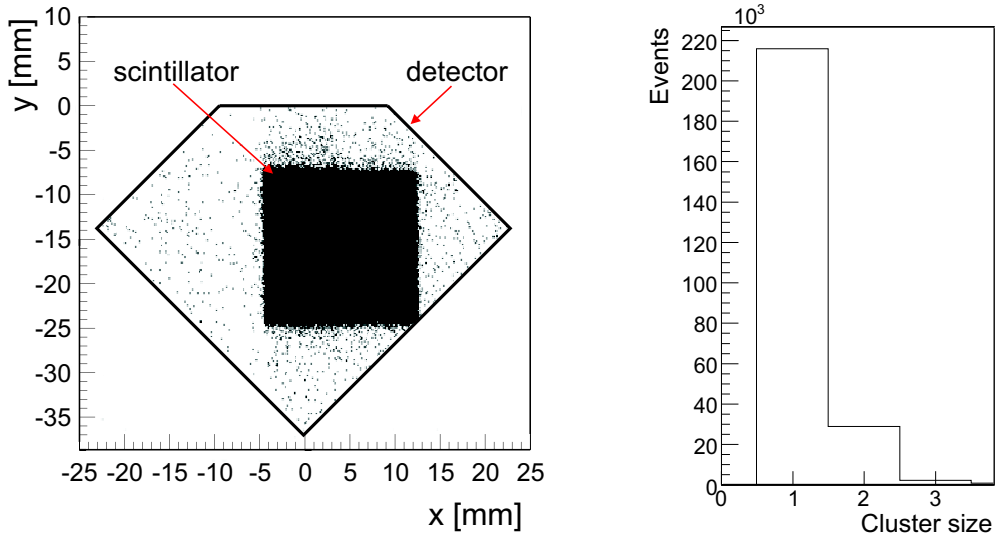

Figure 5.41: Left: The impact point profile reconstructed by the pair of tested CTS detectors. Tracks were defined with a small size scintillator hodoscope. The hodoscope active area is visible as a black square in the centre of the plot. Right: Cluster size in number of strips for particles perpendicular to the detector plane at 150 V detector bias.

Since a reference telescope was not available for the beam tests of the detectors with final digital readout electronics, the precise estimation of the efficiency was not possible. However, the behaviour of the efficiency as a function of the threshold, could have been studied, by counting the number of reconstructed clusters versus the applied threshold value. Several threshold scans were performed with beam particles. In Figure 5.42 is plotted the number of clusters per triggered

event, reconstructed in one VFAT readout chip, versus the discriminator threshold expressed in electrons (e^-). Only the clusters containing at most 2 strips were accepted. The noise starts to become visible at a threshold of 3000 e^- (three times above the average noise, see Figure 5.40). The plateau, of 0.3 clusters per trigger, extends over a range of 10,000 e^-. The strips bonded to the VFAT chip covered only about 1/3 of the active scintillator area and thus the plateau rate is only 0.3 instead of 1.0.

The most probable signal can be estimated from the falling edge of the curve. It is given by the place of the steepest slope. The most probable signal is thus estimated to be in the range of 20,000 – 25,000 e^-. It corresponds to the efficiency loss of about 1/3.

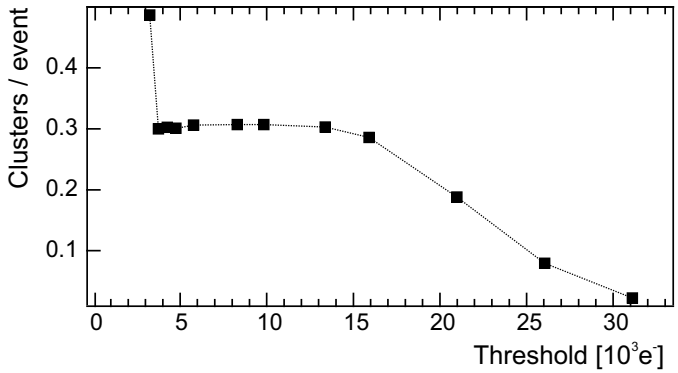

Figure 5.42: Threshold scan for one VFAT readout chip containing 128 detector channels. The detector (operated at 150 V) was placed in the beam. The scintillators were generating the trigger. The number of clusters per triggered event as a function of the discriminator threshold is plotted. The threshold value is expressed in electrons.

The threshold scan shown in Figure 5.42 can be compared to the results obtained with the analogue APV25 readout. Although, in the case of the analogue readout, the precise calibration of the detected signal in terms of equivalent electron charge was not available, the absolute signal value of each cluster was estimated on the basis of the signal-to-noise ratio. The noise of 800 e^- RMS was assumed, as it was obtained in Section 5.1.2.

The signal distribution of a CTS detector bonded to 4 APV25 chips and operated at the bias voltage of 150 V is presented in Figure 5.43. Since, in the digital readout, each of the strips of the cluster has to exceed the threshold value alone, for the compatibility, only the main strip of the analogue cluster (in case of double strip clusters) was used to build the signal distribution. The Landau signal peak

develops for signal values larger than 10,000 e^- while the noise peak is is visible for values lower than 4,000 e^-. The most probable signal is ~22,000 e^-. Let us define the efficiency $\eta(T)$ as a function of the threshold T:

$$\eta(T) = \frac{\eta_0}{N_0} \int_T^\infty \frac{\mathrm{d}N}{\mathrm{d}S} \mathrm{d}S, \tag{5.25}$$

where $\frac{\mathrm{d}N}{\mathrm{d}S}$ is the signal distribution, η_0 is the detector efficiency and N_0 is the number of real tracks traversing the detector. If $\frac{\mathrm{d}N}{\mathrm{d}S}$ is given by Figure 5.43 (left) and $\eta_0 = 0.97$, the efficiency function $\eta(T)$ shown in Figure 5.43 (right) is obtained. The efficiency plots, shown in Figure 5.42 and in Figure 5.43 (right), characterise

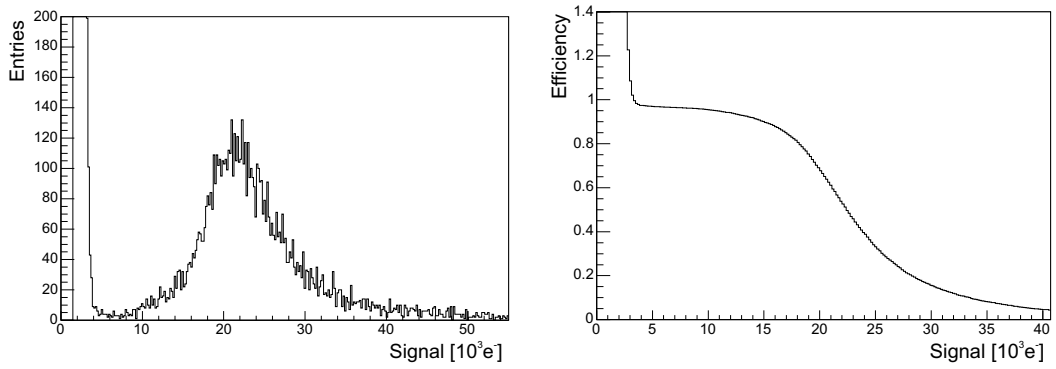

Figure 5.43: Left: Signal distribution of the CTS detector bonded to 4 analogue APV25 chips. The detector was operated at 150 V and the most probable signal was 22,000 e^-. Right: The efficiency of the same detector as a function of the applied threshold. The plot was computed on the basis of the signal distribution with Equation 5.25.

the digital and the analogue readout, respectively. The efficiency curves are of similar shape. The plateau is approximately of the same length and the most probable signal is located in about the same place.

5.3 Test conclusions

The tests performed with the baseline TOTEM CTS detectors demonstrate their reliability up to reverse bias voltages of 500 V (in case of the irradiated detectors [2]). Integration studies of CTS detectors into a Roman Pot prototype gave successful results. The devices worked successfully both with the analogue and the final TOTEM digital readout. The insensitive edge volume has been checked to be smaller than about 50 μm.

The 3D/planar detectors have been also tested. They are efficient at about 35 μm from the cut edge. They proved to work very well with the analogue readout. However, their behaviour with digital VFAT based DAQ still has to be verified. If they are made as thick as the CTS detectors (300 μm instead of 220 μm), higher signal-to-noise ratio should be achieved and then they will be perfect tracking devices for the Roman Pots.

The measured resolution of both CTS and 3D/planar devices, of about 19 μm, is in full agreement with the theoretical value. However, an impact point reconstruction bias in the near edge area has been observed. In the case of CTS detectors the highest observed bias was lower than 40 μm, while the 3D/planar detector exhibited a shift of up to 110 μm. The revealed shifts have to be corrected for in the reconstruction software.

The beam tests also gave suggestions concerning the readout of the silicon devices. The necessity of the jitter correction pointed out, that certain amount of data redundancy and the presence of the headers in the data frames generated by the chips, may be of great use when some resynchronisation is needed. The TOTEM experiment decided to leave the VFAT headers in the data acquisition system at least in the early runs of the LHC.

The system of TOTEM Roman Pot detectors have to be aligned when they are inserted in the LHC. The software alignment problem will be very much similar to the one carried out for the test beam telescope. The residual based alignment method applied in the test beam data analysis (Section 5.1.3) converged very well when the tracks traversing all the aligned detectors were used exclusively. However, a deterioration of precision and much slower convergence of the alignment procedure were observed when all the available tracks were used. This is caused by the fact that the reconstructed tracks used for the alignment are biased since they are reconstructed with the misaligned detectors. When a subset of detectors is used at a time, this bias varies and deteriorates the convergence. Unfortunately, the vertical Roman Pots in the LHC do not overlap and they can be aligned only by means of the overlaps with the horizontal Roman Pots (see Figure 3.17). To assure high precision of the alignment and fast convergence when all the detectors do not overlap, the bias-resistant methods have to be used. One of them is the Millepede algorithm [50] which can fit simultaneously the reconstructed tracks and the alignment corrections.

Chapter 6

LHC proton transport

6.1 LHC layout

6.1.1 Magnet lattice

The LHC has an 8-fold symmetry with eight arc sections and eight straight sections, as can be seen in Figure 2.2. Each straight section is approximately 528 m long and can serve as an experimental or utility insertion. The arcs consist of 23 regular cells, each with six dipole magnets to deflect the particles and two quadrupole magnets to focus the beams (Figure 6.1). The alternating-gradient focusing [35, 36] is used. In each pair of quadrupoles one is focusing while the other is defocusing the particles. This is called the FODO system. More than 400 quadrupole magnets of a gradient of 220 T/m were developed. Small dipole,

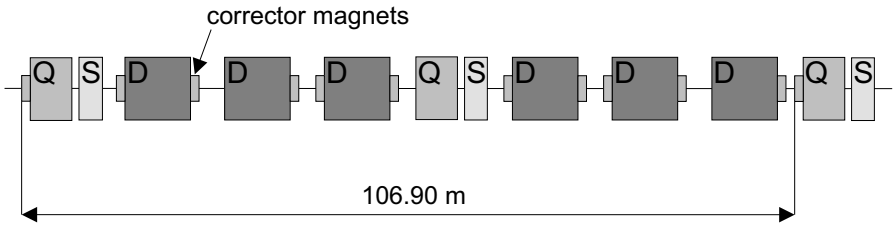

Figure 6.1: Schematic layout of one LHC cell. Letters D, Q and S represent large dipole, large quadrupole and large sextupole magnets, respectively. Small corrector magnets are also visible.

quadrupole, sextupole, octupole and decapole corrector magnets are installed to keep the particles on stable trajectories.

6.1.2 Experimental insertions

The two counter clockwise LHC beams cross in the four interaction points (IP1, IP2, IP5 and IP8, see Figure 2.2). For the standard LHC running conditions, the luminosity $\mathcal{L}$, defined by Equation 2.2, is aimed to be maximised. Thus the size of the colliding beams is only 16.7 μm. In addition, since the bunch number in the rings is high, in order to avoid parasitic beam crossings, a crossing angle of 285 μrad is introduced. However, the TOTEM physics programme requires mainly runs with larger beam sizes ($\sigma_x^* = \sigma_y^* \cong 0.5$ mm) and with no crossing angle present (see Section 6.3).

The beams are brought together by the system of magnets that is shown in Figure 6.2. An inner triplet of superconducting quadrupole magnets is installed at

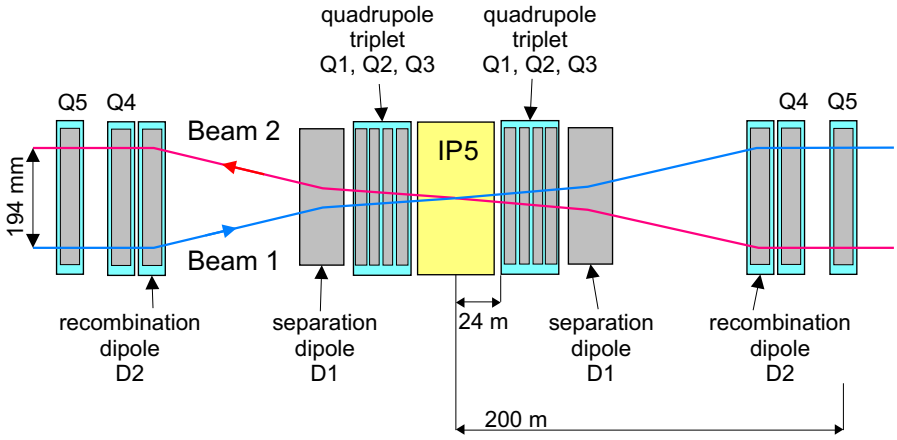

Figure 6.2: A schematic layout of the Interaction Point 5 shared by the TOTEM and the CMS experiments.

a distance of about 24 m from the collision point. The beams are further separated by the dipole magnets. When the distance between the beams increases to about 190 mm, a dipole magnet guides the beams into the separate vacuum chambers.

6.1.3 Utility insertions

Four insertions are intended for accelerator operation and machine safety.

Dump insertion

The purpose of the dumping system, located in IR6, is to remove beam safely from the collider at the end of a physics run, or in case of an equipment failure (for example a quench in a superconducting magnet).

Cleaning insertions

The superconducting magnets need to be protected against the proton losses of the particles travelling far away from the nominal machine orbit, close to an aperture limitation of the ring. Due to high beam energy and intensity, quenches introduced by beam losses would be unavoidable. A collimation system removes the potentially dangerous protons. This is performed with the so-called collimators. Their jaws approach the beam close enough to absorb the potentially dangerous particles which are highly deviated from their nominal orbits. The cleaning is performed in two insertions:

IR7 The insertion houses the Betatron Collimation system. The dispersion function in the long straight section is kept small, in order to reduce the effect of the off-momentum motion on the collimation. The primary betatron cleaning is made with three primary jaws, namely horizontal, vertical and skew, with four secondary jaws per primary collimator. The nominal primary collimator aperture is 7 beam sizes.

IR3 The insertion houses the Momentum Collimation system. In contrast to the betatron halo, which may drift away from the beam in all transverse directions, momentum losses in a ring with only horizontal dispersion are concentrated in the horizontal plane. The momentum range of the nominal circulating beam does not exceed $\pm 1 \cdot 10^{-3}$. Particles outside this range must be absorbed in the momentum cleaning insertion before they can be lost in the arcs. In order to decouple the momentum collimation in IR3 from the betatron-collimation in IR7, the primary collimator jaws in IR3 must be at a location with large dispersion and small betatron function (they are defined in Section 6.2). The optics design in IR3 therefore aims at maximising the normalised dispersion

$$\eta_D = \frac{D_x}{\sqrt{\beta_x}}, \tag{6.1}$$

which results in high displacement of off-momentum particles with respect to the beam size. The apertures of the primary and secondary collimator jaws are $7\sigma_x$ and $8.2\sigma_x$, where σ_x is the RMS beam size.

RF insertion

The particles are accelerated by the radio-frequency (RF) system, which is installed, for each beam, in IR4. The injected beam will be captured and accelerated using the 400.8 MHz superconducting cavity system.

6.2 Transverse beam motion

6.2.1 Equation of motion

The bending magnetic fields of the LHC machine are vertically directed, causing the protons to follow a curved path in a horizontal plane. The bending radius ϱ, the bending magnetic field B and the momentum p of the beam particles, are related by the quantity known as a magnetic rigidity:

$$B\varrho = \frac{p}{e}, \tag{6.2}$$

where e denotes the elementary charge.

The principal focusing elements in modern synchrotrons are quadrupole magnets. Their field shape is such that it is zero on the axis of the device but its strength rises linearly with the radial distance from the longitudinal axis, which is parallel to the main motion of the charged particles. The net result of these fields is a focusing force in one plane and a defocusing one in the plane perpendicular to it. The strength k of the quadrupole is characterised by the gradient $\mathrm{d}B_y/\mathrm{d}x$ of its magnetic field B_y normalised with respect to the magnetic rigidity:

$$k = \frac{1}{B\varrho}\frac{\mathrm{d}B_y}{\mathrm{d}x}. \tag{6.3}$$

Assuming that the magnets are perfectly aligned, a proton with the correct energy and alignment will circulate around the synchrotron ring on the central orbit of the bending magnets and will pass through the centre of each quadrupole. Protons with the wrong alignment (position or angle) are forced to oscillate about this central orbit by the focussing forces produced by the quadrupoles. These oscillations, which are both vertical and horizontal, are called betatron oscillations.

The coordinate system of the particle motion is given in Figure 6.3. The s-coordinate is oriented along the beam nominal closed orbit, which is represented by the red line. The betatron oscillations cause the displacements in x (horizontal) and y (vertical) directions, which are orthogonal to the closed orbit. The particle

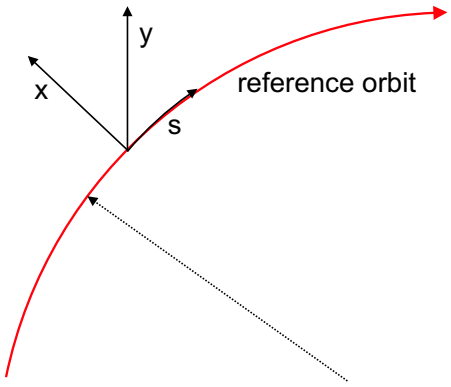

Figure 6.3: Coordinate system of the particle motion in the accelerator. The particle travels along the reference orbit s of the local curvature ϱ and performs transverse oscillations in the horizontal (x) and vertical (y) directions.

trajectory may also have an angle with respect to the closed orbit. Such divergence is expressed as $\Theta_x \cong \frac{\mathrm{d}x}{\mathrm{d}s} = x'$ and $\Theta_y \cong \frac{\mathrm{d}y}{\mathrm{d}s} = y'$.

Without loss of generality, let us consider the horizontal oscillations. The angular deflection given to a particle passing through a short quadrupole of length $\mathrm{d}s$ and strength k at a displacement x is

$$\mathrm{d}x' = -kx\mathrm{d}s. \tag{6.4}$$

Assuming that $k(s)$ is a function of the distance s along the ring resulting from the properties of the magnets, we get:

$$x'' + k(s)x = 0. \tag{6.5}$$

This is Hill's equation of the solution which reads

$$x(s) = \sqrt{\beta_x(s)\varepsilon}\cos[\phi_x(s) + \phi_0], \tag{6.6}$$

where $\beta_x(s)$ is the betatron amplitude function, $\phi_x(s)$ is the phase advance of the oscillation of the particle, $\sqrt{\beta_x(s)}$ defines the amplitude the oscillation and $\sqrt{\varepsilon}$ is a constant. Both $\beta_x(s)$ and $\phi_x(s)$ functions have the same periodicity[1] as the

[1]The betatron amplitude function $\beta(s)$ and the lattice strength $k(s)$ are related via the non-linear second order differential equation: $\beta''(s)\beta(s) - \frac{1}{2}\beta'(s)^2 + 2\beta(s)^2k(s) = 2$. It is obtained from Hill's equation when the general solution, given by Equation 6.6, is substituted and when the relation defined by Equation 6.7 is applied.

accelerator lattice strength $k(s)$ and they are linked by the condition

$$\frac{\mathrm{d}\phi_x}{\mathrm{d}s} = \frac{1}{\beta_x} \quad \text{or} \quad \phi_x(s) = \int_{s_0}^{s} \frac{\mathrm{d}s'}{\beta_x(s')} \,. \tag{6.7}$$

By differentiating Equation 6.6, it is possible to get the divergence equation of the particle's motion:

$$x' = -\sqrt{\frac{\varepsilon}{\beta_x(s)}}\sin[\phi_x(s)+\phi_0] + \left[\frac{\beta_x'(s)}{2}\right]\sqrt{\frac{\varepsilon}{\beta_x(s)}}\cos[\phi_x(s)+\phi_0]. \tag{6.8}$$

Equations 6.6 and 6.8 define an ellipse in the (x, x') phase space. The proton beams in an accelerator obey Liouville's theorem which tells that the area within the ellipse contour is conserved. Even though the ellipse may appear to have many shapes around the accelerator, its area does not change and equals $\pi\varepsilon$, where ε is an invariant of the motion for a single particle (or the emittance of a beam of many particles). Figure 6.4 schematically illustrates the behaviour of the amplitude

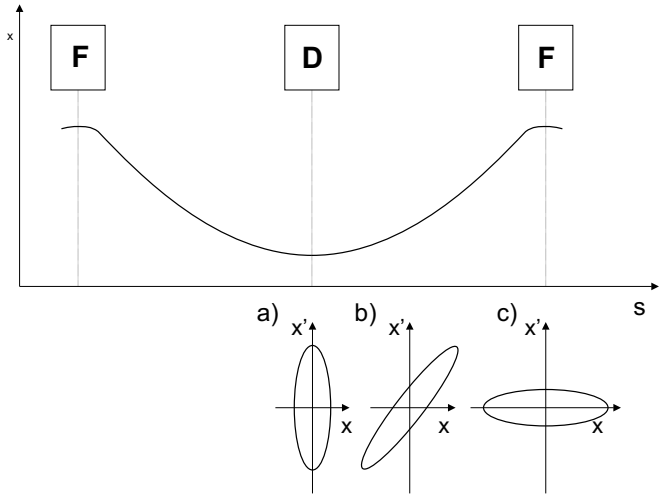

Figure 6.4: Schematic evolution of the beam phase space while it traverses the focusing (F) and defocusing (D) quadrupole magnets. The emittance, represented by the ellipse area, is conserved. The size of the beam is proportional to $\sqrt{\beta_x}$.

function β_x and the conservation of emittance of a beam traversing a sequence of the focusing and defocusing quadrupole magnets. The amplitude function is at minimum in the centre of the defocusing magnet (D), which corresponds to a minimum of a beam size (a). At the focusing magnet (F) beam size attains its maximum (c). Because β_x is a function of position s in the focussing structure, the ellipse changes its orientation and aspect ratio from location to location but its area remains constant.

The evolution of the beam size and the beam divergence is represented by ellipses (a), (b) and (c). Their horizontal and vertical projections are given by

$$\Delta x = \pm\sqrt{\beta_x(s)\varepsilon} \quad \text{and} \quad \Delta x' = \pm\sqrt{\frac{\varepsilon}{\beta_x(s)}}\sqrt{1+\left(\frac{\beta_x'(s)}{2}\right)^2}. \tag{6.9}$$

These equations can be simplified if we consider a place where β_x is at maximum or minimum. There β_x' equals 0 and the ellipse contour is upright so that the correlation between particle displacement and divergence is avoided. The beam size[2] and the beam divergence can be now expressed in terms of the beam emittance ε and the betatron amplitude $\beta_x(s)$ as follows:

$$\sigma(x) = \sqrt{\varepsilon\beta_x}, \tag{6.10}$$

$$\sigma(x') = \sqrt{\frac{\varepsilon}{\beta_x}}. \tag{6.11}$$

The emittance ε is conserved as long as the energy of the particle (or of the beam of particles) remains constant. In order to characterise the beam when the energy changes during the acceleration cycle, the so called normalised emittance

$$\varepsilon_N = (\beta\gamma)\varepsilon, \quad \beta = \frac{v}{c} \tag{6.12}$$

is introduced, where v is the velocity of the particle, c is the speed of light and $\gamma = \frac{1}{\sqrt{1-\beta^2}}$ is the Lorentz factor. The parameter β of Equation 6.12 should not be confused with the amplitude function used for example in Equation 6.6.

The phase advance $\Delta\phi$ during one turn of the particle can be defined as:

$$\Delta\phi = \oint \frac{\mathrm{d}s}{\beta(s)}. \tag{6.13}$$

The number of oscillations performed by a proton in one turn is called the Q-value or tune and is defined as

$$Q = \frac{\Delta\phi}{2\pi}. \tag{6.14}$$

The tunes Q_x and Q_y are of high interest for the accelerator design since the beam stability depends on their values. They are chosen such that the proton does not retrace the same path through the ring on subsequent turns in order to avoid the cumulation of the effects introduced by the nonlinear imperfections of the lattice.

[2]Such defined beam size is sometimes called the betatron beam size, since it does not include the dispersion related beam size component, which is discussed in Section 6.2.3.

In general, the equation $l \cdot Q_x + m \cdot Q_y = n$ should not be fulfilled (l, m, and n are integers). For the LHC the betatron tunes are of the order of 60 and can be adjusted with the corrector quadrupole magnets.

6.2.2 Beam transport matrix

In order to simulate the number and distribution of protons reaching the TOTEM Roman Pot detectors and to compute the proton reconstruction resolutions it is important to introduce the beam transport matrix. The transport of the beam within the accelerator can be represented as a matrix. The solution of the Hill's equation can be traced from one point, s_1 to another, s_2, by a 2×2 matrix, called the transport matrix:

$$\begin{pmatrix} x(s_2) \\ x'(s_2) \end{pmatrix} = \begin{pmatrix} a & b \\ c & d \end{pmatrix} \begin{pmatrix} x(s_1) \\ x'(s_1) \end{pmatrix} = M_{21} \begin{pmatrix} x(s_1) \\ x'(s_1) \end{pmatrix} \tag{6.15}$$

Coefficients a and b are of special interest for the near-beam detector insertions located along the machine. Supposing the interaction point is at s_1, they determine the transverse position of the particles arriving from the interaction point to a given s_2 position. In general, a and b can be treated as functions of s and they are called the optical functions. The parameter $a(s)$ is called the magnification and denoted as $v_x(s)$, while $b(s)$ is the effective length — $L_x(s)$.

There is a general relation between the components of the matrix M_{21} and the amplitude β and phase ϕ of the transverse motion between two points s_1 and s_2. The values of the terms a, b, c and d can be derived from Equations 6.6 and 6.8 — the details can be found in [36]. Defining:

$$w_1 = \sqrt{\beta(s_1)}, \quad w_2 = \sqrt{\beta(s_2)} \quad \text{and} \quad \phi = \phi(s_2) - \phi(s_1), \tag{6.16}$$

the general form of the transport matrix becomes

$$M_{12} = \begin{pmatrix} \frac{w_2}{w_1}\cos\phi - w_2 w_1' \sin\phi & w_1 w_2 \sin\phi \\ -\frac{1+w_1 w_1' w_2 w_2'}{w_1 w_2}\sin\phi - \left(\frac{w_1'}{w_2} - \frac{w_2'}{w_1}\right)\cos\phi & \frac{w_1}{w_2}\cos\phi + w_1 w_2' \sin\phi \end{pmatrix}. \tag{6.17}$$

In fact, the matrix M_{12} can be obtained by calculating a product of elementary transport matrices corresponding to the elements of the accelerator lattice. This is very similar to the transport of light through a system of lenses. For example

the accelerator straight drift section of length l is described by the matrix

$$M_d = \begin{pmatrix} 1 & l \\ 0 & 1 \end{pmatrix}. \tag{6.18}$$

A thin quadrupole magnet of infinitely small length l but finite integrated gradient is represented by

$$M_q = \begin{pmatrix} 1 & 0 \\ -kl & 1 \end{pmatrix}, \tag{6.19}$$

where k is defined by Equation 6.3.

The magnetic lenses of a real accelerator are not normally short compared to their focal length which results in a more complex form of transport matrices than that presented in Equation 6.19. Currently the accelerator design is performed with computer programmes, which include in its routines all the matrix multiplications. All the TOTEM optics related studies were performed with a use of MAD-X [37], which is described in Appendix C.1.

6.2.3 Dispersion and chromaticity

The bending field of the accelerator is matched to the particle of ideal momentum p. If in addition the betatron amplitude of such a particle is 0 it will travel through the centre of quadrupole and dipole magnets. Its path is called the closed orbit of the central momentum particle.

When the particle with a lower momentum $p - \Delta p$ passes down a dipole magnet it is bent horizontally more than the particle of the nominal momentum p. However, this additional bending is compensated later by the lattice quadrupole magnets and the off-momentum particle follows its different closed orbit. This new closed orbit is described by the dispersion function $D(s)$. In fact, the effect of dispersion for off-momentum orbits combines with betatron motion. Thus the horizontal coordinate of the transverse particle motion is given by

$$x(s) = \sqrt{\beta_x(s)\varepsilon}\cos[\phi_x(s) + \phi_{x0}] + D(s)\xi, \quad \xi = \frac{\Delta p}{p}, \tag{6.20}$$

where Δp is the momentum difference. This clearly means that the beam will be wider if it has momentum spread. If $\sigma(x)$ is a beam size related to the betatron oscillations and assuming that the momentum distribution and betatron oscillations

are independent, the full beam size is given by:

$$\sigma_D(x) = \sqrt{\sigma(x)^2 + \left(D_x \frac{\sigma(p)}{p}\right)^2}, \tag{6.21}$$

where $\sigma(p)$ is the RMS of the momentum spread and p is the nominal beam momentum.

The dispersion effect can be included in the matrix accelerator description introduced in Section 6.2.2 by adding a $\Delta p/p$ term:

$$\begin{pmatrix} x(s_2) \\ x'(s_2) \\ \Delta p/p \end{pmatrix} = \begin{pmatrix} a & b & D_x \\ c & d & m_{23} \\ 0 & 0 & 1 \end{pmatrix} \begin{pmatrix} x(s_1) \\ x'(s_1) \\ \Delta p/p \end{pmatrix}, \tag{6.22}$$

with $m_{23} = \frac{\mathrm{d}D_x}{\mathrm{d}s}(s_2)$.

Now each of the accelerator lattice elements is described by a 3×3 matrix. The transport matrix over a given period of the machine can be again computed by multiplying the elementary matrices.

The energy spread in the beam is also a source of the betatron tune Q spread. The change of the tune with momentum $\mathrm{d}Q/\mathrm{d}\xi$, $\xi = \frac{\Delta p}{p}$, is called the chromaticity. Chromaticity arises because the focusing strength of a quadrupole has the $B\varrho = p/e$ term in the denominator:

$$k = \frac{1}{B\varrho} \frac{\mathrm{d}B_y}{\mathrm{d}x}. \tag{6.23}$$

Thus for example the tracks of lower momentum are bent more than the nominal ones. A spread in the beam momentum, $\pm\Delta p/p$, causes a spread in the focusing strength:

$$\frac{\Delta k}{k} = \mp \frac{\Delta p}{p}. \tag{6.24}$$

The chromaticity is corrected with sextupole magnets which are installed close to the quadrupoles, as can be seen in Figure 6.1. Their focusing strength, in one direction, increases linearly with radial position. Since the displacement of the particle trajectories depend also linearly upon their momentum difference Δp (dispersion), the two effects combined make the chromaticity correction possible. At least two sextupole families are required to correct both the horizontal and vertical chromaticity.

In the presence of chromaticity and large momentum deviations the particle transport is no longer linear. The coefficients of the transport matrix in Equa-

tion 6.22 become functions which depend upon the particle momentum deviation $\Delta p/p$, the divergence and the transverse position.

6.2.4 Lattice imperfections

The imperfections of the accelerator lattice cause the angular kicks and thus are the source of orbit distortions. The predominant are the effects of the quadrupole magnet transverse displacement. Figure 6.5 shows how the magnet lattice mis-

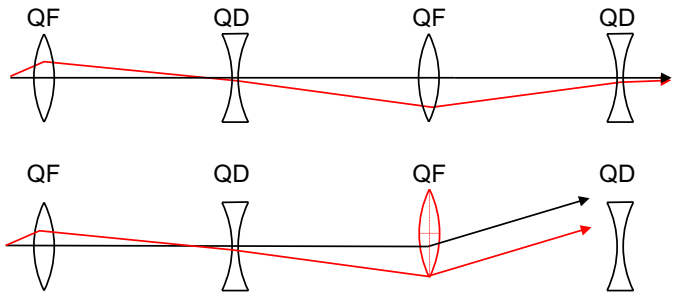

Figure 6.5: Misalignment (in one projection) of the quadrupole magnet. Top: The particle of zero angle and zero displacement travels through the centre of a perfectly aligned accelerator lattice. Other particles are are deflected by the focusing system. Bottom: The effect of the alignment error is visible. The deflection needs to be corrected with a dipole magnet.

alignment affects the proton path. When the magnets are aligned, the particle, of no angle and no amplitude, travels through the centre of the lattice as can be seen in the top plot. When one of the focusing magnets is misaligned, the particle gets deflected and a correcting dipole magnet is needed to compensate it (bottom). In similar way, a tilt of a dipole bending magnet causes a small resultant dipole in the horizontal way. The precision of the LHC lattice transverse alignment is about 0.3 mm.

The magnets should not only reach a field exceeding the design field, also the field quality must be excellent. The magnetic field errors of the LHC should be limited to about $\mathrm{d}B/B_0 = 10^{-4}$ at 10 mm radius. The nonlinear magnetic field imperfections are corrected with multipole corrector magnets.

6.3 TOTEM optics scenarios

For the luminosity independent total cross section measurement TOTEM has to reach the lowest possible values of the squared four momentum transfer $-t \sim p^2\Theta^2$ in elastic pp scattering.

Scattered particles close to the beam can be detected downstream on either side of the Interaction Point (IP)[3] if the displacement at the detector location is large enough (at least $10\sigma_{beam}$ away from the beam centre) and if the beam divergence at the IP, which is proportional to $1/\sqrt{\beta^*}$ (see Equation 6.11), is small compared to the scattering angle. In order to achieve these conditions special high beta optics are required: the larger the β^*, the smaller the beam divergence will be.

Two optics have been proposed: the ultimate one with $\beta^* = 1535\,\mathrm{m}$, probably foreseen at a later stage, and another one with $\beta^* = 90\,\mathrm{m}$. The latter uses the standard injection optics and the beam conditions typical for early LHC running: zero degree crossing-angle and consequently at most 156 bunches together with a low number of protons per bunch.

6.3.1 Properties of the high-β^* optics

As was discussed in Section 6.2.2, the properties of the optics can be expressed by the two optical functions L (effective length) and v (magnification), which are defined by components a and b of the matrix M_{21} in Equation 6.15, respectively. According to the general form of the transport matrix (see Equation 6.17), their values, at a distance s from the IP, depend upon the betatron function $\beta(s)$ and the phase advance $\Delta\mu(s)$. Since $\beta(s)$ is at extremum in the IP, the functions $v(s)$ and $L(s)$ can be expressed as:

$$\begin{aligned} v(s) &= \sqrt{\frac{\beta(s)}{\beta^*}}\cos\Delta\mu(s) \\ L(s) &= \sqrt{\beta(s)\beta^*}\sin\Delta\mu(s) \\ \text{with}\quad \Delta\mu(s) &= \int_0^s \frac{1}{\beta(s')}ds' \end{aligned} \tag{6.25}$$

The transverse displacement $(x(s), y(s))$ of a proton at a distance s from the IP is related to its transverse origin (x^*, y^*) and its momentum vector (expressed by the horizontal and vertical scattering angles Θ_x^* and Θ_y^* and by $\xi = \Delta p/p$) at the IP via the above optical functions and the horizontal dispersion $D_x(s)$ of the machine:

$$\begin{aligned} y(s) &= v_y(s)\cdot y^* + L_y(s)\cdot\Theta_y^* \\ x(s) &= v_x(s)\cdot x^* + L_x(s)\cdot\Theta_x^* + \xi\cdot D_x(s) \end{aligned} \tag{6.26}$$

[3]The "*" superscript of the optical parameter denotes its value in the interaction point.

As a consequence of the high β^*, the beam size at the IP is large ($\sigma^*_{beam} \propto \sqrt{\beta^*}$, see Equation 6.10). To eliminate the dependence on the transverse position of the proton at the collision point, the magnification has to be chosen close to zero (parallel-to-point focussing, $\Delta\mu = \pi/2$). At the same time, a large effective length ensures a sizeable displacement from the beam centre.

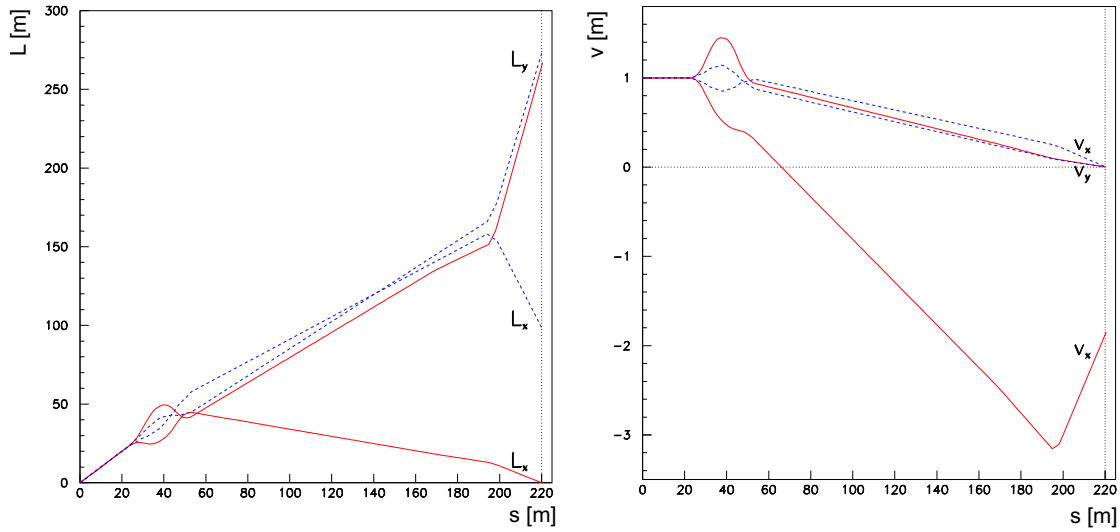

Figure 6.6: The optical functions for β^*=90 m (solid) and 1535 m (dashed) as function of the distance s to IP5: effective length L [in m] (left) and magnification v (right).

Having in mind the above optimisation for the position of the RP station RP220, two scenarios have been studied. Their optical functions are compared in Figure 6.6. For $\beta^* = 1535$ m, the parallel-to-point focussing is achieved in both projections whereas for $\beta^* = 90$ m only in the vertical one. In both cases, the large L_y pushes the protons vertically into the acceptance of the RP detectors.

The minimum distance of a detector from the beam is proportional to the beam size:

$$y_{min} = K\sigma_y^{beam} = K\sqrt{\varepsilon\,\beta_y(s)}\,, \tag{6.27}$$

where ϵ is the transverse beam emittance and K is around 10–15. Assuming perfect parallel-to-point focussing, the smallest detectable angle is:

$$\Theta^*_{y\ min} = K\sqrt{\frac{\varepsilon}{\beta^*_y}}. \tag{6.28}$$

The parallel-to-point focussing condition allows the measurement of both t components (t_x, t_y) for elastically scattered protons at $\beta^* = 1535$ m but only the vertical

component at $\beta^* = 90\,\mathrm{m}$.

Both optics also offer the possibility of detecting diffractive protons almost independent of their momentum loss. To be able to measure the momentum loss ξ with an acceptable resolution, L_x has to vanish to eliminate the dependence on the horizontal scattering angle Θ_x^* (cf. Equation (6.26)). This condition can only be achieved with the $\beta^* = 90\,\mathrm{m}$ optics (Figure 6.6).

6.3.2 Running scenarios

The versatile physics programme of TOTEM requires different running scenarios that have to be adapted to the LHC commissioning and operation in the first years. TOTEM will take data under all optics conditions, adjusting the trigger schemes to the luminosity. The DAQ will allow trigger rates up to a few kHz without involving a higher level trigger.

As has been already discussed, the acceptance and the reconstruction resolution are defined by the optics parameters via Equation 6.26. In particular, the beam divergence limits the $\Theta_{x,y}^*$-reconstruction resolution and thus the t-resolution. Table 6.1 summarises the optical functions, the beam parameters and the Roman Pot distances from the beam, for different running scenarios.

β^* [m]	L_x [m]	L_y [m]	v_x	v_y	D_x [m]	x_{RP} [mm]	y_{RP} [mm]	$\sigma(x^*)$ [μm]	$\sigma(\Theta_x^*)$ [μrad]
0.5	1.5	18	-3.9	-3.8	-0.080	1.26	6.0	16.6	30
2	0.49	18	-3.5	-4.0	-0.086	1.6	3.7	32	16
90	0	262	-1.9	0.0	-0.041	4.5	6.8	212	2.3
1535	100	270	0	0	-0.05	0.8	1.3	450	0.3

Table 6.1: Optics parameters at IP5 and at the RP220 station for the TOTEM running scenarios. L_x, L_y, v_x, v_y and D_x are the parameters of Equation 6.26 at RP220, x_{RP} and y_{RP} are the distances of the horizontal and vertical Roman Pots of the RP220 station from the beam centre, respectively, $\sigma(x^*)$ is the beam size at IP5 and $\sigma(\Theta_x^*)$ is the beam divergence at IP5.

The high-β^* runs (Table 6.2) with 156 bunches, zero degree crossing-angle and maximum luminosity between 10^{29} and $10^{30}\,\mathrm{cm}^{-2}\mathrm{s}^{-1}$, will concentrate on low-$|t|$ elastic scattering, total cross-section, minimum bias physics and soft diffraction. A large fraction of forward protons will be detected even at the lowest $|\xi|$ values.

Low-β^* runs (Table 6.3) with more bunches and higher luminosity (10^{32} – $10^{33}\,\mathrm{cm}^{-2}\mathrm{s}^{-1}$) will be used for large-$|t|$ elastic scattering and diffractive studies for

$-\xi > 0.02$. Hard diffractive events come within reach.

β^* [m]	k	$N/10^{11}$	$\mathcal{L}$ [$\mathrm{cm^{-2}s^{-1}}$]	$\lvert t\rvert$-range for $\xi = 0$ [$\mathrm{GeV^2}$]	$\lvert\xi\rvert$-range
1535	43 – 156	0.6 – 1.15	10^{28} – 2× 10^{29}	0.002 – 1.5	< 0.25
90	156	1.15	3×10^{30}	0.02 – above 10	< 0.25

Table 6.2: Running scenarios for high β^*. k is a number of bunches, N — a number of protons per bunch.

β^* [m]	k	$N/10^{11}$	$\mathcal{L}$ [$\mathrm{cm^{-2}s^{-1}}$]	$\lvert t\rvert$-range for $\xi = 0$ [$\mathrm{GeV^2}$]	$\lvert\xi\rvert$-range
11	936 – 2808	1.15	3×10^{32}	0.6 – 8	0.02 – 0.2
0.5 – 2	936 – 2808	1.15	10^{33}	1 – above 10	0.02 – 0.2

Table 6.3: Running scenarios for low β^*. k is a number of bunches, N — a number of protons per bunch.

6.4 LHC optics modeling

To perform the Monte Carlo studies and the physics reconstruction of the data recorded with Roman Pots, precise modelling of the accelerator optics is required. Since TOTEM plans to profit from all the available LHC running scenarios, several configurations need to be simulated. In addition, the optics modelling should be compliant with MAD-X, because this software is used for the LHC optics design and control. The MAD-X configuration data base will be continuously updated with the observed machine imperfections. The MAD-X LHC model will thus be the most accurate one [38].

The integration of MAD-X within the Monte Carlo software of the Roman Pots was considered, so that the protons are tracked directly with its use. However, since the number of events planned to be recorded with Roman Pot detectors reaches 7.5×10^8 per optics configuration, the MAD-X simulation, even when the fastest tracking mode is used (the thin length tracking mode), is too time consuming.

While performing the proton kinematics reconstruction, numerous calls to proton tracking are also needed by the χ^2 minimisation algorithms. Again, a fast and precise tool capable of computing the proton tracks along the machine is required.

It has been decided to parametrise the proton transport following the transport formula given in Equation 6.22. As has been discussed in Section 6.2.3, the values of the optical functions, depend mainly upon the momentum loss of the proton,

but also upon the proton transverse position and upon the scattering angle. Then the transport formula can no longer be applied directly, since its coefficients are not constant. Figure 6.7 shows the values of the optical functions at 220 m, for

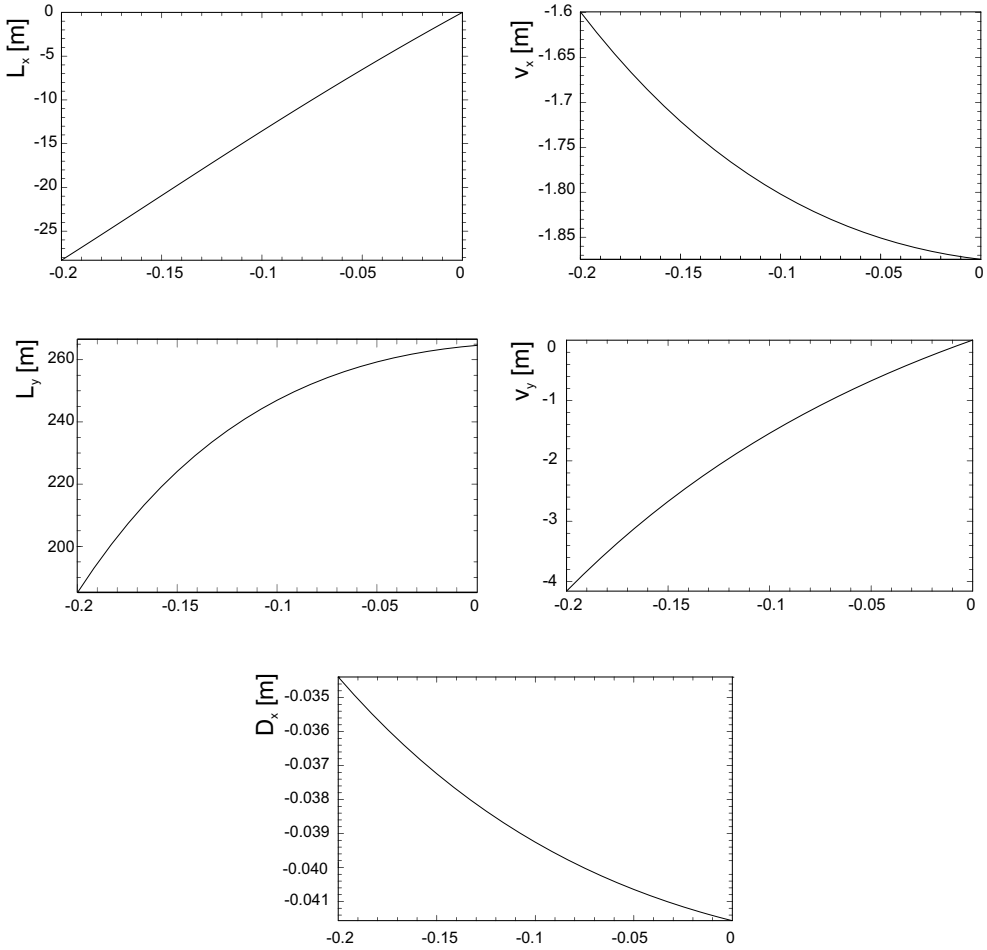

Figure 6.7: The optical functions at 220 m from the IP5, for $\beta^* = 90$ m, versus the proton momentum loss $\xi = \Delta p/p$. Their nonlinearity with respect to ξ is visible.

$\beta^* = 90$ m optics, versus the proton momentum loss. To compute these plots, the proton transverse position and the divergence at the IP5 were set to 0.

While doing the TOTEM acceptance studies, the behaviour of the optical functions was approximated with linear fits for certain running scenarios. For the high-β^* optics ($\beta^* = 1435$ m), the absolute precision of 50 μm was obtained [39]. In the case of low-β^*, the linear parameterisation worked only for low momentum losses ($|\xi| < 1\%$), while the look-up tables were used for $|\xi| \geq 1\%$ [40]. Finally, the error of the proton transport was lower than 100 μm.

Although the precisions obtained with linear approximations were sufficient

for the Roman Pot acceptance studies, for the physics reconstruction studies a more precise tool was needed. The errors introduced by the proton transport parameterisation should be well below the resolution of the Roman Pot detectors. Since at least a precision of 2μm is required, a nonlinear approximation had to be applied.

A software package, able to find automatically a polynomial approximation of the optical functions for any given running scenario, was developed and is reported in this section. MAD-X is used within in to generate the training and testing data. The tests of the obtained proton parameterisations show the differences of less that $1\,\mu$m compared to MAD-X tracking. Since the training and testing data sets are not large ($\sim$12,000 samples), the finest and thus the slowest MAD-X tracking mode can be used to prepare them.

6.4.1 The method

The aim of the parameterisation is to approximate, with the precision significantly better the resolution of the detectors, the transport of protons from a given point s_1 along the accelerator to another one s_2. Equation 6.22 defined a linear transport for one transverse coordinate assuming that there is no coupling between x and y directions. In the general form, the linear model of the transport for the two transverse coordinates is given by:

$$\begin{pmatrix} x(s_2) \\ x'(s_2) \\ y(s_2) \\ y'(s_2) \\ \Delta p/p \end{pmatrix} = \begin{pmatrix} v_x & L_x & m_{13} & m_{14} & D_x \\ v'_x & L'_x & m_{23} & m_{24} & D'_x \\ m_{31} & m_{32} & v_y & L_y & D_y \\ m_{41} & m_{42} & v'_y & L'_y & D'_y \\ 0 & 0 & 0 & 0 & 1 \end{pmatrix} \begin{pmatrix} x(s_1) \\ x'(s_1) \\ y(s_1) \\ y'(s_1) \\ \Delta p/p \end{pmatrix} \tag{6.29}$$

For simplicity, let us define the input and output vectors, respectively, as

$$\vec{\Gamma} = \begin{pmatrix} x(s_1) \\ x'(s_1) \\ y(s_1) \\ y'(s_1) \\ \Delta p/p \end{pmatrix} \quad \text{and} \quad \vec{\Lambda} = \begin{pmatrix} x(s_2) \\ x'(s_2) \\ y(s_2) \\ y'(s_2) \\ \Delta p/p \end{pmatrix} . \tag{6.30}$$

Since, as has been mentioned, the coefficients of the matrix slightly depend

upon the input vector $\vec{\Gamma}$, the matrix in Equation 6.30 is replaced by a function $\mathbf{T}$:

$$\vec{\Lambda} = \mathbf{T}(\vec{\Gamma}) \,. \tag{6.31}$$

The approximator is capable of finding the polynomial expansion T_i, $i = 1, \ldots, 4$, for each output variable Λ_i such that

$$\Lambda_i = T_i(\vec{\Gamma}) \,. \tag{6.32}$$

6.4.2 Multidimensional fits

The software procedure of finding the approximation of optical functions is based on the algorithms implemented in CERNLIB MUDIFI package [41, 42] and ported to the ROOT [43] framework.

The optics parameterisation relies in finding the polynomial expansion of functions $T_i(\vec{\Gamma})$ in the automatic way so that the required precision is achieved. The procedure is independently performed for the output coordinates x, x', y and y' — the components of the vector $\vec{\Lambda}$.

Training and testing data samples

Two data samples, consisting of proton tracks simulated with MADX-X, are used in the process of finding the approximation. The training set is used to find the transport parameterisation while the testing one is needed to check the precision of the results. The both sets are generated in the same manner and are of the same size. They consist of a few thousands of pairs of vectors $\vec{\Gamma}$ and $\vec{\Lambda}$, which specify input and output proton kinematics, respectively. The tracking over the parameterised machine segment is carried out with MADX-X.

The kinematics of the input proton $\vec{\Gamma}$ is generated randomly with uniform distribution in a defined range of the phase space:

$$\Gamma_{i\,\mathrm{min}} \leq \Gamma_i \leq \Gamma_{i\,\mathrm{max}}, \; i = 1, \ldots, 5 \,. \tag{6.33}$$

The input variable range is chosen such that is entirely covers the allowed proton kinematics which is within the acceptance of the experiment for a given running scenario. The obtained approximation is only valid within the training data input range.

Parameterisation definition

Each of the input variables Γ_i is rescaled to be within the $[-1, 1]$ interval:

$$\tilde{\Gamma}_i = \frac{2\Gamma_i - \Gamma_{i,max} - \Gamma_{i,min}}{\Gamma_{i,max} - \Gamma_{i,min}} , \tag{6.34}$$

where $\Gamma_{i,min}$ and $\Gamma_{i,max}$ denote the minimum and the maximum of the input variable Γ_i, respectively.

Let L be the number of polynomial terms used in the approximation and $N = 5$ is the size of the input vector $\vec{\Gamma}$. We try to find the parameterisation $\tilde{\Lambda}_i$, which approximates the output variable Λ_i, of the following form:

$$\tilde{\Lambda}_i = \sum_{l=1}^{L} c_l \prod_{i=1}^{N} p_{li}(\tilde{\Gamma}_i) = \sum_{l=1}^{L} c_l \, F_l(\tilde{\vec{\Gamma}}) , \tag{6.35}$$

where $p_{li}(\tilde{\Gamma}_i)$ are either monomials[4], or Chebyshev[5] or Legendre[6] polynomials, labelled with the term number l, with the input variable index i and of the power P_{li}. Each term $F_l(\tilde{\vec{\Gamma}})$ is defined as a product of N polynomials corresponding to each of the input variables:

$$F_l(\tilde{\vec{\Gamma}}) = \prod_{i=1}^{N} p_{li}(\tilde{\Gamma}_i). \tag{6.36}$$

The orthogonality of Chebyshev and Legendre polynomials slightly improves the precision of the obtained results compared to the monomials. According to [42], to minimise the maximum error Chebyshev polynomials should be used, but to minimise the average error Legendre polynomials are indicated.

The total power of $F_l(\tilde{\vec{\Gamma}})$ is defined as a sum of powers P_{li} of each of the constituent polynomials. For example, the parameterisation containing terms $F_l(\tilde{\vec{\Gamma}})$

[4]A monomial of a single variable x is either 1 or is a power x^n of x, with n a positive integer.

[5]Chebyshev polynomials of the first kind are defined by the recurrence relation $T_0(x) = 1$, $T_1(x) = x$, $T_{n+1}(x) = 2x\,T_n(x) - T_{n-1}(x)$. The polynomials of the first kind are orthogonal with respect to the weight $\frac{1}{\sqrt{1-x^2}}$ on the interval $[-1, 1]$. Each Chebyshev polynomial $T_n(x)$ is an nth-degree polynomial.

[6]Legendre polynomials $P_n(x)$ can be expressed using the following formula: $P_n(x) = \frac{1}{2^n n!}\frac{d^n}{dx^n}\left[(x^2-1)^n\right]$. Each Legendre polynomial $P_n(x)$ is an nth-degree polynomial. They are orthogonal on the interval $[-1, 1]$.

of up to the total power of 1, and based on monomials, is of the following form:

$$\begin{aligned}\tilde{\Lambda}_i = {} & c_1\,\tilde{x}(s_1)^0\,\tilde{x}'(s_1)^0\,\tilde{y}(s_1)^0\,\tilde{y}'(s_1)^0\,\tilde{\xi}(s_1)^0 \\ & + c_2\,\tilde{x}(s_1)^1\,\tilde{x}'(s_1)^0\,\tilde{y}(s_1)^0\,\tilde{y}'(s_1)^0\,\tilde{\xi}(s_1)^0 \\ & + c_3\,\tilde{x}(s_1)^0\,\tilde{x}'(s_1)^1\,\tilde{y}(s_1)^0\,\tilde{y}'(s_1)^0\,\tilde{\xi}(s_1)^0 \\ & + c_4\,\tilde{x}(s_1)^0\,\tilde{x}'(s_1)^0\,\tilde{y}(s_1)^1\,\tilde{y}'(s_1)^0\,\tilde{\xi}(s_1)^0 \\ & + c_5\,\tilde{x}(s_1)^0\,\tilde{x}'(s_1)^0\,\tilde{y}(s_1)^0\,\tilde{y}'(s_1)^1\,\tilde{\xi}(s_1)^0 \\ & + c_6\,\tilde{x}(s_1)^0\,\tilde{x}'(s_1)^0\,\tilde{y}(s_1)^0\,\tilde{y}'(s_1)^0\,\tilde{\xi}(s_1)^1, \end{aligned} \tag{6.37}$$

$$\tilde{\Lambda}_i = c_1 + c_2\,\tilde{x}(s_1) + c_3\,\tilde{x}'(s_1) + c_4\,\tilde{y}(s_1) + c_5\,\tilde{y}'(s_1) + c_6\,\xi(s_1). \tag{6.38}$$

Given a training sample of M tuples of the form $(\vec{\Gamma}_j, \Lambda_{ij})$, $j = 1, \ldots, M$, the objective of the procedure is to determine the terms (functions) $F_l(\tilde{\vec{\Gamma}})$ and to fit the coefficients c_l so that the function

$$S_i = \sum_{j=1}^{M} \left(\Lambda_{ij} - \tilde{\Lambda}_{ij}(\tilde{\vec{\Gamma}}_i)\right)^2 \tag{6.39}$$

is minimised. In addition, it is important to minimise the number of terms used and to obtain the parameterisation consisting of terms of lowest possible powers. S_i will be considered minimised when

$$\sqrt{\frac{S_i}{\sum_{j=1}^{M} \tilde{\Lambda}_{ij}^2}} < \epsilon\,. \tag{6.40}$$

The precision of approximation should be much better that the detector resolution of 19.1 μm. For example, proton transverse displacements of up to 40 mm and the required transport precision of 0.5 μm, yield the relative error $\epsilon \sim 10^{-7}$.

Terms to be studied

Since there are infinitely many terms $F_l(\tilde{\vec{\Gamma}})$ to be considered, before the actual selection takes place, the group of studied terms has to be limited. It turns out that the highest nonlinearities of proton transport are observed in the ξ variable while the transverse position and divergence of proton at IP (x, y, x' and y') affect the transport nearly linearly. Therefore, the terms $p_{li}(\tilde{\Gamma}_i)$ corresponding to ξ should appear in the parameterisation, given by Equation 6.35, as polynomials of higher power. In general, for each of the input variables (components of the vector $\tilde{\vec{\Gamma}}$) the user can define a maximum power $P_{max,i}$ of the polynomials $p_{li}(\tilde{\Gamma}_i)$

to be studied in the procedure of minimisation of S_i, defined by Equation 6.39. Table 6.4 presents the typical maximum powers $P_{max,i}$ of polynomials $p_{li}(\tilde{\Gamma}_i)$ of input variables included in the term selection. Their values differ depending upon the optics scenario and the required precision. Thus the total maximum power of terms $F_l(\vec{\tilde{\Gamma}})$ is between 4 and 16.

Variable	Maximum power
$\tilde{\Gamma}_1, \tilde{\Gamma}_3 \quad (x,\, y)$	1, 2
$\tilde{\Gamma}_2, \tilde{\Gamma}_4 \quad (x',\, y')$	$1 \ldots 4$
$\tilde{\Gamma}_5 \quad (\xi = \frac{\Delta p}{p})$	$4 \ldots 10$

Table 6.4: Maximum powers $P_{max,i}$ of input variables included in the terms selection. The maximum power of ξ variable is higher compared to the others since the transport nonlinearities are mostly caused by the fractional momentum loss of protons.

Gram-Schmidt orthogonalisation

To further reduce the number of functions F_l in the final expression, only the terms that significantly reduce S_i are chosen. The functions F_l generally are not orthogonal and thus it is difficult to evaluate their individual contributions to the reduction of S_i. This is done with the use of the Gram-Schmidt orthogonalisation procedure, which is performed when any new term is added. The terms are studied following the polynomial order, so that the simpler functions are preferred if the contributions are equal.

The selected terms are stored in the orthogonalised $M \times L$ matrix $\mathbf{W}$. The rows of the matrix correspond to the input vectors $\vec{\tilde{\Gamma}}_j$, $j = 1, \ldots, M$. The columns represent the already selected terms F_l which were evaluated for the input vector represented by the rows.

Let us suppose that $L - 1$ steps of the procedure have been performed. This results in a $M \times (L - 1)$ matrix $\mathbf{W}$. The problem now is to consider the Lth function. The contribution of the term is given by the M-dimensional vector of its values evaluated for all the inputs in the sample:

$$\vec{f}_L = \begin{pmatrix} F(\vec{\Gamma}_1) \\ F(\vec{\Gamma}_2) \\ \vdots \\ F(\vec{\Gamma}_M) \end{pmatrix} \tag{6.41}$$

Since the terms already present in the matrix $\mathbf{W}$ are orthogonal, it is enough to orthogonalise the studied term $\vec{f}_L$. The orthogonalised vector is given by

$$\vec{w}_L = \vec{f}_L - \sum_{k=1}^{L-1} \frac{\vec{f}_L^{\mathrm{T}} \vec{w}_k}{\vec{w}_k^{\mathrm{T}} \vec{w}_k} \vec{w}_k \tag{6.42}$$

and $\vec{w}_L$ is the component of $\vec{f}_L$ orthogonal to the columns $\vec{w}_1, \vec{w}_2, \ldots, \vec{w}_{L-1}$ of the matrix $\mathbf{W}$.

The term is selected when it is capable of reducing the approximation error S_i, which is checked by the tests explained in the following section.

Term selection

Let us rewrite the Equation 6.39 using the orthogonalised representation of the selected terms:

$$S_i = (\vec{\Lambda}_i - \mathbf{W}\vec{a})^{\mathrm{T}}(\vec{\Lambda}_i - \mathbf{W}\vec{a}), \quad \vec{\Lambda}_i^{\mathrm{T}} = (\Lambda_{1i}, \Lambda_{2i}, \ldots, \Lambda_{Mi}) \,. \tag{6.43}$$

Vector $\vec{\Lambda}_i$ represents the M outputs of the training sample. Vector $\vec{a}$ is a vector of L coefficients of the linear combination of the orthogonalised terms in the approximation. In order to find it let us differentiate Equation 6.43 with respect to a_l, $l = 1, \ldots, L$. Since the columns of the matrix $\mathbf{W}$ are orthogonal ($\vec{w}_k^{\mathrm{T}} \vec{w}_l = 0$ if $k \neq l$) we get:

$$\vec{\Lambda}_i^{\mathrm{T}} \vec{w}_l - a_l \, w_l^{\mathrm{T}} w_l = 0 \,, \tag{6.44}$$

$$a_l = \frac{\vec{\Lambda}_i^{\mathrm{T}} \vec{w}_l}{w_l^{\mathrm{T}} w_l} \,. \tag{6.45}$$

Now the approximation error, defined by Equation 6.43, can be expressed in the form of individual contributions from the selected terms:

$$\begin{aligned} S_i &= \left(\vec{\Lambda}_i - \sum_{l=1}^{L} a_l \vec{w}_l \right)^{\mathrm{T}} \left(\vec{\Lambda}_i - \sum_{l=1}^{L} a_l \vec{w}_l \right) \\ &= \vec{\Lambda}_i^{\mathrm{T}} \vec{\Lambda}_i - \sum_{l=1}^{L} a_l^2 \vec{w}_l^{\mathrm{T}} \vec{w}_l \\ &= \vec{\Lambda}_i^{\mathrm{T}} \vec{\Lambda}_i - \sum_{l=1}^{L} \frac{(\vec{\Lambda}_i^{\mathrm{T}} \vec{w}_l)^2}{\vec{w}_l^{\mathrm{T}} \vec{w}_l} \,. \end{aligned} \tag{6.46}$$

The contribution of the Lth term to the reduction of S_i, is given by

$$\Delta S_i = \frac{(\vec{\Lambda}_i^{\mathrm{T}} \vec{w}_l)^2}{\vec{w}_l^{\mathrm{T}} \vec{w}_l} \,. \tag{6.47}$$

The more $\vec{w}_l$ is parallel to $\vec{\Lambda}_i$, the higher is the reduction of the approximation error. Thus the Lth term is accepted if the angle ϕ between $\vec{w}_L$ and $\vec{\Lambda}_i$ is smaller that an upper limit ϕ_{cut}.

The angle ϕ_{cut} is readjusted automatically when new terms are added, so that the selection criteria are less and less difficult to be fulfilled. As a result, functions contributing most to the reduction of S_i are chosen first.

Calculation of coefficients

Once the parameterisation, that is the F_l's and L that minimises S, have been found, the coefficients c_l of the Equation 6.35 still need to be determined.

Let us suppose we want to determine the matrix $\mathbf{F} = \left(\vec{f}_1, \vec{f}_2, \cdots, \vec{f}_L\right)$ of the non-orthogonalised contributions (as defined in Equation 6.41), corresponding to the selected functions. To do so we need to invert the Gram-Schmidt procedure given in Equation 6.42. This can be done with the help of the matrix $\mathbf{B}$ defined as

$$b_{ij} = \begin{cases} \frac{\vec{f}_j^{\mathrm{T}} \vec{w}_i}{\vec{w}_i^{\mathrm{T}} \vec{w}_i} & \text{if} \quad i < j \\ 1 & \text{if} \quad i = j \\ 0 & \text{if} \quad i > j \end{cases} \,. \tag{6.48}$$

Then the matrix $\mathbf{F}$ reads

$$\mathbf{F} = \mathbf{W}\mathbf{B} \,. \tag{6.49}$$

The coefficients c_l define the linear superposition of the columns of matrix $\mathbf{F}$ that approximates the output $\vec{\Lambda}_i$:

$$\tilde{\vec{\Lambda}}_i = \mathbf{F}\vec{c} \,. \tag{6.50}$$

Since $\tilde{\vec{\Lambda}}_i$ is also defined as

$$\tilde{\vec{\Lambda}}_i = \mathbf{W}\vec{a} \,. \tag{6.51}$$

we get

$$\mathbf{W}\mathbf{B}\vec{c} = \mathbf{W}\vec{a} \,. \tag{6.52}$$

Hence the vector of coefficients $\vec{c}$ reads:

$$\vec{c} = \mathbf{B}^{-1}\vec{a} \,. \tag{6.53}$$

Parameterisation reduction

While using the parameterisation in the Roman Pot Monte Carlo software, we are concerned both about the precision and the computation time of the approximation. Then, if the required precision can achieved with fewer polynomial terms, the surplus ones should be removed.

Once the parameterisation has been obtained, its precision is evaluated with a test sample. If the observed error distribution is within the aimed precision range, the parameterisation is accepted. In addition, according to the aimed precision, the unnecessary terms are determined and removed.

The values of the normalised input variables $\tilde{\Gamma}_i$, of the polynomials $p_{li}(\tilde{\Gamma}_i)$, and of the products of the polynomials $F_l(\vec{\tilde{\Gamma}})$ are all within the ± 1.0 range. Hence, the coefficients c_l determine directly the influence of the specific terms on the approximation output value $\tilde{\Lambda}_i$ (see Equation 6.35).

Let $\pm E_T$ be the range of the observed error distribution obtained with the use of the testing sample and $\pm E_P$ — the aimed absolute precision. In order to perform the reduction, the terms $F_l(\vec{\tilde{\Gamma}})$ are sorted in an increasing order according to their c_l coefficients. The smallest ones are removed as long as the condition

$$\sum_{r=1}^{R} |c_r| < E_P - E_T \tag{6.54}$$

is fulfilled, where R is the number of removed terms and r defines the sorted order. After the reduction procedure the error of the approximation is still within the required $\pm E_P$ range.

6.4.3 Aperture modelling

In addition to the modelling of the proton transport between the given points along the accelerator, it is also important to simulate the proton losses, which are caused by finite apertures of the accelerator elements. Thus to determine the accelerator acceptance, in principle a check of the proton coordinates should be done at each machine element, as is done by the MAD-X programme. However, a good approximation is to locate the elements which act as key aperture limitations [39, 40].

Their location depends upon the optics configuration used. The optics modelling software package provides the functionality of seeing various distributions related to proton losses within the parameterised machine segment. With their help the limiting apertures can be identified. For the running scenarios which have

been studied, a few key apertures were sufficient to model the machine acceptance with the precision of $\sim$1 %.

Then the proton transport is parameterised up to each of the identified key beam line apertures and its coordinates are checked if they fullfill the conditions defined by the beam screen shape:

$$|x| < a, \quad |y| < b, \tag{6.55}$$

$$\frac{x^2}{r_a^2} + \frac{y^2}{r_b^2} < 1\,. \tag{6.56}$$

The aperture dimensions are defined in Figure 6.8.

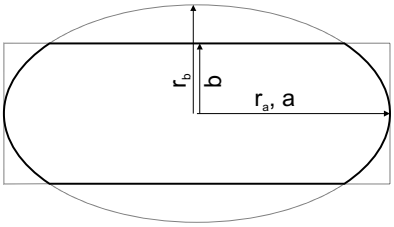

Figure 6.8: Aperture of a machine element.

The proton transport parameterisation to the locations of the identified apertures does not need to be as precise as those towards the Roman Pots. It is enough if the particles are transported with the precision of the machine alignment which is $\sim$100 μm. Hence simpler polynomial transport models are required and thus the aperture treatment is not computationally heavy.

6.4.4 Implementation

The obtained parameterisation of the optical functions, together with the defined apertures, are enclosed in an object-oriented way as a simple to use package, which computes the proton position at the given location and returns a Boolean value saying whether the proton arrives at the location or is lost due to aperture limits. All the details of the polynomial approximation are hidden inside the object. The optics modelling software was easily integrated into the RP simulation and reconstruction software.

6.4.5 Results

The polynomial parameterisations of the optical functions were computed for all the most important LHC optics scenarios ($\beta^* = 1535\,\mathrm{m}$, $90\,\mathrm{m}$, $2\,\mathrm{m}$ and $0.55\,\mathrm{m}$) and were successfully used in the Monte Carlo studies of the reconstruction of elastic and inelastic proton events with Roman Pot detectors. According to the needs of the simulations, the transport of protons through the magnetic lattice of the LHC was parameterised over shorter and longer distances: from IP5 to RP147, from IP5 to RP220, from RP147 to RP220, from IP5 to the possible future Roman Pot locations in IR3. The details of the integration of the proton transport parameterisation into the simulation and reconstruction software are given in Chapters 7 and 8.

The achieved precision of the parameterisation of the proton transverse displacement was always better than a fraction of a micron, which is well below the resolution of the RP detectors ($19.1\,\mu\mathrm{m}$). Also the error of the proton divergence parameterisation, of a fraction of a nanoradiant, was well below the multiple scattering angular deviation, of $\sim 0.5\,\mu\mathrm{rad}$, introduced by the Roman Pot insertions (see Section 7.5).

As has been already mentioned, the proton transport parameterisation became a part of the simulation and reconstruction software. Because of high numbers of proton events used in the Monte Carlo simulations and numerous calls at the reconstruction stage, the speed of the computation of the proton transport over the detector lattice is of high importance. The typical measured execution time[7] is $20 - 60\,\mu\mathrm{s}$ per parameterisation call. It varies with the maximum order of the polynomials, with the number of terms and with type of the polynomials used in the approximation. It is few hundred times faster than the tracking done directly with MAD-X, in the case of the optics configuration used in TOTEM.

An example polynomial approximation of the proton transport from the IP5 down the machine to the beginning of the RP220 station, for β^*=90 m, is given in Table 6.5. The precision of the parameterisation was requested to be $0.5\,\mu\mathrm{m}$ and $0.5\,\mathrm{nrad}$, for the positions and the scattering angles, respectively. The first order terms of the obtained parameterisations, visible in the first lines of the polynomial expansions of $\tilde{x}$, $\tilde{y}$ in Table 6.5, are compatible with the values of optical functions $v(s)$ and $L(s)$ at $s = 220\,\mathrm{m}$ from IP5 (see Figure 6.6). The coefficients of the polynomial approximations are computed with 'double precision' ($\sim$16 decimal digits), however they are quoted in a shorter form.

[7] Intel Pentium 4 3 GHz processor was used for this estimation.

$$
\begin{aligned}
\tilde{x} &= -1.86515\,x^* + 0.0172\,\Theta_x^* - 0.041745\,\xi \\
&+ 0.00986\,x^*\xi + 125.851\,\Theta_x^*\xi - 0.017951\,\xi^2 + 6.4075\,x^*\xi^2 \\
&- 99.25\,\Theta_x^*\xi^2 + 0.03863\,\xi^3 + 92.85\,\Theta_x^*\xi^3 - 0.27161\,\xi^4 \\
&+ 950.84\,\Theta_x^*\xi^4 \\
\tilde{\Theta}_x &= 0.056192\,x^* - 0.53349\,\Theta_x^* + 0.0024843\,\xi \\
&- 0.086586\,x^*\xi - 3.6752\,\Theta_x^*\xi - 0.0024999\,\xi^2 + 0.009553\,x^*\xi^2 \\
&+ 8.5684\,\Theta_x^*\xi^2 + 0.0026192\,\xi^3 + 0.00315\,x^*\xi^3 - 12.310\,\Theta_x^*\xi^3 \\
&- 0.0019076\,\xi^4 - 0.66987\,x^*\xi^4 + 9.644\,\Theta_x^*\xi^4 + 0.0048471\,\xi^5 \\
&- 23.931\,\Theta_x^*\xi^5 - 35.107\,\Theta_x^*\xi^6 \\
\tilde{y} &= 0.0174\,y^* + 264.603\,\Theta_y^* - 1.47\cdot 10^{-6}\,\xi \\
&+ 12.513\,y^*\xi + 52.82\,\Theta_y^*\xi + 0.00002\,\xi^2 - 20.400\,y^*\xi^2 \\
&- 927.6\,\Theta_y^*\xi^2 + 104.387\,y^*\xi^3 + 2271.5\,\Theta_y^*\xi^3 + 0.0002\,\xi^4 \\
&- 7251\,\Theta_y^*\xi^4 - 2724\,\Theta_y^*\xi^5 + 0.0011\,\xi^6 - 44214\,\Theta_y^*\xi^6 \\
\tilde{\Theta}_y &= -0.003749\,y^* + 4.7738\,\Theta_y^* + 1\cdot 10^{-7}\,\xi \\
&+ 0.21569\,y^*\xi + 3.5573\,\Theta_y^*\xi + 4\cdot 10^{-7}\,\xi^2 - 0.41554\,y^*\xi^2 \\
&- 17.109\,\Theta_y^*\xi^2 + 0.7288\,y^*\xi^3 + 37.93\,\Theta_y^*\xi^3 + 2\cdot 10^{-6}\,\xi^4 \\
&- 0.4936\,y^*\xi^4 - 63.27\,\Theta_y^*\xi^4 - 4\cdot 10^{-6}\,\xi^5 + 2.8132 y^*\,\xi^5 \\
&+ 136.81\,\Theta_y^*\xi^5 + 30.73\,\Theta_y^*\xi^6 - 0.000017\,\xi^7 + 667.38\,\Theta_y^*\xi^7
\end{aligned}
$$

Table 6.5: Parameterisation of the proton transport from IP5 down the machine to the beginning of the RP220 station. The vector $(x^*, \Theta_x^*, y^*, \Theta_y^*, \xi = \Delta p/p)$ defines the kinematics of proton at IP5 while $(\tilde{x}, \tilde{\Theta}_x, \tilde{y}, \tilde{\Theta}_y, \xi = \Delta p/p)$ describes the proton arriving at RP220.

The errors of the approximation are shown in Figure 6.9. The precision of the parameterisation was requested to be 0.5 μm and 0.5 nrad, for the positions and the scattering angles, respectively. However the obtained errors are slightly lower. Since the nonlinearities of the optical functions are mostly related to the momentum loss ξ of the transported proton, also the error distributions of the transport approximation exhibit functional dependences upon the ξ variable. Generally, it has been observed that the higher the maximum power of ξ in the parameterisation, the lower the amplitude of the observed oscillations of the error distributions.

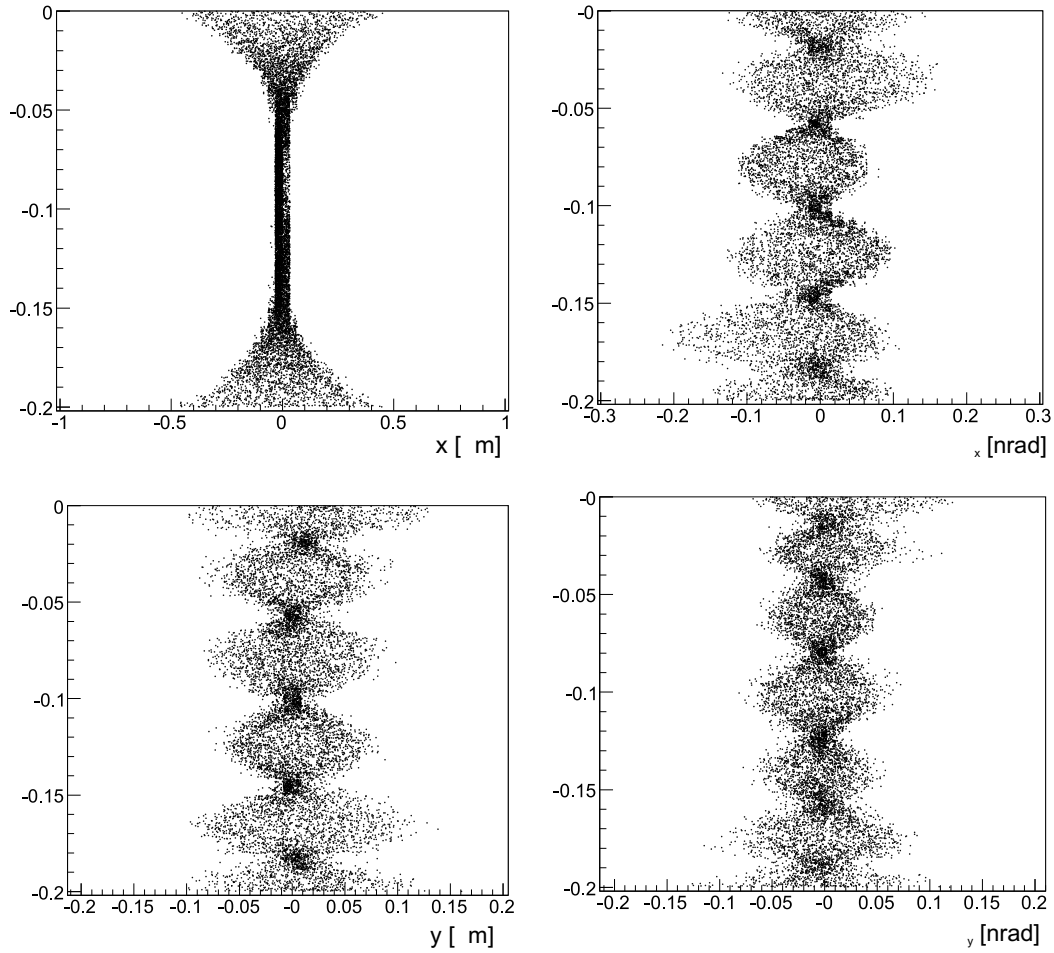

Figure 6.9: The error distributions of the obtained proton transport parameterisation for β^*=90 m optics with respect to the momentum loss ξ of the proton. The approximation was generated with 12,000 training samples and then tested with a different training set. The parameterisation is valid for the proton input kinematics in the following range: $-0.45 \leq x^*, y^* \leq 0.45\,\mathrm{mm}$, $-450 \leq \Theta_x^*, \Theta_y^* \leq 450\,\mu\mathrm{m}$, $-0.2 \leq \xi \leq 0$.

Chapter 7

Roman Pot simulation

In order to fully understand the proton acceptance and the reconstruction resolution for different LHC running scenarios, a software model of the Roman Pot detectors have been developed. Because of partially common physics programme of TOTEM and CMS, TOTEM has decided to adapt the CMS CMSSW [55] software framework and, to certain extent, to follow the CMS computing and data storage model [56]. Since the CMS software has a highly modular structure (see Appendix C.3), TOTEM related packages and data flow patterns can be easily incorporated in it.

The Roman Pot simulation software, which will be discussed in the following sections, is capable of computing the digital response of all the Roman Pot detectors, discussed in Chapter 4, to the forward protons, originating from the interaction point IP5.

A schematic digram of the simulation software is presented in Figure 7.1, which shows its most important modules and their interactions. Each of the modules is configurable according to the running scenario.

The RP stations and the beam pipe are described by the geometry data (1). There is a possibility of simulating both the ideal and the displaced detector system.

The forward protons (2) used in the simulation are generally produced with external Monte Carlo (MC) generators such as PHOJET [89] or PYTHIA [90]. In principle, due to the CMSSW flexibility, any MC generator can be used, provided a proper software interface has been developed.

Generally, the MC generators assume that the trajectories of the incident protons are parallel to each other and that the collisions take place at a fixed point. However, the kinematical parameters of the protons before the interaction follow

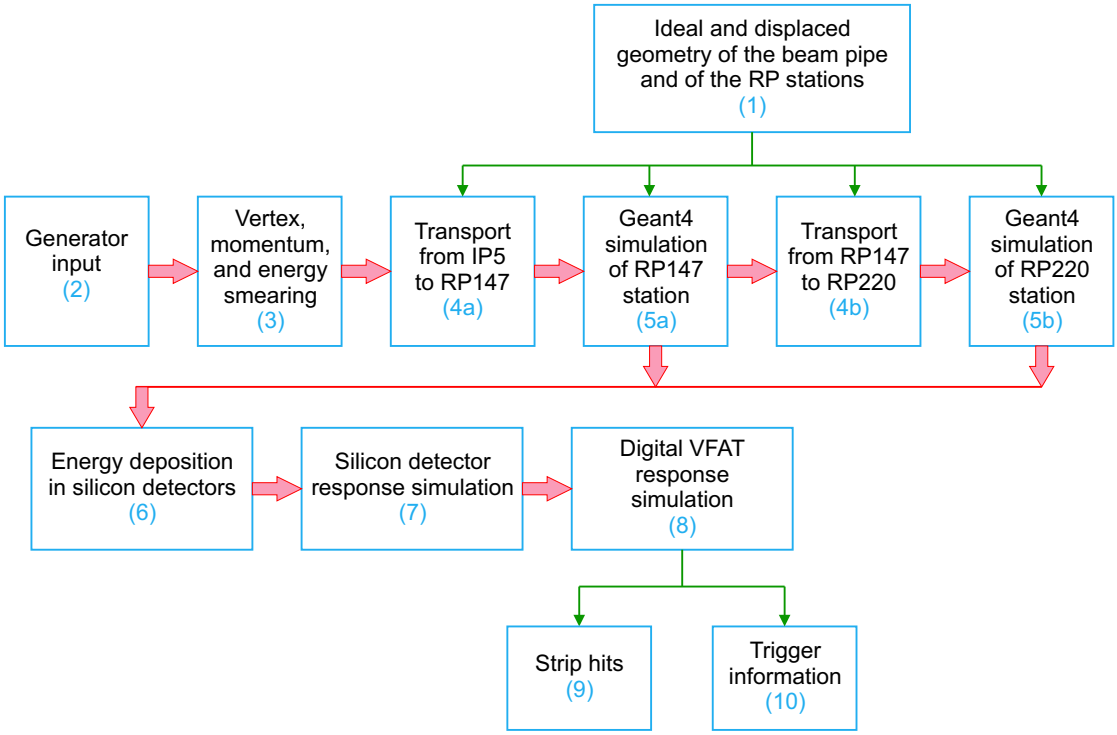

Figure 7.1: Work flow diagram of the Roman Pot simulation software. Red arrows represent the module execution order while the green ones represent the most important data input and output. The constituent modules are described in the text.

certain distributions which depend upon the optics configuration, as it was summarised in Section 6.3. Thus the position, the momenta and the total energy of the event are transformed according to the beam size, the beam divergence, the beam energy spread and the crossing angle, which is schematically represented by the rectangle (3).

On each side of the IP5 there are two RP stations, namely RP147 and RP220, as it can be seen in Figure 3.2. Some of the protons interact with the materials of the RP147 station. The introduced multiple scattering and elastic interactions deviate the proton trajectory, while the inelastic interactions even destroy it. This perturbs the measurements of the RP220 station. Thus, in order to perform precise acceptance and resolution studies, the simulation of this effect is important. As a result, the succeeding RP stations are processed sequentially, which is indicated by letters (a) and (b).

The transport of the leading protons through the accelerator lattice (4a, 4b) is performed with the parameterisation introduced in Section 6.4. The passage of protons through the Roman Pot devices and the energy deposition in the silicon

detectors are simulated with the Geant4 toolkit [3, 4]. Geant4, symbolised by the rectangles 4a and 4b, is described in Appendix C.2.

Finally, on the basis of the deposited energy (6), the signal response of the edgeless silicon detectors (7) and the digital response of the VFAT chips (8) are computed. The most important aspects of the silicon detectors are incorporated in the simulation chain. The values of the key parameters are tuned according to the measurements performed during the beam tests, which are reported in Chapter 5. The resulting simulated strip hits (9) are further fed into the reconstruction software. The trigger patters (10) are used in the TOTEM trigger studies which are carried out in order to optimise the trigger algorithms.

7.1 RP geometry

The geometry of the Roman Pot stations and of the beam pipe is specified with the use of the XML[1] based Detector Description Language (DDL) [96, 97] developed for CMS.

7.1.1 Detector Description Language

A detector is basically a composition of parts. A part is characterised by its shape and material. Parts are composed out of other parts thus forming a hierarchy of components. DDL provides generic XML constructs to describe materials, shapes, compositions of parts, and specification of part specific data.

DDL defines two types of materials: elementary materials and composites. An elementary material is a material consisting of a single chemical element. An elementary material is characterised by its atomic number, density, atomic weight, and an optional symbol. A composite material is a mixture of elementary materials and/or other composite materials. It is characterised by its density and the list of its constituents.

DDL provides a set of elementary solids. Among the most important ones are a box, a trapezoid, a tube or its section, a cone or its section. In addition, the

[1]The Extensible Markup Language (XML) [95] is a general-purpose specification for creating custom markup languages. A markup language is a set of annotations to text that describe how it is to be structured, laid out, or formatted. HTML is an example of a markup language. XML is classified as an extensible language because it allows the users to define their own elements. Its primary purpose is to facilitate the sharing of structured data across different information systems, particularly via the Internet, and it is used both to encode documents and to serialise data.

language enables the user to define complex objects with the Construction Solid Geometry (CSG), which allows a modeller to create a complex object by combining simpler ones with Boolean operators. A solid which is the union, the subtraction and the intersection of two simpler shapes is shown in Figure 7.2. Solids are defined

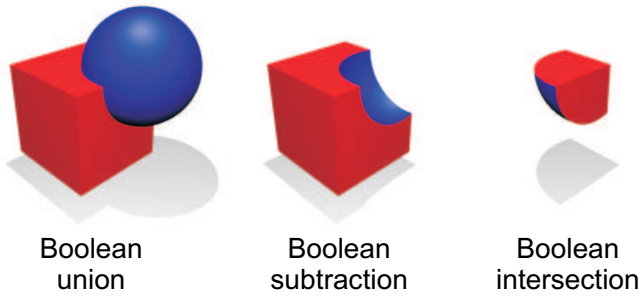

Figure 7.2: Operations in the constructive solid geometry.

by specifying certain dimensions measured in their reference frame. The origin of this reference system also serves as a handle when the solid is positioned.

The detectors are defined as a hierarchy of components. Each component has a shape, a material and consists of sub-components which are positioned and rotated with respect to the reference system of the mother-component.

In order to simulate the active detector parts, the component may be defined as a sensitive detector. Then the energy deposited in it by the traversing particles is recorded by Geant4 kernel and is later accessible for subsequent detector simulation steps.

7.1.2 TOTEM hierarchy of volumes

The TOTEM experiment measurements will be carried out with the Roman Pot detectors (see Chapter 4) placed on both sides of the IP5, at 147 m and 220 m, and with the T1 and T2 telescopes, described in Chapter 3.2, placed in the forward region of the CMS detector. Moreover, the TOTEM physics programme foresees the common runs with the CMS experiment. As a result, the simulation software and the detector geometry, should offer the possibility of performing the commom physics simulation of all the available detectors.

The technical drawings of the Roman Pot detectors and of the machine were analysed. The elements which directly interact with the intact protons were identified and implemented in the simulation geometry. The available XML description of the CMS, T1 and T2 detectors, which will be used in the TOTEM physics pro-

gramme, was also incorporated in the geometry definition. The obtained hierarchy of volumes is visible in Figure 7.3. The hierarchy of components, their dimensions

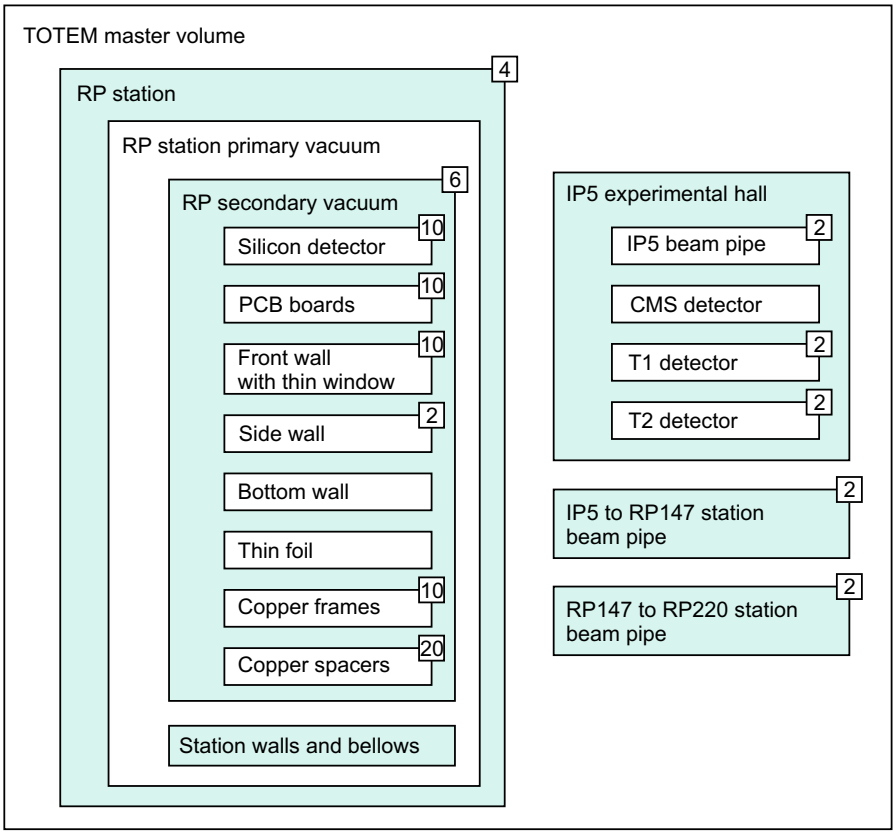

Figure 7.3: Hierarchy of volumes defined for the TOTEM Geant4 simulations. Only the most important components are presented. The rectangles illustrate the hierarchy of component placement. The number of component copies is given in the top right component corner.

and materials were defined in the XML DDL language. Some of the components were described by the primitive solids, while the more complex ones, such as the silicon detectors or the front RP walls with the thin window, were constructed with the use of the Boolean operators.

The TOTEM master volume contains the 4 Roman Pot stations placed on both sides of IP5, the IP5 experimental hall together with the CMS detector, T1 and T2 telescopes and the beam pipe. In addition, as in reality, the master volume contains 4 beam line segments, 2 per arm, spanning between the experimental hall and the RP147 station, and between RP147 and RP220 station. The magnets are not simulated, the protons are transported by means of parameterisation, which will be discussed later.

There are two elements corresponding to the primary vacuum of the machine and the secondary vacuum of the Roman Pot, which are separated by the walls of the Roman Pot, which are inserted into the RP secondary vacuum volume. The parts of the walls directly interacting with protons are made thinner, as in the real design.

There are 6 Roman Pots per station. Each contains 10 silicon detectors which are glued to the PCB boards. The boards are separated and supported by the copper elements. Each of the silicon detector volumes is defined as a sensitive volume, for which the deposited energy is recorded by Geant4.

In Figure 7.4 is presented the visualisation of the key elements of the Roman

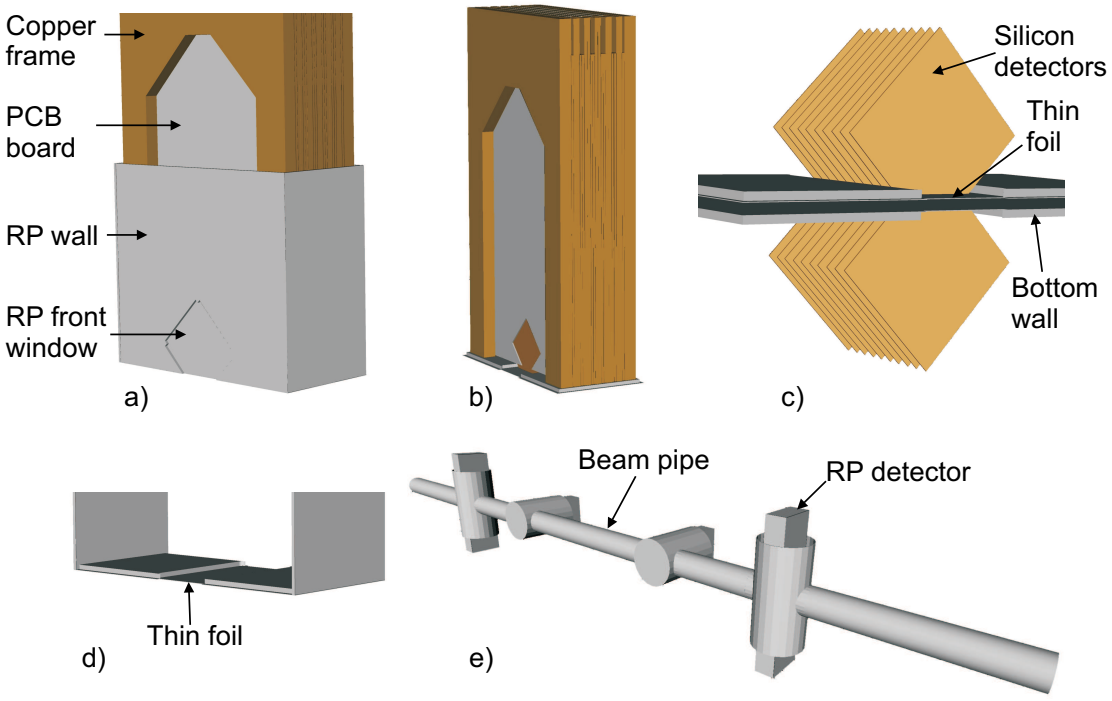

Figure 7.4: Visualisation of the selected parts of the Roman Pot station.

Pot detector system rendered with IGUANA[2]. For readability, certain elements are not shown. Plot a) demonstrates the model of a Roman Pot used in the simulation, with its 0.5 mm thick thin window processed in 2 mm thick RP wall. The contents of the RP detector are presented in picture b). Plot c) shows the silicon detectors of the two vertical Roman Pots in the nominal position for $\beta^* = 1535$ m optics. The devices are placed very closely to the thin foils in order to minimise the insensitive

[2]Interactive Graphics for User Analysis (IGUANA) [98] is a modular C++ toolkit for interactive visualisation. It covers three domains: graphical user interfaces, interactive detector and event visualisation, and interactive data analysis and presentation.

volume. The diamond-like volumes of the silicon detectors are defined as the Geant4 sensitive volumes, for each the deposited energy is recorded. The Roman Pots are separated only by the distance of a few millimetres. The arrangement of the bottom wall and the thin foil is presented in picture d). Plot d) presents an entire simulated RP station.

7.1.3 RP transverse positions

The position of the Roman Pots with respect to the beam centre depends upon the beam size $\sigma_{x,y}$ at the Roman Pot location, which is defined by the optics configuration of the LHC machine. For security reasons, the Roman Pot device must not approach the beam closer than at a the distance of $10\,\sigma_{x,y} + 0.5\,\text{mm}$. The nominal transverse positions of the Roman Pot detectors are a part of the configuration data base. The transverse placement of the Roman Pots, located at 220 m from IP5, for selected running scenarios, is summarised in Table 7.1.

Optics β^* [m]	Horizontal beam size σ_x [μm]	Vertical beam size σ_y [μm]	Horizontal position d_x [mm]	Vertical position d_y [mm]
0.55	76	551	1.26	6.01
2	111	315	1.61	3.65
90	393	631	4.43	6.81
1535	30	81	0.80	1.31

Table 7.1: The nominal horizontal and vertical beam size and the corresponding transverse position of the Roman Pots, located at 220 m from IP5, for selected running scenarios. For $\beta^* = 1535\,\text{m}$ a reduced value of beam emittance is used of $1\,\mu$mrad.

7.1.4 Ideal and real geometry

The technical specifications define the ideal detector geometry. In reality, the precision of the mechanics is limited to 20–100 μm. Moreover, the transverse position of the LHC beam with respect to the beam pipe centre can change.

In order to obtain the reliable physics results, in the real experiment, the mechanical displacements have to be found with the alignment procedures, which are still being designed and tested.

This task can be well accomplished, provided that the effects of various known misalignments are visible in the simulated data. Thus the simulation software must

be capable of displacing the elements of the ideal geometry according to the assumed mechanical precision. The ideal geometry, after applying the displacement procedures, is called the real geometry.

The implemented geometry software module can displace the beams, the entire Roman Pot devices and each of the silicon detectors. The introduced displacements can be recorded for later comparison with the alignment procedure results. However, the displacement package is not mature and well tested, and further work, which is strongly related to the design of the alignment software, needs to be carried out.

7.2 IP5 beam smearing

The MC generated particles are inserted in the centre of the IP5 volume. However, as it has been already mentioned, the parameters of the colliding beams are defined by the optics dependent distributions. As a result, the energy, the momentum and the position of the colliding protons and of the MC generated collision results, have to be smeared before the detector response to the proton tracks is simulated [91].

Figure 7.5 shows the proton-proton collision in the MC frame (left) and in the LHC frame (right).

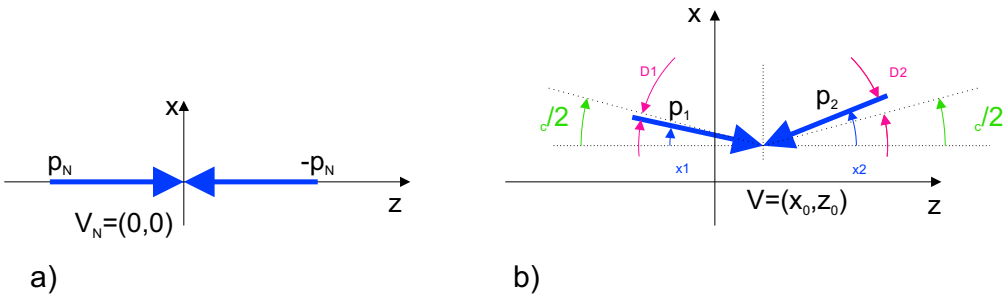

Figure 7.5: Left: Proton-proton collision in the Monte Carlo generator frame. The protons have the nominal momenta $(\vec{p}_N, -\vec{p}_N)$ and the collision takes place in the (0,0) vertex. Right: The LHC proton proton collision. The primary vertex is displaced. The protons collide at the angle being the superposition of the IP5 crossing angle (Θ_C) and the beam divergence $(\Theta_{D1,2})$, which appriximately follows a Gaussian distribution. Moreover, the absolute values of the proton momenta $(p_{1,2})$ are not equal, but they follow the beam momentum (energy) spread.

7.2.1 Momentum transformation

The angles of the colliding protons depend upon the optics scenario. The horizontal longitudinal angle Θ_x of the left proton is given by:

$$\Theta_x = \frac{\Theta_C}{2} + \Theta_{D_x} \,, \tag{7.1}$$

where Θ_C is the beam crossing angle and Θ_{D_x} in the beam divergence component, which is assumed to follow the normal distribution $N(0, \sigma(\Theta_x^*))$. Since in IP5 there is no vertical crossing angle, the vertical longitudinal proton angle Θ_y is smeared only by the beam divergence Θ_{D_y}, also given by the Gaussian distribution $N(0, \sigma(\Theta_y^*))$. Moreover, the absolute momentum of the proton $|p_1|$ follows the beam momentum spread given by $N(p_N, \sigma(p_N))$. The smearing of the beam 2 proton is done in the similar way.

As a result of the smearing procedure, a pair of protons, of momenta p_1 and p_2 in LHC frame, is obtained, as it can be seen in Figure 7.5 (right).

Since the MC generators use a different frame to describe events — a frame where incident particles have the same momenta and the opposite directions parallel to z–axis — a momentum transformation between MC and LHC frames has to be found. After applying such a transformation, the products of the MC event can be inserted in the LHC simulation frame.

Let us first of all find the transformation of the smeared protons in the LHC frame to the frame of the MC generator. This can be accomplished in the following three steps:

Lorentz boost First, we find the Lorentz boost[3] which makes incident particles have equal momenta and opposite directions. Let $\vec{\beta}$ be the relative velocity between the observers and let $\vec{p}_\perp$ ($p_\parallel$) be the perpendicular (parallel) component of momentum $\vec{p}$ with respect to $\vec{\beta}$.

Then the Lorentz transformation of four-momentum $(E|\vec{p})$ to $(E'|\vec{p'})$ is given by

$$\begin{cases} E' = \gamma(E - \vec{\beta}\vec{p}) \\ \vec{p'} = \vec{p}_\perp + \gamma(\vec{p}_\parallel - \vec{\beta}E) \end{cases} , \qquad \gamma = \frac{1}{\sqrt{1-\beta^2}} \,. \tag{7.2}$$

Putting $\vec{p'} = 0$, $\vec{p} = \vec{p}_1 + \vec{p}_2$ and $E = E_1 + E_2$ yields

$$\vec{\beta} = \frac{\vec{p}_1 + \vec{p}_2}{E_1 + E_2} \,, \tag{7.3}$$

[3]Throughout this section units are used in which $\hbar = c = 1$

where $\vec{p}_{1,2}$ and $E_{1,2}$ are the momenta and the energies of the colliding protons in the LHC frame. Let us denote this transformation with $L(\vec{\beta})$ and the boosted momenta of the incident particles with $\vec{p}'_1$ and $\vec{p}'_2$.

Frame rotations Afterwards we find the rotation of the frame so that the momenta $\vec{p}'_1$ and $\vec{p}'_2$ are parallel to the z-axis. In fact there are many possible solutions. Among them, the rotation $R(\vec{a}, \omega)$ about vector $\vec{a}$ of the angle ω is performed, with its parameters defined as:

$$\vec{a} = \frac{p'_1 \times \vec{i}_z}{|p'_1 \times i_z|}, \quad \cos\omega = \frac{p'_1 \cdot \vec{i}_z}{|p'_1|}, \tag{7.4}$$

where $\vec{i}_z$ denotes the unit vector along the z-axis after applying the Lorentz boost.

Event energy scaling The MC generators usually produce events for a fixed centre-of-mass energy $\sqrt{s}$. However, in the real case, $\sqrt{s}$ varies slightly due to the smearing effects, of which the beam momentum (energy) spread $\sigma(p)/p \approx 10^{-4}$ is the highest component. Although this effect is much smaller that the proton momentum reconstruction resolution of the standard TOTEM running scenarios, it has been decided to correct for it, so that the scattering products sum-up to the energy $\sqrt{s}$ of the colliding protons. It has been decided to scale energy E_i^{MC} of each of the MC generated particles

$$E_i^{MC} \to \chi\, E_i^{MC}, \quad \chi = \sqrt{\frac{s^{LHC}}{s^{MC}}}, \tag{7.5}$$

which is denoted as $S(\chi)$.

Finally, the four-momenta of the MC generated particles are smeared with the procedure that can be summarised as

$$(E_i, \vec{p}_i)|_{LHC} = L(-\beta)\, R(\vec{a}, -\omega)\, S(\chi)\, (E_i, \vec{p}_i)|_{MC}. \tag{7.6}$$

7.2.2 Vertex smearing

The IP5 primary vertex position is also optics dependent and is approximately described by the Gaussian distributions of the standard deviations defined by:

$$\sigma_{x,\mathrm{V}} = \frac{\sigma_x}{\sqrt{2}\cos\frac{\Theta_C}{2}}, \quad \sigma_{y,\mathrm{V}} = \frac{\sigma_y}{\sqrt{2}}, \quad \sigma_{z,\mathrm{V}} = \frac{\sigma_z}{\sqrt{2}} \frac{\sigma_x}{\sqrt{\sigma_z^2 \sin^2\frac{\Theta_C}{2} + \sigma_x^2 \cos^2\frac{\Theta_C}{2}}}, \tag{7.7}$$

where σ_x and σ_y are the transverse beam sizes at IP5, σ_z is the machine bunch RMS length and Θ_C is the beam crossing angle. The derivation of the above formulae can be found in [91].

7.3 Geant4 simulation

The simulation of the detector system is done with the Geant4 QGSP physics list, which includes all the key physics processes and particles for the simulations in the energy range of up to 10 TeV.

In addition, Geant4 offers a possibility of defining a parameterisation based physics process, which is applied to certain particles in the specified volumes. Although this approach was primarily intended for simplified shower development treatment, it is also used by the TOTEM software for simulation of the proton transport in the LHC lattice. The four Geant4 so called "physics processes" are defined to treat the proton transport between the IP5 and the RP stations. Each of these processes is based on the proton transport parameterisation introduced in Section 6.4. The parameterisations has to be found for each of the TOTEM running scenarios.

Figure 7.6 demonstrates the arrangements of the fully simulated and the parameterised volumes. The simulated particles are inserted in the centre of the

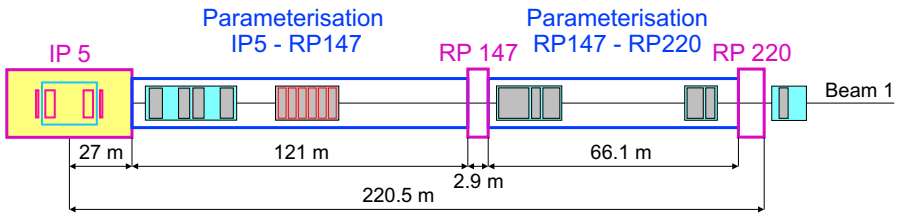

Figure 7.6: Simulation of the TOTEM detector system in Geant4. The volumes of the IP5 experimental hall and of the RP147 and RP220 stations (red rectangles) are fully simulated with Geant4 physics processes. The beam-line transport (blue rectangles) is performed with the optics dependent parameterisation.

IP5. Depending upon the configuration, they are tracked through all the detectors placed in the CMS experimental hall volume including the CMS detector and T1 and T2 telescopes. When the forward protons leave the central volume and enter the volume of the beam line between IP5 and RP147, the Geant4 transport processes are overloaded by the polynomial parameterisation, which transports them directly up to the RP147 station which is entirely simulated with Geant4. The RP220 station in treated in the similar way. The results of the simulation are the energy deposits in the silicon detectors (and other detectors included in the simulation), which are later used in the detector modelling and the digitisation.

There are both advantages and disadvantages of such an approach. On one hand the simulation is faster and it is easier to build such a model of the machine. Besides, by definition, the parameterisation does exactly the same tracking as MAD-X. Thus the tracking validation process is much simpler compared to the full magnetic field simulation. Since the applied strategy simulates the influence of the RP147 station on the measurements carried out at RP220, and since the detected protons interact with no other material but the Roman Pots, such as solution is sufficient for the TOTEM acceptance and resolution studies.

On the other hand, the proton interactions with the machine elements in the parameterised segments are not simulated and the secondaries generated at IP5 and at RP147 are not further propagated. This makes the approach not useful for the direct machine induced RP background studies. They are performed with the other more suitable packages [99, 100, 101, 103]. As their result, distributions and rates of machine background particles at the Roman Pot locations were obtained for certain optics scenarios.

In order to include the influence of the background particles on the proton reconstruction with RP detectors, a module capable of inserting the background particles at the beginning of the Roman Pot stations has been developed [102]. However, the detailed background related RP Monte Carlo simulations still have to be done.

Validation

The proton transport and the Geant4 simulation results have been validated with the expected optics parameters, the geometry data and the properties of the materials. For example it has been checked if the optical functions reconstructed from the Geant4 hits correspond to the ones assumed. Also the tracks of the protons have been carefully analysed in order to find out which volumes and materials they

traverse and in which volumes they are potentially lost, creating the secondaries.

Figure 7.7 shows the proton tracks for a sample of diffractive events for $\beta^* = 90\,\mathrm{m}$ optics. Plots (a) and (c) show the transverse track positions at the beginning of the RP147 and RP220 station, while plots (b) and (d) show the hits in the silicon detector volumes. In the case of RP220 station, the horizontal effective length is very low and the protons are deflected towards the horizontal RP because of their momentum loss. Plot (e) shows the energy deposition distribution in the silicon detectors caused by the traversing 7 TeV protons. The mean energy deposition of 95 keV is close to the theoretical value of 105 keV. Picture (f) shows the secondary vertices of the particles originating from the primary proton interacting with two vertical Roman Pots. The shapes of the front walls, of the bottom foil and of the 10 silicon detectors are visible.

7.4 Silicon detector response

The Geant4 energy depositions are used to simulate the response of the silicon detectors. Each energy deposition entity contains the following information:

- the entry and exit points of the particle, given in local detector coordinate system,
- the entry angle,
- the momentum of the particle,
- the type of the particle
- the energy loss, and
- the detector id.

7.4.1 Energy to charge conversion

As it was discussed in Section 4.2.1, the energy deposited in silicon causes the creation of electron-hole pairs along the particle trajectory. The drift of the charge causes the current flows which are integrated by the front-end of the readout chips. The collected charge is then digitised and saved as a spatial information.

The digitisation of the silicon detectors should be computationally efficient and, at the same time, precise enough to give the correct and realistic output for further studies. In addition, it has been decided that the parameters of the applied simulation algorithms can be easily tuned with the beam test outcomes. As a result, we have resigned from implementing a detailed physical simulation

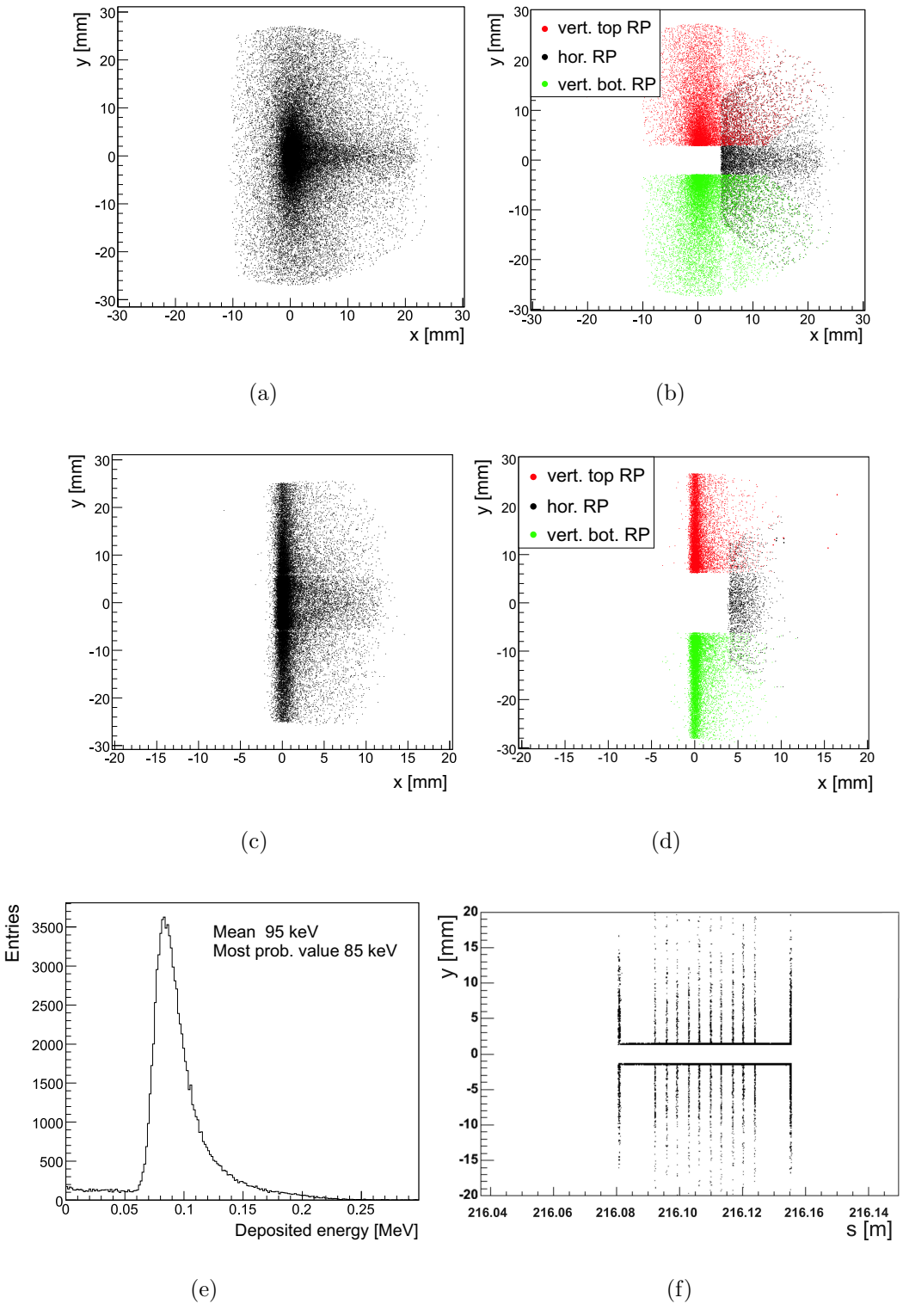

Figure 7.7: Geant4 simulation of the RP detectors for β^*=90 m optics. (a) Track distribution at the beginning of RP147 station. (b) Hits in the detectors of RP147 station. (c) Track distribution at the beginning of RP220 station. (d) Hits in the detectors of RP220 station. (e) Energy deposition in the 300 μm-thick silicon detectors. (f) Origins of secondary particles in two horizontal Roman Pots (RP220 station, β^*=1535 m).

of the silicon devices. Instead, the following simplifications and assumptions have been applied:

- The detectors are fully depleted and the charge generated along the particle track in the detector, in principle, can be entirely collected.
- The electronics integration time is long enough to collect all the generated charge.
- The electrons and holes are treated in a simplified manner.
- The charge diffusion is treated in the simplified manner. Instead of computing the collection time of a given portion of charge and its corresponding diffusion cloud size, the cloud size is parametrised depending on its mean depth in the silicon wafer.
- The induction of charge on the strips is simplified. The clouds are projected geometrically on the detector surface and the charge collected by the strip is computed on the basis of the geometrical strip collection area.
- The presence of no magnetic field is assumed.

The simplified simulation of the signal response of a silicon detector is performed in several steps and is summarised by Figure 7.8.

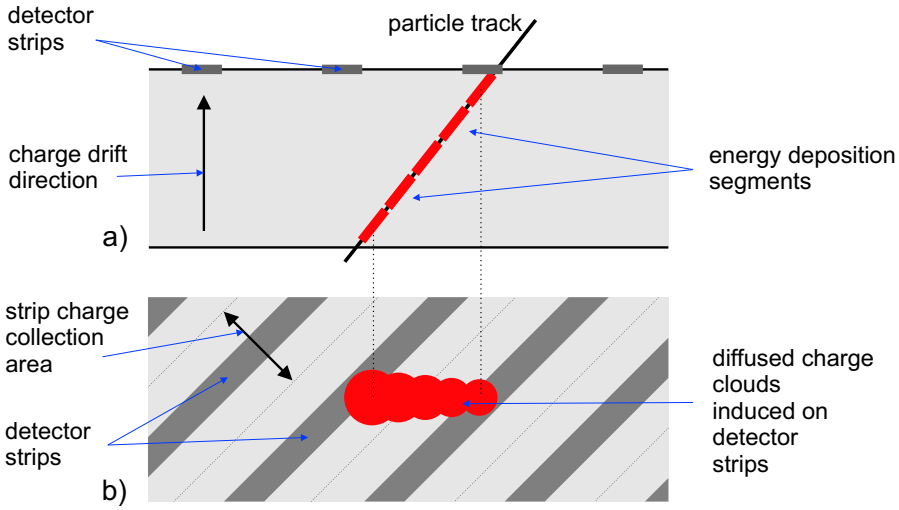

Figure 7.8: Simulation of the energy deposition in the silicon detector volume. (a) Cross-section view. (b) Top view.

Displacement simulation In order to simulate tiny displacements of the silicon detectors there is a possibility of displacing the deposited energy segment. This feature can be particularly important for the studies of the silicon detector alignment.

Energy division The energy deposited in silicon by the traversing particle is usually given by Geant4 in one step, which extends over the whole detector thickness. In order to simulate precisely enough the detector response, especially for the tilted tracks, the deposited energy is divided into several segments, which are visible in Figure 7.8 (a). The energy division is smeared with the application of the Landau distribution. The number of segments is chosen depending on the tilt of the particle track and the required simulation precision.

Energy charge conversion Each segment is converted to a Gaussian charge cloud. Due to speed requirements, the temporal aspect of the simulation is not included. The sizes of the clouds are parameterised. Their values depend upon the depth of the segment in the silicon bulk and are taken from the detailed simulations of silicon detectors [54, 65]. In addition, they were confronted with the test beam results.

Sensitive edge modelling The active edge of the silicon detector is modelled with a use of the Gaussian cumulative distribution function:

$$\eta(w) = \frac{1}{2}\left[1 + \mathrm{Erf}\left(\frac{w - w_0}{\sigma_w\sqrt{2}}\right)\right], \tag{7.8}$$

where w_0 and σ_w are, respectively, the position and the width of the efficiency rise region. The values of w_0 and σ_w were obtained in Section 5.1.4. The charge of the clouds is multiplied by the $\eta(w)$ function, where w is the position of the cloud, measured on the detector surface, in the coordinate system orthogonal to the detector edge. The two other detector edges, which are far from the beam, are simulated in a similar way.

Charge induction on strips The the charge clouds are projected on the detector surface, as it is shown in Figure 7.8, (b). The charge induced on each of the strips in computed on the basis of its geometric acceptance area. During this step the inter-strip couplings are simulated. The fraction of main strip charge that is accepted by the neighbouring strips can be specified in the configuration file.

Signal pile-up The charge induced on strips originating from different tracks is summed-up.

Noise simulation A Gaussian noise distribution is assumed. The noise RMS

value is obtained from the test beam data. A random noise charge is added to all the channels with charge. In addition, basing on the inserted noise value and the applied threshold, a set of strips without charge, that will exceed the threshold due to their noise, is generated.

Dead strips The probability of dead strips in silicon detector can be specified in the configuration file. At the startup of the simulation a set of dead strips is then generated per detector. In their case, the collected charge is always zero.

After applying the above steps, a map of charge collected by the VFAT input channels is obtained.

7.4.2 VFAT based digitisation

The VFAT chip (see Appendix B.1) contains the comparators per each of its 128 input channels. If a particular channel receives a signal greater than the programmable threshold of the comparator, a logic 1 is produced in the output corresponding to that channel. The digitisation is performed in the same way. The threshold value is expressed in e^- and is common for all the channels. Such obtained hits are stored in the Event for later use by the reconstruction procedures.

A hit profile of the RP220 vertical silicon detector is presented in Figure 7.9.

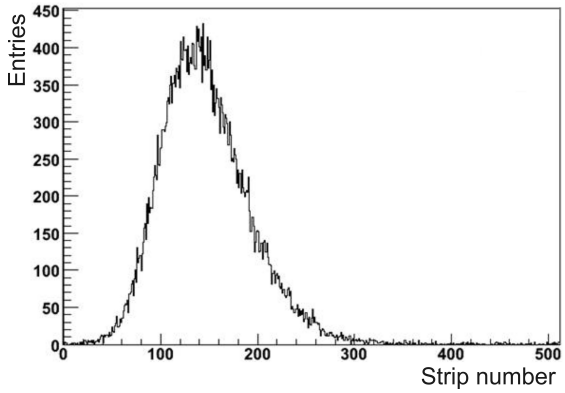

Figure 7.9: Hit profile of the RP220 vertical silicon detector. The plot was generated with a sample of elastically scattered protons, simulated with β^*=1535 m optics.

In addition to the tracking information, the VFAT chip can also produce triggers. The consecutive VFAT input channels are grouped in sectors and the chip

provides fast information if any of the channels in a given group was hit. The number of sectors used can be selected between 1,2,4 and 8. The sectors contain then 128, 64, 32 and 16 channels, respectively. The produced triggers are also recorded in the Event and are used in the trigger analyses.

7.5 RP simulation results

7.5.1 Nuclear collisions in RP

Protons traversing the Roman Pot device may undergo a nuclear reaction. In case of the inelastic process the proton is lost and the secondaries are generated. In case of the elastic nuclear interaction, the momentum and the trajectory of the intact proton get changed in a random way, according to the proton-nucleus elastic differential cross-section. As a result, the proton tracks, measured by subsequent Roman Pots, are deviated from their original trajectory, which may introduce high errors in proton kinematics reconstruction.

The proton acceptance loss, due to nuclear interactions in the Roman Pots, has to be known precisely in order to correctly estimate the detected proton rates. For example, the elastic scattering rate, measured by the Roman Pots, is the input quantity to the total cross-section and luminosity measurement, which are estimated by Equations 3.4 and 3.5. The error of elastic rate measurement directly affects the accuracy of the estimated values.

Nuclear collision probabilities

The probabilities of nuclear collisions in the Roman Pot materials can be estimated with the data provided by [59]. The calculated probabilities are summarised in Table 7.2. For the calculations it was assumed that the protons traversing the Roman Pot are approximately parallel to the beam.

The Roman Pot is designed such that the material budget of protons traversing the sensitive silicon detectors is reduced by introducing the so called thin windows. Then the majority of protons travel only through two 0.5 mm thick thin windows and through ten 300 μm thick silicon detectors. According to Table 7.2, in such a case, the total probability of any nuclear collision in the Roman Pot is $P_{\text{tot}} = 1.98\,\%$ and the one of the inelastic interaction is $P_{\text{inel}} = 1.24\,\%$.

In reality the number of interactions depends upon the position of the Roman Pot with respect to the beam and upon the distribution of the traversing parti-

RP component	material	length [mm]	total coll. prob. [%]	inelastic inter. prob. [%]
front wall thin window	stainless steel	0.5	0.49	0.30
silicon detector	silicon	0.3	0.10	0.064
PCB board	PCB	0.8	0.25	0.17
front wall	stainless steel	2	2.0	1.2
bottom wall	stainless steel	48	47	29
bottom thin foil	stainless steel	48	47	29
a) 10 Si det. + 2 thin windows			1.98	1.4
b) 2 front walls + 10 PCB boards			6.5	4.1

Table 7.2: The probabilities of the interactions in the parts of the Roman Pot. The obtained values are based on material data from [59]. The Roman Pot parts are defined in Figure 7.4. The last two rows give the probabilities of interactions for two typical cases of proton trajectories: the proton traverses 2 thin windows and 10 silicon detectors (a) and the proton enters the RP outside the thin window (b).

cles, since some of them may pass through the RP parts in which the interaction probability is much higher, such as the bottom wall or the bottom thin foil. Figure 7.10 shows the probability of a nuclear collision in various parts of the Roman

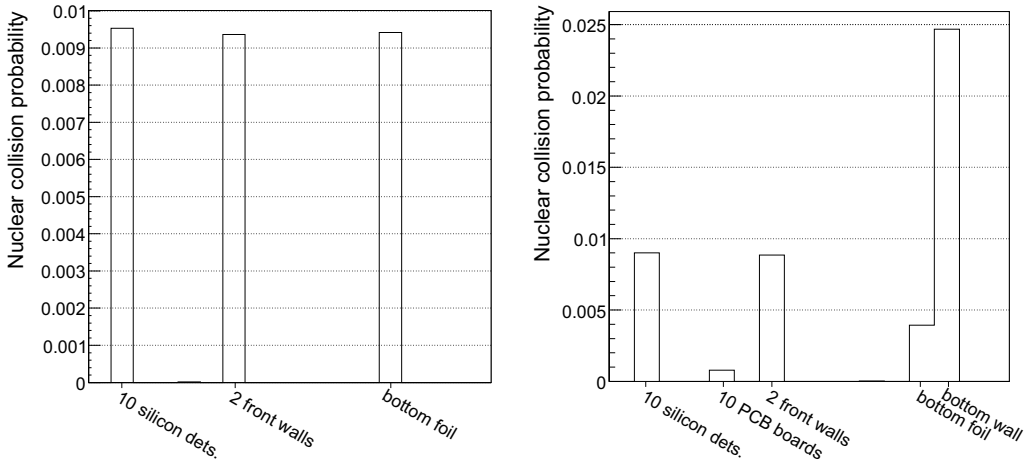

Figure 7.10: Nuclear collision probability of a proton traversing the Roman Pot volume, β^*=1535 m. Left: RP220 vertical RP. Right: RP220 horizontal RP.

Pot, calculated with a Monte Carlo simulation of a pp elastic scattering sample, with $\beta^* = 1535$ m optics. In case of the vertical Roman Pot (left) the particles

pass through the thin window area and the interactions are visible in the two thin windows, in the silicon detectors and in the bottom thin foil. However, in the case of the horizontal RP detectors, the scattered protons spread outside the thin window area and, in addition, the interactions are visible in the PCB electronics boards and in the bottom wall.

The near-beam protons, which traverse the volume of the Roman Pot, are approximately parallel to the bottom wall. Since the protons, which enter the bottom wall, follow its entire length, the probabilities of a nuclear collision and of an inelastic interaction in it are high — 47 % and 29 %, respecively. However, in order to maximise the low-t acceptance of the silicon detectors, the 2 mm thick bottom wall at the bottom edge of the thin window has been removed and the RP is closed by a 150 μm thick thin foil, which separates the silicon detectors from the machine vacuum. Since this is the place of highest proton flux through the RP volume, such an optimisation highly reduces the collision probability. According to the simulations (see Figure 7.10) the probability of a proton nuclear collision in the bottom thin foil is below 1 %.

RP220 acceptance loss due to interactions in RP147

Some of the TOTEM running scenarios, especially with high-β^* optics, foresee the measurements with both RP147 and RP220 stations. Since the RP proton losses lead to the acceptance reduction, the influence of RP147 station on the acceptance of RP220 station is of particular interest. As it has been already discussed, this influence changes with the optics and the type of a physics process studied and has to be evaluated in each particular case.

Figure 7.11 presents the RP220 acceptance loss due to nuclear collisions in RP147. For $-t > 0.013\,\mathrm{GeV}^2$ the protons start to traverse the RP147 detectors before they reach the RP220 station. Since they pass through two Roman Pots on average, the acceptance reduction is $\sim 4\,\%$. At $-t = 0.017\,\mathrm{GeV}^2$ the acceptance deterioration is higher ($\sim 10\,\%$) due to the interactions in the bottom parts of the Roman Pots installed in the RP147 station.

7.5.2 RP multiple scattering

Charged particles passing through matter suffer repeated elastic Coulomb scatterings from nuclei. The vast majority of these collisions result in a small angular deflection of the particle. The cumulative effect of these small angle scatterings is, however, a net deflection from the original particle direction. In order to design

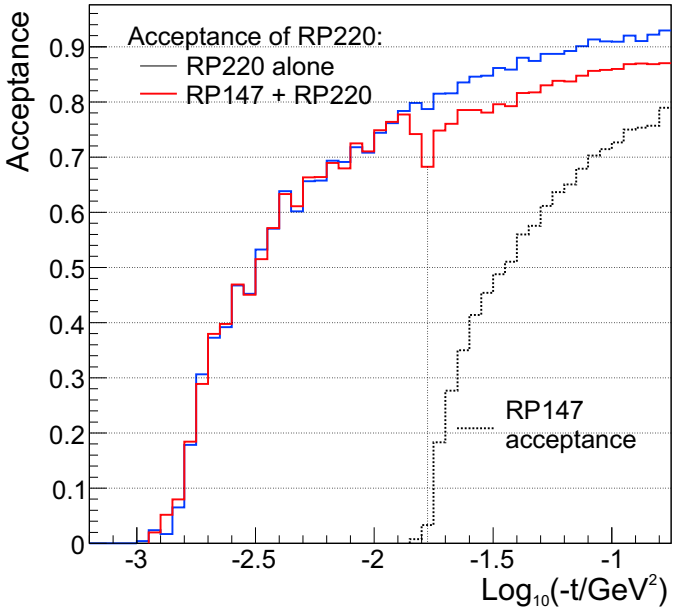

Figure 7.11: Acceptance in t of elastic scattering by RP220 station. Blue line: t-acceptance in RP220 when RP147 station is not inserted. Red line: t-acceptance in RP220 when RP147 station is inserted. The $\sim$4 % loss of acceptance is visible. Black dotted line: t-acceptance of RP147 station.

correctly the proton reconstruction algorithms, it is important to understand the resolution deterioration caused by the proton multiple scattering in the Roman Pot devices.

Multiple scattering of a single RP

The protons which are accepted by the Roman Pot detector have to traverse the two 0.5 mm thick stainless steel windows and the ten 300 μm thick silicon detectors, as it can be seen in Figure 7.4. The standard deviation of the proton multiple scattering in the Roman Pot detector can be obtained theoretically by using the Lynch and Dahl formula [104], which yields results to better than 2 % accuracy:

$$\sigma(\Delta\Theta_{x,y}) = \sqrt{\frac{\chi_c^2}{1+F^2}\left(\frac{1+v}{v}\ln(1+v)-1\right)} \quad \text{[rad]}, \tag{7.9}$$

where $v = 0.5\frac{\Omega}{1-F}$, $\Omega = \chi_c^2/\chi_a^2$, $\chi_c^2 = 0.157\left(\frac{Z(Z+1)}{A}\right)\frac{x}{p^2\beta^2}$ and $\chi_a^2 = 2.007 \cdot 10^{-5}Z^{2/3}[1+3.34(Z\alpha/\beta)^2]/p^2$. The variable p is the proton momentum in MeV/c, β — is the ratio of proton velocity and speed of light c, x — the path length length in g/cm^2, Z and A — the atomic number and weight of the material, respectively,

and α — the fine structure constant. The parameter Ω is the mean number of scatters. In case of a 7 TeV proton interacting in the Roman Pot, $\Omega = 6800$ for 2 thin steel windows and $\Omega = 7870$ for 10 silicon detectors. The total obtained scattering angle standard deviation is $\sigma(\Delta\Theta_{x,y}) = 0.55\,\mu$rad. Figure 7.12 shows the distribution resulting from the Geant4 simulation, which is in full agreement with the expected theoretical value.

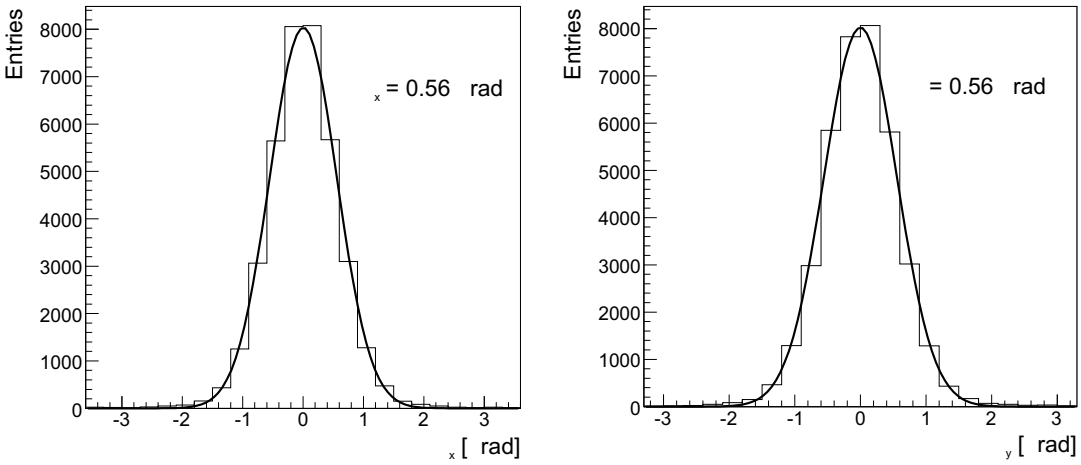

Figure 7.12: Coulomb multiple scattering of 7 TeV protons in the Roman Pots. Left: Horizontal angular distribution. Right: Vertical angular distribution.

Track reconstruction deterioration

The lever arm of the RP147 and RP220 stations is 2 and 6 m, respectively. The multiple scattering of $\sigma(\Delta\Theta_{x,y}) = 0.56\,\mu$rad causes then the proton displacement within the station Δx, Δy of a few microns RMS, which is well below the 19.1 μm resolution of the silicon detectors and thus can be neglected.

However, the angular deviation due to multiple scattering in RP147 can heavily displace the proton in the RP220 station via the optical functions which are shown in Figure 7.13. These optical functions are the same for $\beta^* = 90$ m and $\beta^* = 1535$ m optics. The effective lengths $L_x = 42.2$ – 43.2 m and $L_y = 85.3$ – 97.2 m between the RP147 and RP220 stations are of particular interest since they become in fact long lever arms, which transform the scattering angle at RP147 to the transverse displacement at RP220 station.

The reconstruction resolution deterioration of the RP220 station, due to multiple scattering in RP147 station, can be computed with the matrix formalism introduced in Section 6.2.2. Let $\vec{\Gamma}$ represent the spatial and angular displacements

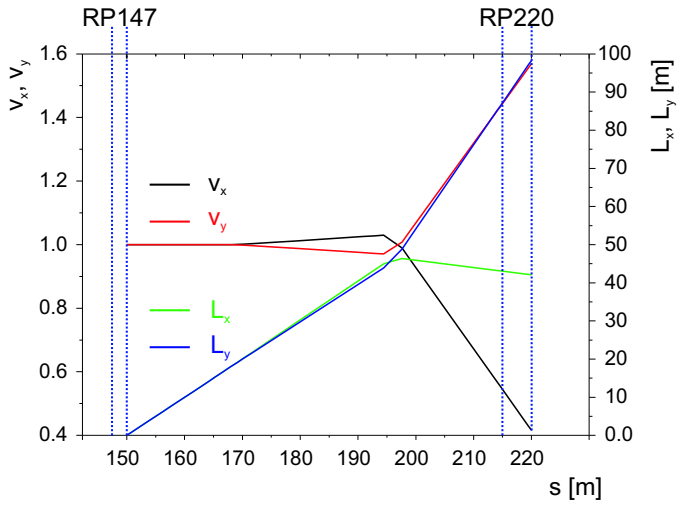

Figure 7.13: The optical functions between the RP147 and RP220 stations for $\beta^* = 90\,\mathrm{m}$ and $\beta^* = 1535\,\mathrm{m}$ optics.

in RP147 station and $\vec{\Lambda}$ the resulting displacements in RP220 station. If $\mathbf{M}_{147-220}$ is the machine transport matrix, the two vectors are related by the following formula:

$$\vec{\Lambda} = \mathbf{M}_{147-220}\,\vec{\Gamma}, \tag{7.10}$$

where the two vectors are defined as

$$\vec{\Gamma} = \begin{pmatrix} \Delta x_{147} \\ \Delta\Theta_{x,147} \\ \Delta y_{147} \\ \Delta\Theta_{y,147} \end{pmatrix}, \quad \vec{\Lambda} = \begin{pmatrix} \Delta x_{220} \\ \Delta\Theta_{x,220} \\ \Delta y_{220} \\ \Delta\Theta_{y,220} \end{pmatrix} \tag{7.11}$$

and the transport matrix reads

$$\mathbf{M}_{147-220} = \begin{pmatrix} 0.429 & 42.2 & 0 & 0 \\ -0.0256 & -0.189 & 0 & 0 \\ 0 & 0 & 1.56 & 97.2 \\ 0 & 0 & 0.0251 & 2.21 \end{pmatrix}. \tag{7.12}$$

The variance matrix $\mathbf{V}_{\vec{\Lambda},\,220}$ of $\vec{\Lambda}$, which represents the resolution deterioration, is given by

$$\mathbf{V}_{\vec{\Lambda},\,220} = \mathbf{M}_{147-220}\mathbf{V}_{\vec{\Gamma},\,147}\mathbf{M}^{\mathrm{T}}_{147-220}. \tag{7.13}$$

$\mathbf{V}_{\vec{\Gamma},\,147}$ is the variance matrix of the multiple scattering in RP147 station, which

can be approximated by the following diagonal matrix:

$$\mathbf{V}_{\vec{\Gamma},\,147} = \begin{pmatrix} \sigma(\Delta x_{147})^2 & 0 & 0 & 0 \\ 0 & \sigma(\Delta\Theta_{x,147})^2 & 0 & 0 \\ 0 & 0 & \sigma(\Delta y_{147})^2 & 0 \\ 0 & 0 & 0 & \sigma(\Delta\Theta_{y,147})^2 \end{pmatrix}. \tag{7.14}$$

When it is assumed that 2 Roman Pots are traversed by the proton in RP147 station, the following $\mathbf{V}_{\vec{\Lambda},\,220}$ matrix is obtained:

$$\mathbf{V}_{\vec{\Lambda},\,220} = \begin{pmatrix} 1.1 \cdot 10^{-9} & -5.1 \cdot 10^{-12} & 0 & 0 \\ -5.1 \cdot 10^{-12} & 2.3 \cdot 10^{-14} & 0 & 0 \\ 0 & 0 & 6.0 \cdot 10^{-9} & 1.4 \cdot 10^{-10} \\ 0 & 0 & 1.4 \cdot 10^{-10} & 3.1 \cdot 10^{-12} \end{pmatrix}. \tag{7.15}$$

From the diagonal terms of matrix $\mathbf{V}_{\vec{\Lambda},\,220}$ we find the RMS of the transverse proton displacements in the RP220 station:

$$\sigma(\Delta x_{220}) = \sqrt{1.1 \cdot 10^{-9}} = 33\,\mu\text{m}, \quad \sigma(\Delta y_{220}) = \sqrt{6.0 \cdot 10^{-9}} = 77\,\mu\text{m}. \tag{7.16}$$

The RMS of both horizontal and vertical displacements is much higher than the resolution of the silicon detectors and thus RP147 deteriorates the reconstruction capabilities of RP220 station.

Figure 7.14 shows the horizontal and vertical Monte Carlo residuals of the tracks reconstructed in the Roman Pot of the RP220 station when the Roman Pots of the preceding station where not inserted. Since the Roman Pot contains 10 silicon detectors (5 per coordinate), the observed resolution of 15 μm is better than the one of the single silicon detector of 19.1 μm. In Figure 7.15 are presented the residuals of the same 220 m Roman Pot in the case when the protons traverse the Roman Pots of the RP147 station. The standard deviations of the presented distributions are in agreement with the values given in Equation 7.16.

Since the deviation of proton angle at RP220, which equals $\sigma(\Delta\Theta_{x,220}) = \sqrt{2.3 \cdot 10^{-14}} = 0.15\,\mu\text{rad}$ and $\sigma(\Delta\Theta_{y,220}) = \sqrt{3.1 \cdot 10^{-12}} = 1.8\,\mu\text{rad}$ for horizontal and vertical projections, respectively, is below the angular resolution of the RP220 station of $4 \div 6\,\mu$rad, the angular reconstruction capabilities of RP220 station are not affected by multiple scattering in the RP147 station.

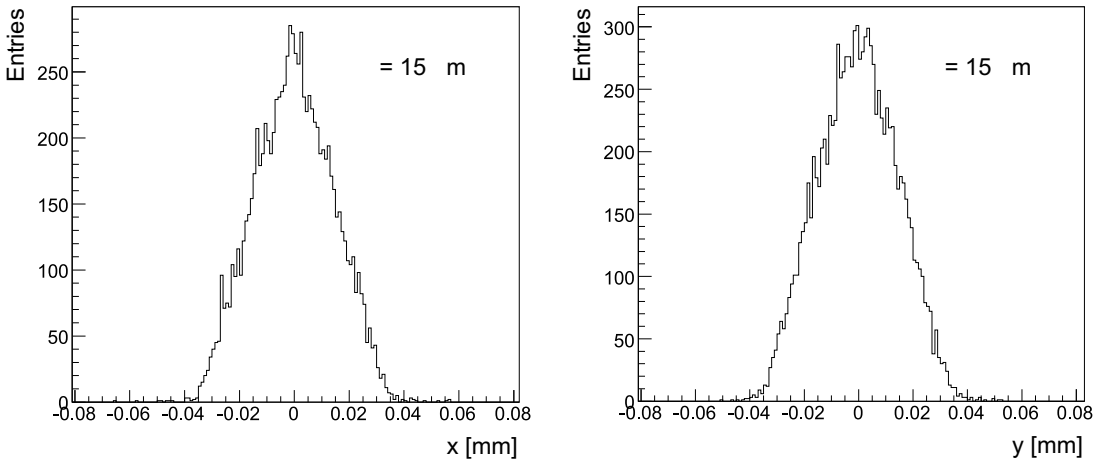

Figure 7.14: Residuals of tracks reconstructed in a horizontal (left) and in a vertical (right) coordinate of the Roman Pot of RP220 station. The RP147 station is not inserted.

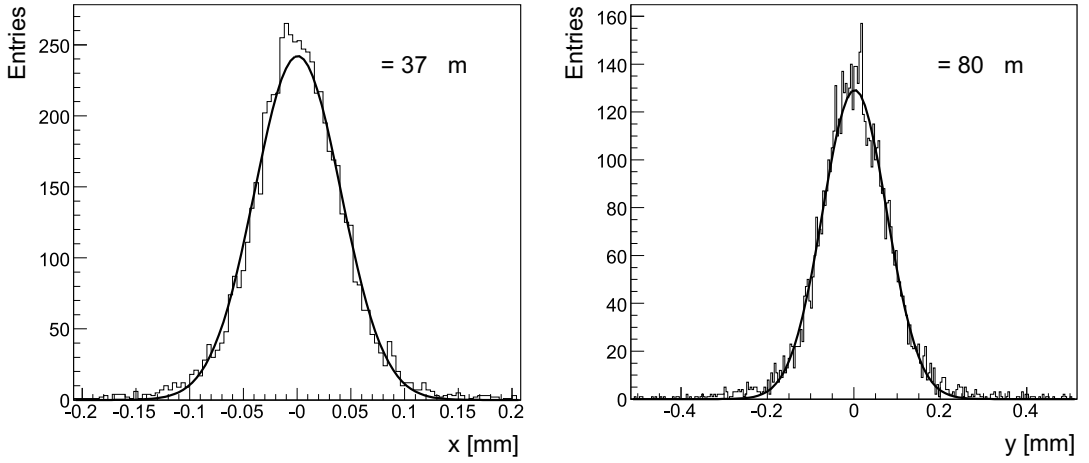

Figure 7.15: Residuals of tracks reconstructed in a horizontal (left) and in a vertical (right) coordinate of the Roman Pot of the RP220 station, when the reconstructed tracks traverse 2 Roman Pots in RP147 station.

Chapter 8

Proton reconstruction

After the collision in the interaction point, some of the intact protons traverse the Roman Pot devices and deposit the energy in the silicon detectors which is converted into strip hits recorded by the Data Acquisition System. The objective of the RP reconstruction software is to find, based on the RP strip hits and the machine optics model, the proton kinematics in the interaction point after the collision.

A schematic digram of the Roman Pot reconstruction software is presented in Figure 8.1, which shows its most important modules and their interactions. The

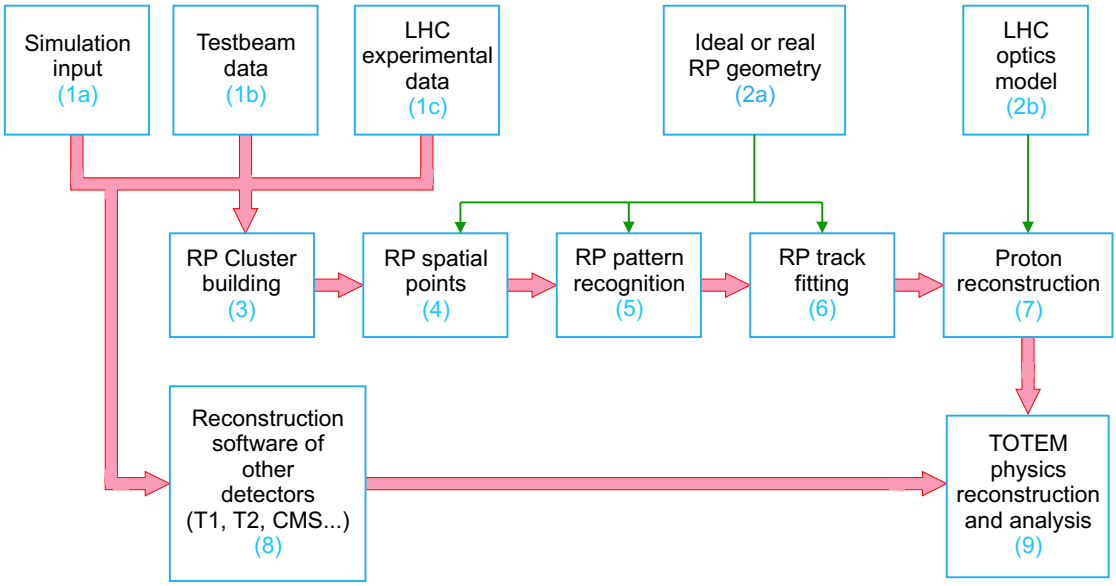

Figure 8.1: Work flow diagram of the TOTEM Roman Pot reconstruction software. The constituent modules are described in the chapter text.

presented packages are implemented in the CMSSW software framework which is

discussed in Appendix C.3.

The reconstruction input data may come from the simulation software (1a), from the beam tests (1b) and from the real experiment (1c). The RP reconstruction software can cooperate with the reconstruction modules of the T1 and T2 TOTEM telescopes (8), as well as with all the other detectors with software implemented in the CMSSW framework and data present in the common data stream.

Another important reconstruction input is the detector geometry. As in the case of the simulation software, two types of geometry are used: ideal and real geometry (2a). The geometry is used in the various stages of the RP local track reconstruction.

The aim of the RP local reconstruction is the computation of the proton tracks in the Roman Pot devices on the basis of the strip hits provided at the reconstruction input. The strip hits are transformed into strip clusters (3), which, afterwards, with the help of geometry information, are converted into spatial points (4). The pattern recognition reconstruction stage (5), is responsible for discovering the proton track candidates composed of the spatial points. The road search algorithm is applied to find the candidates approximately parallel to the beam. Finally, the RP track candidates are fitted with straight lines (6), which constitute the input to the proton reconstruction modules (7).

The RP global reconstruction software is responsible for finding the proton kinematics basing on the tracks reconstructed in the Roman Pots. Various scenarios of proton kinematics reconstruction (7) are foreseen depending upon the LHC running conditions and the physics process considered. For low-β^* optics the use of only the RP220 stations is planned. However, for high-β^* the runs with the RP147 and RP220 stations are foreseen as well as with the RP220 station alone. Also, depending upon the topology of the physics event, a single proton (e.g. SD event) or a pair of protons (e.g. DPE or elastic scattering event) originating from a common vertex is reconstructed. In addition, the TOTEM experiment is interested in constraining the transverse position of the collision vertex with the information from the CMS central detector, especially for the high-β^* optics when the colliding beams are $220 - 454\,\mu$m wide. And finally, the proton reconstruction software has to easily accommodate different optics scenarios and different centre of mass (CM) energies, since the TOTEM experiment is also interested in the early LHC runs of the reduced CM energies.

A versatile proton reconstruction software, which takes account of all the above addressed issues, has been developed and is presented in Section 8.2. The recon-

struction process is based on the parameterisation of the LHC proton transport with polynomials (2b), which were discussed in detail in Section 6.4.

Finally, the software packages responsible for physics reconstruction, analysis and validation (9) have been implemented. They are responsible for reconstruction of the physics quantities like the central mass of a DPE event and for building the histograms and other validation plots of the reconstructed values. Moreover, in this group of packages, the physics analysis which takes advantage of the information available from all the TOTEM detectors will be implemented.

8.1 RP local reconstruction

8.1.1 Reconstruction input

The input of the RP reconstruction software is based on the strip hit objects, which contain the following information:

- arm identification: left/right;
- station number: $1, 2$;
- Roman Pot number: $1, \ldots, 6$;
- silicon detector number: $1, \ldots, 10$;
- strip number: $1, \ldots, 512$.

The strip hits, as has been already discussed, are provided either by the simulation software or, in case of the experimental data, by the Data Acquisition System (DAQ) of the Roman Pots. In case of the experimental data, the TOTEM DAQ is responsible for the transformation of the Roman Pot digital signals to the form compatible with the RP reconstruction software.

8.1.2 Reconstruction geometry

As in the case of the simulation software, addressed in Chapter 7, the geometry used by the reconstruction software can be either an ideal geometry or a real geometry.

The ideal geometry represents the nominal positions of the Roman Pots' elements based on the technical documentation and the ideal beam positions with respect to the Roman Pot detectors. It is used in the reconstruction of a non-displaced detector system.

In reality, the Roman Pot detectors and the position of the beams are displaced, which affects the reconstruction results. The displacements might have been introduced earlied at the simulation stage or may reflect the reality of the experiment. In order to obtain valuable physics results, the displacements have to be found with the alignment procedures before the physics reconstruction is launched. The discovered shifts and rotations of the sensitive detectors, as well as the displacements of the beams at the Roman Pot locations, are included in the real geometry data. The Roman Pot alignment procedures will be based both on track reconstruction in the Roman Pot stations and on physics reconstruction.

8.1.3 Cluster and spatial point building

The particles traversing the sensitive detector, mainly due to charge sharing between detector strips, may cause hits in the subsequent strips of a given detector. Such neighbouring strip hits are converted to a single point called a cluster. Since the hit information is purely digital, the position of the cluster is calculated as a centre of the strip group. The configuration file allows to introduce the cuts on strip multiplicity in a cluster and on cluster multiplicity in the analysed detector.

Before the track reconstruction procedures can be invoked, the position of clusters, expressed in the local detector coordinate system, has to be converted into spatial points appropriate for fitting procedures.

The geometry input provides the information on the position and the rotation of each silicon detector. The silicon detector is assumed to be perpendicular to the beam direction. However, in case of any small RP longitudinal rotation found, the detector frame is projected on the (x, y)-plane orthogonal to the beam direction. On this basis, as it is presented in Figure 8.2, the cluster postion (symbolised in the figure by a red line) is expressed as a three dimensional point (u_{mg}, γ, z), where u_{mg} is the distance between the beam centre and the cluster position, γ is the rotation of the detector and z is the position of the detector along the beam pipe. Both γ and z are provided by the geometry packages and in the reconstruction procedures are assumed to be know perfectly well.

The error of the u_{mg} variable is defined by the detector resolution ($\sim 19.1\,\mu$m), which was determined in the beam tests described in Chapter 5.

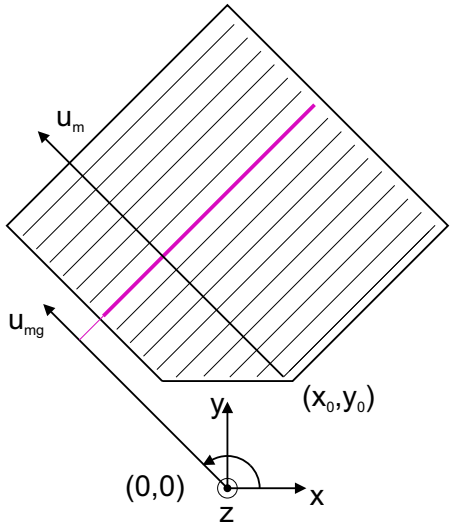

Figure 8.2: Detector cluster seen in local and global coordinate system. The cluster is symbolised by a red line. Its local and global positions are u_m and u_{mg}, respectively. The x and y coordinates are orthogonal to the beam direction z. The angle γ is the rotation of the silicon detector readout with respect to the x-axis of the global coordinate system. The point (x_0, y_0) is the transverse position of the detector local frame in the global coordinate system.

8.1.4 Pattern recognition

The aim of the pattern recognition procedures is to group the reconstructed points of the detectors of given Roman Pot that belong to the same proton track, and in this way to provide a track candidate for the fitting procedure. Since the beam particles arrive at the Roman Pot with the longitudinal angles lower than 1 mrad, only the proton tracks approximately parallel to the beam are of interest, while the tilted ones, which originate from the background, should be rejected.

Road search algorithm

This task is accomplished with a road search algorithm. Each Roman Pot contains 5 pairs of silicon detectors of orthogonal strip directions u and v. Hence, the track candidate search is performed independently for the two detector directions, which correspond to two groups of 5 detectors each.

The procedure The tracks, which are approximately parallel to the beam, in the contrast to the tilted ones, traverse the detector strips of about the same position. In addition, the strips of the 5 analysed detectors are approximately parallel. If the hit positions are histogrammed, the number of entries in the bins

corresponding to the straight tracks will be about 5, while the hits of the tilted ones will spread over many bins, as it is illustrated in Figure 8.3. The bins of the

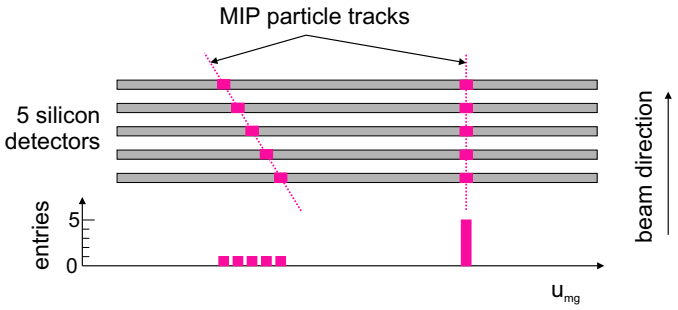

Figure 8.3: The principle of the RP road search algorithm. The hit position of the 5 silicon detectors, of the same readout direction, are histogrammed. The histogram bins of number of entries close to 5 are used to select track candidates parallel to the beam. The hits of the tilted tracks spread over many bins and thus such tracks are discarded.

entries number close to 5 are considered as track candidates.

The implemented algorithm is characterised by the road size parameter w_r which defines the width of the histogram bin. In order to find the tracks efficiently, its value has to be higher than the width of the detector residual distribution augmented by $\sim 40\,\mu$m to compensate for the tilt of the proton tracks. As has been already mentioned, the proton tracks which should be accepted by the Roman Pots are only approximately parallel to the beam. In case of the aligned detectors w_r equals $\sim 150\,\mu$m, otherwise w_r has to be larger in order to accommodate the displacements. The testbeam residuals of both misaligned and aligned detectors were presented in Section 5.1.3.

In reality, the histogramming procedure is more complex than it is presented in Figure 8.3 — it is implemented in a way which optimises the track candidate search. Each hit is associated a weight which reflects the hit occupancy of its detector. In order to promote clean track candidates, the higher is the number of the given detector hits, the lower are the hits' weights.

In addition, the histogram bins are not of fixed positions, but are rather implemented as sets of hits. The position of each set is defined as a weighted centre of its elements. A hit is associated to a hit set on the basis of its distance from the set's centre. If for each already created set this distance is higher than the road half-size $w_r/2$, a new set is created. In this way, the bin edge effects are avoided.

The track candidate The Roman Pot device, for the moment, is equipped with detectors of only two different strip directions. Although it allows for the rejection of the tilted background tracks [106], in such a situation, the pattern recognition of piled-up proton tracks is very limited. As a result, presently, the track candidate is built only if in each analysed direction u and v exactly one straight track is found which traverses at least 3 detectors per each u and v direction.

8.1.5 Track fitting

Each Roman Pot track candidate is a set of $(u_{mg,i}, \gamma_i, z_i)$ points, which are defined in Section 8.1.3, where i is the detector index. The track candidates are fitted with straight lines. The track model and the fitting procedure are exactly the same as those of the testbeam. Their details can be found in Section 5.1.3.

As a result of the track fitting, the proton trajectory in the RP detector is parameterised as

$$\begin{cases} x_i = a_1 (z - z_0) + a_2 \\ y_i = a_3 (z - z_0) + a_4 \end{cases}, \tag{8.1}$$

where x_i and y_i are the transverse horizontal and vertical positions of the proton in the subsequent silicon detectors, a_1 and a_3 are the horizontal and vertical track tilts, and a_2 and a_4 are the horizontal and vertical transverse track positions in the Roman Pot centre z_0.

The tracks reconstructed in the Roman Pots, characterised by $\vec{A} = (a_1, a_2, a_3, a_4)$ vectors, constitute the input to proton kinematics reconstruction procedures, which are described in the following sections.

8.2 Proton reconstruction

Protons emerging from elastic and diffractive scattering at LHC are emitted at very small angles (10 – 150 μrad) and undergo no or small (10^{-7} – 0.1) fractional momentum loss ($\xi = \Delta p/p$), respectively. Hence they are very close to the beam and can only be detected in the RP detectors downstream symmetrically on either side of the interaction point (IP) if their displacement at the detector location is large enough.

The transverse displacement $(x(s), y(s))$ of a elastically or diffractively scattered proton at a distance s from the IP is related to its origin (x^*, y^*, z^*), scattering angles $\Theta^*_{x,y}$ and ξ value at the IP via the optical functions L, v, D as described in Sections 6.2 and 6.3. The optical functions (L, v, D) determining the explicit

path of the particle through the magnetic elements, depend mainly on the position along the beam line (i.e. on all the magnetic elements traversed before reaching that position and their settings which is optics dependent) but also, due to their nonlinearity, on the particle parameters at the IP, as can be seen in Figure 6.7.

The proton reconstruction procedures are based on the parameterisation of the optical functions, which are extracted for each optics configuration from the MAD-X [37] program. As was discussed in detail Section 6.4, their dependency on the kinematic variables, $\Theta^*_{x,y}$ and ξ, is taken into account.

8.2.1 Problem formulation

Using the parametrisation of the optical functions, the positions x_i and y_i of a proton in the i-th Roman Pot device can be expressed by the following equation:

$$\begin{pmatrix} x_i \\ y_i \end{pmatrix} = \mathbf{T}(\vec{\Gamma}), \tag{8.2}$$

where $\vec{\Gamma}$ is the vector of proton kinematic variables at IP,

$$\vec{\Gamma} = \begin{pmatrix} x^* \\ y^* \\ z^* \\ \Theta^*_x \\ \Theta^*_y \\ \xi \end{pmatrix} \tag{8.3}$$

and $\mathbf{T}$ is the parameterised transport function, which was discussed in detail is Section 6.4. Although the transport function $\mathbf{T}$ is, in reality, only capable of transporting the protons originating from $z^* = 0$ transverse plane, the protons longitudinally displaced are processed after applying the following transformation:

$$\begin{cases} \bar{x^*} = x^* - \frac{p_x}{p_z} z^* \\ \bar{y^*} = y^* - \frac{p_y}{p_z} z^* \\ \bar{z^*} = 0 \end{cases}, \tag{8.4}$$

where p_x, p_y and p_z are the components of the proton momentum.

The local reconstruction procedures, discussed in Section 8.1, determine the proton track in the Roman Pots which is characterised by the track parameters, defined by Equation 8.1. Since the longitudinal angle in a single Roman Pot

device is reconstructed very imprecisely ($\sigma(\Theta) \approx 1\,\mathrm{mrad}$), only the track transverse position, given by parameters a_2 and a_4, is used in the proton reconstruction procedures.

Given a set of measured proton transverse positions in the Roman Pot devices, the reconstruction procedure aims at the determination of the kinematic parameters $\vec{\Gamma}$ of the proton. The reconstruction task therefore consists in resolving for $\vec{\Gamma}$ a system of Equations 8.2, one equation per each RP which measured the same proton track.

To obtain a unique solution including the vertex, at least 6 linearly independent measurements are needed which is not possible with the RP220 station alone. However, the transverse and the longitudinal vertex position distribution is known, since it is determined by the optics parameters. As a result, three additional constraints are introduced, $\sigma(x^*) = \sigma_{x,\mathrm{V}}$, $\sigma(y^*) = \sigma_{y,\mathrm{V}}$ and $\sigma(z^*) = \sigma_{z,\mathrm{V}}$, which allow for the proton reconstruction with a single RP station. The standard deviations of the vertex positions, $\sigma_{x,\mathrm{V}}$, $\sigma_{y,\mathrm{V}}$ and $\sigma_{z,\mathrm{V}}$, were defined by Equation 7.7.

Moreover, in the case of the diffractive events, the vertex position can be also constrained by the information from the CMS central detector, which is capable of determining the primary vertex position with the resolution of $30\,\mu\mathrm{m}$ [5], which is much finer than the optics based constraints.

8.2.2 Reconstruction procedure

Without the dependence of the optical functions on the kinematics, the algebraic inversion problem would be linear and could be solved analytically. To take into account the nonlinearity, a numerical procedure has been implemented which is based on the minimisation of the χ^2 function. Its form depends upon the topology of the reconstructed event (reconstruction of a single proton or of a pair of protons) and number of stations used (RP220 alone or RP147 and RP220 together).

Reconstruction with one RP station Let $\mathbf{T}_i(\vec{\Gamma})$ be the parameterised proton transport function from IP to the location of i-th Roman Pot and (x_i, y_i) be the measured proton transverse position. The proton kinematics, described by $\vec{\Gamma}$, is

obtained by the minimisation of

$$\chi^2 = \sum_i \frac{\left(x_i - [\mathbf{T}_i(\vec{\Gamma})]_x\right)^2}{\sigma_{xi}^2} + \sum_i \frac{\left(y_i - [\mathbf{T}_i(\vec{\Gamma})]_y\right)^2}{\sigma_{yi}^2} + \frac{(x^* - x_0)^2}{\sigma_{x,\mathrm{V}}^2} + \frac{(y^* - y_0)^2}{\sigma_{y,\mathrm{V}}^2} + \frac{(z^* - z_0)^2}{\sigma_{z,\mathrm{V}}^2}, \tag{8.5}$$

where σ_{xi} and σ_{yi} are the resolutions of the proton transverse position measurement in the i-th Roman Pot and (x_0, y_0, z_0) is the nominal position of the primary vertex.

Reconstruction with two RP stations In the situation when the detected proton passes through the both RP147 and RP220 stations, according to the results presented in Section 7.5.2, the multiple scattering in the RP147 station has to be taken into account, since it affects the proton position in the RP220 station. As a consequence, the χ^2 has to be minimised with respect to the proton kinematics vector $\vec{\Gamma}$, as well as with respect to the scattering angles $\Delta\Theta_{x,147}$ and $\Delta\Theta_{y,147}$ in the RP147 station.

The proton kinematics thus has to be reconstructed in steps which reflect its trajectory and contribute to the minimised χ^2:

1. The proton is transported from IP to the RP147 station, where it is detected by M Roman Pot devices.
2. Due to the multiple scattering, the proton trajectory is tilted by $\Delta\Theta_{x,147}$ and $\Delta\Theta_{y,147}$ in the RP147 station.
3. The proton is transported from the RP147 station to the RP220 station, where it is detected by N Roman Pot devices.

The parameterised transport function from IP to the i-th Roman Pot of the RP147 station will be denoted as $\mathbf{T}_i(\vec{\Gamma})$, while the transport function from RP147 to the j-th Roman Pot of the RP220 station is denoted by $\mathbf{U}_i(\vec{\Lambda})$. Vector $\vec{\Gamma}$ describes the proton kinematics at IP, while vector $\vec{\Lambda}$ — at the end of the RP147 station. They are related by the formula which reads

$$\vec{\Lambda} = \mathbf{T}_{\mathrm{IP},147}(\vec{\Gamma}) + (0, 0, 0, \Delta\Theta_{x,147}, \Delta\Theta_{y,147}, 0)^{\mathrm{T}}, \tag{8.6}$$

where $\mathbf{T}_{\mathrm{IP},147}$ is the parameterised transport function from IP to the RP147 station. The values of the scattering angles $\Delta\Theta_{x,147}$ and $\Delta\Theta_{y,147}$ can be constrained by the standard deviations $\sigma(\Delta\Theta_{x,y})$ of the RP multiple scattering obtained in

Section 7.5.2. Finally, the χ^2 to be minimised can be written as

$$\begin{aligned}\chi^2 = &\sum_{i=1}^{M} \frac{\left(x_i - [\mathbf{T}_i(\vec{\Gamma})]_x\right)^2}{\sigma_{xi}^2} + \sum_{i=1}^{M} \frac{\left(y_i - [\mathbf{T}_i(\vec{\Gamma})]_y\right)^2}{\sigma_{yi}^2} \\ &+ \sum_{j=1}^{N} \frac{\left(x_j - [\mathbf{U}_j(\vec{\Lambda})]_x\right)^2}{\sigma_{xj}^2} + \sum_{j=1}^{N} \frac{\left(y_j - [\mathbf{U}_j(\vec{\Lambda})]_y\right)^2}{\sigma_{yj}^2} \\ &+ \frac{(x^* - x_0)^2}{\sigma_{x,\mathrm{V}}^2} + \frac{(y^* - y_0)^2}{\sigma_{y,\mathrm{V}}^2} + \frac{(z^* - z_0)^2}{\sigma_{z,\mathrm{V}}^2} \\ &+ \frac{(\Delta\Theta_{x,147})^2}{\sigma(\Delta\Theta_x)^2} + \frac{(\Delta\Theta_{y,147})^2}{\sigma(\Delta\Theta_y)^2}.\end{aligned} \tag{8.7}$$

Proton pair reconstruction In case of the events with two protons detected, one on each side of the IP, which share a common primary vertex, the simultaneous proton reconstruction is advantageous. The χ^2 formulae minimised in such a situation are similar to those given in Equations 8.5 and 8.7, but the reconstructed kinematics vector $\vec{\Gamma}$ now has to include 9 parameters pertinent to the two protons:

$$\vec{\Gamma} = \left(x^*, y^*, z^*, \Theta_{x,1}^*, \Theta_{y,1}^*, \xi_1, \Theta_{x,2}^*, \Theta_{y,2}^*, \xi_2\right). \tag{8.8}$$

8.2.3 Proton kinematics

On the basis of the reconstructed proton scattering angles Θ_x^*, Θ_y^* and the fractional momentum loss ξ the four momentum transfer squared t is calculated:

$$t = (E - E')^2 - (\vec{p} - \vec{p}')^2, \tag{8.9}$$

where E and p is the nominal proton energy and momentum, respectively, before the interaction in the IP, and E' and $\vec{p}'$ are the corresponding parameters after the interaction. The values of E' and $\vec{p}'$ are obtained from the following relations:

$$\begin{aligned} p' &= p(1+\xi) \\ p'_x &= p' \sin\Theta_x^* \\ p'_y &= p' \sin\Theta_y^* \\ p'_z &= \sqrt{p'^2 - p'^2_x - p'^2_y} \\ E'^2 &= p'^2 + m_0^2 \end{aligned} \quad , \tag{8.10}$$

where m_0 is the proton rest mass. The proton azimuth angle ϕ yields from the following formula:

$$\tan\phi = \Theta_y^*/\Theta_x^*. \tag{8.11}$$

8.2.4 Implementation

The proton reconstruction package has been implemented with the use of the ROOT mathematical libraries [43]. The minimisation procedure is based on the gradient-descent algorithms of the TMinuit package.

Since the number of parameters upon which the minimised functions depend is quite high (6 – 13), the correct initialisation of their values have been found crucial for the reconstruction performance. A random initialisation procedure has been thus implemented. At a time one of the input parameters is optimised randomly, within specified range, such that the χ^2 value is reduced. The operation is repeated several times for each of the input parameters. In this way a solution close to the global minimum is obtained. Afterwards the gradient descent algorithm finds the global minimum in a few steps only.

Chapter 9

RP acceptance and resolution studies

9.1 Proton reconstruction with β^*=90 m

9.1.1 Introduction

The software described in Chapters 7 and 8 was used to perform the Monte Carlo studies of the proton reconstruction performance for several running scenarios. In the following sections, the results of the analysis carried out for the $\beta^* = 90\,\mathrm{m}$ optics are reported. The studies were performed with no detector displacement present and with the assumption that the machine optics is precisely known. The simulation software was used to calculate the RP detector response to the diffractive protons while the reconstruction software was used to obtain the proton kinematics.

9.1.2 Proton acceptance

The acceptance of the RP system for elastically or diffractively scattered protons depends on the optics configuration. The proton acceptance of a RP station is determined, by the minimum distance of a RP device to the beam on one hand, and by constraints imposed by the beam pipe or beam screen size [105], on the other hand. The minimum distance of a RP to the beam is proportional to the beam size and equals $10\,\sigma_{x,y}(s) + 0.5\,\mathrm{mm}$.

The acceptance of the RP220 station in t and ξ, obtained with a simulation, is shown in Figure 9.1. The lower bounds of the t- and ξ-acceptance are defined by Equation 6.26. For the $\beta^* = 90\,\mathrm{m}$ optics, the vertical effective length L_y at the

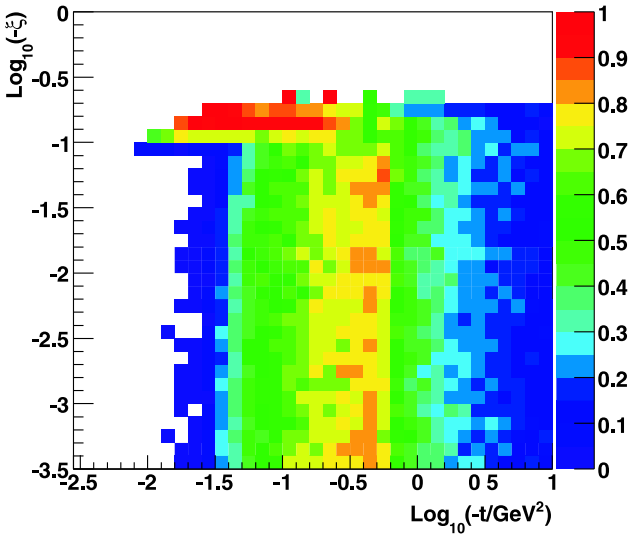

Figure 9.1: Acceptance in t and ξ of diffractively scattered protons at the RP220 station for the $\beta^* = 90\,\mathrm{m}$ optics.

RP220 station equals 262 m (see Table 6.1). Since the vertical Roman Pots are placed 6.8 mm from the beam centre, the lowest detected Θ_y^* is 26 μrad. Therefore, the t-acceptance starts at $0.03\,\mathrm{GeV}^2$. On the other hand, the horizontal effective length L_x is close to 0, which allows for detection of high values of Θ_x^* — up to a fraction of a miliradiant. This leads to the acceptance in $-t$ of up to $\sim 10\,\mathrm{GeV}^2$.

Within the t-acceptance range, diffractively scattered protons are detected independently from their momentum loss, and thus the entire ξ-range can be observed. In addition, for high momentum losses ($-\xi > 0.11$), due to the machine dispersion, the diffractively scattered protons can be observed in the horizontal Roman Pot independently of their t-value, which further enhances the ξ-acceptance. Figure 9.2 presents the ξ-acceptance at RP220 of diffractively scattered DPE[1] [93] protons.

9.1.3 Diffractive proton reconstruction

The reconstruction procedure of diffractively scattered protons aims at a determination of the kinematics parameters $\Theta_{x,y}$ and ξ of the proton, as well as the values derived from them: t and ϕ. This is accomplished with the RP reconstruction software, which covers all the reconstruction phases from cluster building and RP

[1]Double Pomeron exchange is defined as the process $p + p \to p + X + p$, in which a central cluster (X) is separated by large rapidity gaps from quasielastic outgoing protons (p). This event configuration has been studied by several experiments [94].

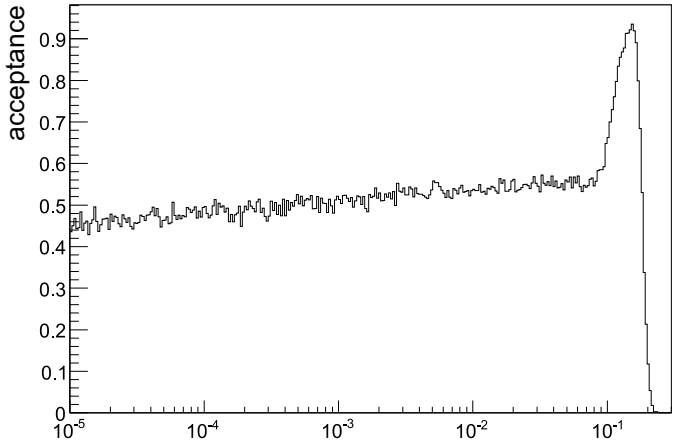

Figure 9.2: ξ-acceptance at right RP220 station of DPE events for β^*=90 m optics. The data sample was generated with PHOJET [89].

proton track fitting to the physics reconstruction.

The full set of kinematic variables, $(\Theta_x^*, \Theta_y^*, x^*, y^*, \xi)$, is reconstructed with the use of the parameterised proton transport functions, discussed in Section 6.4, with the χ^2 based minimisation procedures, which are described in detail in Section 8.2.

The reconstructed proton kinematics parameters are compared with the generated ones and, on this basis, the error distribution histograms are obtained. The RMS values of these distributions, for diffractive protons simulated with the $\beta^* = 90$ m optics, for different running scenarios and for various proton kinematics ranges, are reported in the following sections.

Reconstruction with RP220 station

The resolution in ξ of diffractively scattered protons using only information from the RP station at 220 m is shown in Figure 9.3. The presented points correspond in reality to the resolution values averaged in the range $0.56|\xi_i| \leq |\xi| \leq 1.8\,|\xi_i|$, where ξ_i represents the point in the plot. The ξ-resolution is about 6×10^{-3} – 7×10^{-3}, except for large $|t|$ ($> 1\,\mathrm{GeV}^2$), where it worsens, and large $|\xi|$ (> 0.01) where it improves.

Figures 9.4 and 9.5 present the proton scattering longitudinal angle reconstruction. Since L_x is close to 0, the horizontal component of the scattering angle is reconstructed with the resolution of 2×10^{-5} rad, which is an order of magnitude worse than the beam divergence limit. However, L_y equals 262 m and thus the reconstruction in Θ_y^* is very close to the beam divergence limit of 2.3 μrad.

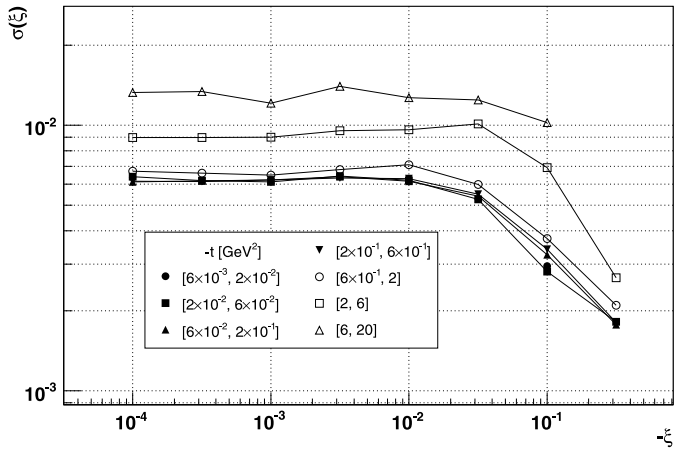

Figure 9.3: Resolution for the ξ-reconstruction of a diffractive proton based only on the information from the RP station at 220 m at $\beta^* = 90$ m optics. The different markers correspond to the resolution at different t-ranges.

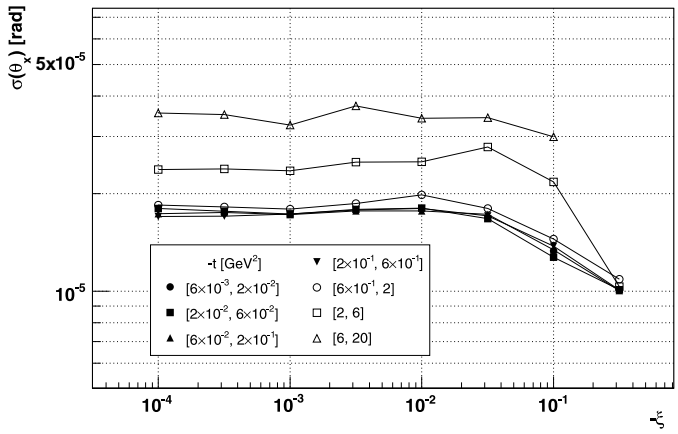

Figure 9.4: Resolution for the Θ_x^*-reconstruction of a diffractive proton based only on the information from the RP station at 220 m at $\beta^* = 90$ m optics. The different markers correspond to the resolution at different t-ranges.

The reconstruction resolutions of both Θ_x^* and Θ_y^* change for $|\xi| > 0.1$: $\sigma(\Theta_x^*)$ is decreasing while $\sigma(\Theta_y^*)$ is increasing. This effect is caused by the machine chromaticity — the optical functions change with the proton momentum loss, which changes the reconstruction.

The reconstruction resolution of the four momentum transfer squared $-t \approx p^2\,\Theta^{*2}$ is determined by the angular resolution $\sigma(\Theta^*)$, with the following relation:

$$\sigma(t) \approx 2p\sqrt{t}\,\sigma(\Theta^*), \tag{9.1}$$

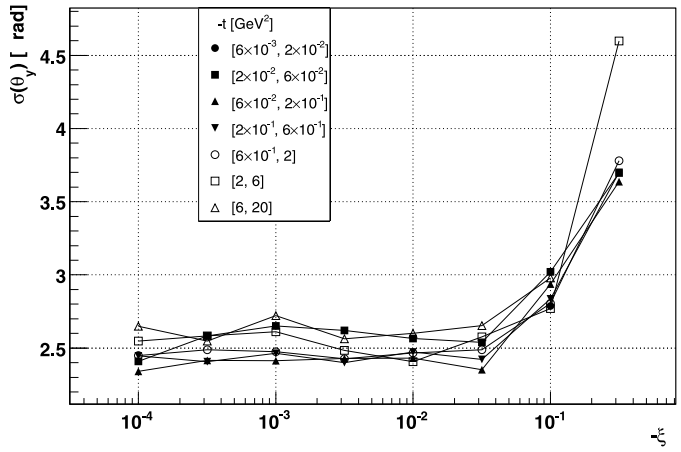

Figure 9.5: Resolution for the Θ_y^*-reconstruction of a diffractive proton based only on the information from the RP station at 220 m at $\beta^* = 90$ m optics. The different markers correspond to the resolution at different t-ranges.

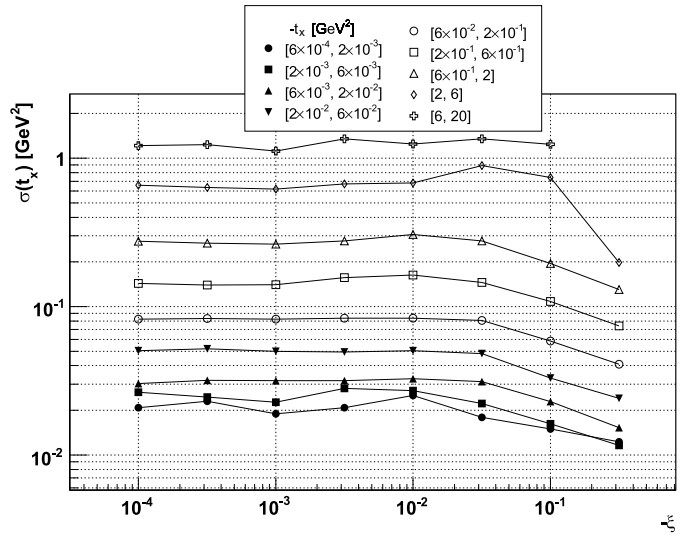

Figure 9.6: Resolution of the t_x-reconstruction of a diffractive proton based only on the information from the RP station at 220 m at $\beta^* = 90$ m optics. The different markers correspond to the resolution at different t_x-ranges.

where p is the momentum of the proton. Since the longitudinal angular resolution is different in the horizontal and the vertical direction, the resolutions in $-t_x \approx p^2\,\Theta_x^{*2}$ and in $-t_y \approx p^2\,\Theta_y^{*2}$ were studied separately.

According to Figure 9.6, for $-\xi < 10^{-2}$, $\sigma(t_x)$ can be approximated by $\sigma(t_x) \approx (0.3 - 0.4)\sqrt{-t_x}$. As in the case of $\sigma(\Theta_x^*)$, $\sigma(t_x)$ improves for $-\xi > 10^{-2}$. The t_x-reconstruction may give the valuable physics input when $\sigma(t_x)/t_x < 1/2$. From Figure 9.7, which shows the relative reconstructruction errors $\sigma(t_x)/t_x$, we get

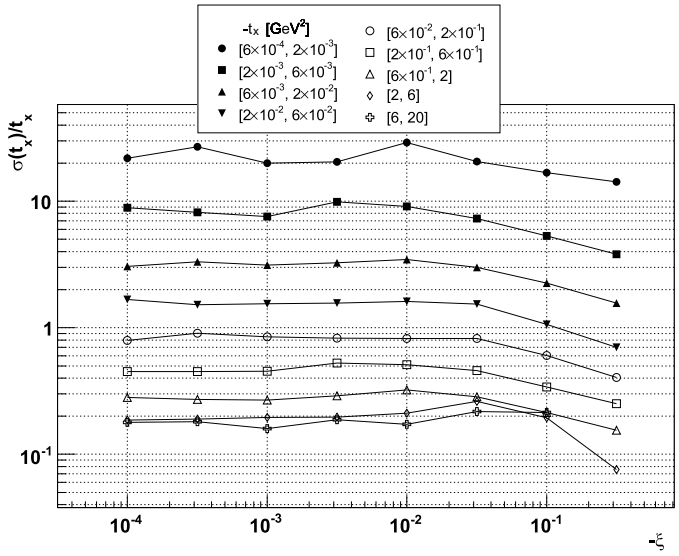

Figure 9.7: Relative error of the t_x-reconstruction of a diffractive proton based only on the information from the RP station at 220 m at $\beta^* = 90$ m optics. The different markers correspond to the resolution at different t_x-ranges.

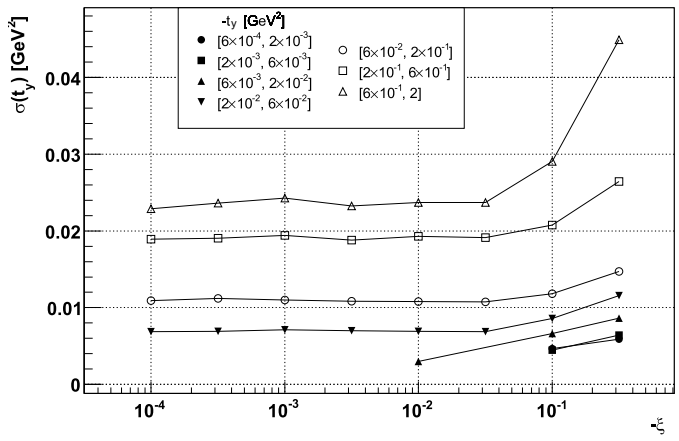

Figure 9.8: Resolution for the t_y-reconstruction of a diffractive proton based only on the information from the RP station at 220 m at $\beta^* = 90$ m optics. The different markers correspond to the resolution at different t_y-ranges.

that this condition is fulfilled for $-t_x \gtrsim 0.2\,\mathrm{GeV}^2$.

Figure 9.8 presents the obtained reconstruction resolution for t_y, which can be parameterised as $\sigma(t_y) \approx 0.04\sqrt{-t_y}$ for $-\xi < 10^{-1}$. For $-\xi > 10^{-2}$ t_y-resolution deteriorates in the same way as $\sigma(\Theta_y^*)$. The relative error $\sigma(t_y)/t_y < 1/2$ for $-t_y \gtrsim 2 \times 10^{-2}\,\mathrm{GeV}^2$, which can be seen in Figure 9.9.

Due to an order of magnitude difference in the t_x and t_y reconstruction res-

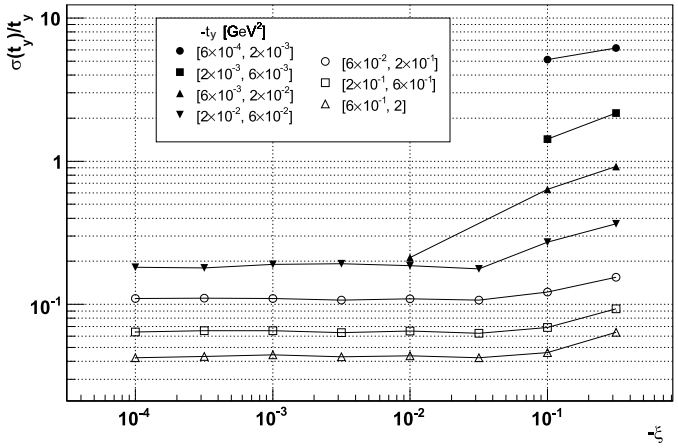

Figure 9.9: Relative error of the t_x-reconstruction of a diffractive proton based only on the information from the RP station at 220 m at $\beta^* = 90$ m optics. The different markers correspond to the resolution at different t_y-ranges.

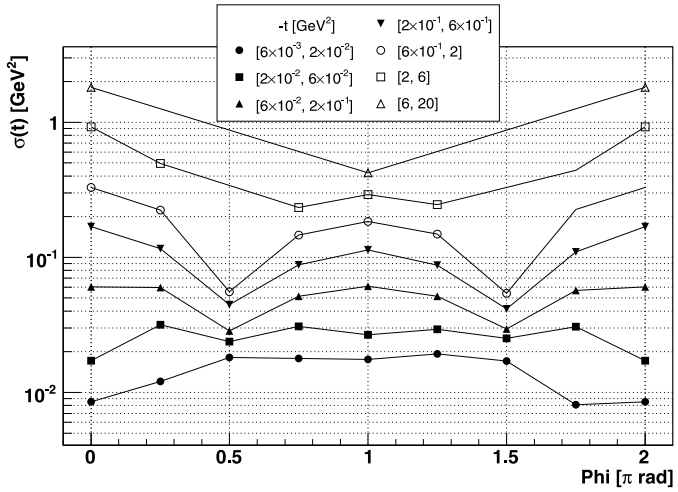

Figure 9.10: Reconstruction resolution in t as a function of the four momentum transfer squared t and the azimuth angle ϕ, of a diffractive proton. Reconstruction is based only on the information from the RP station at 220 m at $\beta^* = 90$ m optics.

olutions, the t-resolution exhibits ϕ-dependence, where ϕ is the scattered proton azimuth angle defined as $\tan\phi = \Theta_y^*/\Theta_x^*$. This dependence can be observed in Figure 9.10. The observed resolution oscillates between the values of $\sigma(t_x)$ and $\sigma(t_y)$ given by Figures 9.6 and 9.8.

TOTEM is also interested in the reconstruction of the proton azimuth angle ϕ. Since ϕ is reconstructed on the basis of Θ_x^* and Θ_y^*, the value of $\sigma(\phi)$ depends

on ϕ and Θ^* of the reconstructed proton. By error propagation $\sigma(\phi)$ equals

$$\sigma(\phi) = \frac{\sqrt{\sigma(\Theta_y^*)^2 \cos^2\phi + \sigma(\Theta_x^*)^2 \sin^2\phi}}{\Theta^*}. \tag{9.2}$$

Since $-t \approx p^2\,\Theta^{*2}$ and the four momentum transfer squared t is of higher interest than Θ^*, it is more convenient to plot $\sigma(\phi)$ as a function of t and ϕ, as can be seen in Figure 9.11. The ϕ resolution, as can be seen in Equation 9.2, improves with

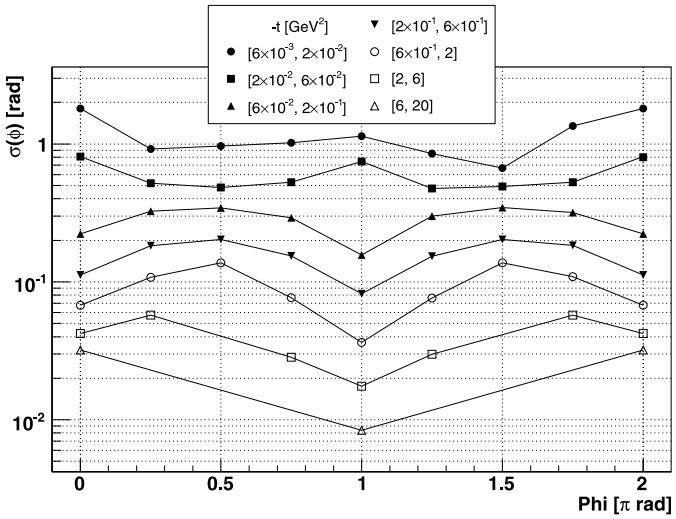

Figure 9.11: Reconstruction resolution in ϕ as a function of the four momentum transfer squared t and the azimuth angle ϕ, of a diffractive proton. Reconstruction is based only on the information from the RP station at 220 m at $\beta^* = 90$ m optics.

the increase in Θ^* which corresponds to higher $|t|$ values. For $\phi = 1/2\,\pi$, $3/2\,\pi$, the observed ϕ-resolution is generally worse compared to $\phi = 0$, π. This results from better resolution in Θ_y^* than in Θ_x^*.

RP147 and RP220 station

Further studies showed that including the information from the RP station at 147 m improves the performance only slightly and only for large $|t|$ due to large contributions to the uncertainty from multiple scattering in the detectors and window material of the RP station at 147 m, which were discussed in Section 7.5.2.

Figure 9.12 shows the ξ reconstruction resolution using the information from

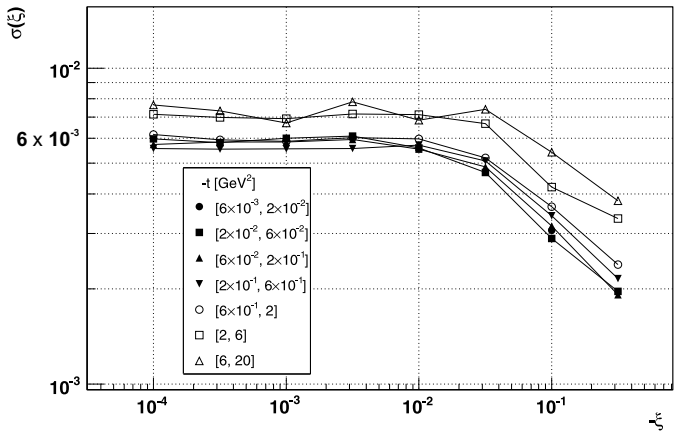

Figure 9.12: Resolution for the ξ-reconstruction of a diffractive proton based on the information from the RP stations at 147 m and 220 m at $\beta^* = 90$ m optics. The different markers correspond to the resolution at different t-ranges.

both RP147 and RP220 stations. An improvement in the reconstruction resolution is seen only for higher $|t|$ values ($-t > 2\,\mathrm{GeV}^2$), where $\sigma(\xi) \approx 7 \times 10^{-3} - 8 \times 10^{-3}$.

Also the error of Θ_x^*-reconstruction, presented in Figure 9.13, is lower: $\sigma(\Theta_x^*) \approx 1.3 \times 10^{-5}$. As a result, the horizontal component of the four momentum transfer squared t_x is reconstructed more precisely and can be expressed as $\sigma(t_x) \approx 0.18\sqrt{-t_x}$ for $-\xi < 0.1$.

TOTEM and CMS common reconstruction

The transverse coordinates of the proton at the IP (x^*, y^*, see Equation 6.26) are considered as additional free variables since their uncertainty contribute significantly to the reconstruction uncertainty, especially for the high-β^* optics characterised by large beam sizes at the IP. For $\beta^* = 90$ m the beam size at IP is 212 μm. However, the central CMS detector will be capable of measuring the primary vertex position to a precision of 30 μm. In order to improve the proton kinematics reconstruction performance, common TOTEM and CMS runs are planned.

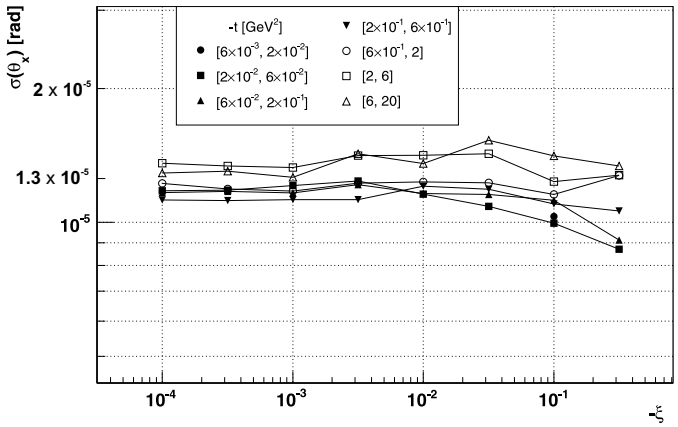

Figure 9.13: Resolution for the Θ_x^*-reconstruction of a diffractive proton based on the information from the RP stations at 147 m and 220 m at $\beta^* = 90$ m optics. The different markers correspond to the resolution at different t-ranges.

Proton reconstruction with RP220 and CMS primary vertex If the scattering vertex can be determined to a precision of 30 μm with the central CMS detector during common data taking, the ξ-resolution improves to about 1.6×10^{-3}, as can be seen in Figure 9.14.

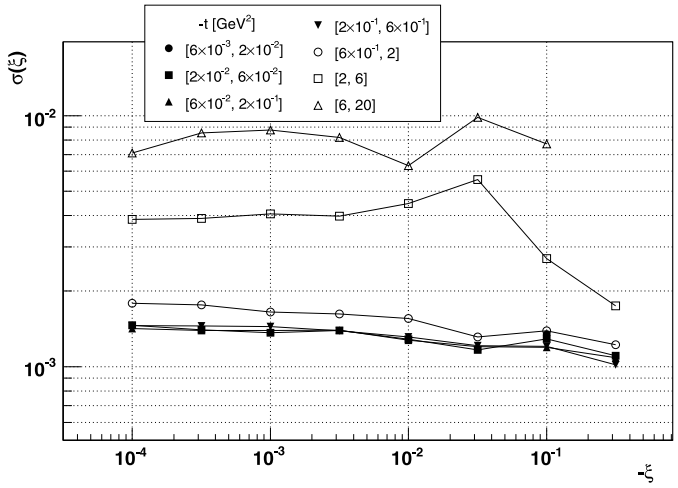

Figure 9.14: Resolution for the ξ-reconstruction of a diffractive proton based on the information from the RP station 220 m and the CMS central detector, at $\beta^* = 90$ m optics. The different markers correspond to the resolution at different t-ranges.

Also the scattering angle reconstruction resolution gets improved when the vertex position from CMS is included in the reconstruction procedures. Figure 9.15 shows the resolution of reconstruction in Θ_x^* variable. Now $\sigma(\Theta_x^*) \approx 10^{-5}$ every-

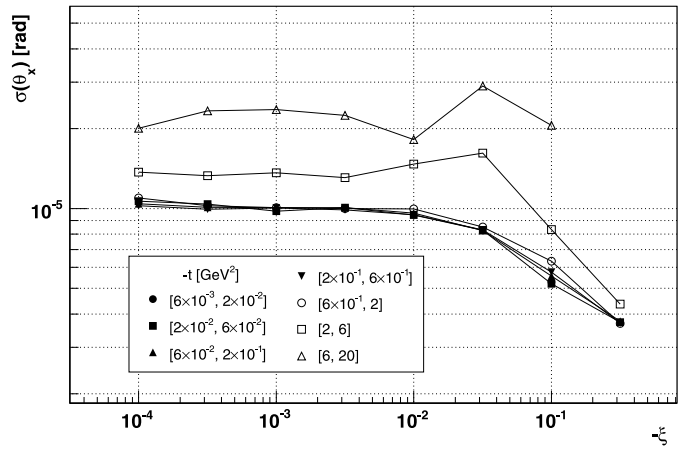

Figure 9.15: Resolution of the Θ_x^*-reconstruction of a diffractive proton based on the information from the RP station 220 m and the CMS central detector, at $\beta^* = 90$ m optics. The different markers correspond to the resolution at different t-ranges.

where except for $-t > 2\,\mathrm{GeV}^2$, where $\sigma(\Theta_x^*) \approx 1.5 \times 10^{-5} - 3 \times 10^{-5}\,\mathrm{GeV}^2$, and for $-\xi > 0.01$, where $\sigma(\Theta_x^*)$ is generally reduced.

The resolution of Θ_y^* (see Figure 9.16) is at its physics allowed minimum:

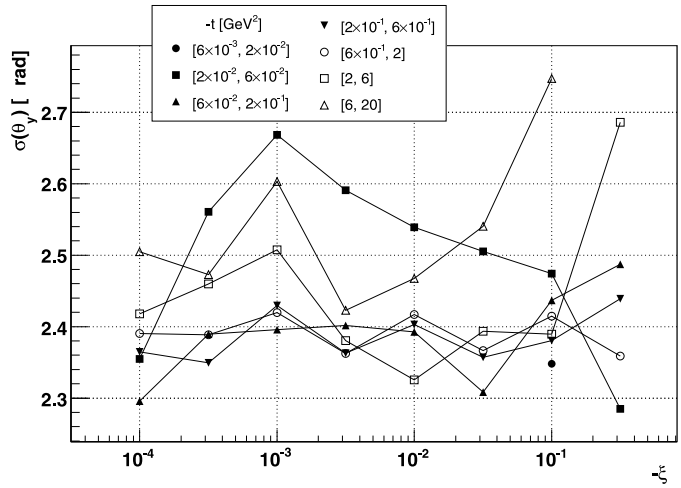

Figure 9.16: Resolution for the Θ_y^*-reconstruction of a diffractive proton based on the information from the RP station 220 m and the CMS central detector, at $\beta^* = 90$ m optics. The different markers correspond to the resolution at different t-ranges.

$\sigma(\Theta_y^*) = 2.4\,\mu$rad, which is the beam divergence limit.

Since t-reconstruction depends upon the estimation of Θ^*, an improvement in t-resolution is also observed. For $-t < 2\,\mathrm{GeV}^2$, $\sigma(t_x) \approx 0.14\sqrt{-t_x}$. The recon-

struction of the horizontal component of t is practically independent of ξ and t, and can be parameterised as $\sigma(t_y) \approx (0.03 - 0.04)\sqrt{-t_y}$.

According to the results presented Figures 9.17 and 9.18, t_x-reconstruction

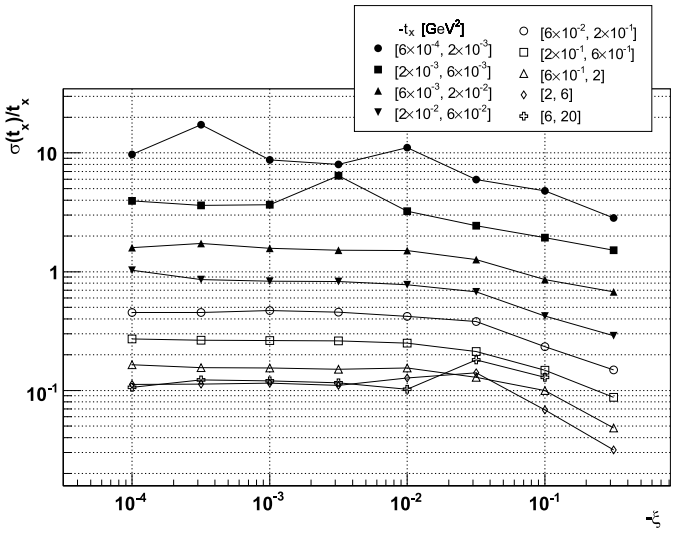

Figure 9.17: Relative resolution $\sigma(t_x)/t_x$ for the t_x-reconstruction of a diffractive proton based on the information from the RP station 220 m and the CMS central detector, at $\beta^* = 90$ m optics. The different markers correspond to the resolution at different t_x-ranges.

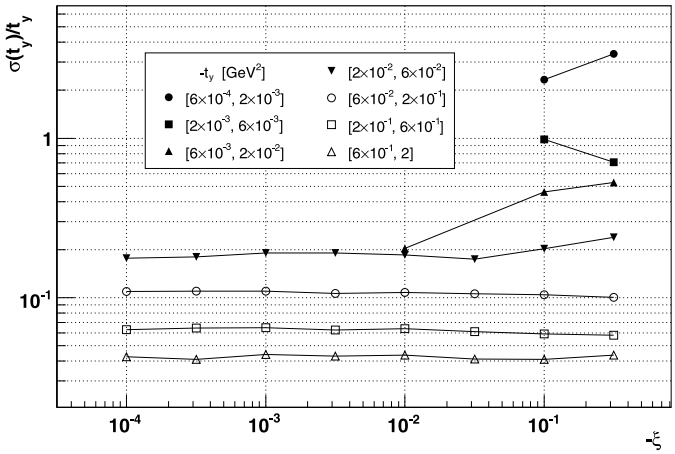

Figure 9.18: Relative resolution $\sigma(t_y)/t_y$ for the t_y-reconstruction of a diffractive proton based on the information from the RP station 220 m and the CMS central detector, at $\beta^* = 90$ m optics. The different markers correspond to the resolution at different t_y-ranges.

is possible for $-t_x \gtrsim 6 \times 10^{-2}\,\mathrm{GeV}^2$, while t_y can be well estimated for $-t_y \gtrsim 6 \times 10^{-3}\,\mathrm{GeV}^2$, when the condition $\sigma(t_{x,y})/t_{x,y} < 1/2$ is fulfilled.

Proton reconstruction with RP147, RP220 and CMS primary vertex
Proton kinematics reconstruction resolution was also estimated for the case when two Roman Pot stations located at 147 m and 220 m are used, together with the primary vertex information from CMS.

The ξ-resolution, presented in Figure 9.19, slightly deteriorated in comparison

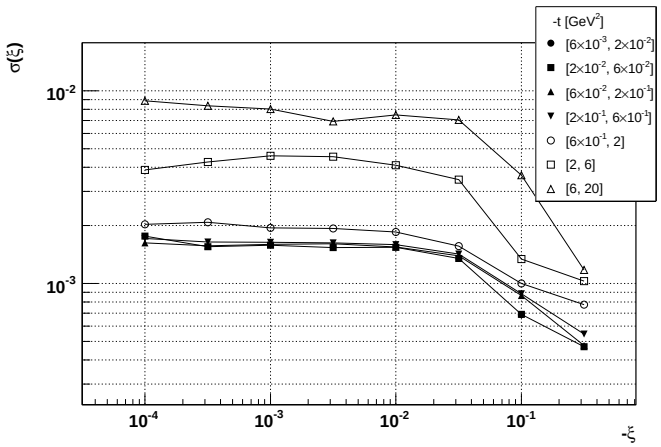

Figure 9.19: Resolution of the ξ-reconstruction of a diffractive proton based on the information from the RP stations at 147 m and 220 m, and the CMS central detector, at $\beta^* = 90$ m optics. The different markers correspond to the resolution at different t-ranges.

to the reconstruction based only on the RP220 station and the CMS primary vertex, which was shown in Figure 9.14. This is mainly the result of the multiple scattering in the RP147 station, which was discussed in detail in Section 7.5.2.

However, due to the presence of RP147 station in the reconstruction process, the resolution of the horizontal component of the longitudinal scattering angle is improved, which is visible in Figure 9.20. In the majority of cases ($-\xi < 0.1$ and $-t < 2\,\mathrm{GeV}^2$) $\sigma(\Theta_x^*) \approx 4$ – $5\,\mu$rad. Therefore, also the t_x-resolution is enhanced and can be now parameterised as $\sigma(t_x) = (0.06$ – $0.08)\sqrt{-t_x}$.

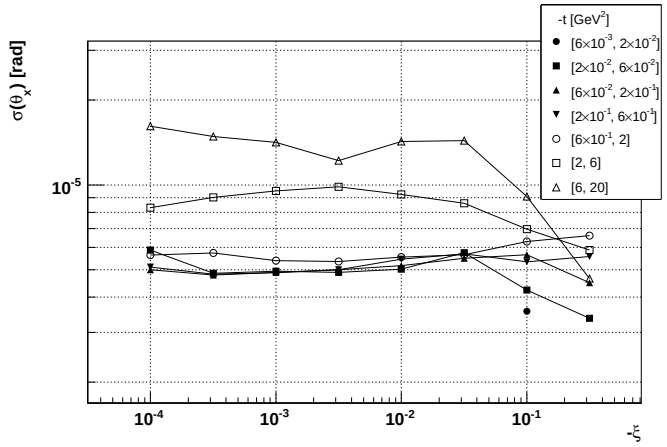

Figure 9.20: Resolution of the Θ_x^*-reconstruction of a diffractive proton based on the information from the RP stations at 147 m and 220 m, and the CMS central detector, at $\beta^* = 90$ m optics. The different markers correspond to the resolution at different t-ranges.

9.1.4 DPE mass reconstruction

DPE acceptance

One of the diffractive physics processes that can be studied with Roman Pot detectors is the Double Pomeron Exchange (DPE), which is presented in Figure 9.21. DPE is characterised by two surviving protons and a diffractive system with mass

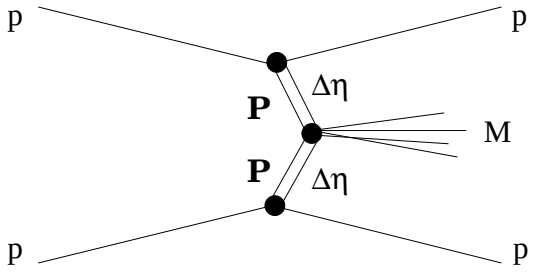

Figure 9.21: Diagram of the Double Pomeron Exchange (DPE).

M. The differential cross-section of Double Pomeron Exchange with respect to M is predicted to have the approximate functional form [93],

$$\frac{d\sigma}{dM} \propto \frac{1}{M^{1+\varepsilon}} \tag{9.3}$$

with $\varepsilon \sim 0.07$ and an integral of the order $\sim 1\,\text{mb}$. The DPE differential cross-section is shown in Figure 9.24. Using the relation

$$M^2 = \xi_1\,\xi_2\,s\,, \tag{9.4}$$

where $\sqrt{s} = 14\,\text{TeV}$, the distribution of diffractive masses M can be fully determined by measuring the momentum losses ξ_1 and ξ_2 of the two protons. The two protons originate from a common scattering vertex and are detected by the Roman Pots on the right and on the left side of the IP.

The distribution of kinematics of a right hand proton (in $\log_{10}(-\xi)$ and $\log_{10}(-t)$), generated by Phojet for the DPE process, is presented in Figure 9.22. The highest proton flux is observed within the t-range defined by $-1.7 < \log_{10}(-t) < 0$, which corresponds to $0.02 < -t < 1\,\text{GeV}^2$. This is also the range of highest proton acceptance by the RP220 station for the $\beta^* = 90\,\text{m}$ optics, which is illustrated by Figure 9.1. Consequently, the DPE acceptance, presented by Figure 9.23, is between 20 % and 35 % and covers the mass spectrum between 20 GeV and 3 TeV. The differential DPE cross-section, multiplied by the acceptance of the Roman

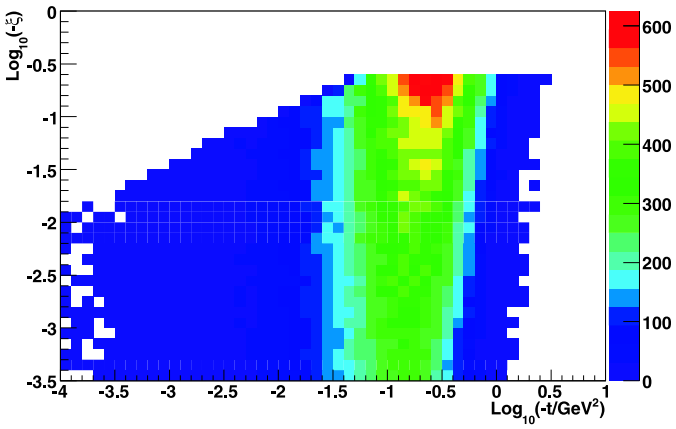

Figure 9.22: Distribution of proton kinematics of DPE events generated with Phojet [89]. The proton kinematics is expressed in $\log_{10}(-t)$ and $\log_{10}(-\xi)$.

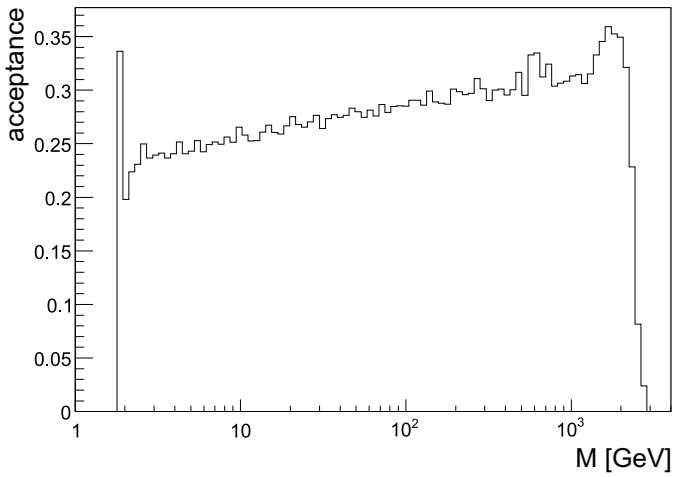

Figure 9.23: DPE mass acceptance in the RP220 stations at β^*=90 m. The data sample was generated with Phojet [89].

Pots located at 220 m, is illustrated by the red line in Figure 9.24.

DPE mass reconstruction resolution

Since the mass M alone is insufficient to describe the two-proton system (ξ_1, ξ_2), the ratio $R \equiv \xi_1/\xi_2$, characterising the momentum symmetry, is introduced as an additional variable.

By differentiation of Equation 9.4 we get:

$$2M\mathrm{d}M = \mathrm{d}\xi_1 s + \mathrm{d}\xi_2 s. \tag{9.5}$$

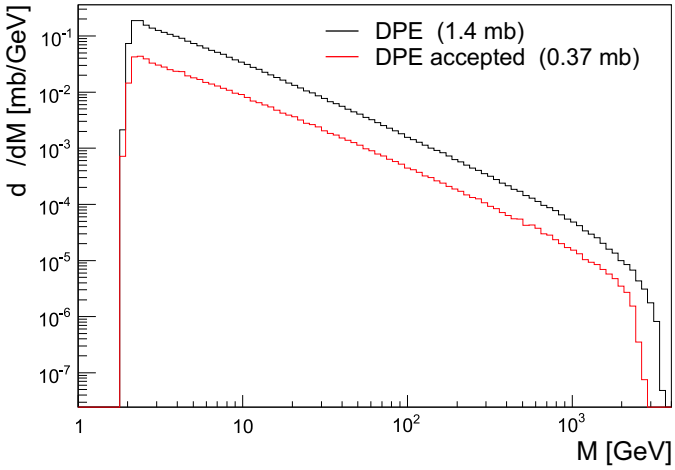

Figure 9.24: Black curve: Diffractive mass distribution for DPE events as predicted by Phojet [89]. Red curve: Distribution of DPE events accepted by left and right RP220 stations at β^*=90 m.

The distributions of measurement errors of ξ_1 and ξ_2 are assumed independent. By error propagation we get the mass reconstruction resolution:

$$\frac{\sigma(M)}{M} = \frac{\sqrt{\left(\frac{\sigma(\xi_1)}{\xi_1}\right)^2 + \left(\frac{\sigma(\xi_2)}{\xi_2}\right)^2}}{2}, \tag{9.6}$$

$$\sigma(M) = \frac{\sqrt{\frac{\sigma(\xi_1)^2\xi_2 s}{\xi_1} + \frac{\sigma(\xi_2)^2\xi_1 s}{\xi_2}}}{2} = \frac{\sqrt{s}}{2}\sqrt{\sigma(\xi_1)^2 R^{-1} + \sigma(\xi_2)^2 R}. \tag{9.7}$$

Since $\sigma(\xi_1)$ and $\sigma(\xi_2)$ are nearly ξ-independent and are mostly determined by the reconstruction scenario (see Section 9.1.3), the mass reconstruction resolution $\sigma(M)$ will strongly depend upon the momentum loss ratio R of the detected protons.

In the following paragraphs, for simplicity, it will be assumed that $|\xi_1| < |\xi_2|$ and that $R \equiv \frac{\xi_1}{\xi_2} = \frac{\xi_{\rm lo}}{\xi_{\rm hi}} \leq 1$, where $\xi_{\rm lo}$ corresponds to the lower and $\xi_{\rm hi}$ — to the higher proton momentum loss.

DPE mass reconstruction with RP220 station

The resolution in the diffractive mass, reconstructed with the information from the Roman Pots located at 220 m on both sides of IP5, is shown in Figure 9.25. The mass resolution ranges from 35 GeV for symmetric events, i.e. those with $\xi_1 \approx \xi_2$, to 190 GeV for the very asymmetric events, where one of the ξ values is three to

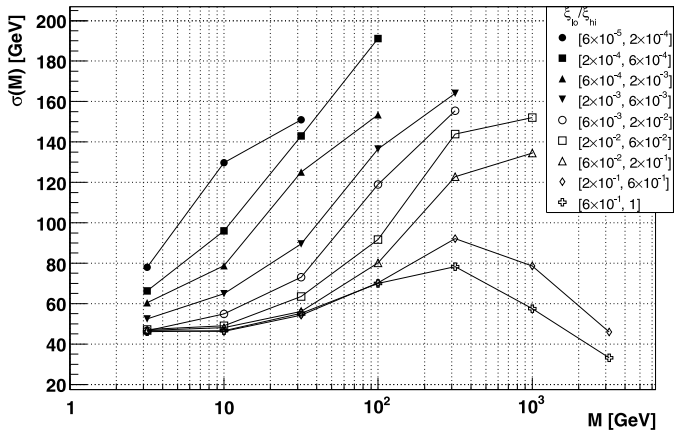

Figure 9.25: DPE mass reconstruction resolution computed for the protons detected with left and right RP220 stations for $\beta^* = 90\,\mathrm{m}$. The markers correspond to different $R = \frac{\xi_{\mathrm{lo}}}{\xi_{\mathrm{hi}}}$ ranges.

four orders of magnitude larger than the other one.

Figure 9.26 presents the relative mass reconstruction resolution $\sigma(M)/M$ for

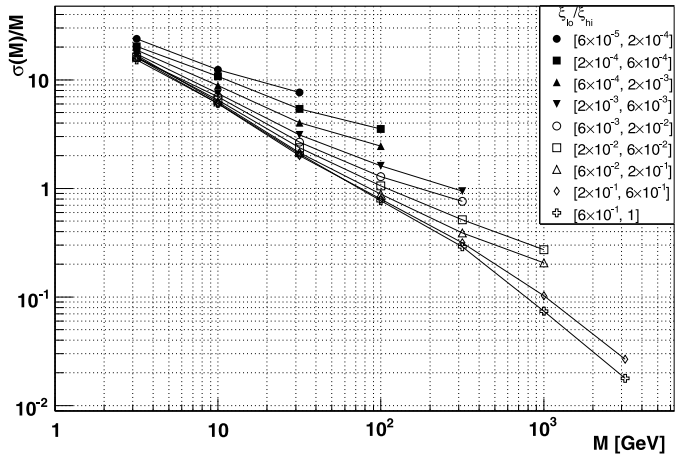

Figure 9.26: Relative error of the DPE mass reconstruction computed for the protons detected with left and right RP220 stations for $\beta^* = 90\,\mathrm{m}$. The markers correspond to different $R = \frac{\xi_{\mathrm{lo}}}{\xi_{\mathrm{hi}}}$ ranges.

the same reconstruction scenario. From the figure we can deduce for which mass ranges a valuable physics reconstruction is possible, when $\sigma(M)/M < 1/2$. For symmetric cases ($R \approx 1$), $\sigma(M)/M$ is lower than $1/2$ for $M \gtrsim 150\,\mathrm{GeV}$, while for $M \gtrsim 400\,\mathrm{GeV}$, $\sigma(M)/M < 1/2$ for all accepted momentum loss ratios R.

DPE mass reconstruction with RP147 and RP220 station

The Monte Carlo resolution studies of DPE mass reconstruction were also performed for the situation when two Roman Pot stations (at 147 m and at 220 m), on each side of the IP5, were used. The results are presented in Figure 9.27. The

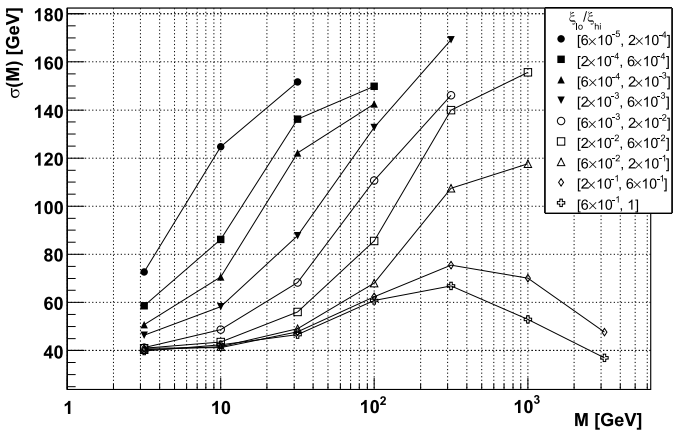

Figure 9.27: DPE mass reconstruction resolution computed for the protons detected with left and right RP147 and RP220 stations for $\beta^* = 90$ m. The markers correspond to different $R = \frac{\xi_{\rm lo}}{\xi_{\rm hi}}$ ranges.

mass reconstruction resolution is slightly improved compared to the reconstruction with RP220 stations only. For example, for the symmetric case ($R \approx 1$), the mass reconstruction error is now between 35 and 65 GeV.

TOTEM and CMS common reconstruction

If the scattering vertex can be determined to a precision of 30 μm with the central CMS detector during common TOTEM–CMS runs, the mass resolution improves by approximatively a factor of three [5]. In this case, the mass resolution $\sigma(M)$ ranges from 12 GeV, for the symmetric case, to 85 GeV, for highly asymmetric one, as can be seen if Figure 9.28.

The relative error distribution of mass reconstruction, which is presented in Figure 9.29, shows that for the symmetric case ($\xi_{\rm lo} \approx \xi_{\rm hi}$), the relative mass reconstruction error is lower than 1/2 for masses higher that $\sim$40 GeV. The valuable physics reconstruction of mass for all accepted $\xi_{\rm lo}/\xi_{\rm hi}$ ratios is possible for $M \gtrsim 300$ GeV.

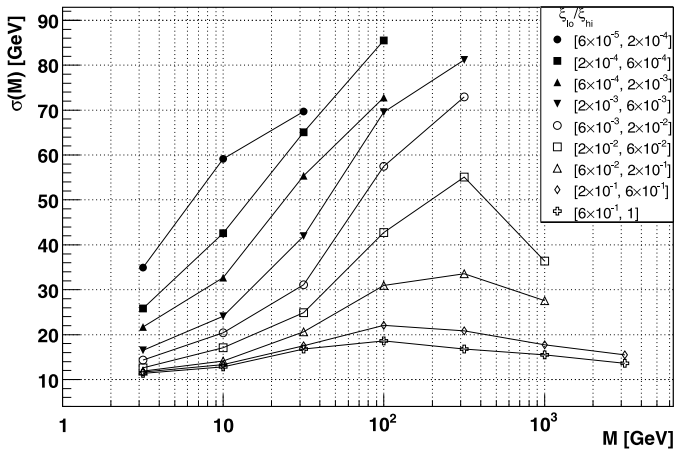

Figure 9.28: DPE mass reconstruction resolution computed for protons detected with left and right RP220 stations with primary vertex position from CMS, for $\beta^* = 90\,\mathrm{m}$. The markers correspond to different $R = \frac{\xi_{\mathrm{lo}}}{\xi_{\mathrm{hi}}}$ ranges.

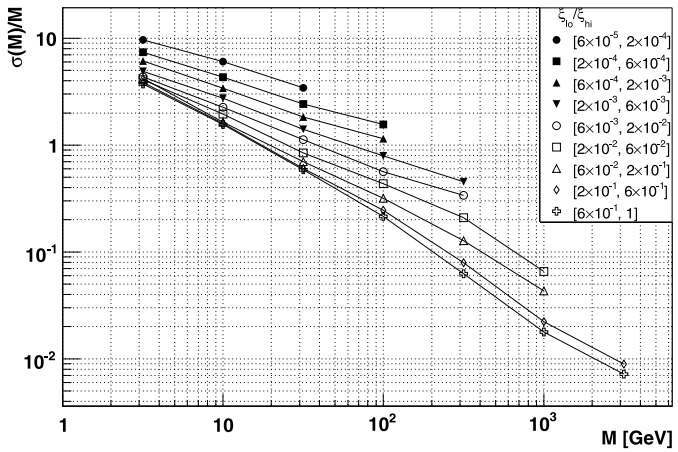

Figure 9.29: Relative reconstruction error of DPE mass reconstruction. The reconstruction was performed for protons detected with left and right RP220 stations with primary vertex position from CMS, for $\beta^* = 90\,\mathrm{m}$. The markers correspond to different $R = \frac{\xi_{\mathrm{lo}}}{\xi_{\mathrm{hi}}}$ ranges.

9.2 IR3 RP insertion study for β^*=0.55 m

9.2.1 Introduction

The IR3 region houses the momentum cleaning insertion (see Section 6.1.3). Its optics have been optimised to absorb the protons with relative momentum deviations $\xi = \Delta p/p$ exceeding $\pm 1 \cdot 10^{-3}$. The idea discussed in this section is to detect diffractive protons in both beams in IR3 just before they are absorbed by the momentum cleaning collimators. The technical aspects of the proposed RP insertions are presented in [108].

This would highly extend the diffractive mass acceptance of the TOTEM experiment. In case of the Double Pomeron Exchange process, the continuous mass acceptance from 25 GeV to 2.8 TeV would be accessible, allowing for promissing diffractive physics programme. In addition, within certain ξ range, the diffractive protons from all LHC interaction points are detected, thus making the on-line inter-experimental luminosity calibrations possible.

As has been discussed in Section 6.2, the transverse displacement $(x(s), y(s))$ of a diffractively scattered proton at a distance s downstream of the interaction point is a function of its transverse origin (x^*, y^*), its horizontal and vertical scattering angles Θ_x^* and Θ_y^* and the fractional momentum loss ξ at the IP:

$$\begin{aligned} x(s) &= v_x(s) \cdot x^* + L_x(s) \cdot \Theta_x^* + \xi \cdot D_x(s) \\ y(s) &= v_y(s) \cdot y^* + L_y(s) \cdot \Theta_y^* + \xi \cdot D_y(s)\,. \end{aligned} \tag{9.8}$$

$L_{x,y}$ and $v_{x,y}$ are the optical functions and $D(s)$ is the dispersion of the machine.

The momentum measurement down to low values of ξ with good resolution requires high dispersion D_x or D_y values compared to the other coefficients of Equations 9.8. Since at LHC the dispersion is predominantly horizontal, we shall concentrate on the x-projection.

The diffractive proton acceptance of detectors near the beam is determined by the ratio D_x/σ_x between the dispersion and the beam size. With larger D_x the protons are deflected further away from the beam centre. The closest safe approach of a detector to the beam is given by a certain multiple — typically 10 to 15 — of σ_x.

By construction, the region in the LHC where the dispersion and the ratio D_x/σ_x are maximised, is the momentum cleaning insertion in IR3, discussed in Section 6.1.3, where off-momentum beam protons are intercepted. The location of

the IR3 region is presented in Figure 9.30.

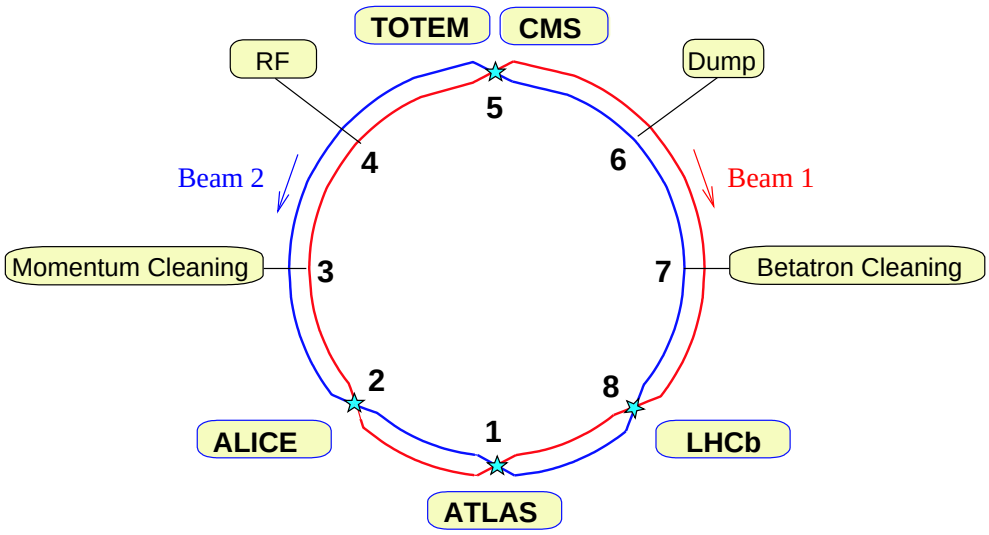

Figure 9.30: Schematic drawing of the LHC with its eight "interaction" points and the momentum cleaning insertion.

Figure 9.31 shows the dispersion and beam width in the IR3 region for both beams and both transverse projections, x and y. The horizontal dispersion D_x at the two potential tracking detector positions, TP1 and TP2, has a magnitude in the range of 2–3 m, as compared to 8 cm at the TOTEM Roman Pot station RP220. Due to high value of the dispersion in IR3 an excellent momentum resolution is available (Section 9.2.3).

The high ratio $D_x/\sigma_x \approx 6.7 \times 10^3$ (as compared to $\approx 1.1 \times 10^3$ at RP220) results in an acceptance down to $\xi = 1.6 \times 10^{-3}$, as illustrated by the hit distribution in Figure 9.32 and discussed quantitatively in Section 9.2.2.

In addition to promising perspectives for diffractive physics, the placement of detectors in front of the momentum cleaning collimators has advantages for machine diagnostics and protection. It enables the study of beam losses at the collimators. Also all showers possibly created by the detector insertion are absorbed immediately downstream by the collimators.

9.2.2 Proton acceptance in IR3 and RP220

The proton acceptance of an experiment, with detectors at the standard TOTEM locations ±220 m from IP5 (RP220) and at ±206 m from IP3, has been studied. The full simulation of protons tracked along the LHC ring was carried out with

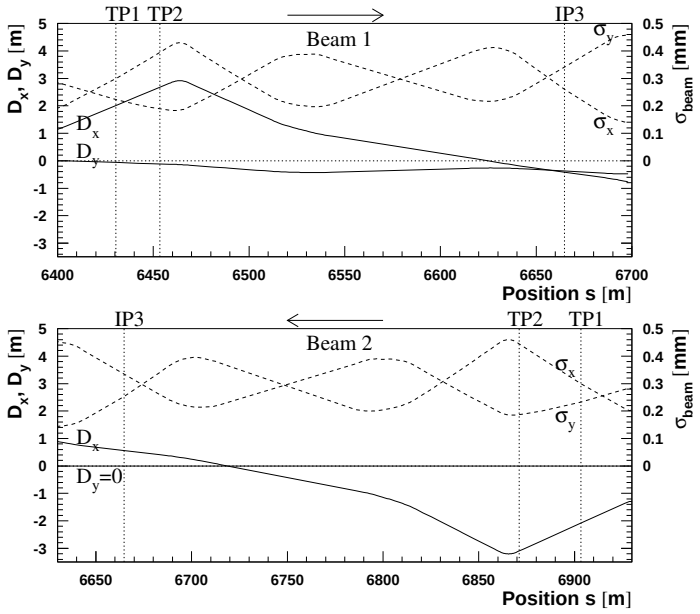

Figure 9.31: Dispersion (left-hand axes) and beam width (right-hand axes) in x and y for both beams in the IR3 region. The dispersion shown is valid for protons with $\xi = 0$ and produced in IP5. The position axis s follows beam 1 and has its origin in IP1. TP1 and TP2 are the two proposed tracking detector planes.

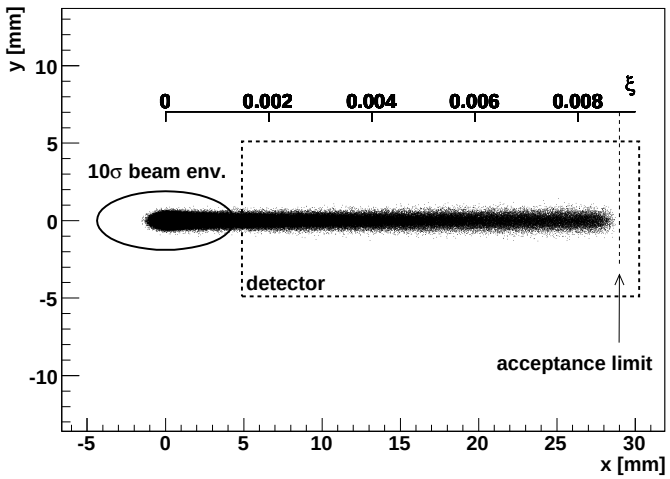

Figure 9.32: Hit distribution in a plane transverse to beam 2 at 206 m from IR3 for DPE events in IP5.

MAD-X [37] as a part of TOTEM optics software described in Section 6.4. The resulting acceptances for both beams are shown in Figure 9.33. The protons are characterised by ξ, integrating over all their other kinematic parametres. The IR3 acceptance for beam 1 protons originating from diffractive scattering in IP5 is reduced since these protons have to pass through the aperture limiting betatron cleaning insertion IR7, described in Section 6.1.3. Beam 2 protons on the other hand have an almost continuous acceptance from $\xi = 1.6 \times 10^{-3}$ to 0.19 (50% acceptance limits) with only a gap between 0.01 and 0.018. This momentum acceptance gives access to diffractive masses ranging from 25 GeV to 2.8 TeV in the case of Double Pomeron Exchange events (Section 9.2.4).

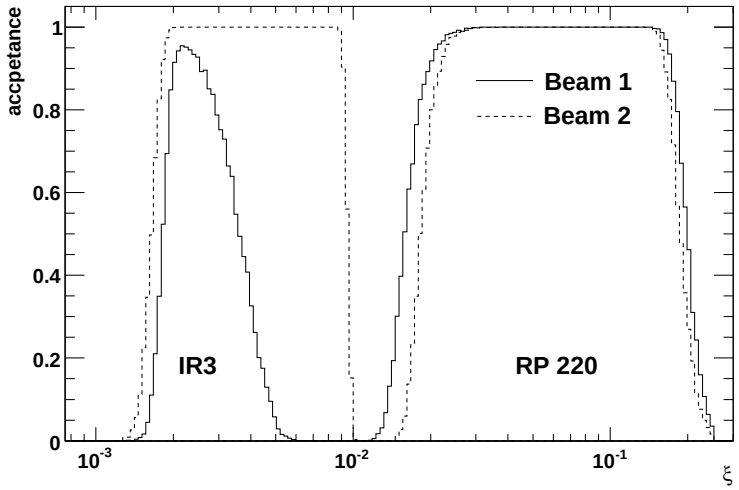

Figure 9.33: Acceptance in ξ at the Roman Pots RP220 and in IR3 for both LHC beams.

9.2.3 Reconstruction of proton momentum in IR3

In order to determine the best possible momentum measurement resolution and the required detector spatial resolution, let us consider the detection, in IR3, of the diffractive proton, originating from IP5. The system of near-beam telescopes in the IR3 region can measure the transverse displacement (x, y) and the scattering angle (Θ_x, Θ_y). Since the value of dispersion, which is of highest importance for fractional momentum loss $\xi = \frac{\Delta p}{p}$ measurement of the scattered proton, is an order of magnitude higher in the horizontal coordinate than in the vertical one, we can limit the resolution analysis to the two-dimensional (x, Θ_x) phase space.

The proton transport equation in x-coordinate is given by:

$$\vec{Y}(s) = \vec{D}(s)\,\xi + \vec{L}(s,\xi)\,\Theta_x^* + \vec{V}(s,\xi)\,x^*, \tag{9.9}$$

$$\vec{Y}(s) = \begin{pmatrix} x \\ \Theta_x \end{pmatrix}, \quad \vec{D}(s) = \begin{pmatrix} D_x(s) \\ D_x'(s) \end{pmatrix},$$

$$\vec{L}(s,\xi) = \begin{pmatrix} L_x(s,\xi) \\ L_x'(s,\xi) \end{pmatrix}, \quad \vec{V}(s,\xi) = \begin{pmatrix} V_x(s,\xi) \\ V_x'(s,\xi) \end{pmatrix},$$

where s is a distance from the interaction point along the accelerator, $\vec{Y}(s)$ is a vector of proton coordinates in IR3, $\vec{D}(s)$ is a dispersion vector, $\vec{L}(s,\xi)$ is the effective length vector and $\vec{V}(s,\xi)$ is the magnification vector.

The precision of proton kinematics reconstruction based on the local track measurements in the IP3 region, can be visually summarised by the distribution of scattered protons in the horizontal phase space $(x, x' = \Theta_x)$ at the detector position considered. Figure 9.34 gives such distributions for discrete values of ξ and typical ranges of the other kinematic variables (the vertex position x^* and the scattering angle Θ_x^* in IP5).

The phase space vector $\vec{V}x^*$ that represents the contribution from the transverse vertex position is approximately parallel to the dispersion contribution $\vec{D}\xi$ to be measured, whereas the component $\vec{L}\Theta^*$ of the beam divergence and the scattering angle is approximately orthogonal to $\vec{D}\xi$. This implies that the resolution of the momentum loss reconstruction is mostly limited by the vertex spread at IP5. The usual problem of disentangling the contributions from ξ and t is therefore not present for measurements in IP5. The big distances between the parallelograms belonging to different ξ-values illustrate the excellent momentum resolution which will be quantified below.

As a result of the LHC chromaticity, the shape of the parallelograms slightly changes for different ξ values.

The large angular spread of the beam in IP5, $\sigma(\Theta_{beam}^*) = 30\,\mu$rad, limits the reconstruction of t to momentum-transfers $|t| > 0.1\,\mathrm{GeV}^2$.

The position of vector $\vec{Y}$ in the phase space depends mostly upon the $\vec{D}\xi$ component. Let us then introduce the $(\vec{u}, \vec{v})$ coordinate system associated with the direction of $\vec{D}$ in the phase space: $\vec{u} = \frac{\vec{D}}{|D|}$, $\vec{v} \perp \vec{u}$. In the new coordinate

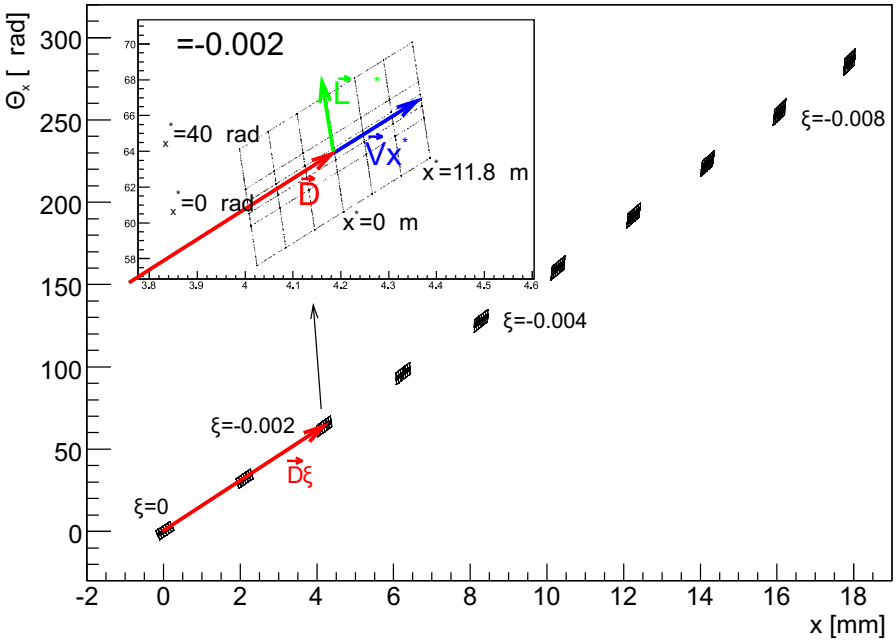

Figure 9.34: The phase space of proton tracks at 206 m upstream of IR3 for LHC beam 2, for $\xi = 0, -1 \cdot 10^{-3}, \ldots, -8 \cdot 10^{-3}$. Each parallelogram corresponds to a given ξ value and represents the phase-space area defined by the spatial vertex distribution ($\sigma(x^*) = 11.8\,\mu$m) and the total angular spread of the scattered protons in IP5, $\sigma(\Theta^*_{tot}) = 40\,\mu$rad. The latter has contributions from the angular spread of the beam, $\sigma(\Theta^*_{beam}) = 30\,\mu$rad, and from the scattering angle, $\sigma(\Theta^*_t) = \sigma(\sqrt{|t|}/p) = 25\,\mu$rad (assuming a diffractive t-distribution $\propto e^{-7\,\mathrm{GeV}^{-2}\,|t|}$).

system, the components of Equation 9.9 read:

$$\begin{aligned} \vec{Y} &= Y_u\vec{u} + Y_v\vec{v}, \\ \vec{L} &= L_u\vec{u} + L_v\vec{v}, \\ \vec{V} &= V_u\vec{u} + V_v\vec{v}. \end{aligned} \tag{9.10}$$

Equation 9.9 can be then rewritten as:

$$\begin{aligned} Y_u\vec{u} + Y_v\vec{v} - (V_u\vec{u} + V_v\vec{v})x^* &= |D|\xi\vec{u} + L_u\Theta^*_x\vec{u} + L_v\Theta^*_x\vec{v}, \\ (Y_u - V_ux^*)\vec{u} + (Y_v - V_vx^*)\vec{v} &= (|D|\xi + L_u\Theta^*_x)\vec{u} + L_v\Theta^*_x\vec{v}, \end{aligned} \tag{9.11}$$

and solved with respect to Θ^*_x and ξ:

$$\Theta^*_x = \frac{Y_v - V_vx^*}{L_v}, \tag{9.12}$$

$$\xi = \left(\frac{\vec{u}}{|D|} - \frac{L_u\vec{v}}{|D|L_v}\right)\vec{Y} + \left(\frac{L_uV_v}{|D|L_v} - \frac{V_u}{|D|}\right)x^*. \tag{9.13}$$

The reconstruction of ξ depends then not only upon the position x and the angle Θ_x, measured by the detectors installed in IR3, but also upon the unknown primary vertex position. By introducing two coefficients

$$\vec{A} = \frac{\vec{u}}{|D|} - \frac{L_u\vec{v}}{|D|L_v}, \tag{9.14}$$

$$B = \frac{L_uV_v}{|D|L_v} - \frac{V_u}{|D|}, \tag{9.15}$$

we can write

$$\xi = A_1x + A_2\Theta_x + Bx^*. \tag{9.16}$$

The error propagation yields the ξ-reconstruction resolution

$$\sigma(\xi) = \sqrt{(|A_1|\sigma(x))^2 + (|A_2|\sigma(\Theta_x))^2 + (|B|\sigma(x^*))^2}, \tag{9.17}$$

where $\sigma(x)$ is the spatial resolution of detectors in IR3, $\sigma(\Theta_x)$ is the angular resolution and $\sigma(x^*)$ is the horizontal beam size in IP5. As has been already seen in Figure 9.34, in reality, because of the accelerator chromaticity, the coefficients of Equation 9.9 change with ξ, as well as the values of $|A_1|$, $|A_2|$ and $|B|$. Table 9.1 gives the ranges of values of parameters $\vec{A}$ and B for both LHC beams for detectors installed in IR3, corresponding to the accepted ξ-values.

Beam	Parameter	Range within ξ-acceptance
Beam 1	$\|A_1\|$ $[m^{-1}]$	$[0, 0.13]$
	$\|A_2\|$	$[31, 62]$
	$\|B\|$ $[m^{-1}]$	$[6.7, 7.8]$
Beam 2	$\|A_1\|$ $[m^{-1}]$	$[0.37, 0.53]$
	$\|A_2\|$	$[0, 2.7]$
	$\|B\|$ $[m^{-1}]$	$[4.6, 6.3]$

Table 9.1: The ranges of coefficients of Equation 9.17 within the momentum acceptance.

Coefficient $|B|$ determines the optimum resolution of ξ-reconstruction for perfect detectors and without the beam momentum spread. If we assume the infinite precision of spatial and angular reconstruction ($\sigma(x) = 0$, $\sigma(\Theta_x) = 0$) and take the nominal IP5 beam size for $\beta^* = 0.55\,\text{m}$ of $\sigma(x^*) = 11.2\,\mu\text{m}$, we obtain the optimal

ξ-reconstruction resolution ranges as given in Table 9.2.

Beam	Optimal resolution $\sigma(\xi)$ range within ξ-acceptance
Beam 1	$[7.9 \cdot 10^{-5}, 9.2 \cdot 10^{-5}]$
Beam 2	$[5.8 \cdot 10^{-5}, 7.5 \cdot 10^{-5}]$

Table 9.2: The optimal resolution of momentum loss reconstruction with infinitely precisely measured proton tracks in IR3. The optimal momentum loss resolution is better than the nominal LHC momentum spread of $\sigma(p)/p \approx 10^{-4}$ which is in fact the limitting factor for diffractive mass reconstruction.

Equation 9.17 also determines the needed spatial and angular precision of the proton track measurement with the near-beam telescopes in IR3. To obtain the best achievable resolution, the $\sigma(\xi)$ value has to be minimised. Hence, the contributions from the errors of the angle and the position measurement should be smaller than the beam size component: $|A_1|\,\sigma(x) < |B|\,\sigma(x^*)$, $|A_2|\,\sigma(\Theta_x) < |B|\,\sigma(x^*)$. Table 9.3 gives the required spatial and angular resolutions.

Beam	Coordinate	Required measurement resolution
Beam 1	x [mm]	$[0.75, 0.96]$
	Θ_x [μrad]	$[1.6, 3.1]$
Beam 2	x [mm]	$[0.19, 0.27]$
	Θ_x [μrad]	$[14, 190]$

Table 9.3: Spatial and angular proton track reconstruction resolution required to optimise ξ-reconstruction in IR3.

The angular resolution given in Table 9.3 determines then the lever arms of the telescopes in IR3. Assuming the usage of the edgeless silicon detectors of spatial resolution of 20μm, the telescope length should be longer than 20 m for beam 1 and longer than 2 m for beam 2.

A detailed reconstruction study, for the detector locations as in Figure 9.31, based on simulated diffractive protons tracked along the LHC ring, led to the ξ-resolution shown in Figure 9.35. Note that the resolutions $\sigma(\xi) \sim 10^{-4}$ achieved for measurements in IR3 reach the limit imposed by the energy uncertainty of the LHC. In all cases, the relative resolution $\sigma(\xi)/\xi$ is better than 10%.

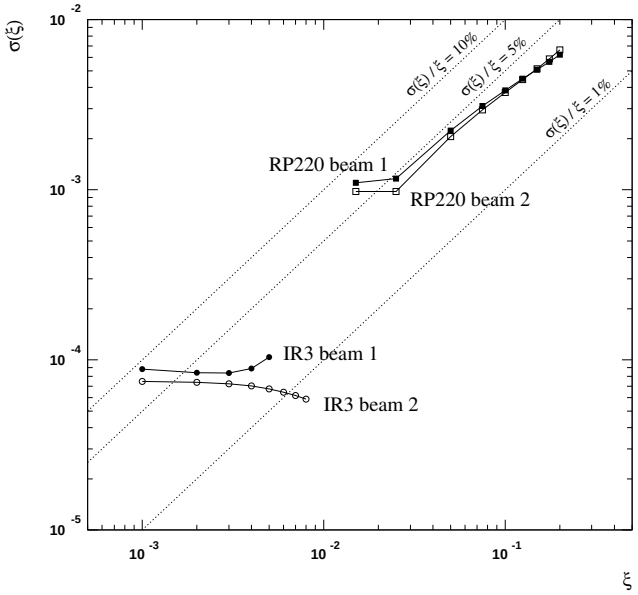

Figure 9.35: Resolution in the reconstructed ξ at the Roman Pots RP220 and 206 m upstream of IP3 for both LHC beams.

9.2.4 Physics

DPE mass spectrum

A promising diffractive process to be studied with proton detectors at RP220 and in IR3 is the Double Pomeron Exchange (DPE), characterised by two surviving protons and a diffractive system with mass M, as we saw before in Section 9.1.4. An important experimental advantage is the two-proton coincidence in the trigger which reduces backgrounds from Single Diffraction, beam-gas scattering and beam halo protons.

Figure 9.36 illustrates that the mass spectrum from ∼25 GeV to ∼3 TeV will be covered by the combination of four distinct trigger signatures:

- Low masses (25 GeV $< M <$ 100 GeV) have both surviving protons (1 per LHC beam) within the acceptance of the IR3 detectors.
- Intermediate masses (60 GeV $< M <$ 600 GeV) are identified by a beam 1 proton in RP220 and a beam 2 proton in IR3 or vice versa.
- High masses (200 GeV $< M <$ 3 TeV) have both protons in the RP220 detectors.

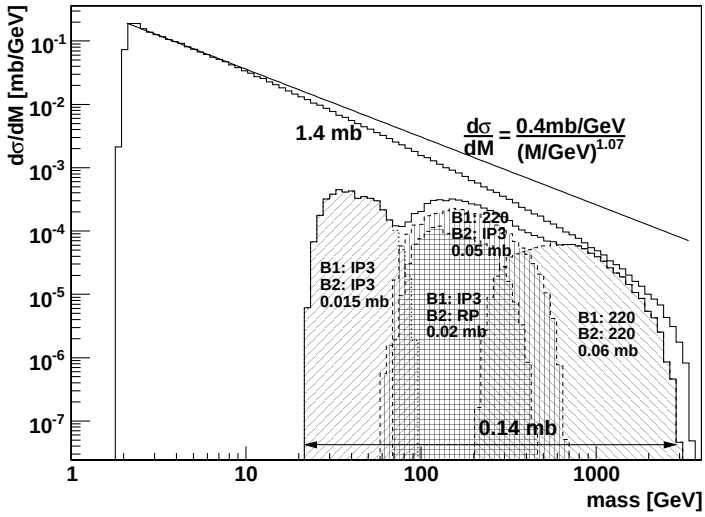

Figure 9.36: Diffractive mass distribution for DPE events as predicted by Pho-jet [89]. The lower curves take into account the acceptance of the proton detectors at RP220 and IR3.

Based on the single-proton acceptances and ξ-resolutions discussed in Sections 9.2.2 and 9.2.3, the mass resolutions for each of the four trigger signatures were calculated. As was already discussed in Section 9.1.4, the mass resolution depends upon the ratio $R \equiv \xi_1/\xi_2$ characterising the momentum symmetry. Again the mass resolution is given by the formula:

$$\sigma(M) = \frac{\sqrt{s}}{2}\sqrt{\sigma(\xi_1)^2 R^{-1} + \sigma(\xi_2)^2 R}. \tag{9.18}$$

In Figure 9.37 are presented the mass acceptance (left) and the relative mass reconstruction resolution $\sigma(M)/M$ (right), as functions of the mass M and of the symmetry ratio R. The four rectangle-like areas visible in the plots correspond to the four trigger scenarios described in Figure 9.36. Relative mas reconstruction resolution typically ranges between 1% and 5%.

Luminosity calibration

So far, we have considered only the detection of protons originating from IP5. It turns out, that the detection in IR3 of both surviving protons from DPE events taking place in all the others LHC interaction points, is also possible. The ξ-acceptances of such protons are very similar to those shown in Figure 9.33. The interaction points can be identified by the difference of the arrival time of protons,

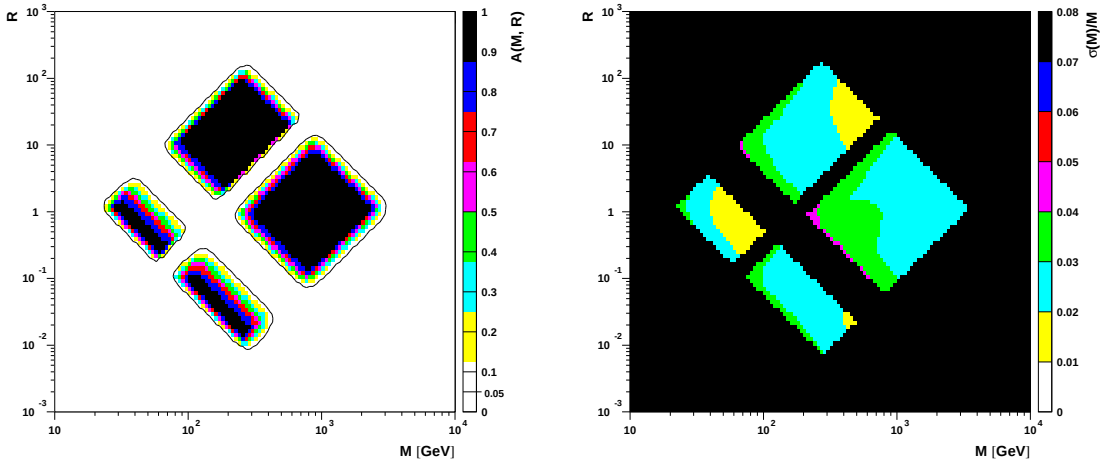

Figure 9.37: Mass acceptance (left) and relative mass reconstruction resolution $\sigma(M)/M$ (right), as functions of the mass M and of the symmetry ratio $R = \xi_1/\xi_2$.

which is given in Table 9.2.4.

Interaction Point	IP5 TOTEM + CMS	IP8 LHCb	IP1 ATLAS	IP2 ALICE
Δt (beam 2 - beam 1)	$-44\,\mu$s	$+22\,\mu$s	$+44\,\mu$s	$+66\,\mu$s

Table 9.4: Differences in the arrival times in IR3 between the two protons from DPE events in the different LHC interaction points.

In this way, the IR3 insertion can determine the low mass DPE spectra for all the experiments independently. Since the number of recorded events is proportional to the luminosity in the given interaction point, the DPE mass distributions can be then used as a means of interexperimental luminosity calibration.

9.3 Diffractive proton reconstruction summary

The acceptance and resolution studies of diffractive proton reconstruction with the Roman Pot devices, performed for the key TOTEM running scenarios, are summarised in Tables 9.5–9.8.

In case of the low-β^* optics (Tables 9.5 and 9.6), which are characterised by short effective length (see Table 6.1), the protons are primarily accepted in the Roman Pots due to their fractional momentum loss ξ, independently from t. Because of the machine dispersion, they are shifted towards the horizontal Roman

β^* [m]	variable	acceptance	resolution
0.5	$\xi = \Delta p/p$	RP220: $0.02 < -\xi < 0.25$	$\sigma(\xi) \approx (1 - 6) \times 10^{-3}$
		IR3: $0.0015 < -\xi < 0.01$	$\sigma(\xi) \approx 10^{-4}$
	DPE M [GeV]	RP220: $250 < M < 3000$	$\sigma(M)/M = 1 - 5\,\%$
		RP220 + IR3: $25 < M < 3000$	
	t [GeV^2]	RP220, inel. coll.: complete t-range for $-\xi > 0.02$	$\sigma(t) \approx 0.45\sqrt{t}$
		RP220, elastic scatt.: $6 < -t_y <$ tens of GeV^2	
	ϕ [rad]	$0 \leq \phi < 2\pi$	$0.2 < \sigma(\phi) < 0.5$ for $1 > -t > 0.18$ GeV^2

Table 9.5: Roman Pot acceptance and reconstruction summary for β^*=0.5 m optics.

β^* [m]	variable	acceptance	resolution
2	$\xi = \Delta p/p$	RP220: $0.02 < -\xi < 0.25$	$\sigma(\xi) \approx (1 - 6) \times 10^{-3}$
	DPE M [GeV]	RP220: $250 < M < 3000$	$\sigma(M)/M = 1 - 5\%$
	t [GeV^2]	RP220, inel. coll.: complete t-range for $-\xi > 0.02$	$\sigma(t) \approx 0.3\sqrt{t}$
		RP220, elastic scatt.: $2 < -t_y <$ tens of GeV^2	
	ϕ [rad]	$0 \leq \phi < 2\pi$	$0.15 < \sigma(\phi) < 0.5$ for $1 > -t > 0.05$ GeV^2

Table 9.6: Roman Pot acceptance and reconstruction summary for β^*=2 m optics.

Pot. In this way all the t-range is accepted.

On the contrary, in case of high-β^* optics (Tables 9.7 and 9.8), the protons are detected because of their four momentum transfer squared t, since the effective lengths are high (except L_x for $\beta^* = 90$ m). This results in full ξ-range acceptance.

The high-β^* optics, due to high effective lengths and low beam angular divergence, are characterised by good t- and ϕ-reconstruction capabilities and by acceptance of low $|t|$ values. The resolution in t changes depending upon the pro-

β^* [m]	variable	acceptance	resolution
90	$\xi = \Delta p/p$	RP220: complete ξ-range	$\sigma(\xi) \approx 0.006$ for $-t < 1$ GeV^2; $0.06 < \sigma(\xi) < 0.015$ for $-t > 1$ GeV^2
		RP220 + CMS primary vertex: complete ξ-range	$\sigma(\xi) \approx 0.0015$ for $-t < 1$ GeV^2; $\sigma(\xi) < 0.01$ for $-t > 1$ GeV^2
		RP220 + RP147 + CMS primary vertex: complete ξ-range	for $-t < 1$ GeV^2 $\sigma(\xi) \approx 0.0017$
		RP220 + RP147: complete ξ-range	$\sigma(\xi) \approx 0.006$ – 0.007
	DPE M [GeV]	RP220: complete M-range	$\sigma(M)/M < 1/2$ for $M > 150$; $\sigma(M) < 80$ for $\xi_{\rm lo}/\xi_{\rm hi} > 0.6$
		RP220 + CMS primary vertex: complete M-range	$\sigma(M)/M < 1/2$ for $M \gtrsim 40$; $\sigma(M) < 18$ for $\xi_{lo}/\xi_{hi} > 0.6$
	t [GeV^2]	RP220: $0.02 < -t <$ tens of GeV^2	$\sigma(t_x) \approx (0.3$ – $0.4)\sqrt{-t_x}$ $\sigma(t_y) \approx 0.04\sqrt{-t_y}$
	ϕ [rad]	$0 \le \phi < 2\pi$	$0.02 < \sigma(\phi) < 1$ for $1 > -t > 0.01$ GeV^2

Table 9.7: Roman Pot acceptance and reconstruction summary for β^*=90 m optics.

ton azimuth angle ϕ, its fractional momentum loss ξ and the azimuth angle of proton. For horizontal protons $\sigma(t_x) = (0.04$ – $0.4)\sqrt{-t_x}$ while for vertical ones $\sigma(t_y) = (0.002$ – $0.03)\sqrt{-t_y}$. The t-reconstruction precision in horizontal direction is generally lower than in the vertical one because of shorter effective horizontal lengths and due to the fact that both the horizontal component of the scattering angle and the momentum loss displace the proton in the horizontal direction. As a result, the reconstruction of the horizontal scattering angle and of the momentum loss both depend upon the horizontal displacement, which limits the resolution. The reconstruction of the azimuth angle ϕ is possible for all the accepted t-values, however its resolution improves for higher four momentum transfers squared t.

In case of the low-β^* optics, the t-reconstruction is primarily limited by the beam divergence and is practically independent from the azimuth angle ϕ. The

β^* [m]	variable	acceptance	resolution
1535	$\xi = \Delta p/p$	RP220: complete ξ-range	$\sigma(\xi) \approx 0.01$
		RP220 + RP150: complete ξ-range $-t > 0.015$ GeV^2	$0.002 < \sigma(\xi) < 0.006$
	DPE M [GeV]	RP220: complete M-range	$0.05 < \sigma(M)/M < 0.6$ for $M > 300$ GeV
	t [GeV^2]	RP220: $0.002 < -t < 1.5$	(t, ξ, ϕ)-reconstruction: $\sigma(t_x) \approx (0.04 - 0.3)\sqrt{-t_x}$ $\sigma(t_y) \approx (0.002 - 0.02)\sqrt{-t_y}$
			(t, ϕ)-reconstruction, $\xi = 0$: $\sigma(t) \approx 0.005\sqrt{t}$
	ϕ [rad]	$0 \leq \phi < 2\pi$	$0.002 < \sigma(\phi) < 0.02$ for $-t = 1$ GeV^2; $0.01 < \sigma(\phi) < 0.1$ for $-t = 0.05$ GeV^2; $0.04 < \sigma(\phi) < 0.4$ for $-t = 0.003$ GeV^2

Table 9.8: Roman Pot acceptance and reconstruction summary for β^*=1535 m optics. The DPE mass resolution is from [107].

ϕ-reconstruction is possible only for $-t > 0.18$ GeV^2 and $-t > 0.05$ GeV^2, for $\beta^* = 0.5$ m and $\beta^* = 2$ m, respectively.

The optics of $\beta^* = 0.5, 2, 90$ m are characterised by good ξ-reconstruction resolution of $\sigma(\xi) = 10^{-3}$ – 10^{-2}. If, in addition to the standard Roman Pot locations at 147 m and 220 m, the proposed insertion in the IR3 region is used, the excellent resolution of $\sigma(\xi) = 10^{-4}$ is achieved for $-\xi < 0.01$, which is the beam momentum spread limit. Then an excellent DPE mass reconstruction of $\sigma(M)/M = (1 - 5)\,\%$ is possible in the nearly complete mass range.

Chapter 10

Conclusions

The Roman Pot detectors are the essential part of the the TOTEM experiment. Together with the T1 and T2 telescopes they will be used to measure the total proton-proton cross-section, with the luminosity-independent method, and to study elastic and diffractive scattering at the LHC.

The tracking and physics performance of the TOTEM Roman Pot (RP) detectors was studied in detail in this dissertation.

The Roman Pot detectors of the TOTEM experiment will be equipped with silicon microstrip detectors. In order to achieve the foreseen physics objectives set by the experiment, the insensitive volume of the edge of these detectors must not exceed 50 – 60 μm, the detectors must be almost "edgeless". The standard planar silicon detectors used in High Energy Physics usually have a guard ring structure surrounding the active volume, resulting in an insensitive dead width of $\sim$500 μm. The development carried out by TOTEM consisted in modifying this structure in order to reduce the dead width down to 50 μm. This has been accomplished by applying the full detector bias across the detector chip cut, and by collecting the resulting current with the Current Terminating Structure (CTS). After successful tests of small prototypes of such devices, the final size detectors have been developed. The performance and resolution of the CTS detectors was studied with both analog and digital readout and is fully compliant with the needs of the TOTEM experiment. In particular, after successful alignment of the test setup to a precision of $\sim 1\,\mu$m, the edge behaviour was studied in detail. The tests confirmed that the CTS detectors have the efficiency $> 90\,\%$ at 50 – 60 μm from their cut edge.

In addition to the planar CTS detectors, TOTEM is considering to equip some RPs partly with another novel type of "edgeless" silicon devices: the planar-3D

detectors. This devices are conventional planar microstrip detectors with active edges introduced with the full 3D technology. In this configuration, the free edges of a planar detector are deep etched and $n+$ dopant is diffused in. As a result, the cut edge becomes the extention of the back side electrode. Prototypes of the planar-3D detectors were also studied during the TOTEM beam tests. Both the efficiency rise at the edge and the spatial resolution of the planar-3D detectors were measured to be very similar to those of the CTS detectors.

The full operation of the Roman Pot prototypes, equipped with both CTS and planar-3D detectors, was successfully tested in a coasting beam experiment in the SPS accelerator at CERN. Beam halo protons were detected at typical rates of 3 kHz. The detector edge efficiency rise was observed to be lower than 50 μm.

The physics performance of the Roman Pot detectors is determined by the optics of the LHC, which depends upon the configuration of the machine lattice. Therefore, the versatile physics programme of TOTEM requires different running scenarios. The high-β^* runs will concentrate on low-$|t|$ elastic scattering, total cross-section and soft diffraction. Low-β^* runs will be used for large-$|t|$ elastic scattering and diffractive studies.

The machine optics is the integral part of the TOTEM simulation and reconstruction software. In order to avoid time consuming proton tracking through the machine lattice while performing RP acceptance and resolution studies for various machine configurations, the fast and precise LHC optics modelling package was developed. Due to machine optics nonlinearities, simple linear parameterisations were not precise enough. Therefore, the machine optics is modelled with multidimensional polynomial approximations, with Gram-Schmidt orthogonalisation based term selection procedure. Basing only on a training sample of proton tracks from any accelerator simulation programme, the package finds automatically the parameterisation of the proton transport between any two given places of the machine, with the precision better than 0.5 μm, and stores it in an easy to use object oriented way. This software was applied to parameterise the proton transport over the distances ranging from hundreds of meters up to three quarters of the LHC ring and was integrated in the simulation and reconstruction routines of the Roman Pots.

The simulation software is based on a detailed description of the geometry and of the materials of the Roman Pot stations, which are all defined in a Geant4 compliant way. The signal generation of the silicon detectors and the response of the electronics is modelled. The proton transport between the interaction point

and the Roman Pot stations is carried out with the use of the already introduced parameterisation. The main output of the simulation software consists of the strip hits in the silicon detectors of the Roman Pots, which are provided to the proton reconstruction procedures. However, the simulation software was also used to study the performance of the Roman Pots in terms of proton interactions with its materials.

The aim of the Roman Pot reconstruction software is to find, basing of the detector strip hits and the machine optics model, the proton kinematics in the interaction point after the collision. This task is accomplished is a few steps. The strip hits are grouped in a form of clusters, which are converted, with the help of the RP geometry, into space points. The pattern recognition procedures aggregate the space points as of RP track candidates, which are finally fitted with straight lines. The proton kinematics reconstruction is performed on the basis of the discovered tracks, with the use of the parameterised proton transport functions, which are inverted with a χ^2 minimisation procedure.

The RP simulation and the reconstruction software was used together to study proton acceptance and reconstruction for selected running scenarios. The studies of the $\beta^* = 90\,\mathrm{m}$ optics has shown that fractional proton momentum loss $\xi = \Delta p/p$ can be reconstructed in a complete ξ-range with a precision of $\sigma(\xi) \approx 6 \times 10^{-3}$, if TOTEM runs standalone, or $\sigma(\xi) \approx 1.5 \times 10^{-3}$, for common runs with CMS. This optics is also characterised by good resolution of the proton vertical scattering angle, which leads to the precision of the squared four momentum transfer of $\sigma(t_y) \approx 0.04\sqrt{-t_y/\mathrm{GeV}^2}\,\mathrm{GeV}^2$.

The analysis of proton reconstruction with $\beta^* = 0.55\,\mathrm{m}$ was also carried out, especially in view of the studied extention of the TOTEM experiment by near-beam telescopes located in the LHC momentum cleaning region — IR3. The proposed devices could detect diffractive protons arriving from any interaction point of the LHC. In particular, the acceptance of the Roman Pots located on both sides of IP5 could be enlarged by the IR3 detectors. The obtained ξ-resolution in Roman Pot detectors at 220 m from IP5 is $\sigma(\xi) \approx (1 - 6) \times 10^{-3}$ for $0.02 < -\xi < 0.25$, while the excellent ξ-resolution in IR3 is only limited by the LHC beam momentum spread of 10^{-4}. Due to high beam dispersion in IR3, low ξ-values are detected: $1.5 \times 10^{-3} < \xi < 0.01$.

Therefore, if the IP5 and IR3 detectors are combined, the proton momentum loss can be measured in the range of $1.5 \times 10^{-3} - 0.25$ with the relative error of a few percent.

The acceptance and reconstruction of the Double Pomeron Exchange process was studied for such a configuration. The central mass M of the diffractive system can be measured in the range of $25 < M < 3000$ GeV with the relative error $\sigma(M)/M = 1 - 5\,\%$.

Chapter 11

Final summary

The TOTEM physics program aims at a deeper understanding of the proton structure by measuring the total and elastic *pp* cross-sections, and studying the diffractive processes. TOTEM will run under all LHC beam conditions to be able to maximise the coverage of the studied processes.

Due to large effective lengths and low beam divergence, the total *pp* cross-section will be measured with high-β^* runs. In case of the $\beta^* = 1535\,\mathrm{m}$ ($\beta^* = 90\,\mathrm{m}$) optics, the elastically scattered protons of $-t > 0.002\,\mathrm{GeV}^2$ ($-t > 0.02\,\mathrm{GeV}^2$) are detected and their four momentum transfer squared is reconstructed with a precision of $\sigma(t) = 0.005\sqrt{t}$ ($\sigma(t_y) = 0.04\sqrt{t_y}$). At an early stage with non-optimal beams and $\beta^* = 90\,\mathrm{m}$ optics, TOTEM will measure σ_{tot} with a 4 – 5 % precision. With improved understanding of the beams and $\beta^* = 1540\,\mathrm{m}$, a precision of $\sim 1\,\%$ should be achievable.

The measurement of elastic scattering in the range $10^{-3} < -t < 10\,\mathrm{GeV}^2$ will be possible by combining data from runs of several optics configurations. This will allow to distinguish among a wide range of predictions according to current theoretical models.

The majority of diffractive events exhibit intact protons. Depending on the beam optics, most of these protons can be detected in the RP detectors. For high-β^* optics ($\beta^* = 1535$, $90\,\mathrm{m}$), the full range of the fractional momentum loss ξ can be observed while for low-β^* optics ($\beta^* = 0.55$, $2\,\mathrm{m}$) only the protons of $-\xi > 0.02$ are detected. However, the advantage of low-β^* runs is a higher luminosity which leads to better statistics for higher diffractive masses. In all the cases the ξ-reconstruction precision is $(1 - 6) \times 10^{-3}$.

Low β^* runs will provide opportunities for measurements of soft diffraction for masses above $\sim 250\,\mathrm{GeV}$ in central diffractive events with a precision of 1 – 5 %.

Having proton detectors at IP3 would highly extend the diffractive mass acceptance of TOTEM for high luminosity runs giving for example a continuous mass acceptance from 25 GeV to 3 TeV for central diffractive events.

Appendix A

Testbeam analog readout

A.1 The APV25 readout chip

The Analogue Pipeline Voltage mode (APV25) [52] readout chip is based on 0.25 μm CMOS technology. Figure A.1 shows the layout of the APV25.

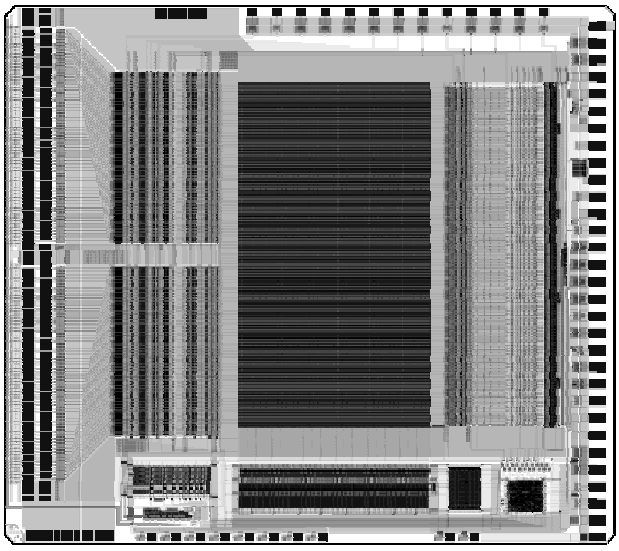

Figure A.1: Layout of the APV25 chip [53]. Detector channels are bonded to the pads on the left edge of the chip.

Each input of the 128 channels of the chip consists of a preamplifier coupled to a shaping amplifier which produces an 50 ns CR-RC pulse shape. A unity gain inverter is included between the preamp and shaper which can be switched in or out. The shaper output of each channel is sampled at 40 MHz into a 192 cell deep pipeline. The pipeline depth allows a programmable level 1 latency of up to 4 μs, with 32 locations reserved for buffering events awaiting readout. If the

chip is triggered the appropriate pipeline cell columns (time slices) are marked for readout, and not overwritten until this is completed. Each pipeline channel is read out by a circuit called the APSP (Analogue Pulse Shape Processor) which can operate in one of two modes. In *peak mode* only one sample per channel is read from the pipeline (timed to be at the peak of the analogue pulse shape). In *deconvolution mode* three samples are sequentially readout and the output is a weighted sum of all three. The deconvolution operation results in a re-shaping of the analogue pulse shape to one that peaks at 25 ns and returns rapidly to the baseline.

After the APSP operation is completed the output is sampled/held and fed to the analogue multiplexer. This 128:1 stage operates at 20 MHz. Due to the tree structure of the analogue multiplexer, the order at which the channels are read out through the analogue output is non-consecutive. The multiplexer is constructed in three stages, if 'n' is the order in which the channels appear (starting at 0, 1, ...), then the physical channel number is defined by:

$$\text{Channel No.} = 32\,(n \bmod 4) + 8\,\lfloor n/4 \rfloor - 31\,\lfloor n/16 \rfloor. \tag{A.1}$$

Figure A.2 (left) shows the APV25 output data stream following a trigger.

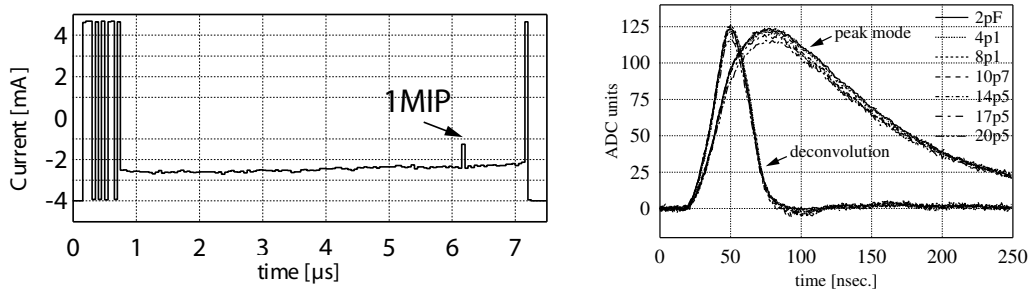

Figure A.2: Left: APV25 output data frame. Right: APV25 amplifier pulse shape in peak and deconvolution modes for a range of input capacitances [53].

The overall frame length is 7 μs, comprising a 12 bit header followed by 128, 50 ns analogue samples. A 1 MIP (24'000 electrons) signal has been injected into one of the chip inputs. The 12 bit header comprises 3 start bits, an 8 bit address of the pipeline column from which the data originates, and one error bit. In this plot a slight pedestal gradient can be seen on the right which is likely to be due to a power supply drop across the chip.

The digital header is designed to occupy approximately an 8 MIP range (256/8 = 32 ADC/MIP). This results in a signal dynamic range of ~5 MIPs plus headroom

to accommodate common mode effects.

Figure A.2 (right) shows the amplifier pulse shape measured for a bonded channel as a function of input capacitance, in both peak and deconvolution modes.

Figure A.3 shows the noise dependence on input capacitance for the APV25 in peak and deconvolution modes for three channels, one close to the middle, the other two close to the top and bottom edges of the chip represented in Figure A.1. No significant difference between channels is observed. The noise performance for microstrip detectors of 1'000 electrons root mean square is achieved for detectors with capacitances up to 10 pF and 18 pF in deconvolution mode and peak mode, respectively.

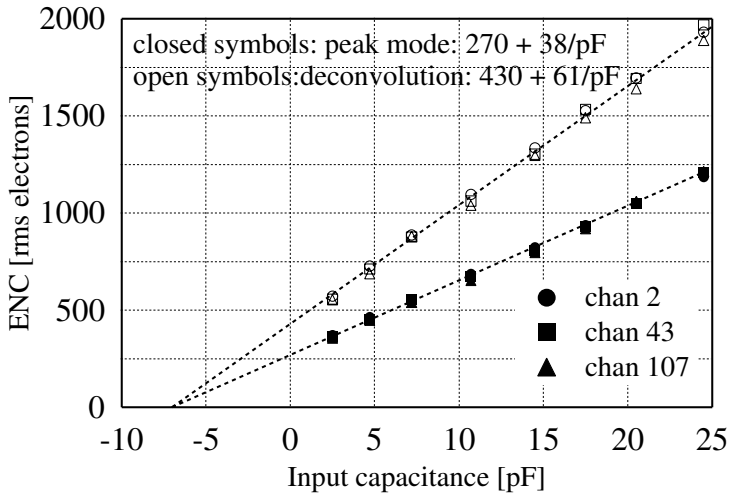

Figure A.3: APV25 noise dependence on input capacitance [53].

A.2 CMS Tracker electronics

A detailed description of the data acquisition system used in the test beams is beyond the scope of this work. More information can be found in [68].

A schematic diagram of the readout and of the control system in shown in Figure A.4. The microstrip detectors are connected to the APV25 chips, each containing 128 channels. Pulse height output data of a pair of APV25 is multiplexed on the detector hybrid by the APVMUX chip and fed to a laser driver. Electrical to optical signal conversion follows. Then the signal transmission takes place over a fibre optic cable to the counting room.

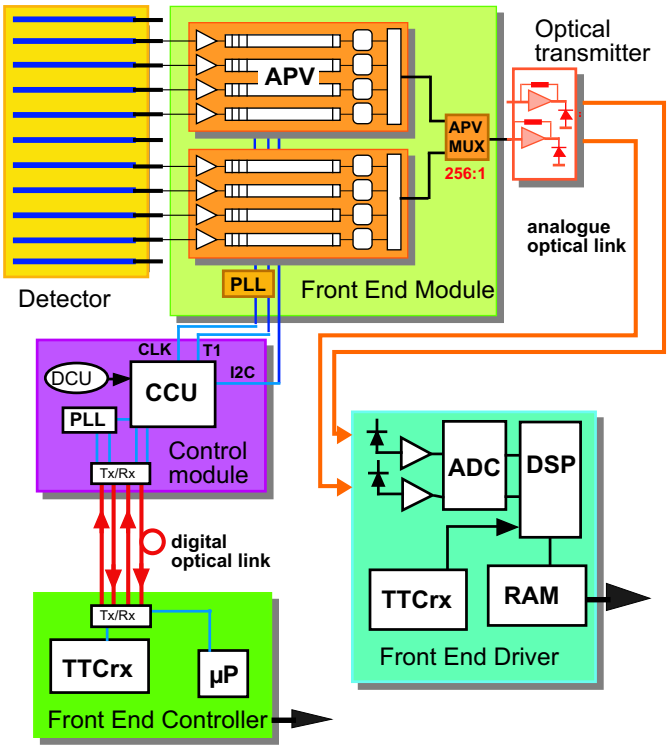

Figure A.4: Schematic diagram of the CMS tracker readout and control system [68].

In the counting room the pulse height data from the front-end chips, with no zero suppression, are converted back to electrical signals matched to the range of a 10 bit ADC. Approximately 2 bits of the range allow for baseline level variations within the system. The remaining 8 bits are sufficient for adequate resolution over the range of signals expected. The Front End Driver (FED) digitises the data, and is capable of reducing the event size. The FPGA chips, incorporated in the design, can perform extensive signal processing including channel reordering, pedestal and common mode subtraction, cluster identification and zero suppression. The resulting data sets are transported to the central data acquisition system.

The Front End Controller (FEC), controls and monitors the electronics system. It distributes the machine master clock and first level triggers received from the LHC Timing Trigger and Command (TTC) system. Digital optical links send and receive trigger, clock and control data at 40 MHz, which are further distributed electrically by a Communication and Control Unit (CCU) to the detector modules. Clock signals are processed by Phase Locked Loop (PLL) chips on each front-end hybrid to ensure high reliability and minimum phase jitter.

A.3 Impact point reconstruction

When the charged particle traverses the silicon detector, it continuously loses energy (see Equation 4.1). This creates the charge collected by the strips and then by the readout chips (see Section 4.2.1). In the case of the APV25 chip, the collected charge value is converted to the analogue readout signal which is later sampled by the FEDs described in Appendix A.2. The readout signal has a pedestal and a noise component.

The *pedestal* P_c of a single channel (strip) c of an APV25 chip is a constant component of the channel output signal D_{cr} for each event (trigger) r. It can be approximated by the mean output value of the channel over N_p triggers, recorded when no particle traversed the detector:

$$P_c = \frac{1}{N_p} \sum_{r=1}^{N_p} D_{cr}, \tag{A.2}$$

where $c = 1, \ldots, 512$, $N_{ch} = 512$ is a number of strips and D_{cr} is the raw output of the r^{th} event of channel c.

The *raw noise* N_c^{raw} of a channel c is the standard deviation of the pedestal of this channel and is defined as

$$N_c^{\text{raw}} = \sqrt{\frac{1}{N_p - 1} \cdot \sum_{r=1}^{N_p} (D_{cr} - P_c)^2} \tag{A.3}$$

and again is computed for the events containing no particles detected. The raw noise quantifies the fluctuations of individual channels. In addition to such fluctuations, groups of 128 channels (512-strip detectors bonded to 4, 128-channel APV25 chips) fluctuate in a correlated way. This effect is corrected by taking into account the common mode C_{cr} defined as

$$C_{cr} = \frac{1}{N_{k(c)}} \sum_{j \in G_{k(c)}} (D_{jr} - P_j), \tag{A.4}$$

where c is the strip number, $k(c)$ is the identifier of the group $G_{k(c)}$ of size $N_{k(c)}$ to which the strip belongs. By definition, all C_{cr} values of the r^{th} event for strips belonging the the same group $k(c)$ are equal. Various sizes of strip groups were used in the analysis, ranging from 128 strips in a group (one group per APV24 chip) down to 8-strip-groups. Contrary to the pedestal and raw noise values, the common

mode is calculated both without running particles (if used for the estimation of common mode subtracted noise) and for physics events (if used for correction of a detected particle's signal). To avoid a situation of a traversing particle affecting the value of C_{cr}, 10% of highest-signal strips and 10% of lowest-signal strips, for a given group and a given event, were rejected from the calculation.

The *common mode subtracted noise* is defined as

$$N_{cr}^{CM} = \sqrt{\frac{1}{N_p - 1} \cdot \sum_{r=1}^{N_p} (D_{cr} - P_c - C_{cr})^2}\,. \tag{A.5}$$

In the data analysis, for simplicity, the notion "noise of the strip c" refers to common mode subtracted noise N_{cr}^{CM}.

The strips exhibiting much higher or much lower noise than the other ones were excluded from the analysis and classified as "noisy" or "dead" strips, respectively.

A signal S_{cr} of a strip c in the event r is obtained by demanding

$$S_{cr} = D_{cr} - P_c - C_{cr} \text{ such that } S_{cr} \geq 4 \cdot N_c^{CM}. \tag{A.6}$$

The set of neighbouring signal strips K_{kr} forms a cluster k. The signal S_{kr}^K of the cluster is defined as a sum of the signals of its strips:

$$S_{kr}^K = \sum_{c \in K_{kr}} S_{cr}. \tag{A.7}$$

The noise N_{kr}^K of the cluster k is given by:

$$N_{kr}^K = \sqrt{\sum_{c \in K_{kr}} (N_{cr}^{CM})^2}. \tag{A.8}$$

The cluster signal to noise ratio S/N is defined by

$$S/N_{kr} = \frac{S_{kr}^K}{N_{kr}^K}. \tag{A.9}$$

Only clusters with $S/N_{kr} \geq 4$ are accepted for further analysis.

The cluster position x_{kr} is defined by means of its signal weighted average strip position:

$$x_{kr} = \frac{\sum_{c \in K_{kr}} c \cdot S_{cr}}{S_{kr}^K}. \tag{A.10}$$

Since the charge sharing between the strips was low (generally less than 25% of clusters containing more than 1 strip), the application of more refined algorithms for computing the cluster centre [69, 70] (for e.g. η–algorithm[1]) did not increase the reconstructed hit position resolution.

[1] η–algorithm is based on the assumption that most of the charge is collected by the two readout strips closest to the impact position. The algorithm is capable of correcting the nonlinearity of charge division when the impact point is reconstructed. If Q_{left} (Q_{right}) is the charge collected on the left(right) side of the impact point, P the readout pitch and x_{left} – the position of the left strip, the hit position x_η can be reconstructed by $x_\eta = P \cdot f(\eta) + x_{\text{left}}$ with $\eta = \frac{Q_{\text{right}}}{Q_{\text{left}}+Q_{\text{right}}}$ and $f(\eta) = \frac{1}{N}\int_0^\eta \frac{\mathrm{d}N}{\mathrm{d}\eta'}\mathrm{d}\eta'$, where N is the number of hits. The η is calculated for each hit, while the probability function $f(\eta)$ is evaluated using all hits of each data sample.

Appendix B

TOTEM digital readout

B.1 VFAT2 readout chip

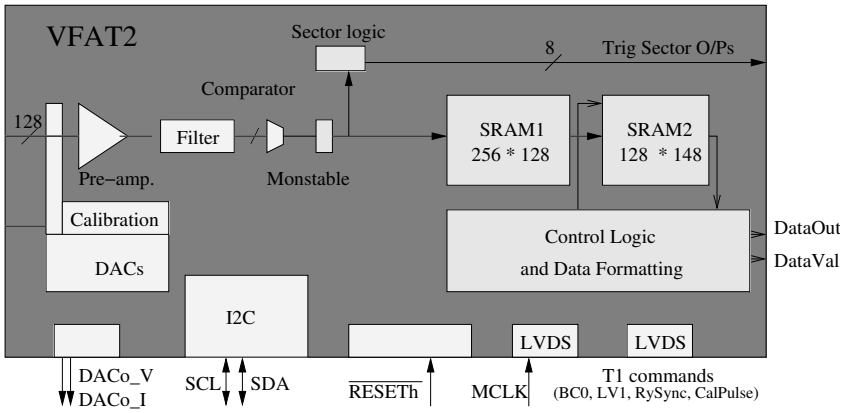

Figure B.1: Block diagram of the VFAT chip [14, 15].

The VFAT2 is a trigger and tracking front-end ASIC. A block diagram of the chip is shown in Figure B.1. The VFAT2 chip has been designed in 0.25 μm CMOS and it has two basic functions. The first (Trigger) is to provide fast regional hit information to aid the creation of a first level trigger (LV1) and the second (Tracking) is for providing precise spatial hit information for a given trigger event.

The VFAT2 chip has 128 identical channels. It is a synchronous chip designed for sampling sensors at the LHC clock frequency of 40 MHz. Each channel consists of a preamplifier and shaper followed by a comparator. If a particular channel receives a signal greater than the programmable threshold of the comparator a logic 1 is produced for exactly one clock cycle. This logic 1 is written into the first two SRAM memories (SRAM1). All other channels that do not go over threshold

record a logic 0 in SRAM1. This occurs in parallel for all 128 channels at 40 MHz. At the same time a fast OR function can be used to set a flag immediately used for creating a trigger. It is foreseen to have up to eight programmable sectors which can be flagged with the fast OR in this way. The assignment of channels to sectors is programmable. There are 8 Low Voltage Differential Signal (LVDS) sector outputs labelled S1 to S8. Not all LVDS outputs need to be used.

On receiving a LV1 signal, data corresponding to the triggered time slot is transferred to a second SRAM memory (SRAM2). The LV1 latency is not expected to exceed 6.4 μs (256 clock periods). Hence SRAM1 is dimensioned to be 256 by 128. SRAM2 contains only triggered data. It is dimensioned to be 128 by 148 for data plus headers, hence the VFAT2 chip can store up to 128 triggered events of data for all channels at any one instant in time.

VFAT2 will label the data with 3 headers. These are the Bunch Crossing Number (BCN 12 bits), Event Number (EN 8 bits), and the chip Identification number (ID 16 bits). The BCN is generated by a 12 counter (BC) that increments every clock cycle. The EN is generated by an 8 bit counter that increments for every LV1. Both counters are cyclic and return to zero at the end of the counter range.

As soon as SRAM2 has data the Read cycle begins. During the Read cycle a Data Formatting block streams out a binary data stream to the Front End Driver (FED) via the Gigabit Optical Link (GOL). The GOL chip operates with a continuous write/read operation without dead time.

B.2 TOTEM RP electronics system

The Roman Pot hybrids contain a silicon detector sub-divided into 512 strips. Four VFATs are bonded directly to each strip with 128 channels per chip. Figure B.2 gives an overview of the electronics used for the Roman Pot system.

The VFAT readout chip produces both Trigger and Tracking data. These two types of data have very different timing requirements hence are treated separately.

Trigger data is used to generate first level triggers hence it has to be read out as fast as possible. The Sector outputs (S-bits) of the VFAT give the results of internal fast OR operations within 1 clock cycle. A Coincidence chip (CC [2]) then performs coincidence operations between VFAT sector outputs. The trigger data is then serialised and transmitted by optical links at 800 Mb/s to the counting room. The module that performs the serialisation and optical transmission is called the

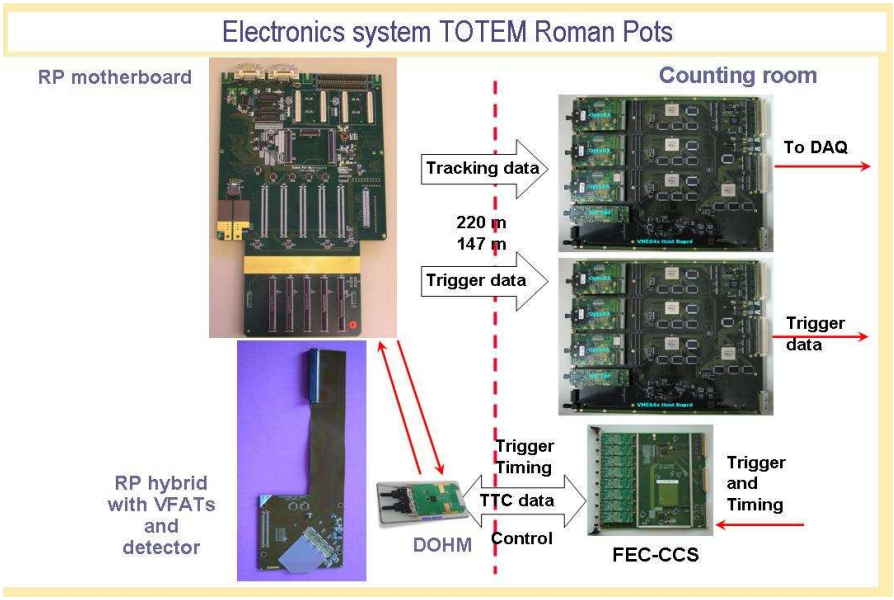

Figure B.2: Overview of the RP electronics system.

Gigabit Optical Hybrid (GOH).

Tracking data are data corresponding to triggered events and are buffered within VFAT for high trigger rates. Data packets are transmitted in serial form from the VFAT chips at a bit rate of 40 Mb/s. The GOH serialises the data for transmission to the counting room via optical links. Up to 16 VFAT signals are multiplexed by one GOH into a serial stream for optical transmission.

Once in the counting room, the optical fibres are connected to the 9U VME64x Host boards (developed by TOTEM) which contain the Front End Drivers (FEDs) used for trigger and event building. There are separate Host boards for the treatment of trigger data and tracking data. TOTEM uses 6 Host boards for the Trigger system and 8 Host Boards for the tracking data. A photograph of the Host Board is shown in Figure B.3.

The incoming optical fibres (grouped in 3 bundles of 12 fibres) are connected to optical receiver modules, called optoRx-12 [85], located on the Host boards.

The first stage of FED data management is performed on the optoRX-12 with the deserialisation of input data streams with FPGA chips using the embedded high-speed deserialisers. The second stage is performed on the Host board with 3 Altera FPGAs Stratix^{TM} devices. Each of them receives raw data from its associated OptoRX-12 module, stores it into its memory and transfers it to the VME64x bus or to the USB for slow spy readout.

In the Trigger Host boards the incoming trigger data is sent to the FPGAs

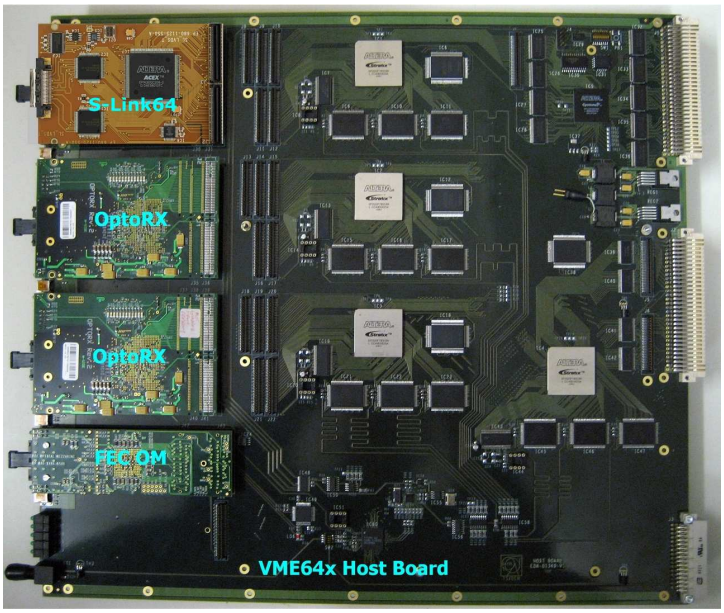

Figure B.3: Photo of the TOTEM FED Host board.

where coincidence logic functions and more complex algorithms can be performed in order to prepare trigger primitives for the global L1 Totem trigger.

There are 3 different possibilities implemented for sending data to the DAQ:

- VME interface: used for TOTEM operation;
- USB interface: alternative for TOTEM operation;
- S-Link64 [86] module: connection to the CMS Front-end Readout Links (FRLs) for common data taking, ensuring full compatibility with the CMS DAQ.

The details of the TOTEM readout system can be found in [2].

Appendix C

Simulation software

C.1 MAD-X

C.1.1 Overview

The MAD-X (Methodical Accelerator Design) programme is a general purpose accelerator and lattice design programme. Its details can be found the MAD-X reference manual [37]. The MAD-X programme is ideally suited for very large accelerator studies but has also been frequently used for small machines and transfer lines. The strength of the code is the flexible MAD input language, a large collection of modules needed for accelerator design and most importantly the very elaborate matching techniques.

The main objectives of the program are:

- to read the elements and their sequence from a file;
- to calculate the optics parameters from a machine description;
- to define and compute (match) the desired properties of such a machine;
- to simulate and correct possible machine imperfections;
- to simulate the beam dynamics in the designed machine.

Both, circular and linear accelerators (or beam lines) are handled.

The basic ingredients of the machine simulated with MAD-X have to be defined. The information has to be supplied in the MAD-X scripting language. The programme input parameters are:

- properties of all machine elements;
- strength of all active machine elements;

- position of all elements in the machine, i.e. the order in which they appear in the accelerator or beam line;
- apertures of the elements.

The elements in a machine can be misaligned with the available MAD-X error actions. The program allows also to assign field errors of any order to the machine elements.

After the machine is defined, the MAD-X commands are used to specify and execute actions on the machines, e.g. calculations of transport functions, input/output of the lattices, particle tracking, lattice matching etc.

C.1.2 Tracking

For TOTEM studies particle tracking is of high importance. Two types of tracking modules are implemented into MAD-X. The first one is the thin-lens tracking module (thintrack). The effects of an element (e.g., a magnet) on the beam are represented as impulses (kicks) at a fixed value s on the reference orbit. The lattice element end effects are simulated by an additional kick on its either end. This method demands a preliminary conversion of a sequence with thick elements into one composed entirely of thin elements. This simplifies the treatment since it allows to treat the machine as a series of linear transformations separated by the kicks at the positions of the thin elements. This method is fast and is therefore best suited for particle tracking. The disadvantage is the loss of precision when the magnets are very long (compared to the size of the machine) or when fringe fields are important.

The second tracking approach in MAD-X is a thick lens tracking module that allows a symplectic treatment of all accelerator elements, giving the user full control over the precision (number of steps and integration type) and exactness of the results. It makes use of the Polymorphic Tracking Code (PTC) and is suited to perform calculations related to beam dynamics in the nonlinear regime [57].

MAD-X has a built-in graphics package which is capable of displaying various aspects of performed simulations.

C.2 Geant4

C.2.1 Overview

The Geant4 simulation toolkit [3, 4] provides comprehensive detector and physics modeling capabilities embedded in a flexible structure. It is a free software which can be used to accurately simulate the passage of particles through matter. The Geant4 software can be either incorporated in the computational frameworks or can be run as a stand-alone application. In case of the TOTEM experiment, Geant4 is used as a module of the CMSSW framework, which is discussed in Appendix C.3.

It is composed of several modules which are responsible for various aspects of the simulations. The key ones will be briefly discussed in the following sections. The detailed user and the application developer manuals can be found in [92].

C.2.2 Geometry and materials

The detector definition requires the representation of its geometrical elements, their materials and electronics properties, together with visualisation attributes and user defined properties. The geometrical representation of detector elements focuses on the definition of solid models and their spatial position, as well as their logical relations to one another, such as in the case of containment.

Geant4 supports the Constructive Solid Geometry (CSG) representations and Boundary Represented Solids (BREPs). CSG solids are defined directly as three-dimensional primitives. They are described by a minimal set of parameters necessary to define the shape and size of the solid. CSG solids are boxes, tubes and their sections, cones and their sections, spheres, and toruses. BREP solids are defined via the description of their boundaries. The boundaries can be made of planar and second order surfaces. For each of the defined solids, the user has to specify the material. Both elementary and complex materials of various phases can be defined. Some of the detector elements can be defined as sensitive (sensitive detectors), for which the energy deposition is recorded.

C.2.3 Physics processes

The physics processes describe how particles interact with a material. The major categories of processes provided by Geant4 are:

- electromagnetic, hadronic, decay, photolepton-hadron,
- transportation,

- optical, and
- parameterisation.

The generalisation and abstraction of the physics processes is a key issue in the design of Geant4. All physics processes, including the transport of particles, are treated in the same manner from the tracking point of view. The Geant4 approach enables anyone to create a process and assign it to a particle type.

In Geant4, a physics process may be characterised by several cross-section tables and physics models appropriate for different energy ranges. Much wider coverage of physics comes from mixture of theory-driven, cross-section tables, and empirical formulae.

The transportation process is responsible for determining the geometrical limits of a step. It calculates the length of step with which a track will cross into another volume. When the track actually arrives at a boundary, the transportation process locates the next volume that it enters. If the particle is charged and there is an electromagnetic (or potentially other) field, the transportation process is responsible for propagating the particle in this field. It does this according to an equation of motion. This equation can be provided by Geant4, for the case an electromagnetic field, or can be provided by the user for other fields. Geant4 is capable of describing and propagating in a variety of fields. Magnetic fields, electric fields and electromagnetic, uniform or non-uniform, can be specified.

Fast simulation or parameterisation allows the user to take over the tracking and implement, for example, a fast algorithm of detector response. The typical use case is shower parameterisation where the several thousand steps per GeV computed in the detailed simulation are replaced by a few tens of energy deposits. In the TOTEM Roman Pot simulation, the parameterisation is used to transport the protons through the accelerator magnet lattice instead of doing the detailed magnet simulation.

Each particle has its own list of applicable processes. At each step, all processes listed are invoked to get proposed physical interaction lengths. The process which requires the shortest interaction length (in space-time) limits the step size.

Each process can act at any of three space-time intervals (all combinations are possible):

- In time — At rest (e.g. decay at rest, e^+ annihilation, absorption at rest)
- Continuously or along a step (e.g. bremsstrahlung, ionisation)
- At a point — at the end of the step (e.g. discrete interactions)

Along step actions are applied cumulatively, while others are selectively applied. Tracking handles each type of action in turn.

In Geant4, two kinds of methods of processes play important roles in tracking: GetPhysicalInteractionLength (called as GPIL) and DoIt. GPIL method gives the step length from the current space-time position to the next space-time point where the DoIt method should be invoked. It does this by calculating the probability of interaction based on the process's cross section information. The DoIt method implements the details of the interaction, changing the particle's energy, momentum, direction and position, and producing secondary tracks if required.

C.2.4 Tracking

Run is the largest unit of simulation. A run consists of a sequence of events. Within a run, the detector geometry, the set up of sensitive detectors, and the physics processes used in the simulation should be kept unchanged. The event related object has four major types of information:

- primary vertices and primary particles,
- trajectories,
- hits collections, and
- Digits collections.

The Geant4 simulation is controlled in a hierarchical way by the run manager, the event manager, the tracking manager and the step manager. The step is the smallest entity of the simulation process. The algorithm to handle one step can be summarised as follows:

1. Each active discrete or continuous physical process must propose a step length based on the interaction it describes.
2. The smaller of the minimum physical-step-length and the geometric step length is taken.
3. All active continuous processes are invoked.
4. The track is checked to see whether or not it has been terminated by a continuous process. The particle's kinetic energy, position and time are updated.
5. The discrete processes are invoked. The energy of the current track particle is updated and the created secondaries are stored for further processing. The track is checked to see whether or not it has been terminated by the discrete process.

In order to optimise the performance of the simulation, in Geant4, the user may define a range cut-off for the production of secondaries. In Geant4, a track is by default tracked down to zero kinetic energy.

The results of the physical interaction of tracks in the sensitive region of a detector is recorded in the so called hits, which contain the following information:

- the position and time of the step,
- the momentum and energy of the track,
- the energy deposition of the step, and
- the spatial position.

The simulation flow can be observed and controlled at various stages by means of the custom user actions, which are invoked at the beginning or end of the run, the event, the track and the step. In this way the evolution of tracking can be observed in great detail.

C.2.5 Visualisation

The Geant4 visualisation system was developed in response to a diverse set of requirements like debugging of complex geometries, analysis of complex event topologies and high-quality plots for publications.

The software can visualise the simulation data: detector components, particle trajectories, tracking steps and hits of particles in detector components. In addition, other user defined objects can be displayed like polylines, coordinate axes, 3D Markers, text, comments, titles, scales and logos.

C.3 CMSSW software

The TOTEM simulation, reconstruction, calibration, alignment and analysis software is built around the CMSSW Framework with its Event Data Model (EDM) and Services. The CMSSW framework implements a software bus model wherein there is one executable, called cmsRun, and many plug-in modules which run algorithms.

The cmsRun executable is configured at run time by the user's job-specific configuration file. This file tells cmsRun which data to use, which modules to run, which parameter settings to use for each module, and in what order to run the modules.

C.3.1 Event Data Model

The CMS EDM is centred around the concept of an Event as a C++ object container for all RAW (or generated) and reconstructed data pertaining to a physics event. During processing, data are passed from one module to the next via the Event, and are accessed only through the Event, which is illustrated in Figure C.1 (left). All objects in the Event may be individually or collectively stored

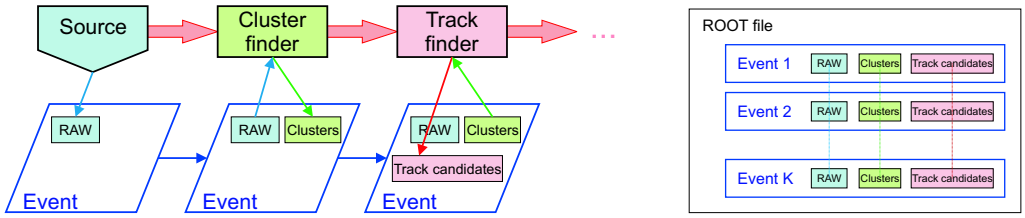

Figure C.1: Left: Processing of one Event. The subsequent modules exchange data via the Event. Each module stores its products in the Event. Right: A ROOT file containing a sequence of Events. Three ROOT trees correspond to the three elements stored in the Event.

in ROOT [43] files, and are directly browsable in ROOT analysis framework. The consecutive Events are stored in ROOT trees which correspond to the contents of the Event, as can be seen in Figure C.1 (right).

The Event also contains metadata describing the configuration of the software used for the reconstruction of each contained data object and the conditions and calibration data used for such reconstruction.

C.3.2 Event Setup

To be able to process an Event, one has to take into account potentially changing and periodically updated information about the detector environment and status. This information (non-event data) is not directly tied to a given event, but rather to the time period for which the given setup information is valid. This time period is called its interval of validity (IOV), and an IOV typically spans over many events. Examples of this type of non-event data include calibrations, alignments, geometry descriptions, magnetic field and run conditions recorded during data acquisition. The Event Setup concept is illustrated by Figure C.2.

The Event Setup system design uses two categories of modules to do its work: ESSource and ESProducer.

ESSource is responsible for determining the IOV of a record, which holds data

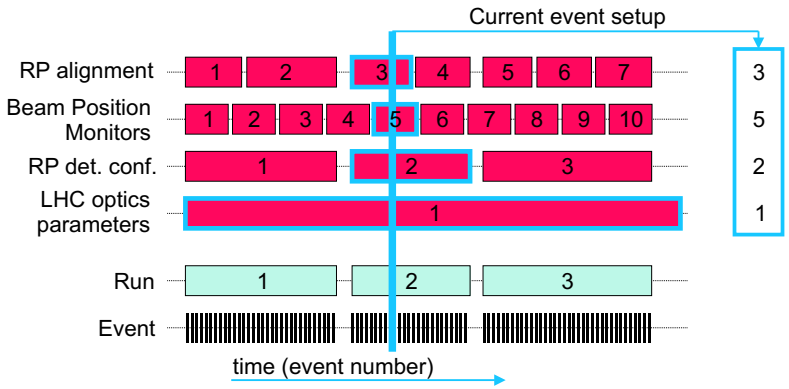

Figure C.2: Intervals of validity of some non-event data and the contents of the Event Setup records.

and services which have identical IOVs. The ESSource may also deliver data/services.

ESProducer is, conceptually, an algorithm whose inputs are dependent on data with IOVs. The ESProducer's algorithm is run whenever there is an IOV change for the Record to which the ESProducer is bound. For example, an ESProducer is used to read the ideal geometry of the Roman Pots as well as the alignment corrections and then create the aligned RP geometry from those 2 pieces of information. This ESProducer is told by the Event Setup system to create a new aligned RP geometry whenever the alignment changes.

C.3.3 Framework

Each module of the CMSSW software encapsulates a unit of clearly defined event-processing functionality. Modules are implemented as plug-ins. The framework takes care to load the plug-in and instantiate the module when it is requested by the job configuration.

When preparing an analysis job, the user selects which module(s) to run, and specifies their various parameters via the configuration file. The module is called for every event according to the module order defined in the configuration file.

There are six types of dynamically loadable processing modules, whose interface is specified by the framework:

Source Reads in an Event from a ROOT file, from a DAQ source or generates a Monte Carlo Event.

EDProducer CMSSW uses the concept of producer modules and products, where producer modules read in data from the Event in one format, produce something from the data, and output the product, in a different format, into the Event. A succession of modules used in an analysis may produce a series of intermediate products, all stored in the Event.

EDFilter Reads data from the Event and returns a Boolean value that is used to determine if processing of that Event should continue.

EDAnalyzer Loops over a specified range of Events and studies their properties. An analyser reads data from the Event but is neither allowed to add data to the Event nor effect the execution of the path. Typically analysers are used to carry out the cumulative analyses of runs, which are stored as histograms.

EDLooper A module which can be used to control 'multi-pass' looping over an input data sources. It can modify the Event setup at well defined times. This type of module is used in the track based alignment procedure.

OutputModule Reads data from the Event, and once all paths have been executed, stores the output to external media.

The user configures the modules in job configuration files.

C.3.4 Processing Model

Events are processed by passing the Event through a sequence of modules. The exact sequence of modules is specified by the user in a configuration file in a form of an ordered list of Producer/Filter/Analyser modules. The components involved in the framework and EDM are shown in Figure C.3.

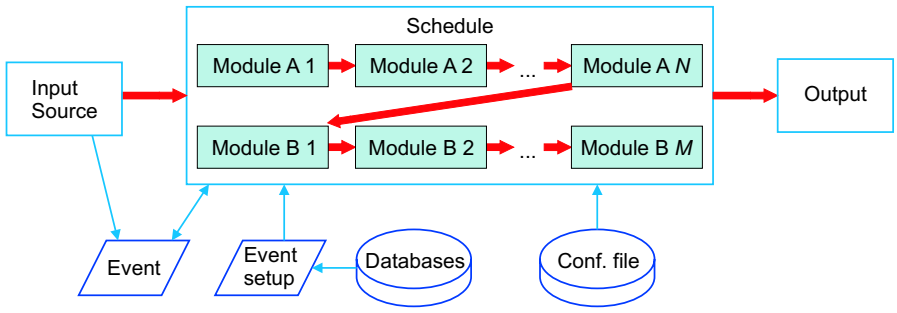

Figure C.3: The CMSSW framework components involved in the Event processing.

Bibliography

[1] TOTEM: Technical Design Report, CERN-LHCC-2004-002; addendum CERN-LHCC-2004-020.

[2] The TOTEM Collaboration, "The TOTEM Experiment at the LHC", 2008 JINST 3 S08007, doi: 10.1088/1748-0221/3/08/S08007.

[3] S. Agostinelli, J. Allison, et al., "Geant4 — a simulation toolkit", Nucl. Instr. and Meth., Vol. 506, Issue 3, July 2003, 250-303.

[4] J. Allison, K. Amako, et al.,"Geant4 Developments and Applications", IEEE Trans. on Nucl. Sci., Vol. 53, No. 1, February 2006.

[5] The CMS and TOTEM diffractive and forward working group: Prospects for Diffractive and Forward Physics at the LHC, CERN/LHCC 2006-039/G-124, 2006.

[6] J. J Blaising, A. De Roeck, J. Ellis, F. Gianotti, P. Janot, G. Rolandi, D. Schlatter, "Potential LHC Contributions to Europe's Future Strategy at the High-Energy Frontier", 2006 Report to CERN Council European Strategy Group.

[7] J. Ellis, "Beyond the standard model with the LHC", Nature 448, 297-301, 19 July 2007; J. Ellis, "The LHC: illuminating the high-energy frontier", CERN Courier, 1 May 2007.

[8] The LHC Conceptual Design Report — The Yellow Book, CERN/AC/95-05 (LHC) (1995).

[9] O. S. Brning, P. Collier, P. Lebrun, S. Myers, R. Ostojic, J. Poole, P. Proudlock et al., LHC Design Report, Vol.1, The LHC Main Ring, CERN-2004-003.

[10] D. J. Griffiths, "Introduction to elementary particles", John Wiley and Sons, ISBN 0-471-60386-4, 1987.

[11] R. Schmidt, "Accelerator Physics and Technology of the LHC", CERN Yellow Report 99-01, 1998.

[12] The TOTEM Collaboration, Letter of Intent, CERN/LHCC 9749, LHCC/I11, 1997.

[13] The TOTEM Collaboration, Technical Proposal, CERN/LHCC 997, LHCC/P5, 1999.

[14] P.Aspell et al., "VFAT2 : A front-end system on chip providing fast trigger information, digitized data storage and formatting for the charge sensitive readout of multi-channel silicon and gas particle detectors", Proceedings of TWEPP-07, Topical Workshop on Electronics for Particle Physics, Prague, Czech Republic 3-7 September 2007.

[15] P. Aspell, "VFAT2 — Digital Specification (Version 5)", 2005.

[16] U. Amaldi et al., Phys. Lett. 44B (1973) 112.

[17] F. Abe et al., Phys. Rev. D50 (1994) 5550-5561, http://link.aps.org/abstract/PRD/v50/p5550.

[18] E811 Collaboration, Phys. Lett. B445 (1999) 419-422.

[19] R.M. Baltrusaitis et al., Phys. Rev. 52 (1984) 1380.

[20] CDF Collaboration (F. Abe et al.), Phys. Rev. D50, (1994) 5550.
E710 Collaboration (N.A. Amos et al.), PRL 63, (1989) 2784; Phys. Lett. B243, (1990) 158.
Phys. Lett. B537, (2002) 41.

[21] J.R. Cudell et al.; Benchmarks for the Forward Observables at RHIC, the Tevatron-Run II, and the LHC; PRL 89, (2002) 201801.

[22] T.T. Wu and C.N. Yang, Phys. Rev. B708 (1965) 137.

[23] N. Byers and C.N. Yang, Phys. Rev. 142 (1966) 976.

[24] T.T. Chou and C.N. Yang, Phys. Rev. Lett. 20 (1968) 1213.

[25] C. Bourrely, J. Soffer and T.T. Wu, Nucl. Phys. B247 (1984) 15.

[26] G. Matthiae et al., Rep. Prog. Phys. 57 (1994) 743-790.

[27] V. Barone, E. Predazzi, "High-Energy Particle Diffraction", Springer-Verlag 2002, ISBN 3-540-42107-6.

[28] Carter et al., REACTION DATA Database: http://durpdg.dur.ac.uk/hep data/react.html

[29] M.M. Islam, R.L. Luddy and A.V. Prokudin, Int. J. Mod. Phys. A21 (2006) 1-41, arXiv:hep-ph/0508200.

[30] D. H. Perkins, "Introduction to High Energy Physics", 4th ed., Cambridge University Press, 2000.

[31] The ATLAS Collaboration, "The ATLAS Muon Spectrometer", Chapter 6, 1997.

[32] The CMS Collaboration, "CMS The Muon Project", CERN-LHCC 97-32, 1997.

[33] M. Alfonsi et al.: NIM A 518, (2004) 106.

[34] G. Lutz, "Semiconductor Radiation Detectors", Springer-Verlag, Heidelberg, 1999.

[35] E. D. Courant and H. S. Snyder, "Theory of the Alternating-Gradient Synchrotron", Annals of Physics 281, 360 408 (2000), 360-408, doi:10.1006/aphy.2000.6012, http://www.idealibrary.com.

[36] E. Wilson, "An Introduction to Particle Accelerators", Oxford University Press, 2006.

[37] The MAD-X Home Page, http://frs.home.cern.ch/frs/Xdoc/mad-X.html.

[38] W. Herr, private communication.

[39] V. Avati, K. Österberg, "Optical functions parametrization: β^*=1540", TOTEM Internal Note 05-1, February 2006.

[40] V. Avati, K. Österberg, "Acceptance calculations methods for low-β^* optics", TOTEM Internal Note 05-2, November 2006.

[41] R. Brun, M. Hansroul, J. Kübler, P. Palazzi, H. Wind, Multi-dimensional fit program (MUDIFI), CERN-DD-75-23-rev-1, Geneva, 1977.

[42] H. Wind, Function parametrization, Proc. 1972 CERN Computing and Data Processing School (CERN 72-21), p. 53.

[43] Root — An Object-Oriented Data Analysis Framework, http://root.cern.ch.

[44] G. Ruggiero et al.: Planar Edgeless Silicon Detectors for the TOTEM Experiment, IEEE Trans. Nucl. Sci. 52 n5 (2005) 1899.

[45] UA1 Collaboration, D. Linglin et. al., Phys. Lett. B122 (1983) 103-116.

[46] R. Frühwirth, M. Regler, R. K. Bock, H. Grote, D. Notz, "Data Analysis Techniques for High Energy Physics, Second edition", Cambridge University Press, 2000.

[47] A. Heikkinen and V. Karimäki, "Fine Calibration of Detector Positions by Tracks in Helsinki Silicon Beam Telescope", CMS NOTE 1999/029.

[48] V. Karimäki, A. Heikkinen, T. Lampen, T. Linden, "Sensor Alignment by Tracks", [arXiv:physics/0306034v2], 2003.

[49] S. Viret, C. Parkes and D. Petrie, "LHCb VELO software alignment", LHCb 2005-101, 2005.

[50] V. Blobel, "Software alignment for tracking detectors", Nuclear Instruments and Methods in Physics Research A 566 (2006), 5-13.

[51] G. Ruggiero et. al., "Planar edgeless silicon detectors for the TOTEM experiment", IEEE Trans. Nucl. Sci. 52, 5, 2005.

[52] L. Jones, "APV25-S1 User Guide Version 2.2", September 2001.

[53] M. Raymond et. al., "The CMS Tracker APV25 0.25 μm CMOS Readout Chip", 6^{th} Workshop on Electronics for LHC Experiments, Krakow, Poland, 2000.

[54] E. Noschis, "Planar Edgeless Detectors for the TOTEM Experiment at the Large Hadron Collider", Ph. D. Thesis, University of Helsinki, Helsinki, Finland, 2006.

[55] The CMS Collaboration, "CMS Physics Technical Design Report Volume I: Software and Detector Performance", CERN-LHCC-2006-001.

[56] The CMS Collaboration, "CMS computing : Technical Design Report ", CERN-LHCC-2005-023.

[57] P. K. Skowronski, F. Schmidt, R. de Maria, E. Forest, "New Developments of MAD-X Using PTC", Proceedings of ICAP 2006, Chamonix, France.

[58] W.R. Leo, "Techniques for Nuclear and Particle Physics Experiments", Springer Verlag, 1987.

[59] R.M. Barnet et al., Phys. Rev. D54 (1998).

[60] C. Amsler et al., Phys. Lett B667, 1 (2008), http://pdg.lbl.gov/.

[61] E.H.M. Heijne, "Muon Flux Measurement with Silicon Detectors in the CERN Neutrino Beams", Ph. D. Thesis, CERN 83-06, Yellow report (1983); H. Bichsel, "Passage of charged particles through matter", AIP Handbook, McGraw-Hill, New York, 1972.

[62] H. Bichsel, Rev. Mod. Phys., 60 (1983) 663

[63] L. Landau, Journ. Phys. U.S.S.R. 8 (1944) 201.

[64] U. Fano, "Penetration of Protons, Alpha Particles, and Mesons", Ann. Rev. of Nucl. Sci., December 1963, Vol. 13, 1-66, (doi: 10.1146/annurev.ns.13.120163.000245).

[65] G. Ruggiero, "Signal generation in highly irradiated silicon microstrip detectors for the ATLAS experiment", Ph. D. Thesis, University of Glasgow, Glasgow, 2003.

[66] S.M. Sze, "Physics of Semiconductor devices", 2nd edition, Wiley, New York, 1985.

[67] P. Murray, "APVMUX user guide version 1.0", May 2000.

[68] A. Marchioro, "CMS Microstrip tracker electronics", http://cern.ch/cmstrackercontrol/documents/GeneralDoc.htm.

[69] E. Belau et al., "Charge collection in silicon strip detectors", Nucl. Instr. and Meth. 214 (1983), 253.

[70] R. Turchetta., "Spatial resolution of silicon microstrip detectors", Nucl. Instr. and Meth. A 335 (1993), 44.

[71] The TOTEM Collaboration, "Tests of a Roman Pot Prototype for the TOTEM Experiment", Proceedings of the 2005 Particle Accelerator Conference, Knoxville, Tennessee, 1701, IEEE 2005. arXiv:physics/0507080. Recent beam-coupling impedance measurements with final ferrite geometry still unpublished.

[72] The TOTEM Collaboration, "Tests of a Roman Pot Prototype for the TOTEM Experiment", poster presentation at PAC05, Knoxville, Tennessee, USA, May 2005. Proceedings published by IEEE, 0-7803-8859-3/05, p. 1701. Available from e-print archive: physics/0507080.

[73] E. Noschis et al., "Final Size Planar Edgeless Silicon Detectors for the TOTEM experiment", Nucl. Instrum. Meth. A563, 41-44, 2006, arXiv:physics/0612105.

[74] F. James, "Statistical Methods in Experimental Physics", World Scientific, ISBN 981-256-795-9, 2006.

[75] V. Blobel and C. Kleinwort, "A new method for the high-precision alignment of track detectors", PHYSTAT2002, Durham [arXiv:hep-ex/0208021].

[76] Status Report on the LHC Machine, CERN-RBB-2002-150 (2006).

[77] F. Pauss and M. Dittmar, "Experimental Challenges at the LHC", CMS CR 1999/008, 1999.

[78] V. Kundrát and M. Lokajíček, Phys. Lett. B661 (2005) 102, arXiv:hep-ph/0510040.

[79] The TOTEM collaboration, "TOTEM Physics", Proceedings of 17th Rencontre de Blois: 11th International Conference on Elastic and Diffractive Scattering. Château de Blois, France, 2005. arXiv: hep-ex/0602025.

[80] J. Kemmer and G. Lutz, Nucl. Instr. and Meth. A273 (1988) 588-598.

[81] C. Kenney et al., "Active-edge planar radiation sensors", Nucl. Instr. and Meth. A 565 (2006) 272-277.

[82] S. Parker, C. Kenney and J. Segal, "3D — A proposed new architecture for solid state radiation detectors", Nucl. Instr. Meth. A 395 (1997) 328-343;
C. Kenney, S. Parker, J. Segal, and C. Storment, "Silicon detectors with 3D electrode arrays fabrication and initial test results", IEEE Trans. Nucl. Sci.,

Vol. 46 nbr. 4 (August 1999) 1224-1236;
C. Kenney, S. Parker and E. Walckiers, IEEE Trans. Nucl. Sci. 48 n6 (2001) 2405.

[83] S. Parker and C. Kenney, "Performance of 3D architecture silicon sensors after intense proton irradiation", IEEE Trans. Nucl. Sci. Vol. 48 nbr. 5 (Oct 2001) 1629-1638.

[84] C. Da Via and S. Watts, "Can silicon detectors survive beyond 10^{15} n/cm^2", Nucl. Instr. Meth. A 501 (2003) 138-145.

[85] G. Antchev, D. Barney, W. Bialas, J. C. Da Silva, P. Kokkas, N. Manthos, S. Reynaud, G. Sidiropoulos, W. Snoeys and P. Vichoudis, "A VME-based readout system for the CMS Preshower sub-detector", IEEE Trans. on Nucl. Sci., Volume 54, Issue 3, Part 2, June 2007, 623-628.

[86] A. Racz et al.: The S-LINK 64 bit extension specification: S-LINK64, CERN EP 2003;
http://cmsdoc.cern.ch/cms/TRIDAS/horizontal/docs/slink64.pdf.

[87] G. Magazzu, A. Marchioro and P. Moreira, "The Detector Control Unit: An ASIC for the Monitoring of the CMS Silicon Tracker", IEEE Trans. Nucl. Sci., Vol. 51, 4 (August 2004), 1333-1336.

[88] I2C Bus Specification, Signetics (1992).

[89] PHOJET, http://www-ik.fzk.de/∼engel/phojet.html.

[90] PYTHIA, http://home.thep.lu.se/∼torbjorn/Pythia.html.

[91] J. Kaspar, "Influence of smearing effects on the TOTEM experiment", TOTEM-NOTE 2007-005.

[92] http://geant4.web.cern.ch/geant4/.

[93] R. Shankar, Nucl. Phys. B70 (1974) 168;
A. B. Kaidalov and K. A. Ter-Martirosyan, Nucl. Phys. B75 (1974) 471;
D. M. Chew and G. F. Chew, Phys. Lett. B 53 (1974) 191;
B. R. Desai et al., Nucl. Phys. B142 (1978) 258;
K. H. Streng, Phys. Lett. B166 (1986) 443;
K. H. Streng, Phys. Lett. B171 (1986) 313;

A. Bialas and P. V. Landshoff, Phys. Lett. B 256 (1991) 540;
A. Bialas and W. Szeremeta, Phys. Lett. B296 (1992) 191.

[94] UA8 Collaboration, "A Study of Inclusive Double-Pomeron-Exchange in $p\bar{p} \to pX\bar{p}$ at $\sqrt{s} = 630\,\mathrm{GeV}$", Eur. Phys. J. C25 (2002) 361-377, arXiv:hep-ex/0205037v3.

[95] http://www.w3c.org.

[96] M. Liendl, "Design and Implementation of an XML based object-oriented Detector Description Database for CMS", Technische Universität Wien, Fakultät für Mathematik und Geoinformation, Institut für Statistik und Wahrscheinlichkeitstheorie, 2003.

[97] M. Case, M. Liendl, F. von Lingen, "XML based Detector Description Language", CMS Note, 1 April 2005.

[98] Interactive Graphics for User Analysis (IGUANA), http://iguana.web.cern.ch/iguana/index.html.

[99] V. Talanov, V. Avati, M. Deile, D. Macina, "First results of the machine induced background estimation for the forward physics detectors in the IR5 of the LHC", LHC-PROJECT-NOTE-360.

[100] N. V. Mokhov et al., "Accelerator Related Backgrounds in the LHC Forward Detectors", Proceedings of the Particle Accelerator Conference PAC 2003.

[101] N. V. Mokhov, "The MARS Code System User's Guide", Fermilab-FN-628 (1995); N. V. Mokhov, "Status of MARS Code", Fermilab-Conf-03/053 (2003); http://www-ap.fnal.gov/MARS/.

[102] J. Kaspar, private communication.

[103] M. Deile, "Estimates on Machine-Induced Background in the Roman Pots", TOTEM-NOTE 2006-004.

[104] W. R. Leo, "Techniques for Nuclear and Particle Physics Experiments. A How-to Approach. Second edition.", Springer-Verlag, ISBN 0-387-57280-5, 1994.

[105] LHC Layout, http://www.cern.ch/lhclayout/.

[106] J. Kaspar, "Reconstruction of elastic events", TOTEM-NOTE 2007-007.

[107] M. Deile, "Algebraic Determination of Roman Pot Acceptance and Resolution with the $\beta^* = 1540\,\mathrm{m}$ Optics", TOTEM-NOTE 2006-002.

[108] K. Eggert, P. Aspell, R. Assmann, V. Avati, M. Deile, H. Niewiadomski, V. Previtali, E. Radermacher, and T. Weiler, "Detection of Diffractive Protons in IR3 at the LHC", in preparation.